Cranfield UNIVERSITY

PhD Thesis

# Conceptual Design Methodology for Blended Wing Body Aircraft

**Paulinus Peter Chukwuemeka Okonkwo**

May 19, 2016

School of Aerospace, Transport and Manufacturing · Cranfield University

# Conceptual Design Methodology for Blended Wing Body Aircraft

PhD Thesis

For obtaining the degree of Doctor of Philosophy in Aerospace Engineering at Cranfield University

Paulinus Peter Chukwuemeka Okonkwo

May 19, 2016

Supervisor: Prof Howard Smith

School of Aerospace, Transport and Manufacturing · Cranfield University

Cranfield
UNIVERSITY

Cranfield University
Department of
Aerospace Engineering

The undersigned hereby certify that he has read and recommend to the School of Aerospace, Transport and Manufacturing for acceptance a thesis entitled **"Conceptual Design Methodology for Blended Wing Body Aircraft"** by **Paulinus Peter Chukwuemeka Okonkwo** in partial fulfillment of the requirements for the degree of **Doctor of Philosophy**.

Dated: May 19, 2016

Supervisor:

Prof Howard Smith

# Abstract

The desire to create an environmentally friendly aircraft that is aerodynamically efficient and capable of conveying large number of passengers over long ranges at reduced direct operating cost led aircraft designers to develop the Blended Wing Body(BWB) aircraft concept. The BWB aircraft represents a paradigm shift in the design of aircraft. The design offers immense aerodynamics and environmental benefits and is suitable for the integration of advanced systems and concepts like laminar flow technology, jet flaps and distributed propulsion. However, despite these benefits, the BWB is yet to be developed for commercial air transport. This is due to several challenges resulting from the highly integrated nature of the configuration and the attendant disciplinary couplings. This study describes the development of a physics based, deterministic, multivariate design synthesis optimisation for the conceptual design and exploration of the design space of a BWB aircraft. The tool integrates a physics based Athena Vortex Lattice aerodynamic analysis tool with deterministic geometry sizing and mass breakdown models to permit a realistic conceptual design synthesis and enables the exploration of the design space of this novel class of aircraft. The developed tool was eventually applied to the conceptual design synthesis and sensitivity analysis of BWB aircraft to demonstrate its capability, flexibility and potential applications. The results obtained conforms to the pattern established from a Cranfield University study on the Blended Wing Body Aircraft and could thus be applied in conceptual design with a reasonable level of confidence in its accuracy.

# Dedication

This thesis is dedicated to my late parents, Mr and Mrs Edwin Okonkwo who despite all odds worked tirelessly to give me a decent life.

# Acknowledgements

I will like to specially appreciate my supervisor, Prof. Howard Smith, for his insight, wisdom, patience and supervision. I also seize this medium to appreciate Petroleum Technology Development Fund (PTDF) for funding this project. I am deeply indebted to the Nigerian Air Force for releasing me to embark on this study. I also appreciate the 'GENUS skunkworks' crew; Dr David Sziroczak and Squadron Leader Godwin Abbe for the cooperation, technical assistance and the friendship developed over several late night studies in the course of this research. I will also like to appreciate Dr Gareth Davies, Dr Sola Adesola, Dr David Judt and Quintain Mecentenggart for their support with proof reading my thesis and providing useful advice on ways to structure and improve the thesis.

My sincere thanks goes to Pastor Biyi Ajala and the entire Holding Forth the Word Ministry for their prayers and moral support. I also wish to thank all members of the Cranfield Pentecostal Assembly for their prayers and support in the course of this academic pursuit.

My thanks also goes to my bosses Air Commodores CN Udeagulu and PO Jemitola for all their assistance. To my friends; Commanders GM Ciroma and OB Ayoade (Nigerian Navy), Wing Commanders PU Okwuego and IB Musa as well as Squadron Leader JK Kalau and Major MU Ugbong, thanks for always been there for me and for your encouragements. It meant a lot.

I wish to thank my siblings, Priscilla, Hyacinth, Jude, Chinyere, Ifeoma and Tochukwu, thanks a great deal for believing in me.

I reserve special mention for my wife, Tayo, for her prayers, unflinching love and provisions throughout the period of the PhD as well as for her patience and exceptional understanding with the extra hours I had to spend away from home. God bless you. To my lovely kids, Maya and Michelle, thanks a great deal for brightening my world. Your smiles and 'Daddy I love you' were reinvigorating and gave me reasons to endure the days of frustrations on the research.

Most of all, I will like to thank the Almighty God for the gift of life, wisdom and understanding to undertake this research. To God be the glory.

Cranfield, United Kingdom
May 19, 2016

Paulinus Peter Chukwuemeka Okonkwo

# Contents

# List of Figures

# List of Tables

# Nomenclature

## Latin Symbols

| | | |
|---|---|---|
| $am$ | Aircraft acceleration | $m/s^2$ |
| $C_D$ | Drag coefficient | - |
| $c_r$ | Root chord | $m$ |
| $c_t$ | Tip chord | $m$ |
| $dist_{TO}$ | Total distance required for take-off | $m$ |
| $e$ | Oswald efficiency factor | - |
| $E_{max}$ | Maximum endurance | - |
| $ft$ | feet | feet |
| $g$ | Acceleration due to gravity | $m/s^2$ |
| $h_s$ | Screen Height | $m$ |
| $h_t$ | Height at the end of transition | $m$ |
| $K$ | Induced drag correction factor | - |
| $m_{AC}$ | Mass of Airconditioning System | $kg$ |
| $m_{bgge}$ | Mass of baggages | $kg$ |
| $m_{fuelTO}$ | Mass of fuel for take - off | $kg$ |
| $m_{furn}$ | Mass of furnishing | kg |
| $m_{hydr}$ | Mass of Hydraulic System | $kg$ |
| $m_{inst}$ | Mass of instruments | $kg$ |

| | | |
|---|---|---|
| $m_{nacgrp}$ | Mass of nacelle group | $kg$ |
| $m_{pax}$ | Mass of passengers | $kg$ |
| $mf_{cr}$ | Mass at the end of cruise | $kg$ |
| $mfuel_{desc}$ | Mass of fuel required for descent | $kg$ |
| $mfuel_{reg}$ | Mass of regulatory fuel | $kg$ |
| $n$ | Load factor | - |
| $n_{eng}$ | Number of engines | - |
| $r$ | Radius of Arc | $m$ |
| $R_f$ | Range function | $m$ |
| $s_s$ | Distance to the screen height | $m$ |
| $s_{accgo}$ | Accelerate - go distance | $m$ |
| $s_{accstop}$ | Accelerate - stop distance | $m$ |
| $s_{desc}$ | Distance covered to decelerate | $m$ |
| $s_{ec}$ | Distance travelled during climb | $m$ |
| $s_{FA}$ | Distance to the start of final approach | $m$ |
| $s_{TMA}$ | Distance from the TMA to the touchdown point | $m$ |
| $sa_{land}$ | Air distance in landing | $m$ |
| $sg_s$ | Ground distance from end of transition to screen height | $m$ |
| $sg_t$ | Ground distance to transition height | $m$ |
| $sg_{land}$ | Ground run distance in landing | $m$ |
| $T$ | Static thrust | $N$ |
| $t_c$ | Time to climb to screen height | $s$ |
| $t_g$ | Time for ground-roll | $s$ |
| $t_s$ | Time required to reach screen height | $m$ |
| $t_t$ | Time for transition | $s$ |
| $T_{desc}$ | Thrust required to maintain ROD | $N$ |
| $t_{ec}$ | Time to climb to a given height | $s$ |
| $T_{id}$ | Idle thrust per engine | $N$ |
| $T_{maxCont}$ | Thrust at maximum continuous setting | $N$ |
| $T_{reg}$ | Regulatory thrust | $N$ |
| $t_{TMA}$ | Time in the TMA | $s$ |
| $u_i$ | Relative speed | - |
| $V_1$ | Critical engine failure speed | $m/s$ |

| | | |
|---|---|---|
| $V_2$ | Take - off climb speed | $m/s$ |
| $V_t$ | Transition speed | $m/s$ |
| $V_{app}$ | Approach speed | $m/s$ |
| $V_{cr}$ | Cruise speed | $m/s$ |
| $V_{LOF}$ | Lift - off speed | $m/s$ |
| $V_{mdi}$ | Minimum drag speed | $m/s$ |
| $V_{TAS}$ | True airspeed | $m/s$ |
| $V_{td}$ | Touch - down speed | $m/s$ |
| $wi_{cr}$ | Mass at the beginning of cruise | $kg$ |

# Greek Symbols

| | | |
|---|---|---|
| $\eta_f$ | Fuel Efficiency | % |
| $\eta_{th}$ | Thermal Efficiency | % |
| $\gamma$ | Climb gradient | % |
| $\lambda$ | Taper Ratio | - |
| $\omega$ | Fuel weight ratio | - |
| $\sigma$ | relative density | - |
| $\gamma_{ht}$ | Heat capacity ratio = 1.4 | - |

# Subscripts

| | |
|---|---|
| $_{app}$ | approach |
| $_{cr}$ | cruise |
| $_{desc}$ | descent |
| $_{EAS}$ | equivalent airspeed |
| $_{eng}$ | engine |
| $_{FA}$ | final approach |
| $_{id}$ | Idle |
| $_{land}$ | landing phase |
| $_{mean}$ | mean |
| $_{reg}$ | regulatory |
| $_{s}$ | screen height |

| | |
|---|---|
| $TAS$ | true airspeed |
| $td$ | touch - down |
| $TMA$ | terminal manoeuvring area |
| $t$ | transition height |

# Abbreviations

| | |
|---|---|
| **AAA** | Advanced Aircraft Analysis |
| **ACARE** | Advisory Council for Aeronautics Research in Europe |
| **ACFA2020** | Active Flight Control for Flexible Aircraft 2020 |
| **APU** | Auxiliary Power Unit |
| **AR** | Aspect Ratio |
| **ATC** | Air Traffic Control |
| **AVD** | Aerospace Vehicle Design |
| **AVL** | Athena Vortex Lattice |
| **BFL** | Balanced Field Length |
| **BLD** | Boundary Layer Diverter |
| **BLI** | Boundary Layer Ingestion |
| **CAE** | Computer Aided Engineering |
| **CDE** | Computational Design Engine |
| **CMBF** | Columned Multi Bubble Fuselage |
| **CPU** | Central Processing Unit |
| **CST** | Class Shape Function Transformation |
| **CWB** | Carry - through Wing Box |
| **DLL** | Dynamic Link Library |
| **EAS** | Equivalent Air Speed |
| **EPNL** | Effective Perceived Noise Level |
| **ESDU** | Engineering Science Data Unit |
| **EU** | European Union |
| **FLOPS** | Flight Optimisation Software |
| **FPR** | Fan Pressure Ratio |
| **GA** | Genetic Algorithm |
| **GD** | General Dynamics |

| | |
|---|---|
| **GMDSO** | GENUS Multi - variate Design Synthesis Optimisation |
| **GUI** | Graphic User Interface |
| **H2O2** | Hydrogen Peroxide |
| **IDEA** | Integrated Design and Engineering Analysis |
| **IDE** | Integrated development Environment |
| **IEEE** | Institute of Electrical and Electronics Engineers |
| **IPPD** | Integrated Product and Process Development |
| **IWB** | Integrated Wing Body |
| **JNI** | Java Native Interface |
| **KEAS** | Knots Equivalent Air Speed |
| **kg** | Kilogram |
| **km** | Kilometer |
| **LAWGS** | Langley Wireframe Geometric Standard |
| **LEthanol** | Liquid Ethanol |
| **LFC** | Laminar Flow Control |
| **LMethane** | Liquid Methane |
| **LOX** | Liquid Oxygen |
| **MBF** | Multi Bubble Fuselage |
| **MDC** | McDonnell Douglas Corporation |
| **MDO** | Multi Disciplinary Optimisation |
| **MGC** | Mean Geometric Chord |
| **MLG** | Mass of Landing Gears |
| **MLM** | Maximum Landing Mass |
| **MOB** | Multidisciplinary Optimisation of a Blended Wing Body |
| **MTOM** | Maximum Take off Mass |
| **MVO** | Multi-variate Optimisation |
| **N2O4** | Dinitrogen Tetroxide |
| **NACRE** | New Aircraft Concept Research |
| **nm** | Nautical Mile |
| **OEM** | Operating Empty Mass |
| **OS** | Operating System |
| **PASS** | Program for Aircraft Synthesis Studies |
| **PFW** | Passenger - driven Flying Wing |

| | |
|---|---|
| **PIO** | Pilot Induced Oscillations |
| **PR** | Pressure Recovery |
| **RFI** | Resin Film Injected |
| **ROC** | Rate of Climb |
| **ROD** | Average Rate of Descent |
| **SAI** | Silent Aircraft Initiative |
| **SFC** | Specific Fuel Consumption |
| **SHABP** | Supersonic/Hypersonic Arbitrary Body Program |
| **SI** | International System |
| **SLS** | Sea Level Static |
| **SP** | Structural Parameter |
| **TAS** | True Air Speed |
| **TMA** | Terminal Manoeuvring Area |
| **TSFC** | Thrust Specific Fuel Consumption |
| **UDMH** | Unsymmetrical Dimethylhydrazine Liquid Ethanol |
| **US** | United States of America |
| **VELA** | Very Efficient Large Aircraft |
| **VLM** | Vortex Lattice Methods |
| **ZFM** | Zero Fuel Mass |

# Other Symbols

| | |
|---|---|
| 2D | 2 - Dimensional |
| 3D | 3 - Dimensional |
| $\bar{\bar{c}}$ | mean aerodynamic chord |
| $\bar{c}$ | mean geometric chord |

# Chapter 1

# Introduction

## 1.1 Background and Motivation for Study

Before the renewed interest in unconventional aircraft configurations, the design of aircraft had shifted from innovative exercise to merely seeking for potential improvement in the efficiency of the *conventional tube and wing* design[1]. However, having reached the limit of conventional design coupled with a growing demand for an environmentally friendly, aerodynamically efficient aircraft that can carry large number of passengers over long ranges at reduced direct operating cost[2], the BWB aircraft was conceptualised.

The BWB has low noise signature because it does not require flaps for take - off and landing nor tailplane for pitch control. This eliminates the need for trailing edge and possibly leading edge devices. Furthermore, the BWB emits less pollutants due to reduced fuel burn and propulsive efficiency in addition to a low noise signature. In a research conducted by Mistry [3] to determine the airframe with the least noise characteristics from a list of 96 aircraft configurations, the discrete BWB airframe, shown in Figure 1.1, obtained the highest score of 64.3% compared to the most optimal high by - pass ratio conventional aircraft, which got 58.7% of the total available points. The airframes were assessed on 12 attributes with noise as the main objective function [3].

The BWB offers increased range and payload capacity due to 27% reduction in fuel burn per seat leading to reduced direct operating costs [1, 2]. These advantages are enabled by blending a lift generating centre - body housing the payload with conventional outer wings, to obtain a compact *aerodynamically efficient flying wing* providing structural,

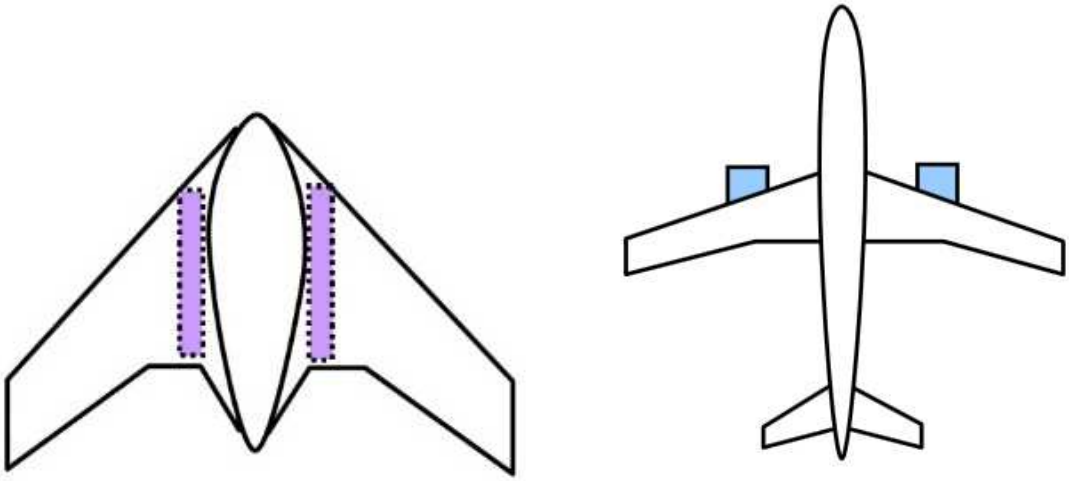

(a) Discrete BWB

(b) High By - pass Ratio Conventional Aircraft

**Figure 1.1:** Discrete BWB Airframe and the High By - pass Ratio Conventional Aircraft Used in Noise Assessment.

aerodynamic and payload synergy [4, 5]. The BWB however differs from a pure flying wing in that a pure flying wing has straight leading and trailing edges with no definite fuselage. Payloads in a flying wing aircraft are stored in the main wing structure. On the other hand, a BWB consists of a *flattened fuselage* for accommodating payload [6]. A plan - view of a flying wing showing the internal span - wise distribution of passenger and cargo bays and the location of the mean aerodynamic chord (dashed line) and its quarter chord point is shown in Figure 1.2. A perspective view of the BWB design is shown in Figure 1.3.

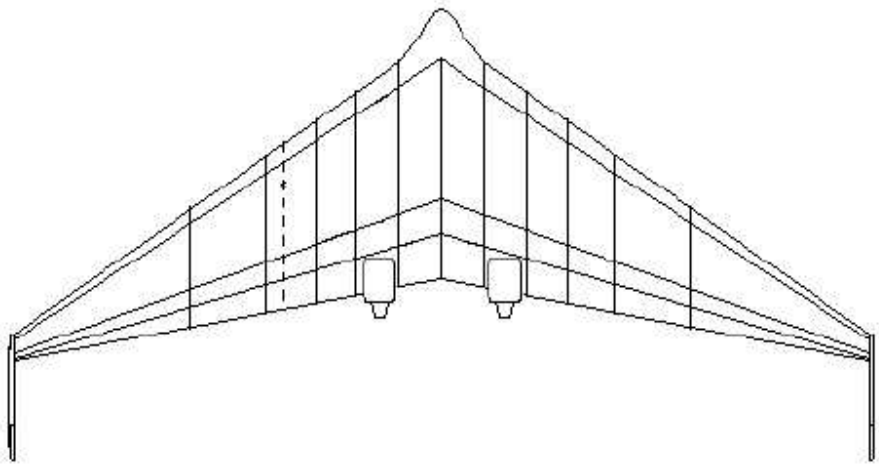

**Figure 1.2:** A Plan View of a Flying Wing Aircraft[6].

Other advantages of the BWB design includes 15 - 20 % increased lift to drag ratio (L/D)

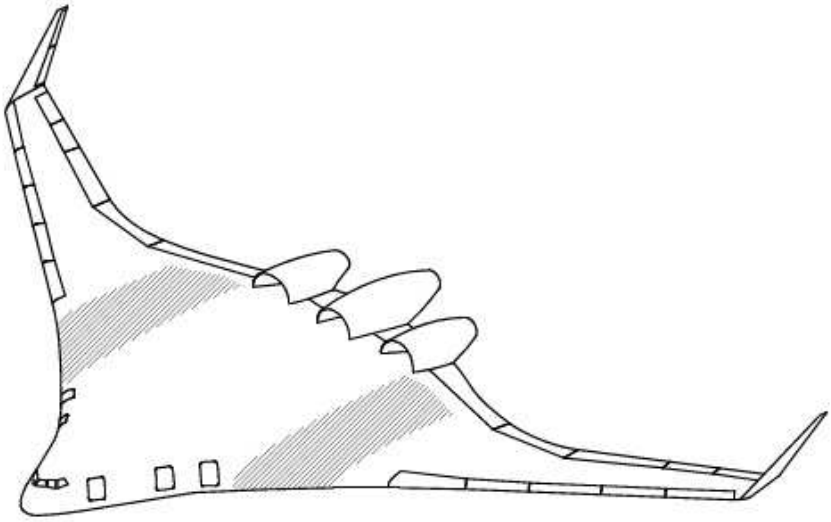

**Figure 1.3:** A Plan View of the Blended Wing Body Aircraft[6]

due to reduced drag resulting from a 33% lower wetted surface area compared to a conventional tube and wing aircraft [1]. The effect of the foregoing is a 12% decrease in operating empty weight and a lower acoustic signature [1, 4]. Despite these attractive potentials, the BWB is yet to be developed into a commercial airliner due to several challenges. The challenges include stability and control deficiencies, propulsion - airframe - aeroacoustic integration issues and the intricacies of achieving optimal trade - offs from conflicting design requirements in a tightly coupled aircraft configuration. In order to minimise these challenges, researchers have continued to apply different concepts and design techniques in BWB aircraft design.

Traditionally, aircraft design is categorised into the conceptual, preliminary and detail design phases. The conceptual phase identifies market requirements, decides on the most appropriate configuration and conducts initial sizing of aircraft geometry. The preliminary phase employs intermediate fidelity tools to effectively assess the performance and feasibility of the design before deciding whether to proceed to the detailed design phase. In the detail design phase, the design is extended to such a level that it can be manufactured and sold.

Within the traditional aircraft design phases, trade studies could be performed using carpet plots or the 'try and cut' approaches. This is because conventional or 'Kansas type' aircraft could easily be decomposed into different parts with distinct functions. This reduces number of variables that need to be manipulated to achieve a design aim. The case is however different in unconventional configuration where tight disciplinary couplings

and greater complexity does not allow for decomposition of airplane into distinct parts. For instance, in a BWB, the wing is also the fuselage, an inlet for the engines and a pitch control surface. Consequently, parametric trade studies with carpet plots are no longer sufficient to handle resulting design trade - offs due to increased number of variables. Hence, the need for multi - variate optimisation.

Optimisation is a *methodology for design of complex engineering systems and subsystems which coherently exploits the synergism of mutually interacting phenomenon*[7]. In order to formulate an optimisation scheme for this study, there is the need to develop a design synthesis tool for conceptual design of the BWB.

## 1.2 Aim of the Research

The aim of this research was to develop a multi - variate design synthesis and optimisation tool that enables a knowledgeable user to accurately and rapidly perform the conceptual design synthesis as well as methodically explore the design space of the BWB commercial passenger transport.

## 1.3 Objectives of the Research

The objectives of this research are:

1. To develop algorithms for the estimation of several variables within an aircraft design synthesis.

2. To incorporate packaging module early in the conceptual design process.

3. To create a multi-variate optimisation tool to rapidly perform the conceptual design synthesis and analysis of the BWB commercial passenger aircraft.

4. To explore the design space of the BWB aircraft configuration.

## 1.4 Structure of the Thesis

This thesis reviews evolving trends involving current state of the art methodologies and techniques in the design of the BWB airplane in Chapter 2. Chapter 3 discusses the methodologies and techniques developed for the design synthesis. This is followed by the implementation and creation of the design tool in Chapter 4. Chapter 5 presents and discusses some results obtained using the tool while Chapter 6 highlights major findings, limitations and recommendations potential areas for future studies on the subject.

# Chapter 2

# Literature Review

## 2.1 Introduction

Interest in the design of the BWB has risen dramatically over the past few years following the recognition of the huge potentials of the configuration over conventional fixed wing aircraft. Consequently, there has been increased research activities to develop concepts, design techniques and evolve technologies that will minimise the observed challenges and facilitate the realisation of a BWB commercial passenger transport aircraft. However, many of the findings have been documented in isolation because research evolves and has often been conducted in parallel. Hence the need to carry out an exhaustive review of the existing BWB research to identify existing gaps in knowledge.

The most prominent publications on the BWB airplane design are those by Liebeck [1] and Martinez-Val et al.[8, 9]. Liebeck compiled Boeing researches on the BWB [1], while Martinez-val et al.[8, 9] highlighted the prospects and challenges of a 'C' and 'U' types flying wing airplanes. Despite these efforts, no comprehensive review of emerging trends and concepts in BWB design has ever been undertaken. In this Chapter, relevant publications on the BWB is reviewed in order to identify state of the art concepts as well as highlight challenges in BWB design. To this end, a brief history of the development of the BWB is presented followed by discussions of multidisciplinary challenges, potentials and proposed solutions to BWB design.In addition, the applications of multi - variate optimisation in BWB design shall be examined.

It is imperative to state that efforts have been made to separate the challenges and benefits by disciplines. However, due to the strong inter-disciplinary couplings in BWB airplane configuration, occasional disciplinary overlaps might be observed.

## 2.2 History of Tailless/Flying Wing Design

Recent resurgence in BWB research began in 1988 following Dennis Bushnell challenge to academia and industry to develop innovative concepts for long-range passenger transport [10]. However, the idea of a tailless flying wing airplane has been around for a long time. The first recorded tailless flying wing aircraft was the D-8 aircraft designed by John Dunne in 1911 [2, 11]. The D - 8, shown in Figure 2.1, is a tailless biplane with swept wing and washout to prevent *premature tip stall* and improve pitch stability [11–13].

**Figure 2.1:** The D-8 Tailless Aircraft at the 1914 Farnborough Airshow [14].

In the years between 1924 and 1931 [11], Captain (Later a Professor) Hill designed a series of tailless aircraft(Figure 2.2) known as the Hill's Pterodactyl. These aircraft culminated in the MK IV, the first tailless aircraft capable of looping and rolling manoeuvres [11]. The main features of the Pterodactyl series are its flight - controlled variable sweep, operated to trim the aircraft at different loading conditions [11].

Convinced of the aerodynamic benefits of fewer non-lifting surfaces, Jack Northrop[12, 16] established the Northrop's Corporation in 1927 to explore the potentials of the flying wing configurations. The Corporation developed a *semi-flying wing* aircraft in 1928 and the N-1M pure flying wing in 1940 [12, 16]. The semi - flying wing aircraft shown in Figure 2.3 comes fitted with external control surfaces and curried outrigger twin booms [12, 16].

**Figure 2.2:** Westland-Hill Pterodactyl V Aircraft with Fully Moving Wingtips[15].

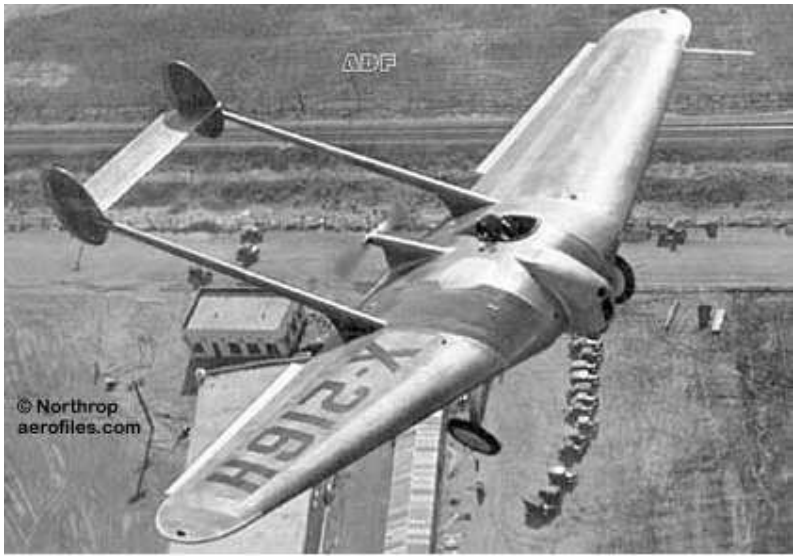


**Figure 2.3:** The Northrop Semi -flying Wing Aircraft (Source:Smithsonian NASA Museum).

The N-1M 'pure' flying wing aircraft, shown in Figure 2.4, incorporates ground -controlled variable sweep, dihedral and control surfaces [12]. The aircraft can also change its centre of gravity location and tip configuration while on the ground. Overall, the N-1M, with its elevons and wing - tip drag rudders, performed creditably well and proved the possibility of the flying wing concept. However, the engines hidden in the airfoil suffered from overheating while the drooped wing tips used for stability were found to be unnecessary[12]. Nonetheless, the performance was sufficient to convince the United States Air Force to award Northrop Corporation the contract to assess the feasibility of a flying wing bomber [12].

The N-9M (Figure 2.5) was developed as a scaled mock - up of the proposed bomber. The N-9M is an 18 m span twin - engine aircraft with a take - off weight of 6326 kg [17]. This is approximately one - third the size of the subsequently developed long range heavy bombers, the XB - 35 and YB - 35. The XB - 35 aircraft (Figure 2.6), which came into service in 1946, is powered by four piston engines, each driving two contra - rotating four - blade pusher propeller through a long shaft and gear box [17]. The YB - 35, on the other hand, is powered by jet engines. Both the XB - 35 and the YB -35 were unstable

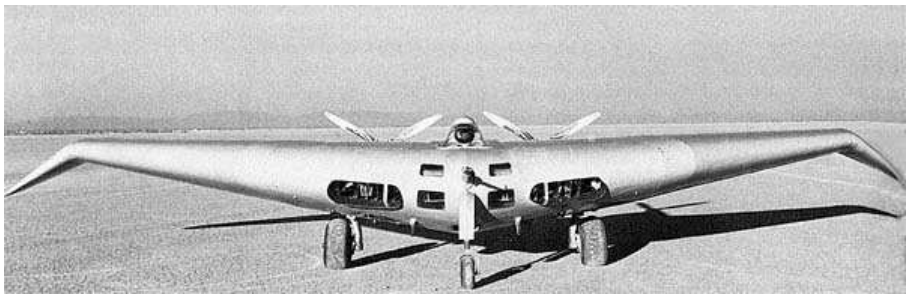

**Figure 2.4:** The Northrop N-1M Aircraft (Source:Smithsonian NASA Museum).

**Figure 2.5:** The Northrop Northrop N-9M Aircraft(Source:Smithsonian NASA Museum).

with poor handling qualities [18]. Both design suffered from engine/gearbox problems. Despite these defects, they provided practical knowledge on the design of flying wing bombers which later proved useful in the development of the YB - 49 in 1947 and the famous Northrop - Grumman B2 Spirit in 1981 [11, 12]. The success of the Northrop - Grunman B2 - Spirit shown in Figure 2.7 spurred renewed interest in the BWB configuration [19].

Other notable proponents of the flying wing concept were the Horten brothers. The Horten brothers, Walter and Reiman Horten [12], worked on the flying wing concept from 1931 until 1944. In the process they developed the Ho - series flying wing aircraft. These aircraft incorporates inboard flaps, elevons and tip-mounted drag rudders [12]. The Horten brothers are credited with the development of the world's first turbojet - powered flying wing aircraft, the Ho - IX [11, 12] shown in Figure 2.8.

The BWB aircraft, as it is known today, was conceptualised in 1988 by Robert Liebeck of the then McDonnell Douglas Corporation (MDC) now Boeing Company [12, 16, 20]. The aircraft provides improved aerodynamic efficiency by merging the fuselage and wing sections into a single lifting surface [12, 16, 20]. Subsequently, in 1997, the BWB con-

**Figure 2.6:** Northrop XB - 35 Piston - engined Long - range Bomber (Source: Virtual Aircraft Museum).

**Figure 2.7:** 'B2-Spirit' Stealth Bomber (Source: Xairforces Military Aviation Society).

figuration was adopted in the design of a 17 ft span, radio - controlled model aircraft, the BWB - 17 (Figure 2.9), by a combined team of researchers from MDC, NASA and Stanford University.

Following the success of the BW - 17, NASA further explored the possibility of applying

**Figure 2.8:** Turbojet Powered Ho-229 Flying Wing Aircraft(Source:Military Factory).

**Figure 2.9:** BW - 17 Radio Controlled Model Aircraft(Source:Stanford University).

the BWB tailless aircraft concept to commercial passenger transport. This led to the birth of the BWB - 450 in 2003 [1]. The BWB - 450 (Figure 2.10), is a 450 passenger capacity commercial transport airplane incorporating an ultra - efficient engine technology with Boundary Layer Ingestion (BLI) inlets and Active Flow Control [1]. The BWB - 450 design heralded several NASA programs that studied the feasibility of using the BWB

concept for commercial passenger transport. The 450 - passenger capacity was selected because it permits the validation of developed design tools and methods with the A380 conventional tube and wing aircraft [1].

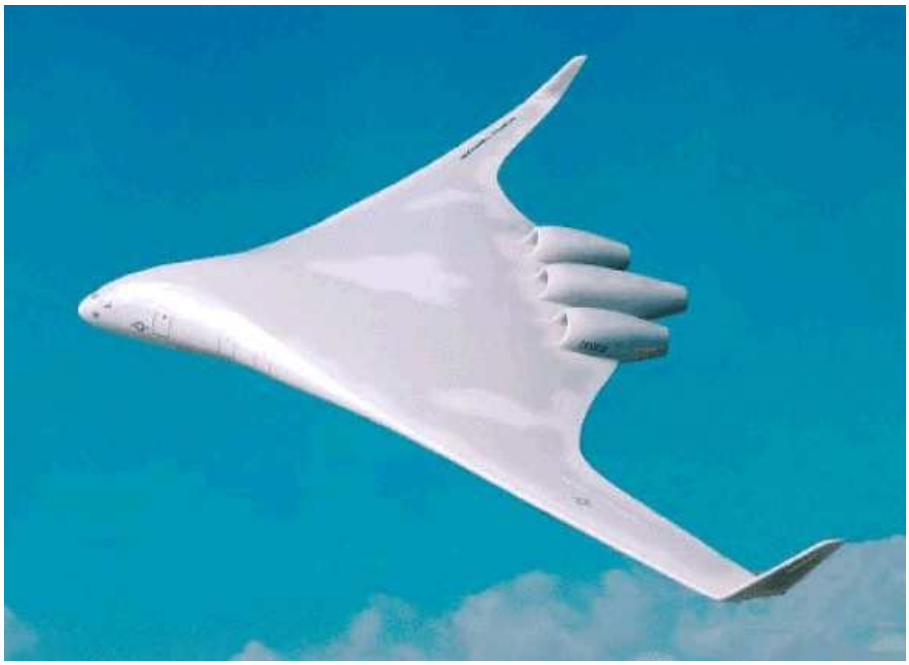

**Figure 2.10:** BWB - 450 Commercial Passenger Transport Aircraft(Source:NASA).

The Quiet Green Transport study is a NASA Revolutionary Aerospace Systems Program to assess potential technologies that could be implemented on the BWB commercial transport in order to minimise noise and pollutant emissions [21]. The Quiet Green Transport Aircraft is derived by integrating distributed liquid hydrogen fuel cell propulsion system unto a BWB - 450 geometry [21]. This radically advanced propulsion system eradicates toxic emissions and the formation of consistent contrails. In addition, the concept reduces the areas exposed to noise level of 55 dBA or above, during take off and landing, by 10% [21]. This minimises the noise available at FAA certification points by about 8 - 22 dB Effective Perceived Noise Level (EPNL) [21]. However, a drastic technological advancement would be required to realise the overall objectives of the Quiet Green Concept. This is because the concept relies on the hydrogen - based fuel cell which is still much heavier than conventional aircraft engines [21].

The anticipated benefits of the BWB concept spurred several organisations into researches on various aspects of the aircraft. Notable among the researches is the European Union (EU) 5 - tiered project to develop innovative, efficient, long - range, large - capacity, passenger transport and cargo aircraft [22]. The project comprised 3 wholly funded EU

framework Programs and a program jointly funded by the EU and the United States (Figure 2.11).

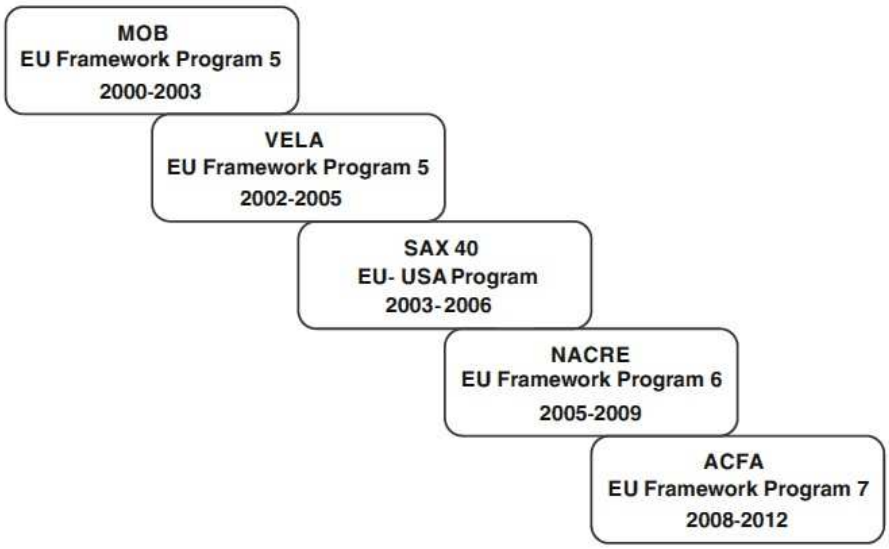


**Figure 2.11:** European Union Sponsored BWB - Related Research Programs [22].

The 3 EU Framework Programs are the 5th, 6th and 7th EU Framework Programs respectively. The 5th EU Framework Program consists of the Multidisciplinary Optimisation of a Blended Wing Body (MOB) and the Very Efficient Large Aircraft (VELA) projects. The MOB project is a 3 year research project carried out in distributed environments across 4 European countries [23]. The project involved 15 partners [23, 24]. This includes 3 aerospace companies, 4 research institutes and 8 universities [23, 24]. The aim of the MOB project was to develop tools and methods that will enable distributed design teams to create innovative and complex aeronautical products using either commercial off the shelf methods or proprietary codes [23, 24]. Using, a modified Cranfield designed "BW - 98" airframe (Figure 2.12) as the baseline, the MOB project created a Computational Design Engine (CDE) for the multidisciplinary design and optimisation of a BWB [25]. The CDE integrates multi - level disciplinary tools with multi - disciplinary optimisation methodologies to determine the optimal range at constant maximum take off weight [25].

The VELA project was set up to develop the necessary skills set, capabilities and methodologies appropriate to the design and optimisation of Very Efficient Large Aircraft concepts. The VELA project, which ran from 2002 - 2005, investigated 2 extremes of a BWB configuration, in terms of the placement and blending of the outboard wing. This gave rise to the 2 baseline concepts VELA 1 and VELA 2 shown in Figures 2.13 and 2.14 respectively.

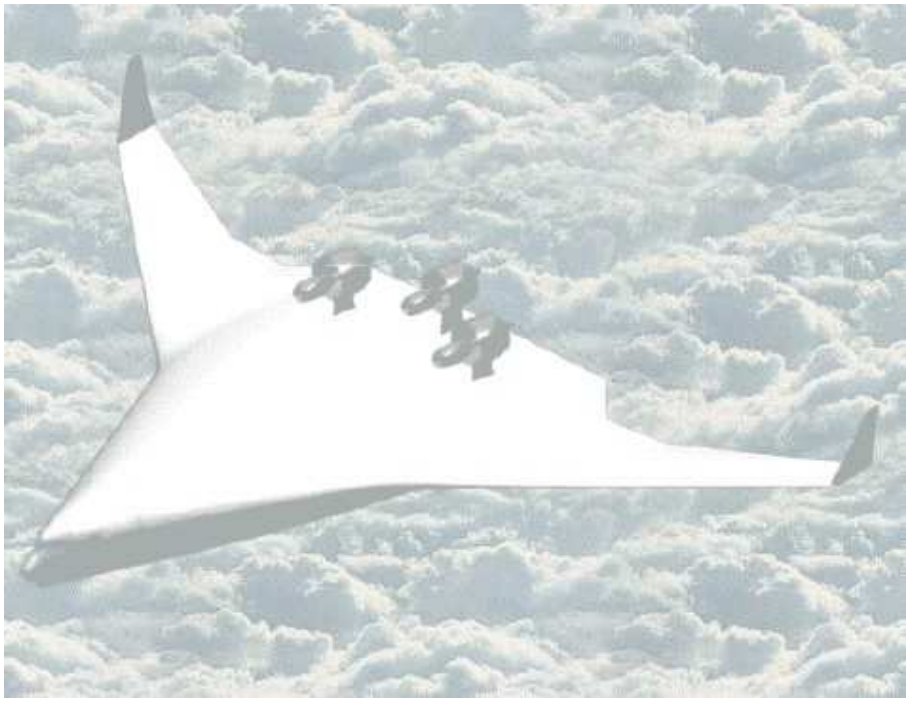

**Figure 2.12:** Cranfield BW - 98 BWB Study [2].

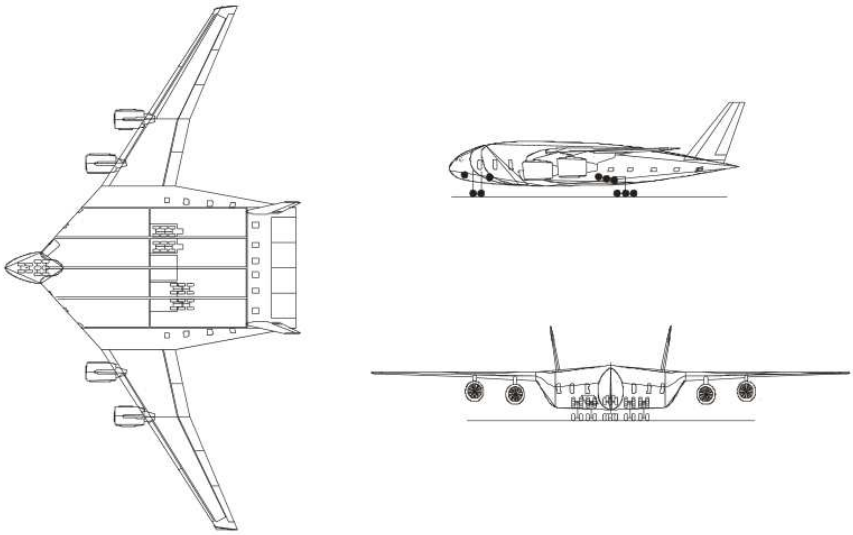

**Figure 2.13:** VELA 1 Baseline Concept (Source:DLR, Martin Hepperle 2005).

From the 2 baseline concepts, the VELA 3 configuration shown in Figure 2.15 was derived. The VELA 3 is a 750 passenger capacity, 3 class cabin arrangement, very long - range aircraft powered by 4 under the wing mounted engines. The VELA 3 is designed to cruise at Mach 0.85 to a range of 7200 nm. The VELA 3 aircraft offers improved stability and control issues together with a $4-8\%$ better L/D and a 10% savings in the maximum take off weight [22].

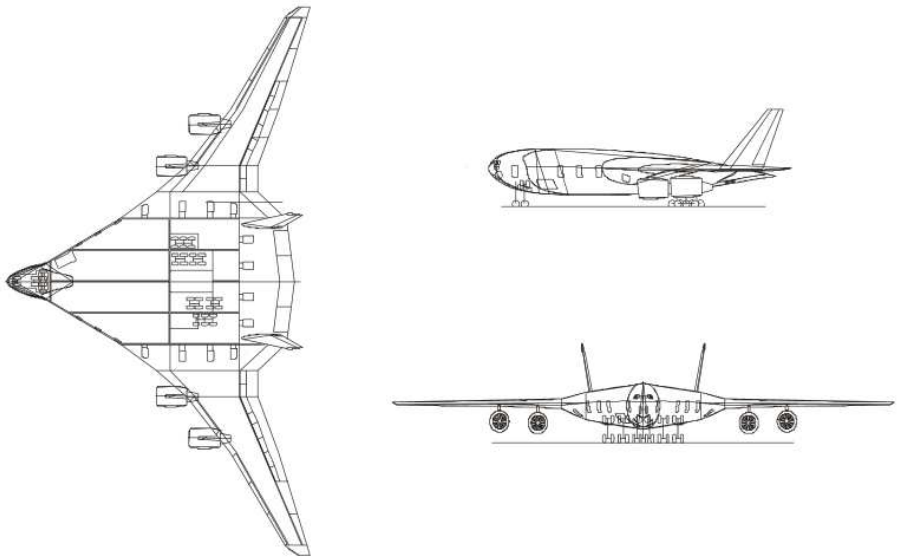

**Figure 2.14:** VELA 2 Baseline Concept(Source:DLR, Martin Hepperle 2005).

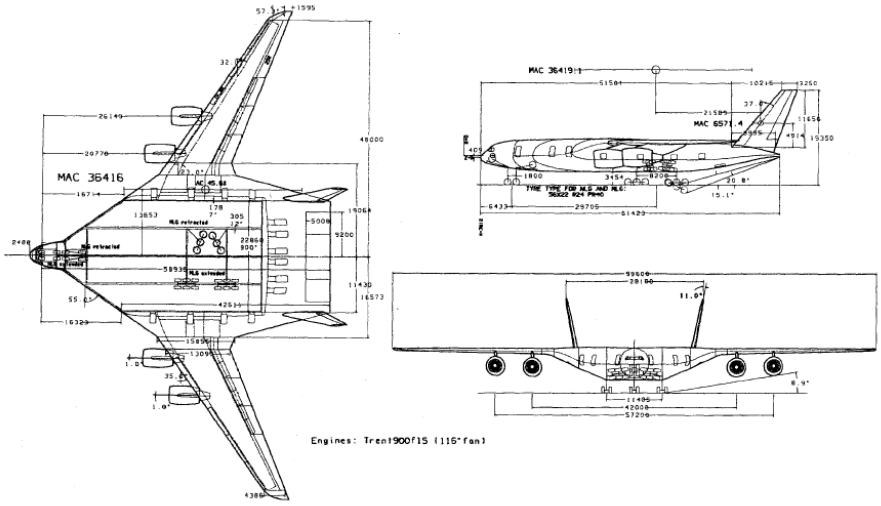


**Figure 2.15:** 3 - view Diagram of the European Commission Very Efficient Large Aircraft (Source:DLR, Martin Hepperle 2005).

The 6th Framework Programme also known as the New Aircraft Concept Research (NACRE) began in 2005 and was completed in 2009. The NACRE Integrated Project was undertaken to integrate and validate technologies that enable new aircraft concepts to be assessed [26]. The Project, which was led by Airbus, involved 36 partners from 13 European countries [22, 26]. The Project advanced the design of BWB aircraft through its Passenger - driven Flying Wing (PFW) configuration. The NACRE - PFW version 1 (Figure 2.16) was derived by modifying the centre - body airfoil and applying outer wing twist to the VELA 3 aircraft. This gives the NACRE - PFW1 a satisfactory aerodynam-

ics, stability and control characteristics [26].

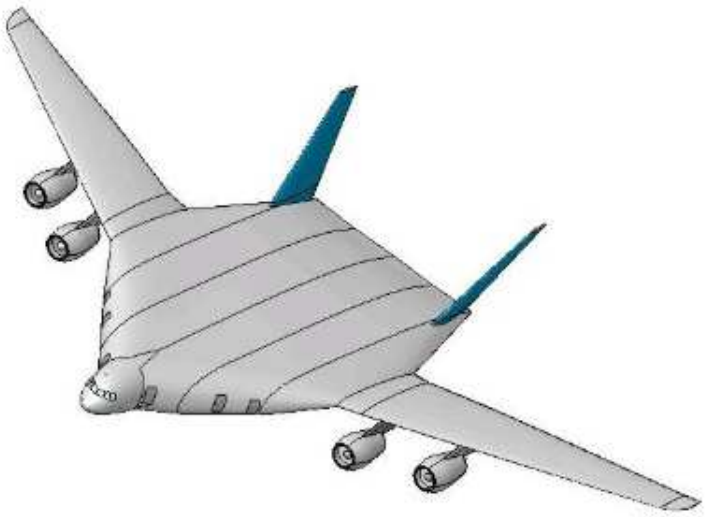

**Figure 2.16:** Surface Model of the NACRE PFW - 1 Aircraft [26].

Similarly, NACRE PFW2 shown in Figure 2.17 is derived from NACRE - PFW1 by changing the location of the engines, kinematics and position of the main landing gear. The engines were moved from under - to over - the - wing to minimise forward radiated noise. The kinematics of the main landing gears which retracted sideways were made to retract longitudinally and positioned beside instead of behind the cargo bay. Adjustments were also made to the aisle widths, position, alignment and shapes in order to reduce the evacuation time from 90 seconds to 84 seconds [26]. Further to this, the plan - form area was reduced from 2050 $m^2$ to 2000$m^2$ resulting in increased aspect ratio, reduced wetted surface area and an increase in the length of the centre - body. This lowers structural mass and improved aircraft performance. Split aileron was also introduced to enhance the handling quality as well as the stability and control of the NACRE - PFW 2. These modifications, however, created compressibility challenges with a destabilizing effect on the zero lift pitching moment, limited lift on the centre body due to cabin floor slope and high induced drag resulting from loaded outboard lift distribution [26].

Cambridge and MIT investigated the feasibility of an ultra low noise, fuel efficient BWB, dubbed the Silent Aircraft Initiative((SAI)). The SAI was an ambitious 3 - year project by a team of 35 researchers, beginning in 2002. The research was aimed to design an airplane that is radically quieter than current passenger transport aircraft. The result of the SAI is the SAX - 40 BWB aircraft unveiled in September, 2006. The SAX - 40 BWB aircraft, shown in Figure 2.18, integrates novel and advanced noise minimising air-

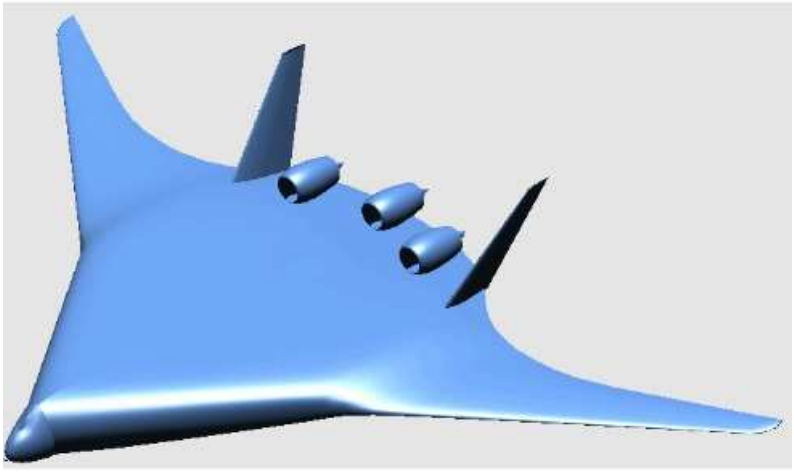

**Figure 2.17:** Surface Model of the NACRE PFW - 2 Aircraft [26].

craft systems with aerodynamic shaping of the airframe centre-body [27]. Implemented systems include embedded boundary layer ingesting distributed propulsion system, deployable drooped leading edge and faired under-carriage. Others are the combined use of thrust vectoring and elevons for control in low speed approach. These features increased the induced drag through in - efficient lift distribution thus providing the needed drag for a quiet approach [27]. Additionally, The SAX - 40 aircraft incorporates variable area exhaust nozzles to tune the engine for optimum cruise efficiency [28].

According to Hileman [27], a 215 passengers capacity SAX - 40 with a design range of 5000 nm and cruise speed of Mach 0.8 generates a far - field noise of 63 dBA [27]. This is 25 dB lower than the noise produced by the Boeing 777 - 200 aircraft. Additionally, since most of the features responsible for noise reduction also lower profile drag, the SAX - 40 aircraft offers a 25% improved fuel consumption. This is achieved through improved passenger miles per gallon, from 101 passenger - miles per gallon on the Boeing 777 to 124 passenger - miles per gallon [29] on the SAX - 40. According to Lee et al. [29], these figures were derived with assumed passenger weight of about 110 kg/passenger for the SAX and 100 kg/passenger for existing aircraft. Also, the specific fuel consumption of 0.49 Ib/Ib/hr used in the fuel burn prediction includes the effect of BLI [27]. Notable challenges limiting the realisation of the SAX - 40 design, which is scheduled for entry into service in 2030, are the manufacturing and scaling of the unique body shape which changes over the entire fuselage, inlet distortion noise and forced vibration issues due to non - uniform inlet flow [27].

The 7th Framework Programme focuses on the development of innovative active control concepts for advanced 2020 aircraft configurations. The project called Active Flight

**Figure 2.18:** Cambridge MIT Silent Aircraft Concept(Source:The Cambridge-MIT Institute).

Control for Flexible Aircraft 2020 (ACFA2020) involves 13 partners from 11 European countries [30]. The mandate for ACFA2020, which is derived from the strategic goal of the Advisory Council for Aeronautics Research in Europe (ACARE), is the design of an innovative ultra - efficient 450 passenger aircraft together with a robust, adaptive multi - channel control architecture suitable for the aircraft. The result of the 7th Framework Programme is a 450 capacity BWB aircraft with highly swept back centre - body and 2 podded turbofan engines as shown in Figure 2.19.

**Figure 2.19:** The ACFA BWB Configuration [22].

The TsAGI project was undertaken by Russia, in conjunction with Airbus and Boeing, to compare 4 new large aircraft configurations based on the VELA configuration. This

was necessary in order to asses the most critical issue affecting the design of the BWB. The study identified 3 candidate concepts for analysis. These are the Integrated Wing Body (IWB), lifting body configuration and a pure flying wing. With a 750 passenger capacity, a range of 13700 km and a cruise M0.85, these concepts were compared with a similarly designed conventional configuration in terms of the aerodynamics, weight and fuel efficiency. The results found the IWB as the most optimal configuration with a L/D ratio of 25 at a Mach 0.85. Additionally, it identified airworthiness requirement for emergency egress as the most critical design issue [31].

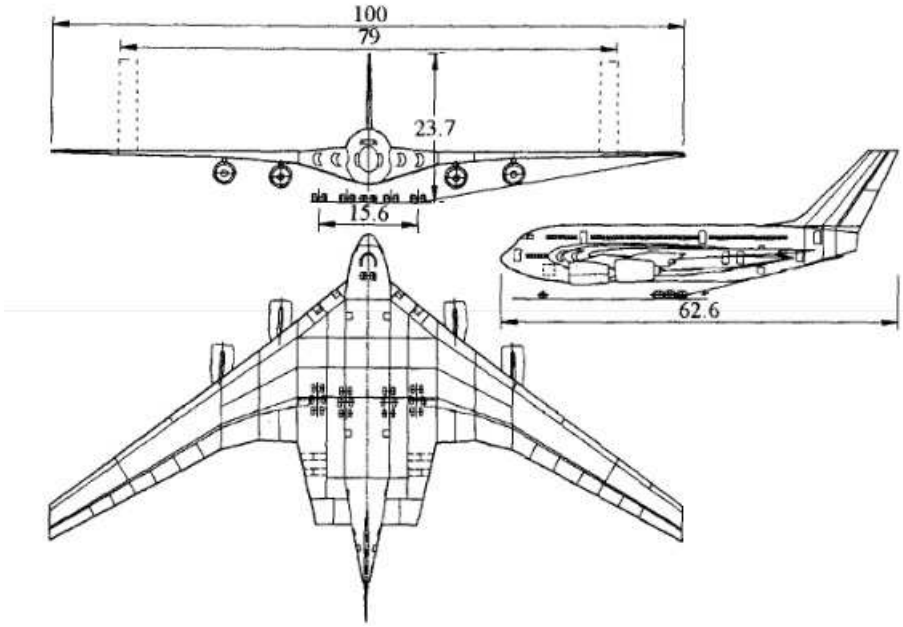


**Figure 2.20:** 3 - view Diagram of the Russian TsAGI Integrated Wing Body Aircraft.

Following on from these projects, Cranfield University Aerospace Vehicle Design Group, in 2011 conducted a preliminary design of a state of the art BWB ultra - high capacity configuration with BLI distributed propulsion system consisting of 2 turbo - shaft engines driving 14 electric fans [32] as shown in Figure 2.21. The foregoing studies highlighted the enormous potentials and advantages of the BWB but also exposed several design challenges which need to be addressed in order to realise the potentials of the BWB.

**Figure 2.21:** Cranfield BWB Design showing the BLI Distributed Propulsion System. (Source:Cranfield Aircraft Design Group).

## 2.3 Potentials and Challenges of the BWB Design

The BWB aircraft by virtue of its unique configuration and potential benefits is well suited to the role of environmentally - friendly, long - range, high - capacity airliner. However, issues of control and stability, cabin pressurisation and aircraft handling qualities amongst others need to be addressed. Consequently, it was necessary to review the potentials and challenges of the BWB airplane configuration with a view to identifying critical design issues which needs to be addressed. To aid understanding, these issues have been organised by disciplines.

### 2.3.1 Aerodynamics

The aerodynamic benefits of the BWB are derived from the integration of its 'fuselage' and wings to obtain low wetted surface area to volume ratio and reduced interference drag. This lowers total drag and provides higher L/D ratio compared to conventional configuration [33–35]. However, the BWB fuselage has a low aspect ratio. This results in a rapid increase in induced drag with lift coefficient thus generating a very low optimum lift coefficient [22]. Kozek et al. [22] compared the L/D ratio and optimum lift coefficient of a BWB and a Conventional aircraft with Carry - through Wing Box (CWB)(Figure 2.22). The study revealed that a BWB with 470 passengers has a L/D ratio of 24.2 and an optimum lift coefficient of 0.25 while the CWB with 464 passengers has a L/D ratio of 21.7 and an optimum lift coefficient of 0.47 [22]. The higher optimum coefficient obtained for the conventional aircraft is due to its high aspect ratio leading to a reduced induced drag [22].

Similarly, Liebeck [1], compared the effect of reduced wetted surface area on the lift coefficient of an 800 - passenger BWB and a conventional tube and wing aircraft of same capacity. This phenomenon was investigated by transforming a 650 square meter ball into a cylinder and a lifting body and then sizing the streamlined options to accommodate 800 passengers (Figure 2.23). Subsequently, following the integration of the wing, empen-

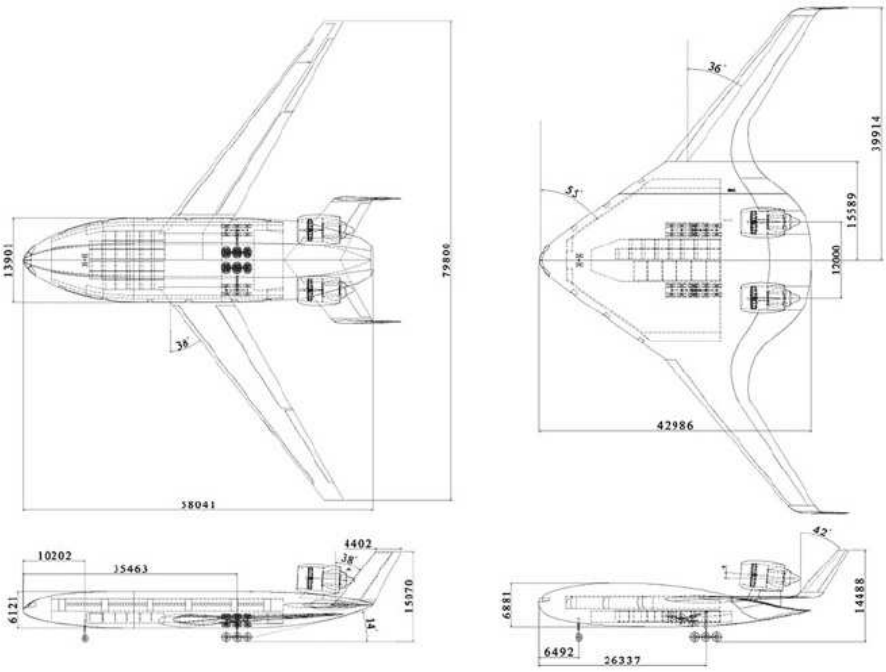


**Figure 2.22:** Sketch of the CWB (left) and the BWB (right).

nage and engines, Liebeck [1] showed that a conventional aircraft with 4 under the wing engines has a wetted surface area of 4100 square meters while the BWB with trailing edge BLI engines has only 2800 square meters for same passenger capacity. The 33% reduction in wetted surface area, lowers the BWB profile drag thus increasing the L/D by $10 - 15\%$ when compared to a conventional configuration. This result is supported in separate studies by Statzer et al.[12] and Moreno et al. [36].

Stazer et al. [12] compared the minimum drag coefficients of the XB - 35 flying wing with a wingspan of 52 m and the C - 5 conventionally configured military transport aircraft with a a span of 68 m. The result indicate a 47% decrease in the zero lift drag from 0.023 for the conventionally configured C-5 aircraft to 0.012 for the XB - 35 flying wing Bomber. Similarly, Moreno et al. [36] investigated the aerodynamic characteristics of an 800 passenger BWB aircraft and its conventional counterpart at Mach 0.82. The BWB model gave an $ML/D$ of 17.6 compared to 15.6 for a conventional configuration[36]. However, due to the strong coupling between disciplines on the BWB, a careful aerodynamic shaping of the BWB centre - body would be required in order to obtain the aerodynamics gains and satisfy stability and cruise deck angle requirements [1, 27, 37–39].

The requirement for the BWB cruise deck angle demands the use of positive aft - cambered centre - body airfoil in order to obtain the less than 3 degrees deck angle required

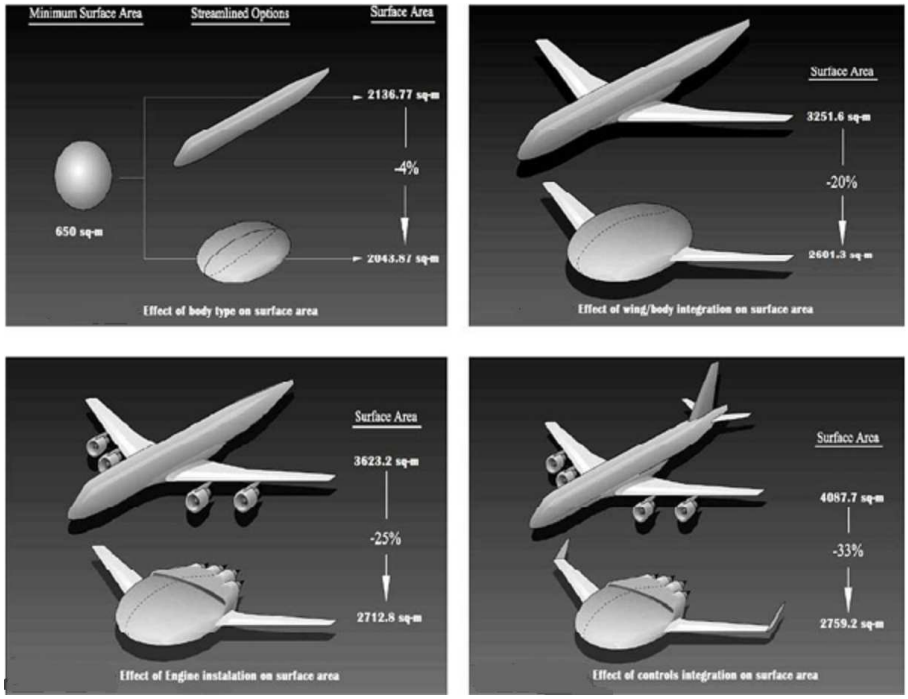


**Figure 2.23:** Transformation of a $650m^2$ Ball into a Conventional and BWB Aircraft.

in cruise [1, 27, 38–41]. Positive aft - cambered airfoil however generates a nose down pitching moment which increases the BWB trim requirement [1, 39]. Minimal aft-camber on the other hand causes the aerodynamic centre of pressure to coincide with the aircraft centre of gravity, thereby minimising nose-down pitching moment and enhancing the BWB pitch - trim and static stability [1, 27, 38, 39, 41].

Minimal aft - camber airfoil also *enhances external pre-compression* of upstream flow [27, 39] in BLI engine arrangement. This provides uniform flow at the engine inlet hence reducing the aerodynamic challenge of integrating an embedded BLI propulsion system [1, 27, 39]. Consequently, in order to satisfy the cruise deck angle, trim and engine-out control requirements and still retain the aerodynamic gains of the BWB, a multi - variate optimisation approach would be required to ensure conflicting constraints are satisfied. An illustration of the aerodynamic shaping of a BWB geometry for SAX - 40 is given in Figure 2.24. Unshaded area in the figure use airfoil interpolated from neighbouring sections.

The BWB cross - sectional area, unlike the conventional MD - 11 aircraft, is uniformly distributed along its span like a Sears - Haack body of minimum wave drag [1, 42] as shown in Figure 2.25. According to Equation 2.1, wave drag varies proportionally to the second derivative of the cross - sectional area. This suggests that a smooth, linear

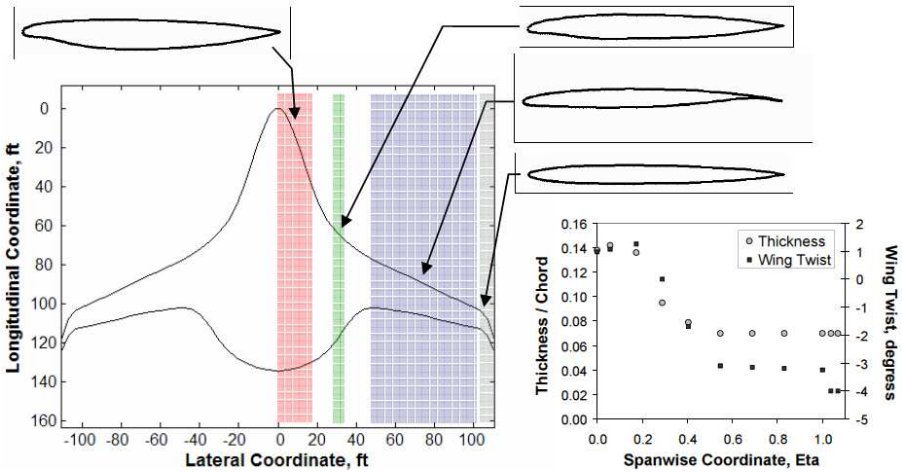


**Figure 2.24:** Aerodynamic Shaping of the SAX - 40 Aircraft [27].

variation of the cross - sectional area provides the least wave drag [42, 43]. Consequently, since the BWB geometry is smoothly defined with uniform area distribution across either sides of the centre-body, the BWB configuration is well suited for high speed flight. This is because high Mach number can be obtained with the BWB without the added cost of waist tailoring [1, 42, 43]. Nevertheless, higher Mach numbers increase installed engine specific fuel consumption thus decreasing payload weight fraction [42]. This influenced Liebeck [42] to investigate the effect of increasing Mach number on the aerodynamic efficiency, $ML/D$, of a BWB. The study shows that M0.9 provides maximum aerodynamic efficiency, $ML/D$. However, assessing the economic value of speed, in terms of $MP/D$, where $P$ is the payload weight, the study finds that maximum payload efficiency is obtained at Mach 0.85. These phenomenon is illustrated in Figure 2.26.

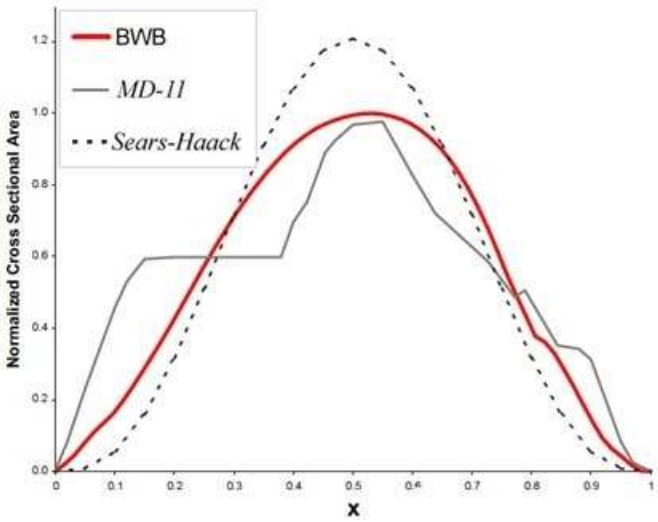


**Figure 2.25:** Cross-sectional Area Distribution of a Sears-Haack Body [1, 42]

$$\frac{D_w}{q_0} \approx \int_0^1 \int_0^1 S^{"}(x) S^{"}(\xi) log \frac{1}{\left| x - \xi \right|} \mathrm{d}x \mathrm{d}\xi \tag{2.1}$$

Where :
$D_w$ is the wave drag.
$q_0$ is the free stream dynamic pressure.
$S$ is the reference area.

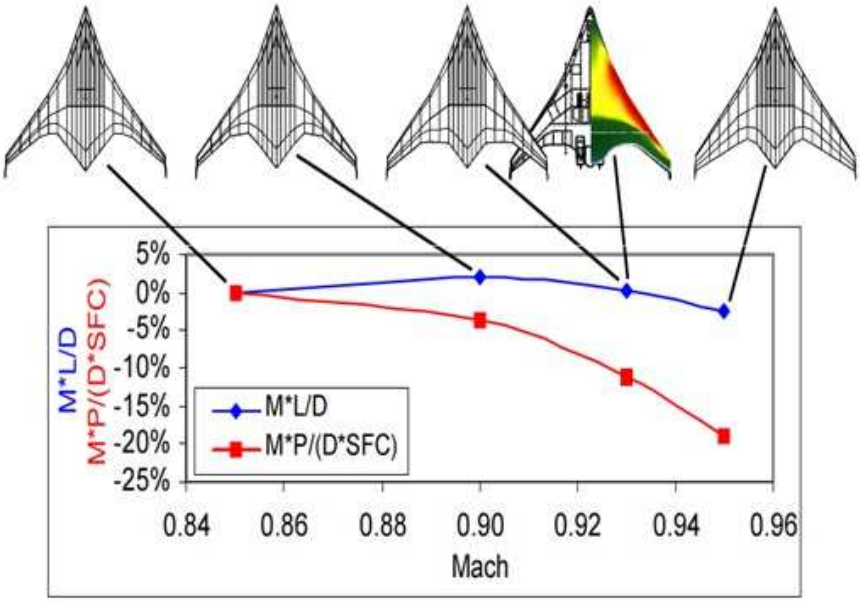


**Figure 2.26:** Variation of the BWB Plan - form, $ML/D$ and $MP/D$ with Mach Number [1, 42].

The BWB generates a near perfect elliptic span-wise lift distribution by combining reflexed centre-body airfoil for pitch-trim stability with outboard supercritical airfoils in wash-out arrangement [1]. The supercritical airfoil moves the outboard wing loading behind the aircraft centre of gravity counteracting the lift produced in the forward part of the centerbody [39]. Nevertheless, the outboard wing loading creates an excessive shock wave which increases the wave drag thus degrading aerodynamic efficiency [34]. Additionally, outboard wing loading increases bending moment and hence the required structural weight [34].

Liebeck [1] suggests the use of a moderately loaded outboard wing to optimise wetted area and strength of the shock wave, while Qin et al.[34] propose inboard shifting of the outboard wing loading. Shifting the outboard wing loading inboard alters the spanload distribution and shifts the aerodynamic centre closer to the centre of gravity [34]. This

improves trim requirements and decreases the wing bending moment thus reducing the required structural weight [34]. Hileman et al.[39] on the other hand advocate for the use of positive leading edge cambered airfoil with minimal aft-loading at the BWB centre-body to provide pitch trim and reduce flow Mach number at the engine inlet thus increasing the efficiency of BLI; minimal leading edge camber at the intersection of the centre-body and middle wing to minimise loading at that junction; symmetric profile at the winglets to minimise wave drag for winglets and supercritical airfoil with washout at the outboard wing.

According to Green et al. [44], the maximum L/D ratio of an aircraft, in subsonic cruise condition, is obtained from the ratio of the span and the square root of the product of induced drag factor and the wetted surface area as defined in Equation 2.2. This provides that the elliptic lift distribution provides the best L/D in cruise. However, it had earlier been established that the BWB is well suited for operation in the transonic cruise regime. Consequently,it is probable that the elliptic lift distribution which provides the least induced drag factor in subsonic cruise might be less attractive in transonic flight condition. This is because wave drag rather than induced drag is the main challenge in this regime. In view of this, Qin et al. [34] conducted a study to determine the most efficient span - wise lift distribution for the outer - wing of the BWB in transonic cruise condition.

$$\left(\frac{L}{D}\right)_{max} = \sqrt{\frac{\pi AR}{4kC_{d0}}} = b\sqrt{\frac{\pi}{kS_{d0}}} \tag{2.2}$$

This is derived in level flight condition and with the value of dynamic pressure at maximum L/D given by Equation 2.3.

$$(q)_{max} = 0.7 \times \left(PM^2\right)_{max} = W \times \sqrt{\frac{k}{\pi \times b^2 \times S_{d0}}} \tag{2.3}$$

Where:
$P$ = is static pressure in $N/m^2$.
$M$ = is the Mach number.
$b$ = is the span in $m$.
$W$ = is the maximum take-off weight of the aircraft in $N$.
$AR$ is the Aspect Ratio.
$C_{d0}$ is the zero lift drag coefficient.
$k$ = is the vortex or induced drag factor.
$S_{d0}$ = is the reference area at zero lift drag in $m^2$.

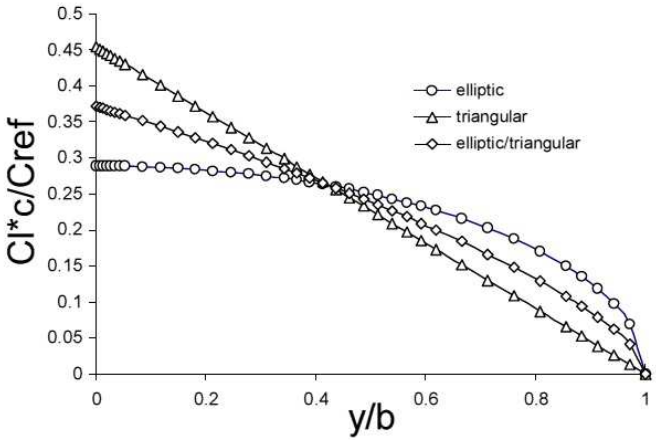


**Figure 2.27:** Investigated Span - wise Lift Distribution [34]

Adopting the EU MOB geometry with a span of 77.5 $m$ as the baseline, the twist and camber distributions are varied at the centre - body, inner and outer wings to obtain the elliptic, triangular and elliptic/triangular span - wise lift distribution shown in Figure 2.27. Then using continuous and adjoint optimisation methods and optimising for minimum total drag at M0.85, Qin et al.[34] find that elliptic lift distribution generates strong shock wave at the outer wing due to high local lift. This results in wave drag which diminishes aerodynamic performance. The averaged elliptic - triangular lift distribution, on the other hand, offers the least total drag and minimum trim requirement resulting in a 16% increase in L/D ratio compared to the baseline [34]. In terms of structural consideration, high outer wing loading increases bending moment thus requiring stronger and potentially heavier structures [1, 34]. Contrastingly, the triangular lift distribution has the least bending moment and hence the least structural weight [34].

In a related development, Siouris and Qin [45] investigated the aerodynamic effect of sweep on a BWB with constant twist and airfoil sections. The study varied the leading edge sweep angle of the outer wing leading from - 40° (forward sweep) to 55° (backward sweep). The geometry employed for this analysis is an optimised BWB with an aft sweep angle of 38.6°, span of 76$m$, an aspect ratio of 6.98, a mean chord length of 10$m$, a centre of gravity from trailing edge of 18$m$ and a trapezoidal area of 828$m^2$ [45]. Analysis was carried out in cruise condition at an altitude of 10000$m$ and a cruising speed of Mach 0.85 [45]. The study finds that forward sweep reduces tip stall but increases wave drag resulting in low L/D [45]. Additionally, forward sweep increases nose - up pitching moment leading to longitudinal instability [45].

Aft sweep increases tip stall but minimises wave drag. Additionally, aft sweep increases nose - down pitching moment leading to enhanced longitudinal stability [45]. Varying aft -

sweep angle between 20 and 40° increases L/D ratio by 80% at the optimised sweep angle of 38.6° (Figure 2.28) due to a substantial reduction in wave drag [45]. Further increases in aft-sweep angle, however, decreases L/D ratio and increases structural weight due to increased bending moment and structural stressing [45]. Additionally, a large aft-sweep angle displaces aircraft weight and centre of gravity creating adverse longitudinal moment and correspondingly increased trim drag [45].

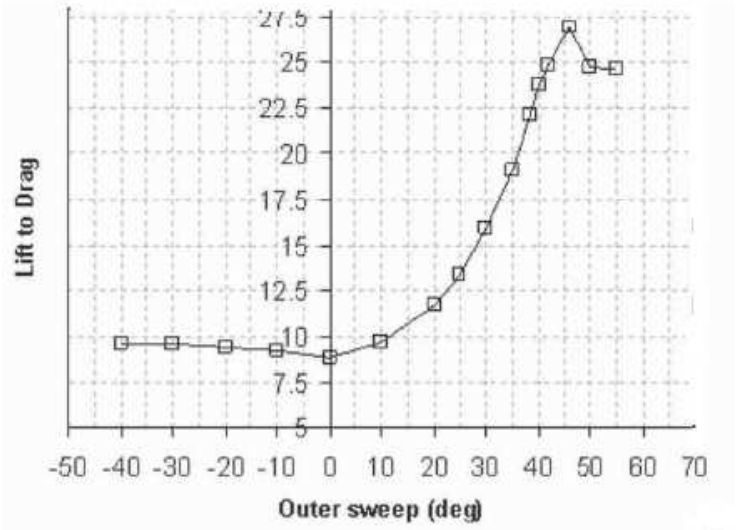


**Figure 2.28:** Effect of Varying Outer Wing Sweep Angle on Aerodynamic Characteristics of a BWB[45]

The BWB tends to have poor departure characteristics due to its lower maximum lift coefficient resulting from the absence of/or limited number of high lift devices [4]. Slats and slots could be used to improve the low speed maximum lift coefficient and to provide the desired angle of attack [4, 39]. However, stall recovery might be difficult because of the *hysteresis characteristics of slats and slots* [4]. Consequently, Liebeck advocates the use of outboard leading edge slats *for low - speed stall protection* [1]. Preferably, the drooped outboard leading edge slats is proposed to aid noise reduction [27, 46].

In view of the strong disciplinary interaction on the BWB, different combinations of geometric parameters produce desirable and undesirable characteristics in varying measures. Therefore, in order to obtain a BWB aircraft with specific desired performance, there is the need for a multidisciplinary study involving structural weight, aerodynamics and flight control and stability as well as performance models. This is akin to developing a design synthesis methodology to explore the design space of the BWB.

### 2.3.2 Flight Control and Stability

The tailless nature of BWB makes it better suited to exploit revolutionary control concepts like vectored thrust and active flight control [9]. Additionally, strong coupling of inertial forces, aerodynamic loads, elastic deformations and flight control system responses on the BWB also affect the performance and stability of the airplane [47]. For instance, mounting the engine over the wing near the trailing edge centralizes the thrust axis and brings the thrust vector closer to centre of gravity thereby producing less nose - down pitching moment and engine out yaw [48, 49]. This alleviates the BWB trim problems enabling the use of smaller control surfaces and reduced power demands [48, 49].

Trailing edge devices are not used as flaps because the BWB has no tail to trim out the resulting pitching moment [1, 13, 38]. Consequently, the maximum lift coefficient of a BWB is lower than that of a conventional configuration. Furthermore, due to the large reference area provided by the absence of non - lifted surface and the lift generating centre - body of the BWB, the configuration shows a lower wing loading compared to conventional configuration [1, 9].

Low wing loading reduces take - off and landing speeds thus decreasing the required field lengths. Also, it enables superior climb performance due to a higher rate of climb produced by the airplane. The increased rate of climb is derived from the much reduced airspeed required to generate the additional lift needed to increase altitude with a low wing loading. Furthermore, low wing loading enhances sustained turn performance. This because the aircraft is able to generate more lift for a given quantity of engine thrust compared to a conventional tube and wing aircraft. However, due to low wing loading, the BWB will produce maximum lift coefficient at a relatively higher angle of attack than a conventional aircraft. This leads to a high approach flight path. The attendant flight path attitude coupled with the higher wing surface area increases the sensitivity of the BWB to gust loads. This further increases the local angle of attack to near stall conditions, thereby decreasing control surface effectiveness [13, 41].

The BWB pitch trim requirement can be reduced using a reflexed centre - body airfoil because they generate zero pitching moment about the aerodynamic centre [27, 38, 39, 41]. However, a reflexed airfoil requires large twist which reduces the effective lifting area thus degrading cruise performance [27, 37–39, 50]. Additionally, a large twist entails large control surfaces and hence high control power to achieve rotation during take-off [27, 38, 39]. Valiyff [37] recommends the use of all-moving wing - tips to optimise lift distribution when the use of active controls is not viable.

The BWB has low pitch and yaw control authority due to its short moment arm [1, 51, 52] (Figure 2.29). Hence, multiple, rapidly moving control surfaces are required to provide sufficient control force for longitudinal and lateral control [1, 27, 35, 39]. Large down - force generated by negative elevon deflection however creates substantial loss in lift causing the BWB to first plunge before pitching to the desired angle of attack [35, 53]. This degrades flight path control especially during take-off rotation and landing flare. Furthermore, excessive power is required to actuate large multi-functional control surfaces with high hinge moments [1]. This feature of the BWB increases the challenge of improving lateral and longitudinal stability.

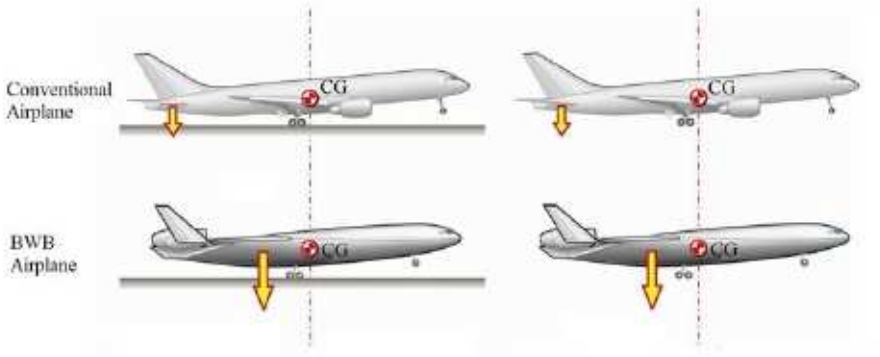


**Figure 2.29:** Comparison of Moment Arms and Pitch Control Effectiveness with Gears on Ground and In-flight Between a Conventional Aircraft and a BWB [35].

Several concepts have been applied to improve the stability and control of the BWB. These include thrust vectoring, aerodynamic shaping of the centre-body combined with advanced airframe design as well as the intelligent combination of elevons and belly flaps. Thrust vectoring generates the same pitching moment as a 10° elevon deflection [9]. However, while elevons unload the outer wings causing an increase in angle of attack, thrust vectoring will maintain the cruise deck angle below 3 ° [27, 39]. Nevertheless, thrust vectoring adds extra weight and complexity to the design [27, 39] as well as reduce the net axial thrust [13]. Additionally, thrust vectoring increases specific fuel consumption. Liebeck [1] proposes the use of elevons as primary pitch and roll control device while Hileman et al.[27] suggest using thrust vectoring at take - off climb-out and combined thrust vectoring and elevon deflection for take - off rotation.

Thrust vectoring is preferred at take - off climb - out because it improves climb - out performance and minimises the loss in L/D ratio associated with elevons deflection [27].

Nevertheless, by combining cambering and aerodynamic shaping of the BWB with elevons deflection and thrust vectoring, pitch trim and static stability could be enhanced without using a reflexed airfoil [27]. Other control device that could be used for pitch control is the belly flaps.

Staelens et al. [35, 53] studied the effect of belly flaps on lift coefficient and pitching moment of the BWB. The study shows that using belly flaps near the CG of the BWB (Figure 2.30) increases the static pressure ahead of the CG and decreases it aft, producing a pitch-up moment that helps to rotate the BWB during take - off and landing [35, 53]. Staelens finds that belly flap deployed to 90 ° increases the lift - off lift coefficient and enhances pitching moment by 35% and 10% respectively with only 10% increase in lift - off drag and a negligible loss in lift [35, 53]. Trimming the generated pitching moment could be a major issue though.

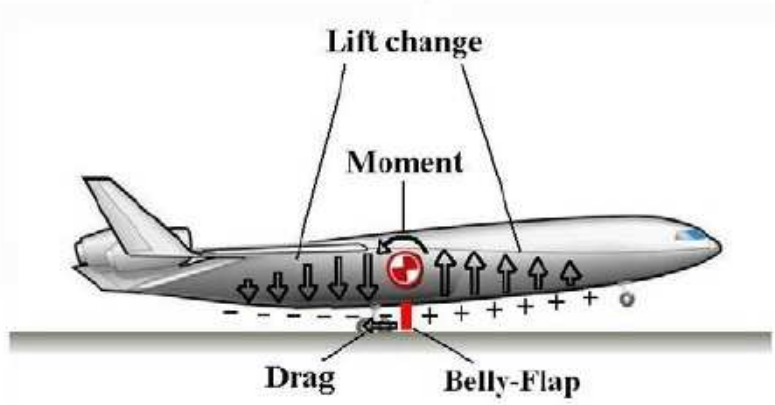


**Figure 2.30:** Pressure Fields Induced by Belly Flap on a BWB [35].

The BWB is subject to high yaw rates and auto - rotation tumble [4, 51, 54]. This calls for an effective means of providing sufficient yaw control and stability without a vertical tail [54]. Wildscheck et al. [54] demonstrated that simple winglet flaps are insufficient for yaw control especially in the one engine in - operative case because of their limited height and total winglet area. Thus, they recommend the use of crocodile flaps as effective yaw stabilization device [54]. This view is shared by Liebeck [1] who proposes the use of winglet rudders as primary directional stability and control surface while split outboard elevons are deployed in the low-speed engine - out condition.

### 2.3.3 Aero-structures

The BWB provides efficient payload distribution and permits over the wing engine placement. Additionally, the BWB centre - body generates lift due to its low aspect ratio thereby reducing the wing load. These features minimise wing bending moment and shear force, thus creating favourable inertia relief (Figure 2.31) and hence reduced structural weight[16, 40, 55–58]. Additionally, by blending the fuselage and outer wings, lower wetted surface area is obtained. This translates to a higher wetted aspect ratio and hence a structurally more efficient wing [40].

The box - shape nature of the BWB centre - body presents a structural design challenge. Because passengers are accommodated within the centre-body, the cabin is subjected to both pressure and span - wise bending loads [55, 56, 59–61]. The combined pressure and bending loads create very high non - linear stresses as shown in Figure 2.32. The non-linear stress arises because the BWB resists pressure loads by bending stresses unlike the uniform stretching or hoop stress that occurs in the cylindrical pressure vessels used in conventional aircraft. Under extreme manoeuvres or gusts, these non - linear stresses produce severe deformations and increased stress levels that are difficult to predict [8, 55, 56, 58–60].

Several structural concepts have been proposed to handle the high, non - linear stresses on BWB cabins. Among these concepts are the separate pressure shell (Also known as the double - skin vaulted shell) and the integrated skin and shell concepts (sometimes referred to as the thick flat sandwich shell) [1, 8].

The separate pressure shell concept shown in Figure 2.33 consists of a thin arched pressure vessel above and below each cabin creating an inner and outer skins together with inter-cabin walls [1]. The inner skin carries the pressure load in tension, the cabin walls support the weight of the structure above the cabin bay while the outer panel takes the bending loads and shear force due to aerodynamic loads acting on the aircraft [1, 2, 8]. The use of separate pressure vessel permits seamless integration of laminar flow control thus decreasing skin friction drag [8, 9, 62]. Additionally, separate pressure shell prevents fatigue crack propagation and increases bulking rigidity [8, 9]. Furthermore, separate pressure vessels would guarantee a lighter structure with *efficient load diffusion and fail-safe* characteristics [8, 9].

The major defect of the separate pressure shell, is that it requires the outer skin to be sized to carry pressure load should there be a rupture of the inner skin thereby incurring

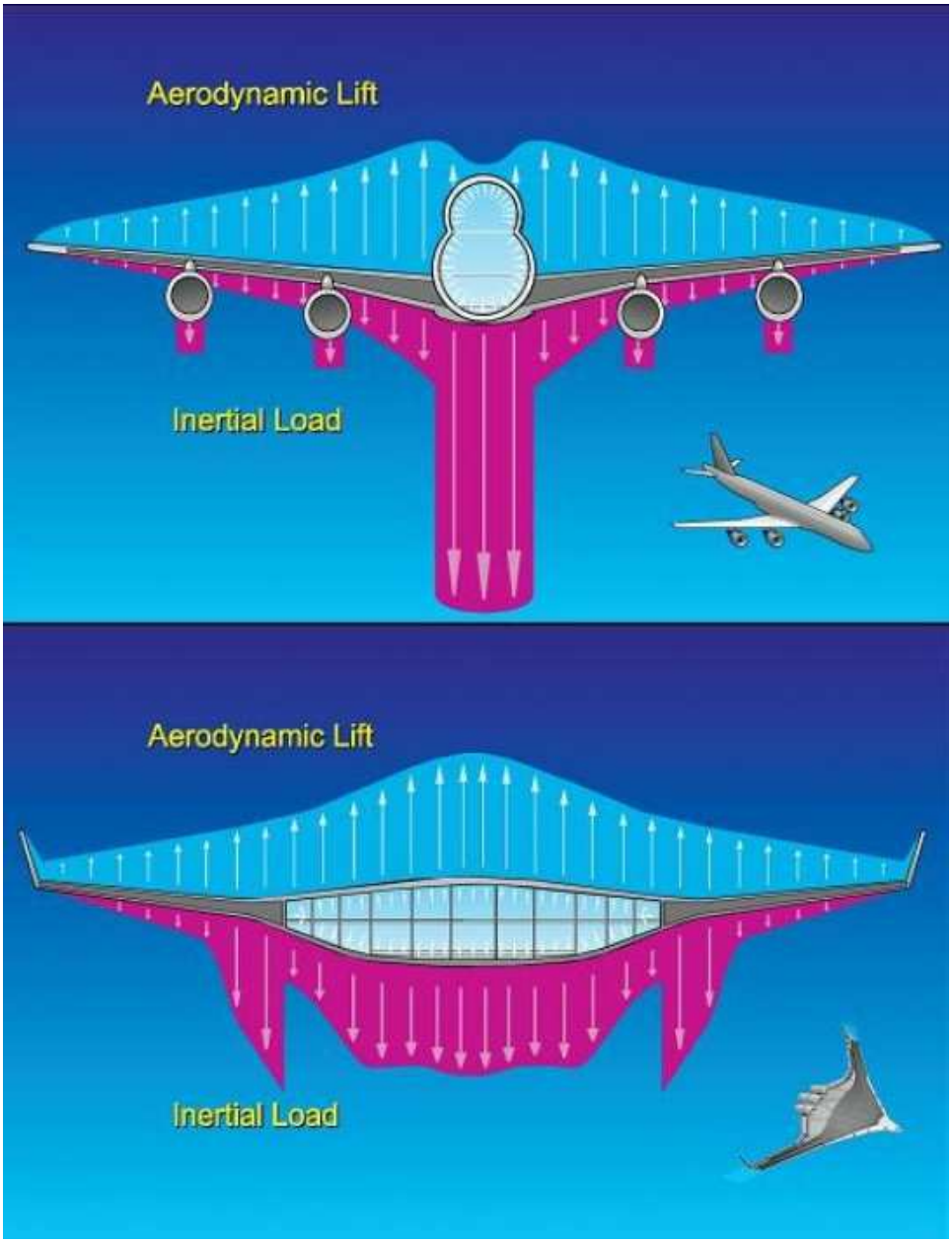


**Figure 2.31:** Comparison of the Aerodynamic and Inertia Load Distribution Between a Conventional Aircraft Configuration and the BWB [1].

extra weight [1]. Martinez-Val et al.[8] however argued that there would be no need to over-size the outer skin if the inner skin is appropriately sized, since pressure loss from rupture would then be minimal. Nevertheless, Bradley [63] suggests eliminating the double skin concept and sufficiently strengthening the outer skin to cope with pressure loads thus eradicating rupture concerns.

Bradley's design [63] matches Liebeck's second cabin concept[1] shown in Figure 2.34. In

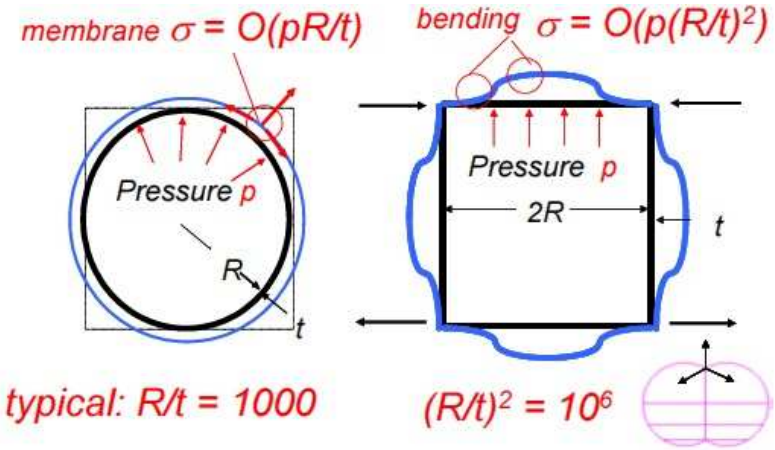


**Figure 2.32:** High Bending Stresses Resulting from the Effect of Pressure on the Box-like Shape of the BWB [61].

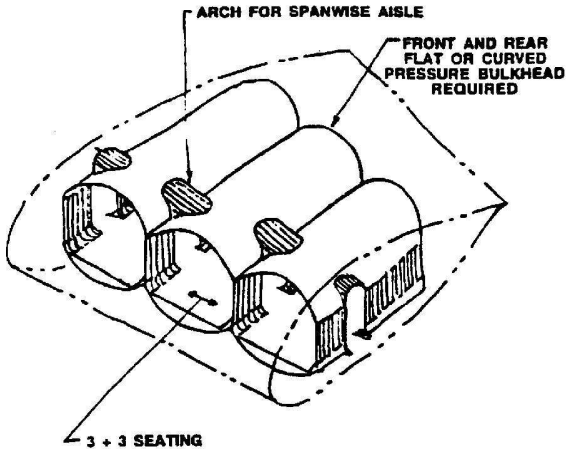


**Figure 2.33:** Liebeck's Separate Pressure Shell Concept [1]

Liebeck's integrated skin and shell design[1], pressure, bending and torque loads are taken by the thick sandwich structures at the top and bottom of the cabin [1]. The integrated skin and shell concept is robust and does not yield additional design demands in case of rupture [1, 63]. However, it is susceptible to non-linear stresses from the coupling of pressure and bending loads. This adds structural weight and increases maintenance demands [8, 61].

NASA developed the Multi Bubble Fuselage (MBF) shown in Figure 2.35. The MBF comprises 2 or more cylindrical fuselages sharing inter - cabin walls such that the inner membrane stresses counteract inter-cabin walls tensile stresses while the outer shell takes bending loads [61]. Additionally, the inter - cabin walls serves as the wing rib of the inner wing [55, 56, 59, 61]. However, the MBF is difficult to manufacture [56, 59, 64], hence the introduction of the Y - braced boxed fuselage [61].

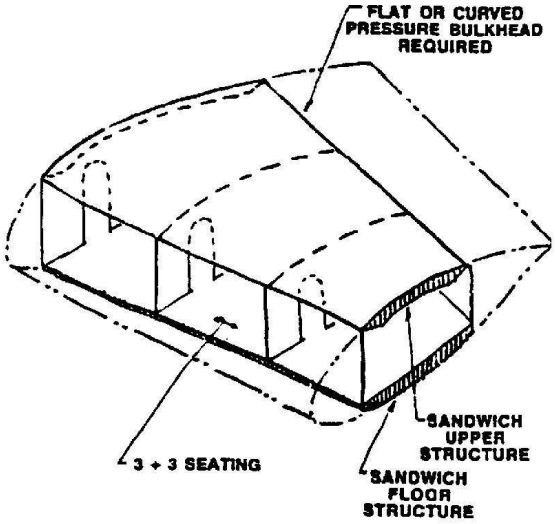


**Figure 2.34:** Liebeck's Integrated Skin and Shell Concept [1]

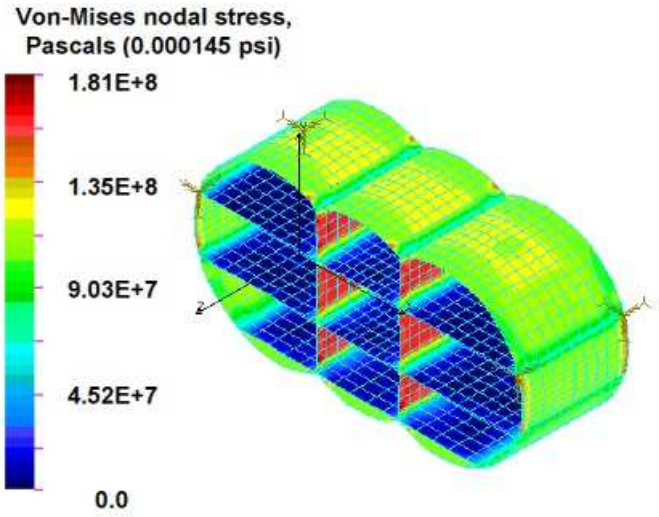


**Figure 2.35:** Nodal Von - Mises Stress Analysis of the NASA Multi-bubble BWB Fuselage Structure Concept [1]

The Y - brace shown in Figure 2.36 is designed with special Resin Film Injected (RFI) carbon composite with foam core. The Y - brace fuselage concept is easier to manufacture than the MBF [61]. Merits of the Y-brace include decreasing bending at the *roof joints and cabin walls* [61]. Additionally, the Y - brace increases the flexural rigidity while the RFI skin provides higher bending stiffness with minimal weight gain [61]. The Y - braced boxed fuselage is suitable for passenger and commercial cargo but cannot carry bulk loads [56].

Cho et al. [56, 59] investigated several structural concepts for the centre body of a BWB

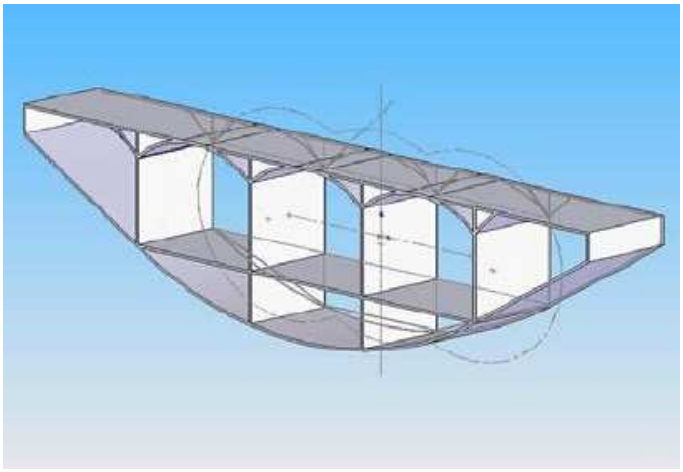

**Figure 2.36:** Vaulted Shell Y - braced BWB Fuselage Structural Concept [61]

military cargo aircraft. The study finds that the oval fuselage [56, 59] makes good use of available space to ensure efficient cabin design. However, there is an increase in bending stress and required structural weight due to decrease in curvature with growing oval radius [56, 59]. This led to the invention of the Columned Multi Bubble Fuselage (CMBF). The CMBF shown in Figure 2.37 is obtained by replacing inter - cabin walls of a MBF with *chord - wise equidistant columns* [55, 56, 59].

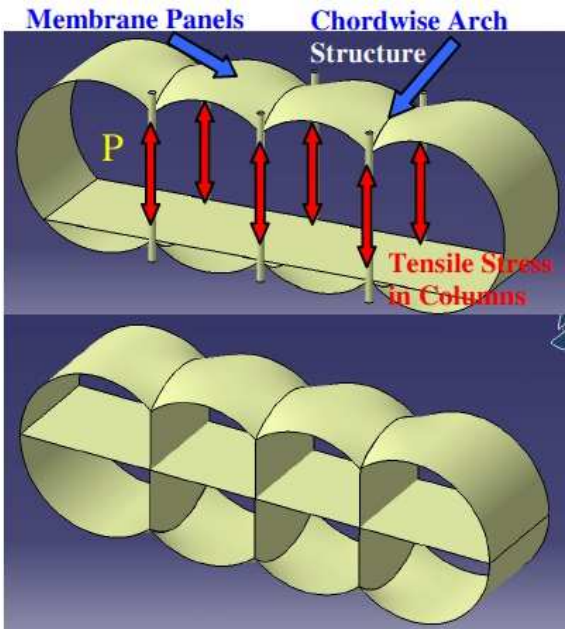


**Figure 2.37:** CMBF Subjected to Pressure Loads and its Application to Passenger Transport [55]

The CMBF is subjected to chord - wise bending stress at the *structural discontinuity of*

*the cylindrical panels* due to the absence of the inter - cabin walls [55, 56, 59]. However, by incorporating chord - wise and span - wise curvature to the CMBF, membrane stress offsets the tensile stress of the columns thus decreasing the stress level [59]. Consequently, the CMBF shows a 50% more deformation to combined pressure and bending loads compared to the MBF [59].

The severe CMBF deformation to combined pressure and bending loads influenced Cho et al.[59] to create a BWB fuselage structure with separate inner skin and outer panel to decouple the loads and provide buckling stability. The space between the inner and outer walls was also filled with ambient pressure to insulate the outer walls from pressure loads. This ensures the inner skin has sufficient stiffness to withstand cabin pressure loads [55]. The CMBF resists pressure loads resulting from membrane stress of the inner skin, while the bending load is taken by the outer walls [56]. This provides a lighter solution and eliminates the complex non - linear stress behaviour experienced when the skin is subjected to combined pressure and bending loads [19, 56, 59]. In addition, a carry through structure is provided to ensure the aerodynamic efficiency of the outer panel is not affected by the deformation of the inner membrane skin [55, 56].

Other structural consequences of the BWB concept are the issues of rotor burst and structural fatigue. Over the wing distributed propulsion system increases the threat of rotor burst due to proximity of engines to one another. Un - contained engine blade burst could thus have severe impact on adjacent engines [49]. Similarly, frequent pressurisation and de - pressurisation could lead to structural fatigue [49, 59]. In view of this, Liebeck [1] recommends the use of composites for the centre-body structure due to its immunity to fatigue and weight advantage.

### 2.3.4 Propulsion Airframe Integration

The engines on the BWB aircraft are often located over the wing, aft of the aircraft centre-body. This arrangement helps to offset the weight of the payload, furnishing and other systems thus ensuring a balanced airplane [65]. Over the wing mounting allows higher by-pass ratio engines to be installed without the risk of violating ground clearance limits [49, 66]. Furthermore, mounting jet engines above the wings takes advantage of the Coanda effect to increase lift and improve short - field take - off and landing performance. Over the wing engine placement also reduces the risk of foreign object damage as they are less prone to sucking debris. However, over the wing engine mounting distorts lift distribution creating poor cruise aerodynamics [49]. Nevertheless, the distortion could be minimised through careful centre - body design to obtain a synergy between aero -

structural and propulsion airframe integration.

Positioning the engine aft of the aircraft centre body moves the centre of gravity aft to coincide with the centre of lift thereby minimising pitching moment and reducing trim requirement [67]. Location of the engine aft of the centre - body also enhances laminar flow thus reducing surface friction drag [19]. BLI is also more effective with aft - mounted engines because boundary layer is fully developed in the aft region of the centre - body [65]. Furthermore, aft engine mounting increases the range of options available for engine installations [1]. The engine could be podded on pylon or embedded in a BLI or Boundary Layer Diverter (BLD) arrangement [1]. However, podded installation creates an unwanted nose - down thrust moment, increases weight and total wetted area thus increasing drag [1, 66].

Embedded propulsion system, shown in Figure 2.38, enables better integration of the propulsion system with the airframe minimising ram drag and decreasing the wetted area. This improves cruise performance and lowers structural weight compared with a podded system [46, 48, 49, 66, 68]. Additionally, embedded engines brings the thrust line closer to the centre of gravity thereby reducing nose - down pitching moment [69]. This also minimises trim problem together with control surface size and power requirements. Also, embedded engines do not use pylons. This leads to a 20% decrease in weight compared to podded engines [70].

Yang et al. [71] investigated the effect of embedding the inlet on the aerodynamic performance of the BWB using CFD analysis. The study shows that embedding the inlet improves flow separation at higher lift coefficient thereby increasing the maximum lift coefficient and stall angle [71]. However, embedded propulsion is prone to greater unsteady forcing from inlet flow distortion thus increasing fan vibration which could lead to fan blade and disk crack [48, 68, 69, 71]. The fans in an embedded engine arrangement must therefore be designed to withstand inlet flow distortions and be compatible with a variable exhaust. Furthermore, embedded propulsion involves complex aerodynamic design with respect to surface integration. Embedded propulsion require an S - duct to guide the flow into the engine. This creates extra frictional losses approaching the engine leading to a reduction in pressure recovery [69].

A comparison of the pressure recovery (PR) of podded and embedded engines in cruise condition indicates that podded engines have a PR of 0.995, while an embedded engine with S - duct inlet has a PR of 0.95 [69]. According to Equation 2.4, a reduction in PR decreases the thermal efficiency, $\eta_{th}$, thereby reducing the thrust from the engines. In

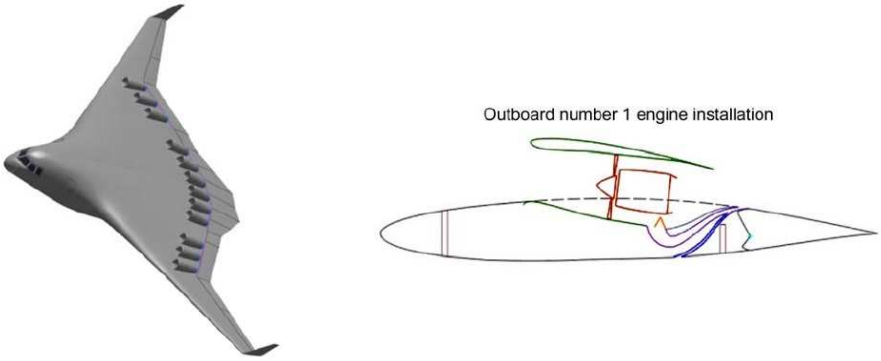


**Figure 2.38:** Partially Embedded Propulsion System Showing Boundary Layer Ingestion [72]

view of the foregoing, embedded engines will produce less thrust compared to podded engines.

The variation of $\eta_{th}$ with inlet PR at 3 different ideal fan pressure pressure recovery (FPR) is given in Figure 2.39. From the Figure 2.39, the effect of the reduced pressure recovery of 0.95, due to inlet losses on a low pressure ratio fan, is an increase in Thrust Specific Fuel Consumption (TSFC) by over 10% [69]. The variation of $\eta_{th}$ with inlet PR is obtained from Equation 2.4.

$$\eta_{th} = \frac{FPR \times PR^{(\gamma_{ht}-1)/\gamma_{ht}} - 1}{FPR^{(\gamma_{ht}-1)/\gamma_{ht}} - 1} \times \eta_f \tag{2.4}$$

Where:

$\eta_f$ is the fuel efficiency.

$\gamma_{ht}$

BLI has lower $\eta_{th}$ compared to the BLD. This is due to the decrease in the kinetic energy of the flow entering the engine intake in a BLI. The reduction in kinetic energy leads to further reduction in net thrust due to the additional inlet PR relative to the free stream conditions. According to Hall [69], the PR for S - shaped inlet is 0.94 for BLI and 0.96 for BLD. In view of this, the net thrust in a BLI engine is further reduced because of the need to overcome the additional airframe drag resulting from boundary layer ingested into the engine. However, propulsive efficiency is improved with BLI because of the reduction in the jet velocity relative to flight speed.

BLD arrangement diverts the boundary layer flow coming from centre - body leading

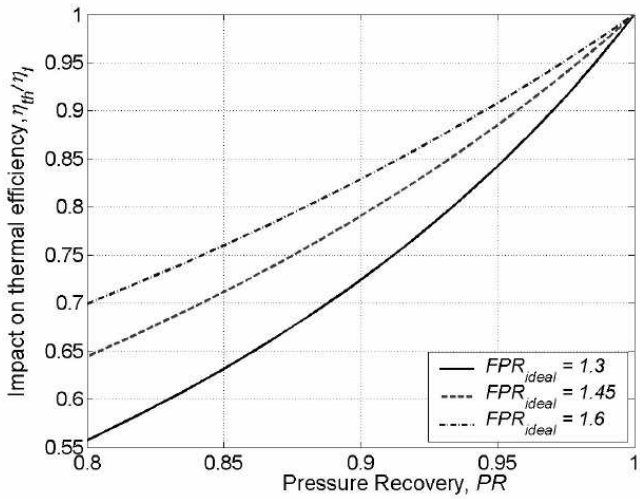


**Figure 2.39:** Effect of Inlet Pressure Recovery on Thermal Efficiency for Three Fan Pressure Ratios [69]

edges away from engine intakes [66]. This differs from the BLI arrangement which pulls boundary layer from the centre - body leading edge into the engine intakes thereby reducing ram drag and increasing thrust [65]. BLI decreases fuel burn and improves propulsive efficiency [65, 66]. The distribution of a large number of small BLI engines along the trailing edge to force sufficient boundary layer into engine intakes has also been advanced [68].

Distributed propulsion reduces engine - out over-sizing requirements and provides synergy between aircraft aerodynamics, structures, controls and high lift devices [49, 73]. Additionally, distributed propulsion replaces separated trailing edge flow with exhaust jet thus reducing induced drag and improving propulsive efficiency [10, 49, 74]. According to Ko et al.[10], the combined effect of lower induced drag with improved propulsive efficiency reduces take - off gross weight and fuel weight by 5.4% and 7.8% [74] respectively. Distributed propulsion can be used with thrust vectoring for control or as high lift devices [2, 49]. Thrust vectoring decreases low speed airframe noise due to reduced trim drag [49, 73].

Distributed propulsion engine arrangement decreases the amount of directional control power required in critical engine out conditions due to much reduced asymmetric thrust moment [49, 68]. Further to this, it redistributes engine weight over the airframe providing passive load alleviation and reduced wing weight [10]. Consequently, distributed propulsion allows for a lighter wing and increase the L/D ratio compared to pylon-mounted engines. They are however heavier with a higher specific fuel consumption due to the scale effects of small engines used in distributed propulsion system [20, 68]. Scale effects refers to decreasing engine performance with reduced engine size [68]. Smaller engines are

subject to increased pressure and heat losses due to lower Reynolds number and a relative increase of leakage flow [68]. Consequently, the use of embedded multiple fan propulsion system was proposed [66, 75].

Embedded multiple fan uses a single core to drive multiple fans in separate ducts thereby maintaining the benefits of a greater number of engines without a reduction in core size. Embedded multiple fan propulsion system increases boundary layer ingestion, reduces weight through span loading effect, improves fuel efficiency and lowers fan noise through increased fan blade passing frequency and better liner attenuation [46, 75]. However, multiple fan propulsion suffers from inlet distortion noise and forced vibration. This is caused by distorted inlet flow and difficulty in designing a geared fan transmission system that is compatible with the variable area thrust vectoring exhaust nozzles [27]. While inlet flow distortion could be minimised with active flow control and vortex generators among others, the design of engine fans, that can withstand inlet flow distortions and permit variable exhaust, is still a challenge [1, 75, 76].

The external aerodynamics of the BWB is tightly coupled with the multiple fan engine core distributed propulsion system. Hence, engine failure could reduce lift available at the rear of the airplane thus deteriorating the stability of the airplane [64]. Additionally, asymmetric drag and un - contained engine blade burst would have greater impact on adjacent engines due to the proximity of the engines to one another[64]. Consequently, the effect of a critical engine - out condition is more significant in the embedded multiple fan propulsion system.

### 2.3.5 Safety and Environmental Consideration

The BWB is a highly integrated aircraft. Safety is enhanced by ensuring that internal arrangement of components within the aircraft does not constitute potential hazards to passengers. Some potential arrangements of the BWB interior is shown in Figure 2.40. Placing the engines at the trailing edge behind the pressure vessel, minimises the risk of injury to passengers in the event of un - contained engine failure as the pressure vessel will help to keep shrapnel from the failed engine out of the cabin [40]. Also, cargo bays are located between fuel tanks and the cabin in some configurations to shield the cabin from any fire surge [40].

Compared to conventional cylindrical tube fuselages, the center body pressure vessel of a BWB is much stronger. The cabin structure is strengthened to carry both pressure and

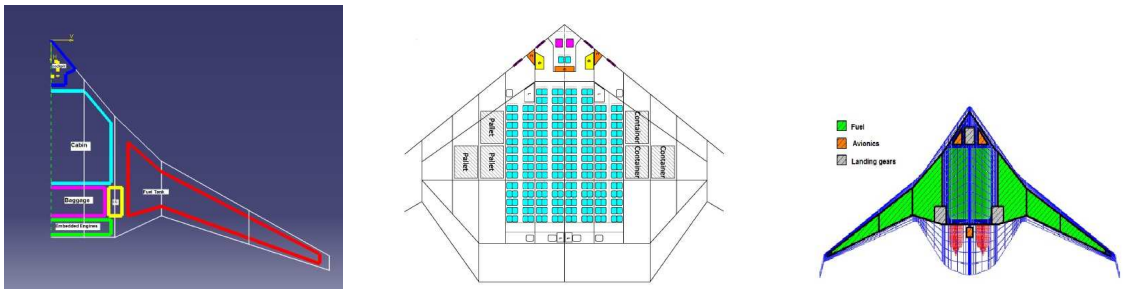


(a) Option 1 (b) Option 2 (c) Option 3

**Figure 2.40:** Some Interior Arrangement of the BWB.

wing bending loads thus ensuring crash-worthiness [1, 40].

The BWB provides a lot of space underneath the cabin for the center tank. This can be used to efficiently trim the aircraft in cruise flight. However, this makes the fuel system safety critical because it must always be operational to keep the aircraft center of gravity within an acceptable range. Fuel transfer between the central and outboard fuel tanks could be used, in approach, to shift the center of gravity aft in order to align it with the center of pressure without deflecting the elevon, so minimising trim drag. Therefore, its crucial to ensure the fuel system is designed to cope with the centre of gravity variations resulting from different payload level (baggage and passengers) and fuel volume on-board a long the flight [22].

Environmentally, the BWB has reduced pollutant emission and a lower noise signature due to lower installed thrust, reduced fuel burn, efficient aerodynamic configuration, use of simple trailing edge devices and a lighter airframe [1, 5, 38, 66]. According to Liebeck [1], the BWB offers 17% reduction in NOX emissions due to it lower fuel burn.

The absence of a horizontal tail and the effect of wing load alleviation offered by the BWB's span loading and efficient payload distribution yields a more compact and cleaner aerodynamic configuration with a lighter airframe [17]. With a reduced empty weight and a lower parasite drag, the BWB configuration is approximately 20% more efficient in terms of lift-to-drag ratio. This translates to about $20 - 30\%$ savings in fuel when compared with a conventional aircraft of the same weight [1, 17]. Reduce fuel consumption lowers pollutant emission.

Similarly, the BWB aircraft permits the use of laminar flow control (LFC) technologies over the wing with correspondingly higher fuel savings. Applying LFC over easily laminarized areas reduces the fuel consumption to just 14.6 $g/pax.km$ of fuel in a 10,000 $km$

flight for a fully loaded 300 - seat BWB aircraft [5, 77]. This amounts to 46 $g/pax.km$ of CO2 which is approximately 40% lower than the C02 emitted from a conventional aircraft of similar capacity and mission range [5, 77]. Optimal implementation of laminar flow technology is, however, hindered by joint discontinuities and improper surface finish.

Using the Engineering Science Data Unit (ESDU) method, Matinez - Val [5] compared the approach noise generated by B777 and a 300 capacity BWB at three reference points of $1150m$, $2300m$ and $3450m$ as shown in Figure 2.41. The noise produced in approach by the 300 - seat BWB and the B777 - 200 is shown in Figure 2.42. The result reveals that the BWB produces 7 - 10 $dB$ less sound pressure level, at all frequencies, than the conventional B777-200 aircraft. The EPNL obtained by integrating the sound pressure levels over audible frequency is 79.6 $dB$ for the 300 - seat BWB and 88.2 $dB$ for the B777 -200 [5].

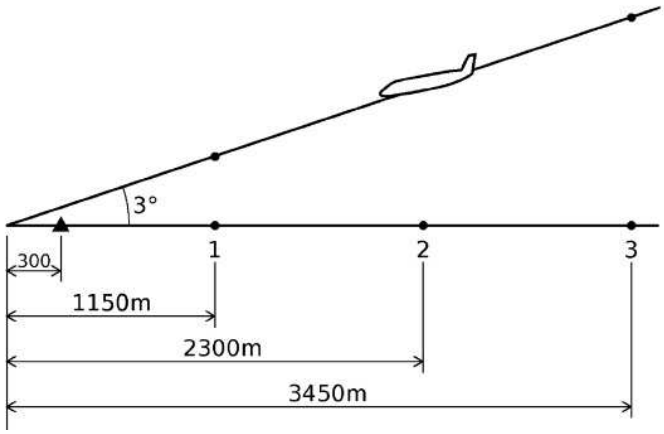


**Figure 2.41:** Glide - path of an Aircraft in IFR Final Approach Showing Noise Measurement Points. [5].

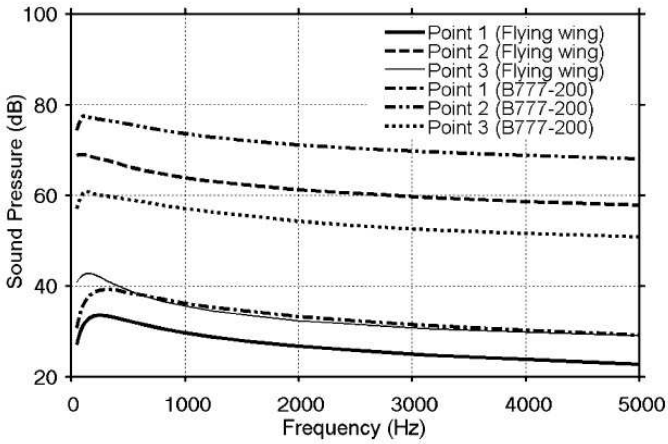


**Figure 2.42:** Comparison of Noise Produced at 3 Reference Points During Final Approach by B777 - 200 and a 300 - passenger BWB [5].

Positioning engines over the wing shields the surface from forward radiated fan noise and reflected jet noise [1, 49, 66]. Radiated jet engine noise, however still needs to to be minimised [27]. Several measures have been proposed to minimise radiated jet engine noise. These measures include moving the engine forward, use of fixed and retractable aft fuselage extension, and thrust vectoring. Moving the engine forward is not viable because positioning of engine is set by the transonic line located at or about the 75% chord [49, 73]. A fixed airframe aft extension minimises radiated jet noise and increases the elevon moment arm thereby improving longitudinal control effectiveness [73]. However, fixed airframe aft extension increases weight and skin friction drag thus decreasing mission range [49, 73]. Additionally, fixed airframe aft extension must be limited to below 3 engine diameters in order to prevent tail strike on take off [49, 73]. Retractable aft extension on the other hand eliminates the cruise drag penalty associated with fixed aft extension but incurs additional subsystem weight [49].

Thrust vectoring on its part enables a quiet approach by reducing turbulent noise mixing at the trailing edge as well as eliminate the noise caused by cavities and edges of deflected control surfaces [27, 38, 39]. Additionally, thrust vectoring provides quiet high lift devices and enables longitudinal control [1].

Satisfying the emergency egress rule might pose a challenge for BWB designers especially when the number of passengers is more than 400 [1]. This results from the unequal variation of payload capacity and available area for egress with length scale. This limits the space available for exit placement [1, 2] as shown in Figure 2.43. Positioning of emergency evacuation is affected by crowd behaviour [76] and the distance to emergency exits. Liebeck [1] proposed a cabin design which gives passengers a direct view of one or more exits from most locations in the cabin, without needing to make a $90\hat{c}irc$ turn to reach the door from the aisle [1]. This is obtained by positioning a main cabin door in front of each aisle and an exit through the rear pressure bulkhead behind each aisle together with 4 span - wise aisles intersecting with longitudinal aisles as shown in Figure 2.44.

Liebeck's [1] cabin design was validated by Galea [79] for a 1000+ seat BWB aircraft. The study shows that improved visual access and awareness of the aircraft layout improves emergency egress [40, 79]. It should be stated that Liebeck's [1] cabin concept was for a single deck BWB. Hence, issues of long slides, slides interference and over-wing exits do not apply.

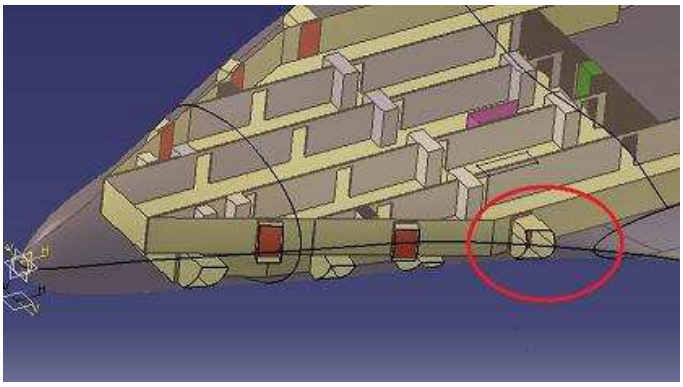

**Figure 2.43:** Emergency Egress Problem [78]

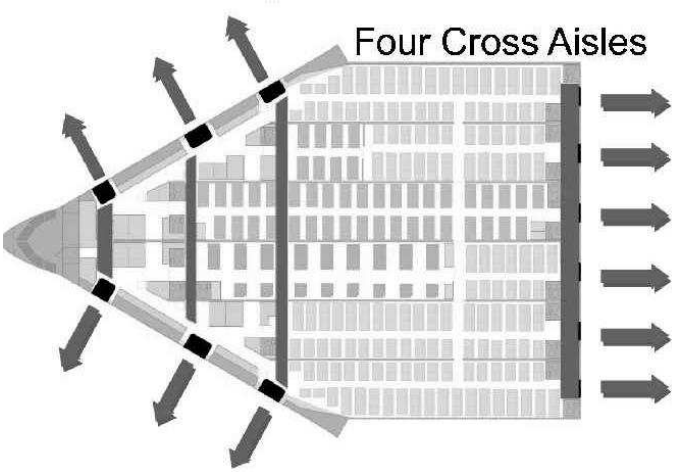


**Figure 2.44:** Liebeck Cabin Concept to Aid Emergency Evacuation[1]

### 2.3.6 Handling and Ride quality

The BWB aircraft has large volumetric capacity and flexible cabin layout hence greater passenger leg - room could be incorporated [16, 42]. However, it has few windows which could affect passenger experience [4, 42]. Consequently, the use of multi - view liquid crystal displays on every seat is advocated to provide passengers with a multi - dimensional view of the cabin and external environment [1, 4, 40].

Besides, the issue of few windows, there is the added worry that the ride quality in the outer segments of the 'fuselage' could be degraded by the lateral offset of passengers from the BWB centre of gravity [1, 40]. This prompted a comparison of worst seats on a BWB and the B747 - 400 airplane (aft for the B747-400 and outboard and aft for the BWB). The comparison, which was conducted using NASA Jacobsen ride quality model, shows only a 4% decrease in ride quality on the worst seats on the BWB compared to the worst

seat on the B747-400 [1, 42].

The longitudinal and lateral dynamics of the BWB are coupled thereby creating a tendency for the airplane to get stuck in Dutch roll [80]. A high side - slip angle creates pitch up movement which diverges Dutch roll motion setting up a destabilising couple [80]. Also, it is difficult to achieve turn coordination due to a rapid increase of side - slip angle [80]. This increases pilot workload, degrading handling quality. Furthermore, the BWB has low natural frequency and Dutch roll damping [80]. Consequently, Dutch roll control is difficult as a result of the long period of oscillation and insufficient damping [80]. The long period of oscillation and insufficient damping is caused by short moment arm and large moment of inertia of the BWB which leads to reduced yaw damping and weathercock stability derivatives [80].

The BWB is prone to Pilot Induced Oscillations (PIO) due to slow response to control inputs causing pilot's to aggravate Dutch roll motion while trying to compensate for fast build-up of the side - slip angle [80]. Slow response to control inputs is caused by large control surfaces and associated moments of inertia [80].

The BWB Dutch roll characteristics and handling quality can be improved using active control. According to an in - flight simulation by Ehlers et al. [80], active control system increases the Dutch roll damping and natural frequency thus improving roll characteristics and aircraft handling quality. Active control however does not prevent high side - slip angles during turn initiation nor the slow response of the roll axis arising from high moment of inertia about the aircraft centre line [80]. Hence, the need for dynamic surface control allocation to support the control and stability augmentation system [80].

### 2.3.7 Marketing and Manufacturing Potential

The BWB provides aerodynamic advantage over a conventional tube and wing aircraft leading to the reduction in fuel burn by 20 - 25%. This translates to 10 - 12% savings in direct operating cost with a corresponding increase in revenue yielding payload [1]. Carrying out a multidisciplinary optimisation using the Boeing proprietary code, WingMOD [1, 42, 81], Boeing engineers compared the fuel burn between the BWB - 450 and A380 - 700 for a payload capacity of 480 passengers, at Mach 0.85 and a range of 8700$nm$. Results obtained showed the BWB - 450 has a 32% lower fuel burn per seat compared to the A380 - 700 [1, 42].

A related study carried out by Leifsson et al. [20, 74] at the Virginia Tech, reveals that replacing over the wing podded engine with distributed propulsion system gives a 7.8% reduction in fuel weight over the A380 - 700. This gain is due to the beneficial effect of trailing edge jet on the induced drag and the overall aerodynamic/propulsion efficiency [20, 74].

The BWB is simply a wing with no empennage [1, 48]. Hence there are no complex wing/fuselage and fuselage/empennage joints, fillets or highly loaded structures at 90° to one another [1]. In addition, the BWB trailing-edge control surfaces are hinged without track motion, and there are usually no spoilers [1]. This leads to 30% fewer parts counts, reduced manufacturing difficulties and lower manufacturing costs [1, 40, 42].

The BWB has a short centre - body, therefore loading and unloading could be accomplished in a shorter time [40]. Furthermore, the BWB can take off from a shorter runway without the need for complicated high lift devices [40]. However, it requires a thick airfoil centre - body section to accommodate passengers and payloads thereby creating the challenge of manufacturing such airfoil and still maintain a low profile drag [40].

The BWB aircraft configuration is derived from a combination of distinct parts [1] notably the centre - body passenger bays, outer wing panels and the nose section or cockpits. While the outer wing panels and nose section are identical for any capacity of a BWB airplane, the dimensions of the centre - body vary with payload capacity. In a study conducted by NASA in conjunction with Boeing, it is stated that a family of BWB aircraft could be manufactured to meet operators *fleet mix* demands by the span - wise addition or removal of passenger bays to or from the centre - body [1, 42, 63] as shown in Figure 2.45. The study determined that the commonality offered by the BWB, in going from 250 to 450 passengers, decreases non - recurring cost by 23% and the recurring cost by 12% [42]. This study however did not consider the aerodynamic, structural and engine changes which would likely accompany lateral expansion of the configuration to increase passenger capacity.

In a bid to understand the effect of aircraft size on performance and thus determine the limit size of aircraft, Kroo [82] conducted a quantitative evaluation of aircraft size on performance. The study finds that while a variety of practical issues may limit the size of aircraft, basic structural weight and aerodynamic performance considerations permit the operation of aircraft with over 600 - 800 passengers. This is due to increased L/D with increasing aircraft size resulting from Reynold's number effects and low wetted surface area to volume ratio. However, consideration needs to be given to the the requirement

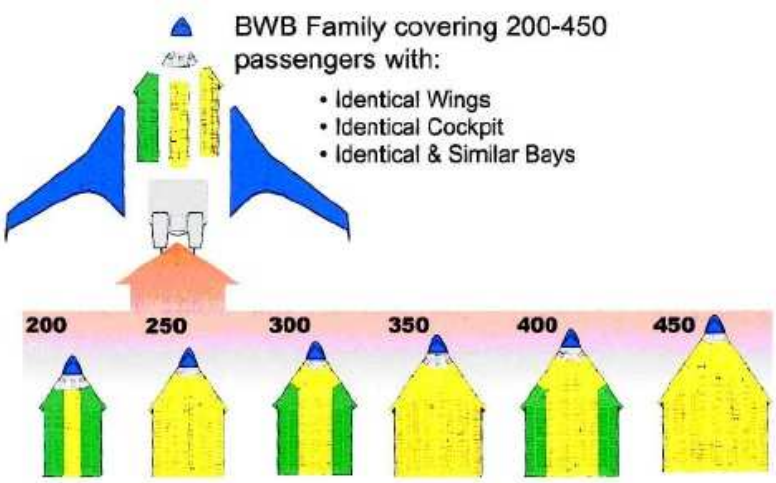


**Figure 2.45:** Commonality of the BWB Aircraft [1]

to ensure that the resulting aircraft fit into the $80m$ box specified for Class VI airports. Another issue that could arise from growth in BWB family is the effect of the Square Cube Law.

The Square Cube Law was first described in 1638 by Galileo Galilei [83]. The Law states that when a physical object maintains the same density and is scaled up, its mass is increased by the cube of the multiplier while its surface area only increases by the square of the multiplier. This implies that when an object is increased at the same rate as the original, more pressure will be exerted on the surface of the larger object. Consequently, developing a BWB family concept will cause the mass to grow by $Wb^3/S$ ($W$ is the wing weight, $b$ is the wing span and $S$ is the wing area). This will increase the bending moment and hence the structural mass leading to increased wing loading with negative consequences on critical low speed performance [82]. There is also the added challenge of propulsion and aerodynamics changes that will accompany any extension of the BWB span due to growth in passenger capacity. In view of this, Bradley [63] recommends for a maximum extension of a single deck cabin up to a capacity of 450 passengers and the use of a double deck if number of passengers exceeds 450.

The span - wise extension of the centre - body increases the span and wing area as well as permits high passenger carrying capacity with a minimal increase in root chord length [42, 63]. However, lateral extension of the centre-body as a ruled surface while maintaining aerodynamic efficiency and trim requirements is quite an intricate challenge [1, 42]. Furthermore, because the BWB cabin consists of chord - wise bulkheads representing different passenger bays across the fuselage, it cannot be converted easily from a passenger to a cargo airplane [4].

### 2.3.8 Operations, Maintenance and Engineering Capacity

The relative height of engines above the ground on a BWB poses a challenge due to the sophisticated ground support equipment that would be required to carry out maintenance work on the engines [64]. Similarly, as a revolutionary concept, the BWB will require radical changes in engineering, maintenance set - up and technician training to realise and operate [18]. However, while the required technology is still being developed, existing concepts and technologies need to be adapted in the rudimentary stage of the BWB design process [2]. This entails modifying existing or creating new design tools that has the flexibility to model non - conventional configurations [2]. Challenges with manufacturing and ensuring the structural integrity of the BWB cabin pressure vessels must also be addressed [27].

The vortex tube generated by aircraft in flight creates a swirling effect which results in dangerous rolling moment for any aircraft in flight crossing the wake [84]. While cruise encounters are easily managed because the aircraft has sufficient time to react and regain control, the effect in landing and take - off is severe and could alter the flight path of the follower aircraft leading to an accident [5]. According to Equation 2.5, the maximum tangential velocity induced by the vortex tube, $\nu_{\theta max}$, or the intensity of wake turbulence governing airport separation time and distance between leading and follower aircraft depends on the downstream distance, $x$, flight speed, $V$, and overall aircraft circulation, $\Gamma_0$.

$$\nu_{\theta max} = \frac{\Gamma_0}{4\pi r_c} = \frac{20}{\pi}\sqrt{V\Gamma_0/x} \tag{2.5}$$

Aircraft circulation is determined from Equation 2.6. Looking closely at Equations 2.5 and 2.6, it could be seen that the main variable controlling the wake intensity is the span - loading, $W/b$.

$$\Gamma_0 = \frac{4W}{\pi\rho V b} \tag{2.6}$$

Where:
$W$ is the aircraft weight in $N$.
$\rho$ is air density in $kg/m^3$.
$b$ is the wingspan in $m$.

The BWB has lower maximum weight and span loading compared to conventional aircraft of same payload capacity. A comparison of the wake intensity generated by a 300

passenger capacity BWB and the B777 provides that the BWB generates wake that is 20% and 25% less intense than the wake produced by the B777 in approach and take - off respectively [5]. In approach, the B777 produces a maximum induced velocity of $12.6m/s$ at $5nm$, while the 300 passenger capacity BWB generates $9.4m/s$ [85]. In take - off, on the other hand, the B777 generates a maximum induced velocity of $12.8m/s$ at $6nm$ while the BWB generates $9.3m/s$ [85].

Further to the foregoing, Martinez - Val [5] finds that the 300 - passenger capacity BWB, which could be classed as heavy aircraft, generated similar wake turbulence as the medium category A320 or B737, with about 150 seats, in the approach and take - off flight phases (Figure 2.46) [5, 85]. Therefore, it holds that the BWB could be given smaller separation than a conventional aircraft of similar size. This would permit more and larger aircraft operation without requiring huge investment in new runways and taxiways. However, there would be the need for optimised ground traffic management to ensure that taxiway capacity and terminal facilities are able to cope with the increased traffic of between 40 - 60 % more passengers [5].

Given that lift equals weight in cruise as defined in Equation 2.7 and the lift coefficient in optimum range condition is derived from Equation 2.8. Combining Equations 2.7 and 2.8 and determining the static pressure gives Equation 2.9.

$$W_{cr} = L = \frac{\gamma P_{cr} {M_{cr}}^2 C_{Lcr} S}{2} \tag{2.7}$$

Where:
$P_{cr}$ is the static pressure.
$M_{cr}$ is the cruise Mach number.
$C_{Lcr}$ is the cruise Mach number.
$S$ is the wing gross area.
$\gamma$, the air specific heat ratio.

$$C_{Lcr} = \sqrt{\beta C_{d0} \pi AR \phi} \tag{2.8}$$

Where:
$\beta$ is a parameter related to the Mach number dependence of the specific fuel consumption. It is taken to be around 0.6 for high bypass ratio turbo - fan engines.
$AR$ is the Aspect ratio.

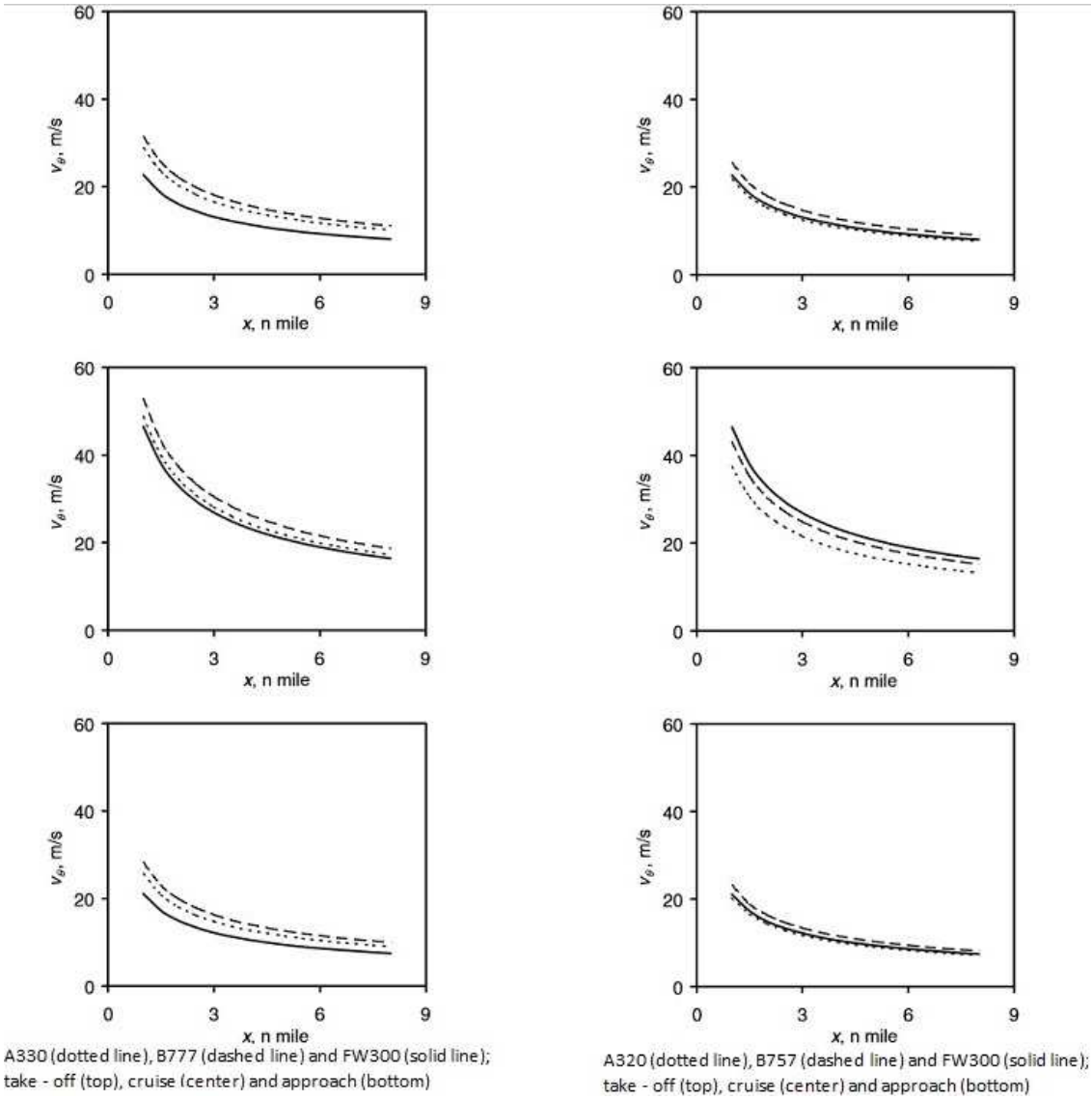


A330 (dotted line), B777 (dashed line) and FW300 (solid line); take - off (top), cruise (center) and approach (bottom)

A320 (dotted line), B757 (dashed line) and FW300 (solid line); take - off (top), cruise (center) and approach (bottom)

**Figure 2.46:** Evolution of Maximum Induced Velocity With Downstream Distance [85].

$\phi$ is the induced drag factor = 1 for elliptical lift distribution.

$$p_{cr} = \frac{2}{\gamma} \frac{W_{cr}/S}{{M_{cr}}^2 \sqrt{\beta C_{d0} \pi AR\phi}} \tag{2.9}$$

Now, applying Equation 2.9 to a BWB and a conventional aircraft and assuming both are flying with same Mach number and $\beta\pi AR\phi$, the BWB due to its low profile drag and wing loading will need to fly at a much higher altitude than conventional airplane in order to be efficient (Figure 2.47). This has the benefit of freeing up lower congested flight levels (9000 $m$ -11000 $m$) while utilizing the unused flight levels around 13000 $m$ - 15000 $m$.

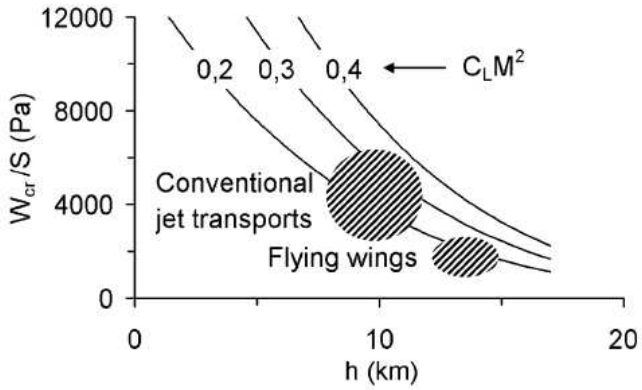


**Figure 2.47:** Wing Loading versus Cruise Conditions for a BWB and Conventional Aircraft [5].

## 2.4 Optimisation in the Design of Blended Wing Body Aircraft

Optimisation have been widely applied in the design of the BWB. Kuntawala [40] performed aerodynamic shape design optimisation of a BWB using a high fidelity inviscid Euler solver with adjoint based gradient evaluation and sequential quadratic programming optimisation. The objective of the optimisation was to minimise the sum of induced and wave drag of a BWB in transonic conditions by varying control points of B - spline geometric parameterization of the BWB aerodynamic surface. The optimisation, performed with both fixed and variable airfoil sections, shows significant reduction in drag compared to the baseline geometry.

Antoine and Kroo [86, 87] coupled product and program design in a Multi Disciplinary Optimisation (MDO) framework to explore the feasibility of reducing operating cost of a commercial airline while satisfying noise and emission constraints. Using a non - linear optimiser, the study recommends the BWB as the most environmentally benign configuration due to its inherent low noise signature and reduced emissions [86].

The European MOB project [23, 25] performed a multi-level optimisation that coupled aerodynamics, structures and flight mechanics disciplines on a BWB with a response surface optimiser. The product of this combination is a CDE that maximises the range of a BWB at constant take - off weight subject to controllability margin and stress level constraints [23, 25]. This study was however performed in a distributed environment across Europe and does not consider turbulence, packaging, propulsion and some other disciplines affecting the design of a BWB.

Diedrich et al. [65] applied MDO technique in the SAI program to obtain aerodynamically efficient and economically competitive BWB with reduced noise signature. Using WingMOD, a Boeing MDO code [81], this study reduced the aircraft noise level but could not achieve the target set for the SAI. Nevertheless, the study reveals the risk of using noise as the objective function in an MDO scheme. Consequently, Leifsson et al. [20] suggest optimising for performance while ensuring that certain noise constraints are met.

Ko [10] performed a conceptual design of a BWB with distributed propulsion using MDO technique. The study revealed increased control effectiveness and a 5.4% reduction in take - off gross weight due to reduced induced drag and improved propulsive efficiency. There was also a 3% reduction in required thrust and 7.8% fuel savings [10] with these propulsion arrangement. This study is one of the most comprehensive undertaken for the synthesis of the BWB. However, it does not consider handling or ride quality in the problem formulation.

## 2.5 Identified Gaps in Knowledge

The BWB offers several advantages but also a lot of design challenges. To address these challenges and investigate the effect of the integration of advanced systems and concepts would require a multi - variate optimisation approach. This is due to the strong coupling between various disciplines on the BWB. This review finds that designing the BWB with noise reduction as the objective function could degrade the potential aerodynamic benefits of the configuration and increase operating cost of the airplane. Since, safety and profitability are the main concerns of commercial aviation, it is proposed that the BWB should be designed to maximise productivity. Productivity in aircraft design involves designing with the ultimate aim of maximising payload and minimising drag and operational cost. This will involve creating a BWB that is not just aerodynamically efficient but also with minimal structural weight, good stability and trim characteristics. This is necessary in order to minimise fuel burn thereby maximising payload as well as to enhance controllability and improve passenger safety and comfort.

The BWB is a revolutionary concept whose design tools are still being created. Additionally, aspects of the disciplinary interactions are still being investigated. This review established that current conceptual design tools employing empirical aerodynamics and structural mass models based on conventional aircraft is not sufficiently accurate for the design of the BWB. Consequently, there is the need for a design tool that integrates

physics based aerodynamic model with a BWB - specific structural mass model in the design synthesis models in order to allow for the rapid, accurate design and enable the exploration of the design space.

The unique shape of the BWB structure due to its non - uniform cross - section also raises a packaging problem which if not addressed early in the design process could constitute a bigger challenge later in the design process. This review identified the need to integrate a packaging module in the conceptual design synthesis of the BWB in order to reduce costly geometry redesign later in the design process.

## 2.6 Chapter Summary

Research on the BWB has increased exponentially over the last few decades with major industry players including universities and agencies undertaking studies on different aspects of the BWB. This Chapter reviewed relevant publications on the BWB design to establish emerging trends, concepts and challenges on the configuration. The review highlights the enormous potentials of the BWB as well as the attendant design challenges which have slowed its entry into market. From this, the author identified the need for the development of a multi - variate design synthesis optimisation tool that enables a knowledgeable to user rapidly design and explore the design space of the BWB as the main gap in knowledge. To enhance its usefulness, the design synthesis tool should incorporate packaging, handling and ride quality assessment.

# Chapter 3

# Methodology

## 3.1 Introduction

Aircraft design is a complex process involving the balancing of considerations from several interacting disciplines. The complex and cyclic nature of the process increase the time required for the design of new aircraft. With the growth in the aircraft industry in the past few decades, pressure is increasing on manufacturers to review their design process and strategies in order to reduce the development cost as well as the time-to-market for new aircraft.

The BWB is a novel aircraft configuration. As such, knowledge of the concept and tools required for its design are still being developed. This adds to the complexity of the design as well as the challenge of reducing the time - to - market. As a novel unconventional configuration, a suitable tool for the design of a BWB must be capable of distinguishing and capturing the unique features of the design. This is necessary in order to identify the inherent potential and highlight the limitations of the tool. Additionally, the tool must be efficient in time and cost as well as capable of exploring the design space. This Chapter discusses the design philosophy adopted in this work and the disciplinary models implemented in the development of a conceptual design methodology for the Blended Wing Body Aircraft.

## 3.2 Evolution of Aircraft Design Philosophy

Aircraft design is continuously being challenged by the demands for increased efficiency without compromising product quality. An analysis of the aircraft design industry in the 21st century suggests a paradigm shift from designing to improve performance to creating a *Leaner, Meaner, Greener* [88] aircraft. With the increasing complexity of technically advanced, environmentally friendly novel concepts, the need for a more efficient design tool to reduce the time-to-market and cost of design while exploring the design space has risen exponentially. Such tools require the intelligent use of computers in the design process.

Traditionally, aircraft design proceeds through the conceptual, preliminary and detailed design phases [89] as shown in Figure 3.1. The main aim of the conceptual phase is to determine if an aircraft can be built which meets some given or assumed design requirements. Consequently, assuming basic mission requirements [90], conceptual design phase applies simple and time - efficient methods to perform *top - level exploration of the design space* [91]. This enables several concepts to be generated and evaluated. Subsequently, the most feasible concept is selected for further analysis. Only limited details is required at the conceptual phase. Hence, low fidelity and efficient disciplinary analysis tools are employed as speed rather than accuracy is the focus of this phase.

In the preliminary design phase, selected concept(s) is/are matured and validated by detailed analysis and computer simulations. The aim of this phase is to develop an optimized configuration with sufficient details and potentials to proceed to the detailed design phase. The detailed design phase is where all components and parts are defined in detail, extensive validation is performed, manufacturing documentation is produced and product is released for manufacturing. Accuracy rather than speed is the focus in this phase, hence only high fidelity analysis tools are employed.

The design activities within each phase of the design process are classified into synthesis and analysis [92]. Synthesis refers to the process of defining, refining and combining all technical disciplines into an optimum solution [93]. On the other hand, analysis comprises the methods, tools and expertise used to generate data and evaluate concepts and configurations. A detailed description of the roles of synthesis and analysis in the design process is given in Figure 3.2.

Before 1960, the use of computers in the design of aircraft was limited to the execution of self contained analysis programs in batch-mode operation [93]. The interchange of infor-

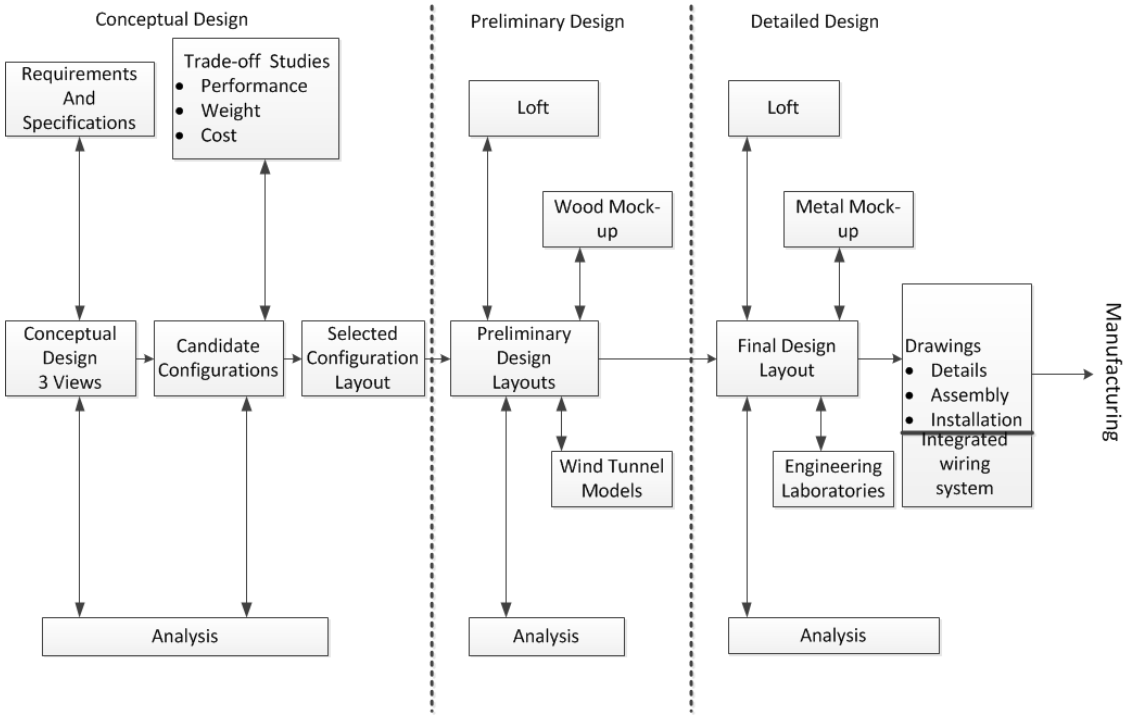


**Figure 3.1:** Aircraft Design Process

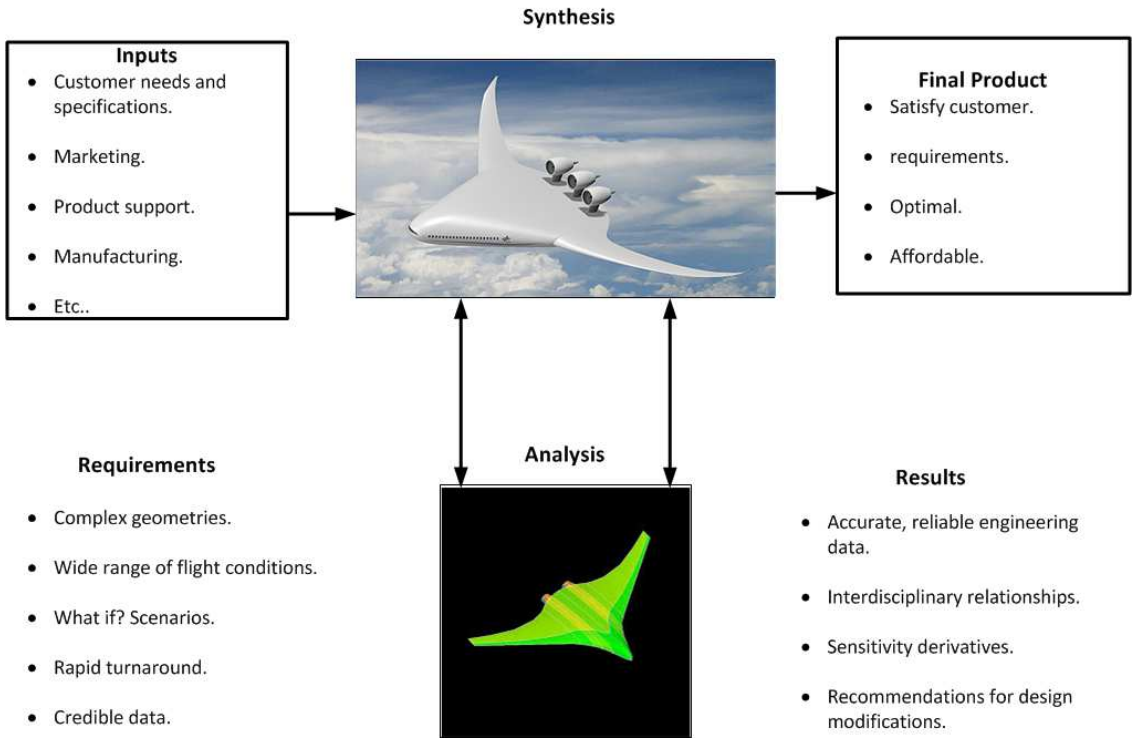


**Figure 3.2:** The Role of Synthesis and Analysis in the Aircraft Design Process

mation between these stand - alone programs was nevertheless still a time consuming and error prone manual process [93]. However, with the appreciable advances in interactive

computer technology, computers has evolved into a powerful design tool. This initiated a trend towards integrating self-contained programs into design systems through Computer Aided Engineering (CAE).

Early applications of CAE in aircraft design iclude the NASA's Integrated Design and Engineering Analysis (IDEA) [94], DARcorporations Advanced Aircraft Analysis (AAA) [95] and the Stanford University's Program for Aircraft Synthesis Studies (PASS) [96] among others. Though these programs increased productivity and reduced design time, they did not support innovation. This because they handle discipline sequentially. Novel aircraft concepts by virtue of the strong inter - disciplinary couplings and interactions (Figure 3.3) create conflicting demands which needs to be addressed simultaneously. Such conflicts influenced aircraft designers to adopt the Integrated Product and Process Development (IPPD) design approach.

The IPPD involves the concurrent investigation and analysis of the effect of different disciplines and objectives early at the conceptual design stage of aircraft design[97, 98]. This permits design trade - off to be made early at the conceptual design phase thereby reducing considerably the costly effect of altering a design later at the detailed phase [92]. Additionally, it enables the determination of a globally optimal design, which may not have been possible if disciplines are handled sequentially. The chief means of implementing IPPD in aircraft design is through multidisciplinary design or multivariate optimisation.

The multi-variate optimisation (MVO) is a design technique that is capable of rapidly improving the design of complex novel aircraft configuration with cross - couplings and synergies between different disciplines [99]. As each discipline often have conflicting optimal solutions, optimizing the disciplines separately would most likely lead to a sub-optimized aircraft. Consequently, MVO framework combines several disciplinary models to obtain a holistic perspective of the aircraft and achieve a balanced global optimal design [100, 101].

The MVO is defined as a *methodology for the design of complex engineering systems and subsystems that coherently exploits the synergism of mutually interacting phenomena* [102]. MVO allows for a systematic exploration of the design space [103] enabling a designer to capture the relations and dependences between disciplines. A MVO process is illustrated in Figure 3.4.

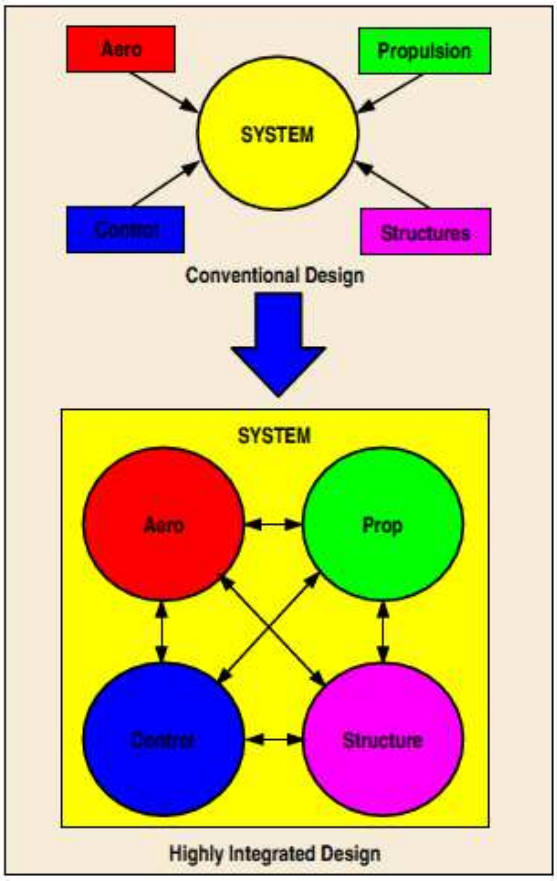


**Figure 3.3:** Coupling Between Highly Integrated Novel Configuration and Conventional Aircraft [99].

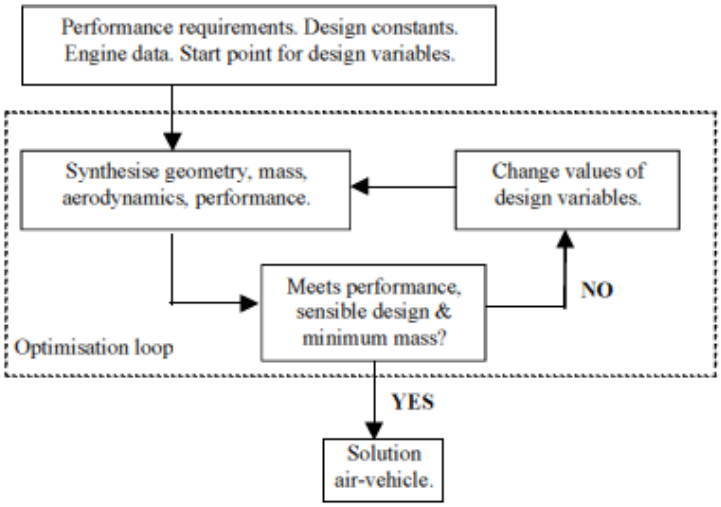


**Figure 3.4:** MVO Design Synthesis Framework [104]

## 3.3 Implementation of Disciplinary Modules

This section describes the theory of various models implemented in the disciplinary modules of the developed multivariate optimisation tool for the conceptual design of a BWB aircraft. The models include atmospheric, geometry, mass, propulsion, aerodynamics and the packaging models. These models constitute the design synthesis segment of the developed tool. The analysis models comprising the performance and stability models are treated differently in the next chapter.

### 3.3.1 Atmospheric Module

The atmospheric model is used to predict the value of atmospheric properties at different altitudes. The model implements the 1976 United States of America (US) standard atmospheric model [105]. The 1976 US standard atmospheric model divides the earth atmosphere into 5 segments based on similarity of properties within certain altitude ranges. Only the first 3 segments are currently used for commercial aviation. These segments are the troposphere which extends from 0 - 11 km; the lower stratosphere which goes from 11 - 20 km and the middle stratosphere which extends from 20-32 km.

Within the troposphere, the temperature lapse rate is -0.0065K/m. There is no change in temperature in the lower stratosphere while temperature increases at the rate of 0.001K/m at the middle stratosphere. The detailed description of the 1976 Atmospheric model is given in Appendix A.

### 3.3.2 Geometry Module

The geometry module generates configurations and external dimensions using their geometric properties. Aerospace components are often categorised into 2 main groups. These are the lifting surfaces and the body components. Lifting surfaces are used to define lift producing geometric parts such as the wings, vertical and horizontal tail plane. Body components on the other hand describes non - lift generating components such as nacelle, fuselage etc. Details of the modelling of the different geometric parts are given in Appendix D.

The BWB is defined in the developed tool's geometry module using the lifting surface geometry component. The module calculates the reference surface area of a straight

tapered wing using Equation 3.1.

$$S_{ref} = \frac{b^2}{AR} \tag{3.1}$$

The wetted surface area is obtained from Equation 3.2 as a function of the wing span, $b$, taper ratio, $\lambda$, and root chord, $c_r$.

$$S_{wet} = \frac{b^2}{2} \times c_r \left(1 + \lambda\right) \tag{3.2}$$

The taper ratio, $\lambda$ is the ratio of the tip chord, $c_t$, to the $c_r$. Accordingly, the taper ratio is derived from Equation 3.3.

$$\lambda = \frac{c_t}{c_r} \tag{3.3}$$

The mean aerodynamic chord for a straight tapered wing in terms of the root and tip chords is obtained from Equation 3.4.

$$\bar{\bar{c}} = \frac{2}{3}\left(c_r + c_t - \frac{c_r \times c_t}{c_r + c_t}\right) \tag{3.4}$$

This translates, in terms of the reference surface area, aspect and taper ratio, to the expression in Equation 3.5.

$$\bar{\bar{c}} = \frac{4}{3}\left(\frac{S_{ref}}{AR}\right)^{0.5}\left[1 - \frac{\lambda}{(1+\lambda)^2}\right] \tag{3.5}$$

The wing sweep is commonly referenced to the leading edge, trailing edge and the quarter - chord locations as a ratio of the normalised chord $(\frac{x}{c})$. The sweep at each of these locations is obtained from the AR and $\lambda$ using Equation 3.6.

$$\Lambda_2 = \Lambda_1 + \tan^{-1}\left[\frac{4}{AR} \times \left(\frac{x}{c_1} - \frac{x}{c_2}\right) \times \frac{1-\lambda}{1+\lambda}\right] \tag{3.6}$$

In a multi - kinked trapezoidal wing arrangement, the geometry variables are defined as given in Figure 3.5.

The panels constituting the wing is indexed for $k = 1 \leq k \leq N$. Where $N$ is the total number of panels. Each panel is described by the $c_r$ and $c_t$ as well as their corresponding span - wise locations $(y_r(k), y_t(k))$, local span, $b_i(k)$, area of the panel, $S_i(k)$, local sweep,

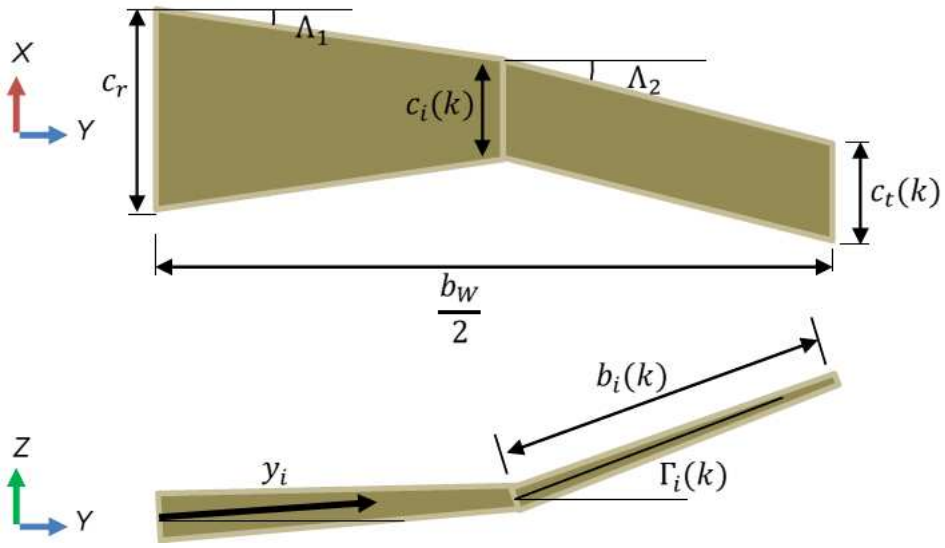


**Figure 3.5:** Definition of Wing's Geometry Variables

$\Lambda_{\frac{x}{c}}(k)$ and a dihedral or anhedral angle, $\Gamma_i(k)$. Therefore, the effective total span of a multi - panelled wing is obtained from Equation 3.7.

$$b = \sum_{k=1}^{N} b_i(k) \times \cos\left[\Gamma(k)\right] \tag{3.7}$$

Similarly, the total planform area for a multi - panelled wing is obtained from Equation 3.8.

$$S_{ref} = \sum_{k=1}^{N} S_i(k) \times \cos\left[\Gamma(k)\right] \tag{3.8}$$

The aspect ratio is derived from Equation 3.9.

$$AR = \frac{\sum_{k=1}^{N} b_i(k)^2}{\sum_{k=1}^{N} S_i(k)} \tag{3.9}$$

The MAC is the the sum of each panel's MAC. Often, each panel's MAC, $\bar{\bar{c}}_k$, is calculated from Equation 3.10.

$$\bar{\bar{c}}_k = \frac{2}{3}\left(c_r(k) + c_t(k) - \frac{c_r(k) \times c_t(k)}{c_r(k) + c_t(k)}\right) \tag{3.10}$$

The aerodynamic and geometric mean chords are often used as a reference length to non

- dimensionalise pitching moment coefficients. They are usually positioned so that their quarter - chord coincides. For a multi - kinked wing, this is illustrated in Figure 3.6.

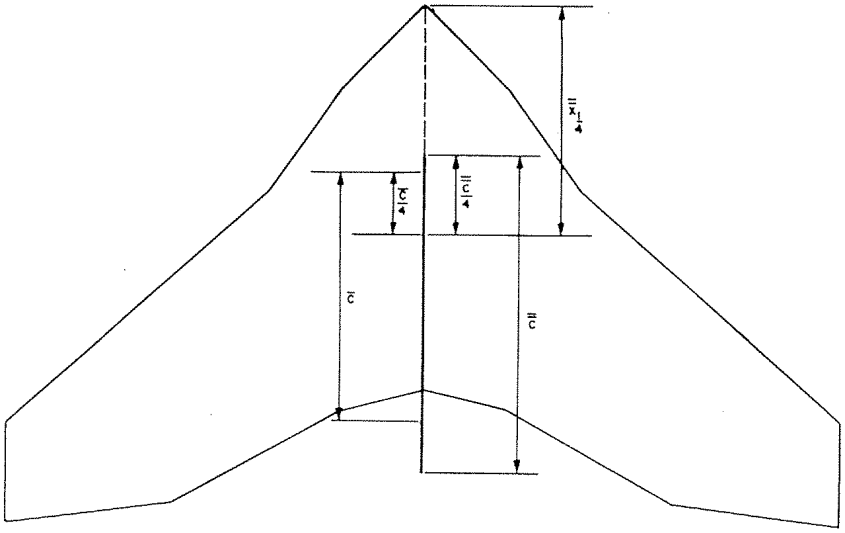

**Figure 3.6:** Position of Reference Chords.

Similarly, the Mean Geometric Chord (MGC), $\bar{c}$,, and the MAC, $\bar{\bar{c}}$,, for a multi - kink wing are evaluated from the geometric properties shown in Figure 3.7.

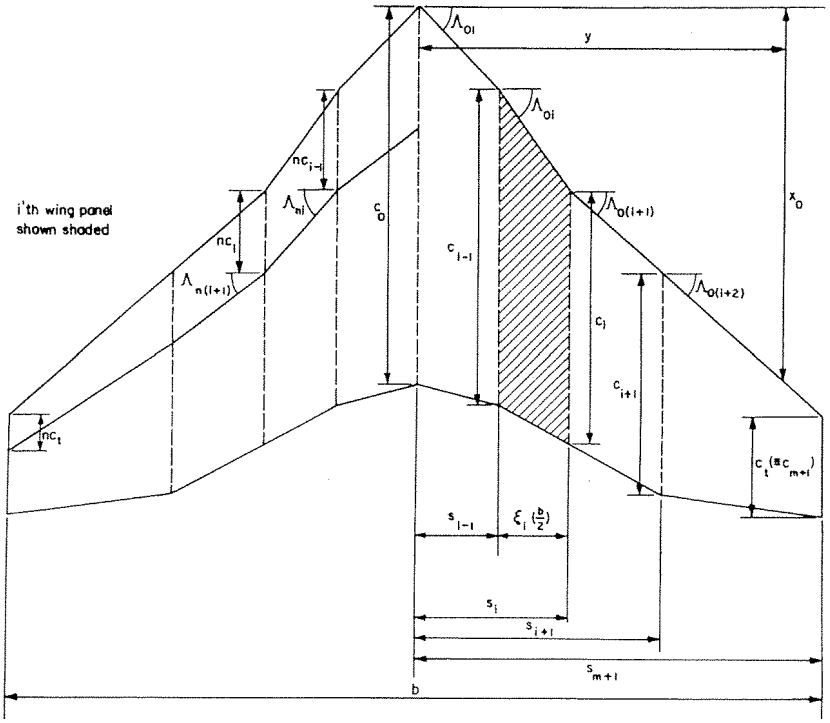


**Figure 3.7:** Multi - crank Wing.

According to the ESDU, the MAC of a multi - cranked flying wing configuration is derived

from Equation 3.11 [106].

$$\bar{\bar{c}} = \frac{\sum_{i=1}^{m+1} \bar{\bar{c}}_i S_i}{\sum_{i=1}^{m+1} S_i} \tag{3.11}$$

This translates to the expression in Equation 3.12.

$$\bar{\bar{c}} = \frac{2}{3} \left\{ \frac{\sum_{i=1}^{m+1} {c_{i-1}}^2 \left(1 + \lambda_i + {\lambda_i}^2\right) \zeta_i}{\sum_{i=1}^{m+1} c_{i-1} \left(1 + \lambda_i\right) \zeta_i} \right\} \tag{3.12}$$

In a similar way, the x - position of the quarter chord point of each panel of the MAC is determined from Equation 3.13.

$$\bar{\bar{x}}_{1/4} = \int_0^{b/2} \left(x_0 + \frac{c}{4}\right) cdy \int_0^{b/2} cdy \tag{3.13}$$

Which leads to Equation 3.14.

$$\bar{\bar{x}}_{1/4} = \frac{\sum_{i=1}^{m+1} \bar{\bar{x}}_{(1/4)i}}{\sum_{i=1}^{m+1} S_i} \tag{3.14}$$

Where :
$\bar{\bar{x}}_{1/4i} = x_{0(i-1)} + \left(x_{0i} - x_{0(}i-1)\right) \frac{(1+2\lambda_i)}{3(1+\lambda_i)} + \frac{\bar{\bar{c}}_i}{4}$

and

$S_i = \frac{\zeta_i b(1+\lambda_i)c_{i-1}}{4}$

$\zeta_i = \frac{s_i - s_{i-1}}{b/2}$

$S_i = \zeta_i (b/2) \bar{c_i}$

The MGC, $\bar{c}_i$, is determined from Equation 3.15.

$$\bar{c} = \frac{\int_0^{b/2} c dy}{\int_0^{b/2} dy} \tag{3.15}$$

Leading to Equation 3.16.

$$\bar{c} = \frac{\sum_{i=1}^{m+1} \int_{s_{i-1}}^{s_i} c dy}{\sum_{i=1}^{m+1} \int_{s_{i-1}}^{s_i} dy} \tag{3.16}$$

Further manipulation of Equation 3.16 simplifies to the expression in Equation 3.17.

$$\bar{c} = \sum_{i=1}^{m+1} \frac{c_{i-1}\,(1+\lambda_i)\,\zeta_i}{2} \tag{3.17}$$

### 3.3.3 Mass Module

Mass prediction is an essential part of the aircraft design process [107]. It affects cost as well as performance characteristics of an aircraft [108]. Mass prediction can be categorised into finite element, empirical and the semi-empirical approach. Finite element weight prediction provides accurate and reliable estimate of airframe mass but they are problem specific; not readily generalised and would increase the computational cost of an MVO scheme. Empirical methods are sometimes referred to as the Class II weight estimation method. Class II weight approach estimates the mass of the aircraft main component group using empirical equations that combine geometric parameters, aircraft design speeds, load factor and statistically derived coefficients. Empirical methods are easier to implement and more efficient than finite element approach. However, they are of low fidelity.

Semi - empirical methods comprise analytically derived equations corrected with *statistical correlation from historical data* [109]. The semi - empirical method is the most suitable weight prediction method for conceptual design synthesis. This is because they are fast and easy to implement as well as sufficiently accurate for the conceptual design phase. This thesis implements the Class II empirical component weight estimation methods alongside the Bradley semi - empirical and the Howe *empirically weighted theoretical* BWB airframe mass estimation approach.

### Howe Airframe Mass Prediction

The Howe airframe mass prediction is based on the models provided in Howe's *Blended Wing Body Airframe Mass Prediction*[19, 110] paper. The structural mass of a conventional aircraft comprises the mass of fuselage, wing, control surfaces and the empennage. For a BWB, however, the structural mass is idealised to the mass of the outer and inner wings corrected for deviations from the ideal mass.

The MTOM is given by Equation 3.18 [40].

$$MTOM = m_e + m_{fuel} + m_{payload} \tag{3.18}$$

Where:
$m_e$ is the empty mass.
$m_{fuel}$ is the mass of fuel.
$m_{payload}$ is the mass of payload.

According to Howe[110], aircraft empty mass comprises the mass of structures, operational items, system and power-plant. From [19], the structure is idealised to the inner and outer wings.

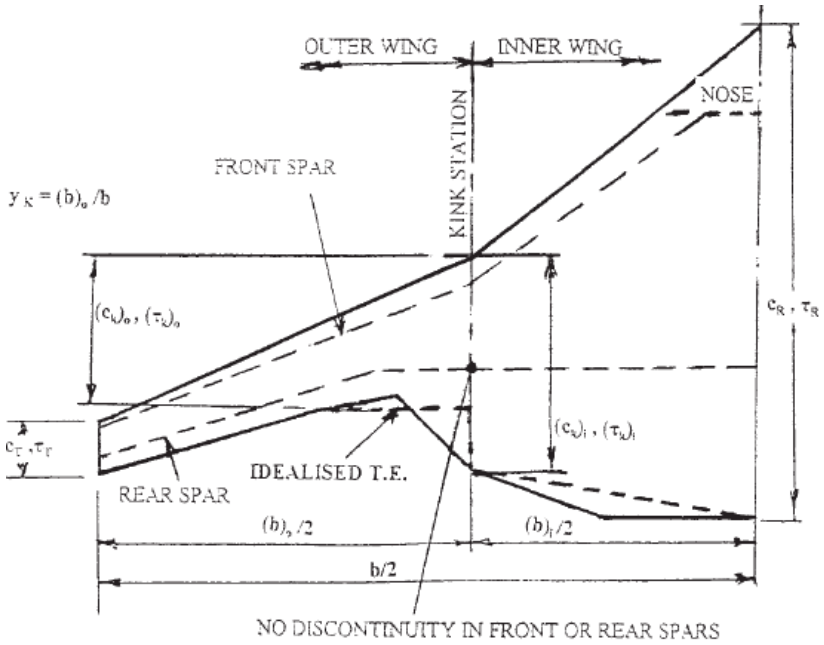


**Figure 3.8:** Howe Idealisation of the BWB Geometry [19]

The mass of each of the idealised segments is derived from Equation 3.19. All variables

used in this and subsequent equations are in the International System (SI) units.

$$m_{wing} = m_c + m_r + f_{pen} \tag{3.19}$$

Where:
$m_c$ is the mass of covers and shear webs of the structural box.
$m_r$ is the mass of ribs.
$f_{pen}$ is the penalty factor due to the departures from the ideal and allowance for the secondary structure.

The mass of covers and shear webs of the structural box $m_c$ is given by Equation 3.20.

$$m_c = n_{ult} \times MTOM \times b^3 r(e)(\sec \Lambda_{0.25})(\sec \Lambda_{0.5})^{0.5} \times \frac{\rho}{\bar{A}} \frac{c_c}{\tau}^{0.25} \times 10^{-5} \tag{3.20}$$

Where:
$n_{ult}$ is the ultimate load factor determined as $1.65n_z$.
$r$ is the wing bending relief factor.
$e$ is the ratio of the width of the structural box to the MAC.
$\Lambda_{0.25}$ is quarter-chord sweep.
$\Lambda_{0.5}$ is the mid-chord sweep.
$\bar{A}$ is the material allowable compressive stress factor.
$c_c$ is the root-chord of the wing.
$\tau$ is the maximum airfoil thickness to chord ratio.
$\rho$ is the material density.

The mass of ribs $m_r$ is obtained from Equation 3.21.

$$m_r = 4.4 S_{ref}(e)(c_c \times \tau)^{0.5}(1 + 0.35\Lambda_{0.5})\rho \times 10^{-3} \tag{3.21}$$

Where:
$S_{ref}$ is the reference area of the aircraft.

The penalty factor is given by Equation 3.22.

$$f_{pen} = 0.1 \times MTOM \times \left(\frac{2S_{fin}}{S_{ref_0}}\right) \tag{3.22}$$

$S_{ref_0}$ is the reference area of the outer wing.

The mass of fin is defined by Equation 3.23.

$$m_{fin} = 0.1 \times v_{div} \times S_{fin}^{1.15} \tag{3.23}$$

Where:
$m_{fin}$ is the mass of fin.
$v_{div}$ is the aircraft divergence speed in $m/s$.
$v_{div}$=1.25 $\times$v$_{cr}$ [111].
$v_{cr}$ is the cruise speed in $m$.

Now, applying Equation 3.19 to the outer wing, the mass of covers is given by Equation 3.24.

$$m_{co} = 0.85[N_{ult} MTOM b^3 r_o e_o \sec\Lambda_{0.5} \sec\Lambda_{0.25} {y_k}^4 (1 + 0.375 \times y_k)]^{0.5} \times \left(\frac{s'_o}{S_o}\right)\left(\frac{\rho_o \bar{f}}{\bar{A}}\right)\left(\frac{c_k}{\tau_k}\right)_o^{0.25} \times 10^{-5} \tag{3.24}$$

Where:
$b$ is the total span.
$\tau_k$ is the thickness to chord ratio at the intersection of the inner and outer wing.
$y_k$ is the ratio of the outer wing span to the total span. It is expressed mathematically by Equation 3.25.

$$y_k = \frac{b_o}{b_{total}} \tag{3.25}$$

$\bar{f}$ is the ratio of allowable compressive stress to the maximum upper limit [19]. It is obtained from Equation 3.26.

$$\bar{f} = \frac{f_k}{f_{limit}} \tag{3.26}$$

Where:

$$f_k = \bar{A} \times 10^{-5} \times$$
$$\ldots \left[ 0.727\bar{n} \times MTOM \times AR_o \times r_o \left(1 + \lambda_o\right) \sec \Lambda_{0.25} \times \sec \Lambda_{0.5} \times {y_k}^2 \times \left( \frac{1 + 0.375 y_k}{e_o \left(c_k \tau_k\right)_o} \right)^{1.5} \right]^{0.5} \tag{3.27}$$

$f_{limit} = 350 \times 10^6$.

and $\bar{f} \geq 1$.

The mid-chord sweep, $\Lambda_{0.5}$, is derived from the leading edge sweep by Equation 3.28 [112].

$$\Lambda_{0.5} = \tan^{-1} \left( \tan \Lambda_{LE} - \frac{40.5}{AR} \left( \frac{1 - \lambda}{1 + \lambda} \right) \right) \tag{3.28}$$

Similarly, the quarter-chord sweep is calculated in terms of the leading edge sweep from Equation 3.29 [112].

$$\Lambda_{0.25} = \tan^{-1} \left( \tan \Lambda_{LE} - \frac{40.25}{AR} \left( \frac{1 - \lambda}{1 + \lambda} \right) \right) \tag{3.29}$$

$r_o$, the bending relief of outer wing is obtained from Equation 3.30.

$$r_o = 1 - \left[ 0.042 + 0.84 Q_o \left(0.1 + 2R \times 10^{-5}\right) + \frac{4.55 \times m_{fin}}{MTOM} \right] y_k \tag{3.30}$$

Here:
$m_{fin}$ is the mass of fins.
$Q_o$ is the proportion of fuel carried in the outer wing.
$R$ is the mission range in km. $e_o$ is defined by Equation 3.31.

$$e_o = \frac{w_{wingbox}}{MAC} \tag{3.31}$$

$w_{wingbox}$ is the width of the wing box. This is obtained from Equation 3.32.

$$w_{wingbox} = r_s \times \cos \Lambda_{0.25} \tag{3.32}$$

The structural chord, $r_s$, is defined by Ardema et al. [113] in Equation 3.33.

$$r_s = c_{sr} - \frac{y}{b_s}(c_{sr} - c_{st}) \tag{3.33}$$

Where:
$b_s$ is the structural semi-span.
$y = (1 - 0.25)c$.
$c_{sr}$ and $c_{st}$ are the structural root and tip chords respectively.

The variables used in estimating the width of the wing box are shown in Figure 3.9 and Figure 3.10.

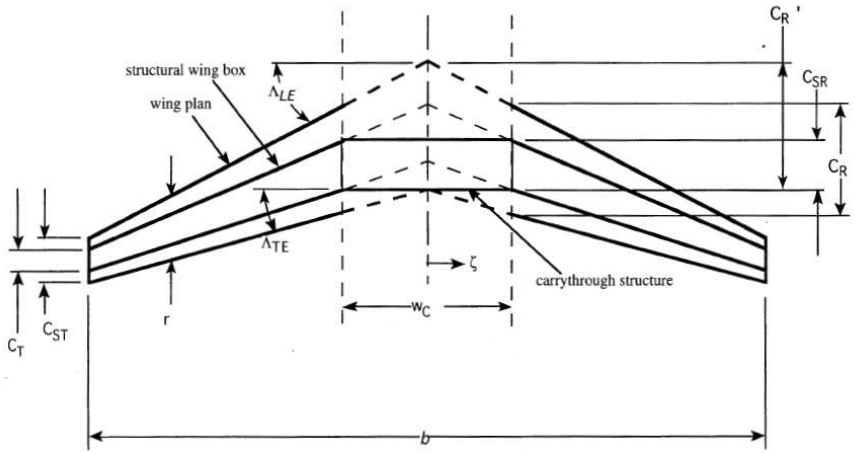


**Figure 3.9:** Wing Structural Planform Geometry [113]

The structural semi-span is obtained from Equation 3.34.

$$b_s = \frac{b - w_i}{2\cos\Lambda_{0.5}} \qquad [113] \tag{3.34}$$

$w_i$ is the width of the inner wing which in most cases is the width of the cabin.

The structural root and tip chords, $c_{sr}$ and $c_{st}$ are defined by Equation 3.35 and Equation 3.36 respectively.

$$c_{sr} = (1 - c_{s1} - c_{s2})\, c_r \qquad [113] \tag{3.35}$$

$$c_{st} = (1 - c_{s1} - c_{s2})\, c_t \qquad [113] \tag{3.36}$$

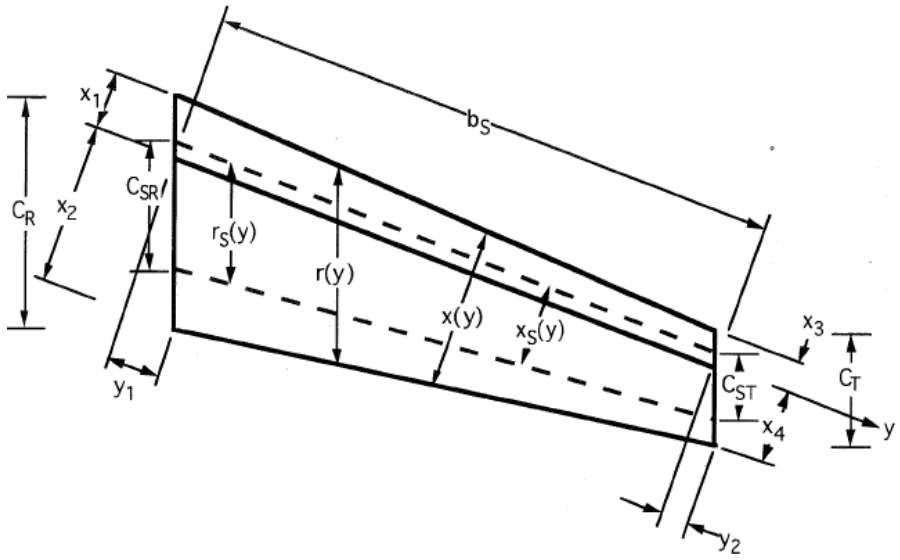


**Figure 3.10:** Structural Semi-span [113]

Where:
$c_{s1}$ is the location of the front spar.
$c_{s2}$ is the location of the rear spar.
$c_r$ is the root chord of the wing segment.
$c_t$ is the tip chord of the wing segment.

The mass of ribs in the outer wing is determined from Equation 3.24.

$$m_r = 4.4 s_o e_o (c_k \tau_k)^{0.5} (1 + 0.35 \times \Lambda_{0.5}) \rho_o \times 10^{-3} \tag{3.37}$$

The penalty factors for the outer wing is given by Equation 3.38.

$$f_{pen\,o} = (0.02 + 0.007 + 0.003 + 0.0015 - 0.005)\, MTOM \times y_k + 0.002 MTOM \tag{3.38}$$

Therefore, total mass of the outer wing is given by Equation 3.39.

$$m_{wingo} = m_{co} + m_{ro} + f_{peno} \tag{3.39}$$

The mass of the inner wing is determined in similar manner to the outer wing by applying Equation 3.19 to the idealised dimensions of the inner wing. The mass of the covers of the inner wing is obtained from Equation 3.40.

$$m_{ci} = 1.52\left(\frac{n_{ult} \times MTOM \times b^{3} r_i \times e_i \times \sec\Lambda_{0.25i}\sec\Lambda_{0.5i}}{\tau + 1}\right)^{0.5} \times \left[(1 - y_k) - 0.46(1 - y_k)^{2.5}\right] \times (1 + 0.53\bar{r}) \times \left(\frac{c_{rt}}{\tau_{rt}}\right)^{0.25} \left(\frac{\pi}{\bar{A}}\right) \times 10{-}5 \quad (3.40)$$

Where :
$\bar{\tau} = \frac{\tau_i}{\tau_o}$.

The subscripts, $i$ and $o$ refers to the inner and outer wing respectively.
$c$ represents centreline value,
$rt$ is the root value,
$k$ is kink station value and
$j$ represents one of a number of items.

$\bar{r}$ is defined as $\frac{r_i}{r_o}$.

Where:
$r_i$ is derived from Equation 3.41.

$$r_i = 1 - [A + B] \quad (3.41)$$

Where:
$A = 0.12 + 0.114(1 - 0.63y_k) + 2.27(1 - 0.63y_k)(Q_o + Q_i)(0.1 + 2R \times 10^{-5}) + 4.55\frac{m_v}{MTOM}$

$B = 0.76(\frac{m_{payload}}{MTOM})\left[\frac{c_r t + 2(c_k)_i}{c_{rt} + (c_{ki})}\right] + 4.55\left(\frac{\sum p_j Y_j}{MTOM}\right)$

However, $r_i \geq 0.1$.

$Q_i$ refers to the proportion of fuel contained in the inner wing.
$p_j$ refers to concentrated such as a power plant or landing gear unit.

The mass of inner wing ribs is calculated from Equation 3.42.

$$m_{ri} = 4.4 s_i e_i (c_{rt}\tau_{rt})^{0.5}(1 + 0.35\Lambda_{0.5i})\rho_i \times 10^{-3} \quad (3.42)$$

The penalty factors for the inner wing is then given by Equation 3.43.

$$f_{pen\,o} = (0.02 + 0.007 + 0.003 + 0.0015 - 0.005)\, MTOM \times (1 - y_k) + (0.0005 + 0.00025 n_{pplant}) \times MTOM + 0.004 \times n_{MG} \times MTOM \quad (3.43)$$

As usual, total mass of the inner wing is given by Equation 3.44.

$$m_{wingi} = m_{ci} + m_{ri} + F_{peni} \quad (3.44)$$

Combining the mass of the inner and outer wings gives the mass of the aircraft structures in Equation 3.45

$$m_{struct} = m_{wingi} + m_{wingo} \quad (3.45)$$

### Bradley Prediction Model for Airframe Mass

Bradley mass prediction method is a semi - empirical structural mass model implemented in the Flight Optimisation Software (FLOPS) [63]. The model idealised the structural mass of the BWB to the mass of the centre-body consisting of the cabin and aft - cabin corrected for engine placement, and the wing mass. According to Bradley [63], the mass of the centre-body is obtained from a semi - empirical relationship between the MTOM, area of the cabin and statistically derived coefficients. This relationship is given by Equation 3.46.

$$m_{cab} = k_s \times 0.316422 \times MTOM^{0.166552} \times {s_{cabin}}^{1.0161158} \quad (3.46)$$

Where:
$k_s = \frac{5.698865}{450} \times n_{pax}$ [63].
$s_{cabin}$ is the area of the cabin in $sq.ft$ .
$m_{cab}$ is the mass of the cabin in $lbs$.

The aft centre- body is assumed to also house the engines in a distributed propulsion or boundary layer ingestion arrangement. Bradley [63] estimates the mass of the aft centre-body $m_{aft}$ by Equation 3.47.

$$m_{aft} = (1 + 0.05 \times n_{eng}) \times 0.53 \times s_{aft} \times MTOM^{0.2} \times (\lambda_{aft} + 0.5) \quad (3.47)$$

Where:
$n_{eng}$ is number of engines.
$s_{aft}$ is the area of the aft centre-body in $sq.ft$
$m_{aft}$ is mass of aft centre-body in $lbs$.

$\lambda_{aft}$ is taper ratio of aft centre-body.

Outer wing mass is estimated using Howe's [114] wing mass prediction method. Howe's outer wing model is selected because it contains most of the essential parameters driving wing structural mass. Additionally, the parameters are available at the conceptual design stage. Howe's model was however for a metallic wing. Consequently, in order to apply it to a BWB model, correction was made for potential weight reduction resulting from the likely use of composites. Howe's wing mass model corrected for use of composites is thus redefined in Equation 3.48.

$$m_{wing} = 0.8 \times c_1 \left[ \left( \frac{bs}{\cos \Lambda_{0.25}} \right) \left( \frac{1+2\lambda}{3+3\lambda} \right) \left( \frac{MTOMn}{s} \right)^{0.3} \left( \frac{v_D}{\tau} \right)^{0.5} \right]^{0.9} \tag{3.48}$$

Where:
$c_1 = 0.028$ for long range transport aircraft [114].
$b$ is the wing span in $m$.
$m_{wing}$ is wing mass in $kg$.
$MTOM$ is maximum take off mass in $kg$ .
$\tau$ is the average thickness to chord ratio.
$\lambda$ is the wing taper ratio.
$\Lambda_{0.25}$ is the quarter chord sweep angle in $deg$ .
$S$ is the wing area $m^2$ .
$n$ is design normal acceleration factor.
$v_D$ is the design dive speed in $m/s$ $EAS$.

The design dive speed $v_D$ is determined in terms of the cruise speed, $v_{cr}$, from Equation 3.49.

$$v_D = 1.25 \times v_{cr} \tag{3.49}$$

### Landing Gears

The mass of landing gears (MLG) is derived as a percentage of the MTOM [115] from the expression in Equation 3.50.

$$m_{LG} = 0.0445 MTOM \tag{3.50}$$

### Propulsion System

The mass of propulsion system consists of the mass of propulsion and nacelle group. The propulsion group consists of the engine, engine exhaust, thrust reverser, starting, control, lubricating and fuel system. According to Raymer [107], the mass of propulsion group is estimated from the expression in Equation 3.51.

$$m_{eng} = 14.7 \times {T_{TO}}^{1.1} \times e^{-0.045 \times BPR} \tag{3.51}$$

Where:
$m_{eng}$ is the mass of the engine in $kg$.
$T_{TO}$ is the take of thrust in $kN$.

Similarly, the mass of the nacelle group ($m_{nacgrp}$) is also derived as a fraction of the mass of the engines. According to Torenbeek [116], the nacelle group is about 5.5% of the mass of the engines as given in Equation 3.52.

$$m_{nacgrp} = 0.055 \times Tp_{TO} \times n_{eng} \tag{3.52}$$

$Tp_{TO}$ is the take - off thrust in pounds of force.

Combining the masses of the propulsion group and the nacelle group gives the mass of the propulsion system, $m_{propsys}$, in kg, as found in the expression in Equation 3.53.

$$m_{propsys} = m_{nacgrp} + m_{propgrp} \tag{3.53}$$

### Auxiliary Power Unit

The mass of the Auxiliary Power Unit (APU) is obtained from Kundu [117] as defined in Equation 3.54.

$$m_{APU} = 0.001 \times MTOM \tag{3.54}$$

Where:
$m_{APU}$ is the mass of the APU in $kg$.
Where $s_{cabin}$ is in $sq.ft$.

### Instruments

Instrument consists of all instrumentation, avionics and electronics. The mass of instruments, ($m_{inst}$), is determined from the modified General Dynamics (GD) [118] method given in Equation 3.58. The method groups instruments into flight, engine and other instruments.The mass of engine instrument is calculated from Equation 3.55.

$$m_{enginst} = n_{eng} \times \left(5 + \frac{0.006 \times 2.2046 \times MTOM}{1000}\right) \tag{3.55}$$

The mass of flight instrument is obtained from Equation 3.56.

$$m_{fltinst} = 2\left(15 + \frac{(0.032 \times 2.2046 \times MTOM)}{1000}\right) \tag{3.56}$$

The mass of other instrument is estimated from Equation 3.57.

$$m_{otherinst} = \frac{(0.15 \times 2.2046 \times MTOM)}{1000} + 0.012 \times 2.2046 MTOM \tag{3.57}$$

Consequently, the total mass of instruments used on a commercial passenger transport aircraft in kg is derived from Equation 3.58.

$$m_{inst} = 0.4536 \times (m_{enginst} + m_{fltinst} + m_{otherinst}) \tag{3.58}$$

### Hydraulic System

The mass of hydraulic system ($m_{hydr}$) is calculated using the equation given in the Cranfield lecture note [119]. The note expresses the combined mass of hydraulics and pneumatics with powered control by Equation 3.59. The equation is determined based on the MTOM of the aircraft and hence does not require any additional factor or correction for the number of redundant hydraulic system. It is assumed that the effect of redundant systems is already incorporated into the MTOM.

$$m_{hydr} = 3.2 \times MTOM^{0.5} \qquad [119] \tag{3.59}$$

Where:
$m_{hydr}$ is the mass of hydraulic system in kg.

### Furnishing

The mass of furnishing comprises the masses of the seats, insulation, galley structure and provisions, lavatory and associated systems, escape provisions, fire - fighting equipments, sound proofing, instrument panel, control stands, lighting and wiring, oxygen and paints [118]. For a commercial passenger aircraft, the modified GD model gives the mass of furnishing ($m_{furn}$) by Equation 3.60.

$$\begin{aligned} m_{furn} &= 0.4536\left[(55\times n_{fdcrew})+(32\times n_{pax})+(15\times n_{ccrew})+klav(n_{pax})^{1.33}\right. \\ &\quad +kbuf(n_{pax})^{1.12}+109\left[\left(n_{pax}\frac{(1+p_c)}{100}\right)\right]^{0.505}+ \\ &\quad \left.+0.771\left(\frac{2.2046\times MTOM}{1000}\right)\right] \end{aligned} \tag{3.60}$$

Where:
$p_c$ is the design cabin pressure in $psi$.
$klav = 1.11$ for long range airplane.
$kbuf = 5.68$ for long range airplane.
$n_{pax}$ is the number of passengers.
$n_{ccrew}$ is the number of cabin crew. It is estimated at 1 cabin crew for every 30 passengers onboard the aircraft.
$n_{fdcrew}$ is the number of pilots.

### Air - conditioning

The mass of the air-conditioning ($m_{AC}$) includes the masses of pressurisation, anti - icing and de - icing systems. It is derived in terms of the cabin length using the Torenbeek method [118] given in Equation 3.61.

$$m_{AC} = 0.4536\times\left(6.75\times 3.2808\times {l_{cab}}^{1.28}\right) \tag{3.61}$$

$m_{AC}$ is the mass of air - conditioning, pressurisation, anti - icing and de - icing in kg.
$l_{cabin}$ is the length of the passenger cabin in $ft$.

### Payload

The mass of payload refers to the mass of passengers ($m_{pax}$) and their baggages ($m_{bgge}$). The mass of each passenger is assumed to be equal to 83 kg [120]. Additionally, each

passenger is entitled to a baggage weighing 30 kg. Subsequently, the overall mass of payload is derived from the expression in Equation 3.62.

$$m_{payload} = n_{pax}\left(m_{pax} + m_{bgge}\right) + m_{container} \tag{3.62}$$

Where:
$m_{payload}$ is the mass of payload.
$m_{pax}$ is the mass of passenger.
$m_{bgge}$ is the baggage allowance per passenger.
$m_{container}$ is the mass of the ULDs holding the baggages.

### Operational Items

The mass of operational item refers to the masses added to the aircraft empty weight to bring it to the operating empty condition. It consists of the masses of the crew and associated personal items, safety and freight equipment, water and food. It is estimated using the Howe model [110] expressed in Equation 3.63.

$$m_{ops} = 85 \times n_{fdcrew} + (fop + n_{pax}) \tag{3.63}$$

Where $m_{ops}$ is the mass of operational items.
$fop$ is the operational factor. For long range airline $fop = 16$ [110].
$n_{pax}$ is the number of passengers.
$n_{fdcrew}$ is the number of pilots.

### Electrical

The mass of electrical equipment is obtained as a fraction of the MTOM using the expressions given in the Cranfield lecture note on mass of powerplants, equipment system [119]. The model determines the mass of the electrical systems for a commercial aircraft as a function of the MTOM as given in Equation 3.64.

$$m_{elec} = 0.75(MTOM)^{0.67}[119] \tag{3.64}$$

### Flight Control

The mass of flight control system is derived as a percentage of the MTOM using Equation 3.65 obtained from the Cranfield Lecture Note [119].

$$m_{fltcon} = 0.11 MTOM^{0.8} \tag{3.65}$$

### Fuel

The mass of fuel required to accomplish the aircraft assigned mission is estimated as a fraction of the MTOM as given in Equation 3.66. The derived mass is further compared with the mission fuel to obtain the required fuel mass.

$$m_{fuel} = fuel_{frac} \times MTOM \tag{3.66}$$

### Mass Groupings

Other mass quantities required in the conceptual design synthesis analysis are the Maximum Landing Mass (MLM), Zero Fuel Mass (ZFM) and the Operating Empty Mass (OEM). The MLM is estimated from Howe [110] as a function of the MTOM and design range. For short haul transports with design ranges between 1000 - 4500km, the MLM is derived from Equation 3.67.

$$MLM = \left(0.98 - 2(R - 1000) \times 10^{-5}\right) \times MTOM \tag{3.67}$$

For medium or long range aircraft, the $MLM$ is given by Equation 3.68.

$$MLM = \left(1 - 2(R - 1000) \times 10^{-5}\right) \times MTOM \tag{3.68}$$

The ZFM, as the name implies refers to the weight of airplane without any fuel. It can be estimated from Equation 3.69.

$$ZFM = MTOM - mfuel \tag{3.69}$$

The other mass quantity relevant to the design synthesis is the aircraft OEM. The OEM is derived from the MTOM by Equation 3.70.

$$MZFM = MTOM - mfuel - m_{payload} \tag{3.70}$$

### Summary of Implemented Mass Prediction Methods

This research adopts a class II weight estimation methods. The class II weight estimation method predicts the weight of aircraft components using empirical equations that combine geometric parameters, aircraft design speeds, load factor and statistically derived coefficients from the mass breakdown of existing aircraft[121]. The list of the Class II methods applied in this research is given in Table 3.1.

**Table 3.1:** List of Implemented Class II Weight Prediction Methods.

| Components | Model |
|---|---|
| Wing | Howe/Bradley |
| Fuselage | Howe/Bradley |
| Landing Gears | Jenkinson |
| Engine | Raymer |
| Nacelle Group | Torenbeek |
| APU | Kundu |
| Instrument | GD |
| Hydraulics | Cranfield Lecture Note |
| Furnishing | GD |
| API | Roskam |
| Electrical | Cranfield Lecture Note |
| Flight Control | Cranfield Lecture Note |
| Operational Items | Howe |

## 3.3.4 Propulsion Module

The propulsion model implemented in this thesis is derived from Howe [110]. The Howe [110] propulsion model determines the thrust and Specific Fuel Consumption (SFC) of a propulsion system given the flight speed, altitude, BPR and the sea level static thrust. The model is particularly important in the conceptual design phase given that available power - plant data are often inadequate to cover all the required flight conditions. Hence, being able to calculate propulsion characteristics at any given flight condition improves the accuracy of the conceptual design tool. The Howe [110] propulsion model accurately determine vital power - plant characteristics at the different flight phases needed for conceptual design synthesis. Using Howe [110] propulsion model, the available operating thrust, $T$, at any given condition is obtained from Equation 3.71.

$$T = T_{fac} \times T_{static} \tag{3.71}$$

Where:
$T_{static}$ is the sea level static thrust.

$T_{fac}$, the thrust factor, depends on the flight speed, altitude and engine operating conditions.

For a subsonic flight between Mach 0 and 0.9, $T_{fac}$ is given by Equation 3.72.

$$T_{fac} = F_\tau \left[k_{1\tau} + k_{2\tau} \times BPR + (k_{3\tau} + k_{4\tau} \times BPR)\, M\right] \sigma^{alt_{factor}} \tag{3.72}$$

$alt_{factor}$ is the Altitude factor. Above Mach 0.9, $T_{fac}$ is derived from Equation 3.73.

$$T_{fac} = F_\tau \left[k_{1\tau} + k_{2\tau} \times BPR + (k_{3\tau} + k_{4\tau} \times BPR)\, (M - 0.9)\right] \sigma^{alt_{factor}} \tag{3.73}$$

$F_\tau = 1$ in dry operating conditions.

However, when after - burning or reheat is used, $F_\tau$ is obtained from Equation 3.74.

$$F_\tau = \left(\frac{T_w}{T_D}\right) / \left(1.32 + 0.062 \times BPR\right) \tag{3.74}$$

In Equation 3.73 and Equation 3.74:
$BPR$ is the Bypass ratio.
$T_w$ is the sea level static thrust in wet condition.
$T_D$ is the sea level static thrust in dry condition.

$k_{1\tau}$, $k_{2\tau}$, $k_{3\tau}$ , $k_{4\tau}$ and $alt_{factor}$, the altitude factor, are constant for a given Mach number, $M$, and operating condition. Typical values are given in Table 3.2.

**Table 3.2:** Powerplant Thrust Parameter [110]

| BPR | $M$ | Operating Condition | $k_{1\tau}$ | $k_{2\tau}$ | $k_{3\tau}$ | $k_{4\tau}$ | $alt_{factor}$ |
|---|---|---|---|---|---|---|---|
| 1 | 0-0.4 | Dry | 1.0 | 0 | -0.2 | 0.07 | 0.8 |
| or | | Wet | 1.32 | 0.062 | -0.13 | -0.27 | 0.8 |
| lower | 0.4-0.9 | Dry | 0.856 | 0.062 | 0.16 | -0.23 | 0.8 |
| | | Wet | 1.17 | -0.12 | 0.25 | -0.17 | 0.8 |
| | 0.9-2.2 | Dry | 1.0 | -0.145 | 0.5 | -0.05 | 0.8 |
| | | Wet | 1.4 | 0.03 | 0.8 | 0.4 | 0.8 |
| 3 to | 0-0.4 | Dry | 1.0 | 0 | -0.6 | -0.04 | 0.7 |
| 6 | 0.4-0.9 | Dry | 0.88 | -0.016 | -0.3 | 0 | 0.7 |
| 8 | 0-0.4 | Dry | 1 | 0 | -0.595 | -0.03 | 0.7 |
| | 0.4-0.9 | Dry | 0.89 | -0.014 | -0.3 | 0.005 | 0.7 |

The altitude factor, $alt_{factor}$, listed in Table 3.2 is valid up till an altitude of $11000m$. At higher altitude, the value is fixed to one. Similarly, the specific fuel consumption varies

with altitude, bypass ratio and the Mach number, $M$, up to an altitude of $11000m$ as given in Equation 3.75.

$$SFC = c' \left(1 - 0.15 \times BPR^{0.65}\right) \left[1 + 0.28 \left(1 + 0.063 \times BPR^2\right) M\right] \sigma^{0.08} \tag{3.75}$$

The value of $c'$, the specific fuel consumption factor, varies with the BPR.

For supersonic engines with a $BPR \leq 1$, $c' = 27mg/N/s$.
For low bypass ratio subsonic engines, $c' = 24mg/N/s$.
Large subsonic engines have a $c' = 20mg/N/s$.

Equation 3.75 applies to dry engines without after - burning. When after - burning is used, the specific fuel consumption is obtained from Equation 3.76.

$$SFC = 1.05 \left(\frac{T_w}{T_D}\right) (1 + 0.17M) \sigma^{0.08} \tag{3.76}$$

### 3.3.5 Aerodynamic Analysis Module

The aerodynamic analysis model is an essential component of the conceptual design synthesis tool. It provides the forces and moments for stability and control as well as propulsion and performance analyses. Hence, it is expedient to use appropriate aerodynamic analysis model to enhance the efficiency and effectiveness of the conceptual design tool. This demand is increased for a novel aircraft concept like the BWB aircraft. This is because there is currently no commercial transport BWB in operation. Consequently, efficient statistical or data-sheet aerodynamic analysis methods are either not available or unreliable. This increases the need for the use of computational aerodynamic models based on fluid mechanics theory. These models are often pre - coded, stand - alone tools requiring some form of geometric input for aerodynamic analysis model.

Pre - coded, external stand - alone tools impose the challenge of integrating software probably created in one programming language into a design synthesis models developed in a different programming language. The conceptual design tool described in this research is being developed on the JAVA programming language environment. Java was chosen for this tool because it is platform independent and an open source software which could be downloaded at no extra cost from the internet. Additionally, JAVA is easy to learn with great community support. JAVA is equipped with several features and rich Graphic User Interface design properties which increases the flexibility, robustness and appeal. The use

of JAVA presents a challenge of integrating the pre - coded aerodynamic analysis code, often programmed in legacy codes, into the design environment.

### Selection of a Suitable Aerodynamic Analysis Tool

Several aerodynamic analysis solvers with different levels of complexity and fidelity can be employed in the design synthesis of the BWB Aircraft. Ordinarily, it would have been preferred to utilize the full viscous Navier - Stokes equations enhanced by the addition of turbulence model for aerodynamic analysis. This is because the Navier - Stokes code provides the most accurate prediction of aerodynamic forces and moments around complex geometry with separated flows which may occur at high angles of attack [122]). However, Navier - Stokes solvers are generally difficult to implement and computationally inefficient especially when used in a multi-variate design synthesis optimisation.

Efficient flight is achieved by the use of smooth, streamlined shapes which avoid flow separation and minimize viscous effects [123]. Hence, neglecting the viscous and heat - conduction effects (diffusion terms) from the Navier - Stokes equations yields the inviscid Euler equations. The inviscid Euler equations permit the solution of rotational, non - isentropic shocks flows. They are therefore sufficiently accurate for the prediction of wave drags due to their ability to capture the correct position of shock waves. However, Euler solvers cannot predict viscous drag. They are also computationally expensive due to the need to solve at least five coupled first - order partial differential equations. Euler and Navier - Stokes solvers are therefore not suitable for the conceptual design phase where speed is the essential requirement rather than accuracy. This creates the need for lower fidelity but faster non - linear and linear potential flow solvers. A summary of the level of fidelity, computational cost and accuracy is given in Figure 3.11.

Non - linear potential methods or the full potential flow equations determines the velocity of a flow from the gradient of a scalar component, the velocity potential [92]. They are derived from the inviscid Euler equations by assuming the flow is irrotational. Non-linear potential methods can model transonic flows with weak shocks as all compressibility terms are included. However, it can neither be applied to flows with strong shock nor regions with large vorticity such as leading edge vortices because such flows or profiles are rotational and not isentropic [121]. Neglecting compressibility in the full potential flow equations and assuming small transonic perturbation yields the Prandtl - Glauert equations or linear potential equations [124, 125].

Both the linear and full potential equations are solved by panel or vortex lattice methods.

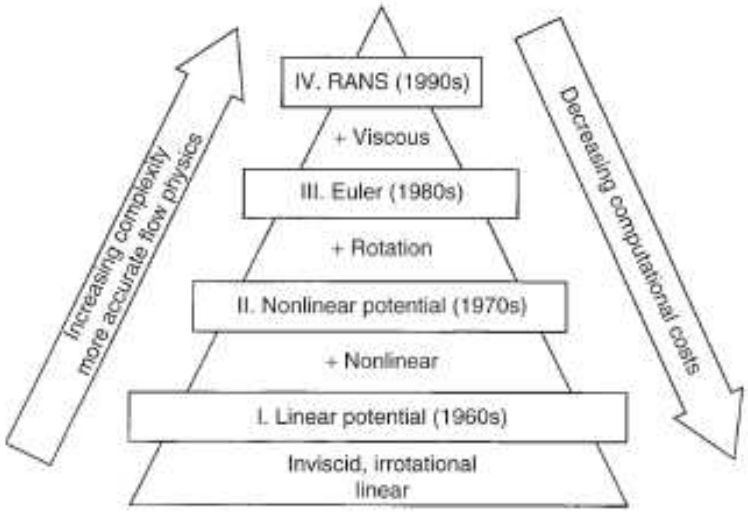


**Figure 3.11:** Hierarchy of Aerodynamic Solvers with Corresponding Complexity and Computational Cost [121]

Panel methods calculate the strength of singularities distributed over the entire actual surface of a geometry of interest. They provide approximate solution that is fast and easy to implement. The accuracy of a panel method could be enhanced by the use of higher order modelling, introduction of lifting capability, solution of unsteady flows and the addition of boundary layer effects [126].

The VLM like the panel methods solve the Laplace equations by calculating the strength of singularities placed on the mean surface of a geometry of interest. VLMs differ from panel methods in that they are oriented towards thin lifting surface and does not model thickness while panel methods models have no thickness constraints. Consequently, VLMs are not capable of predicting the effect of thickness on pressure distribution. The main advantage of VLMs over panel methods is that its solution inherently contains the leading edge suction force. This ensures that induced drag could be calculated without using the Trefftz - plane Theorem [125]. VLMs and panel methods cannot handle turbulence, viscosity and flow separation. However they are easy to use and implement as well as computationally efficient. Hence, they are widely used in the aircraft conceptual design phase.

Several open source panel methods and VLMs were surveyed for use in this research work. These included XFLR5, WINGBODY, PANAIR and the Athena Vortex Lattice (AVL). A summary of the comparison of the panel methods and VLMs is given in Table 3.3.

WINGBODY is a panel method designed for the analysis of simple 3D geometry. It is

**Table 3.3:** Comparison of Some Open Source Windows Compatible Panel Methods and VLMs.

| Analysis Tool | Type | Program Language | Availability | Modelling Capability | Outputs |
|---|---|---|---|---|---|
| WingBody | Panel | FORTRAN | Free | Limited suite of airfoils. Cannot model complex sections | Forces and moments. No derivatives. |
| AVL | VLM | FORTRAN | Free | All geometry variables. Easily model control surfaces | Forces and moments. Aerodynamic and stability derivatives. |
| XFLR5 | VLM | C++ | Free | All geometry variables. Difficulty modelling control surfaces | Forces and moments. Aerodynamic and No stability derivatives. |
| Panair | Panel | FORTRAN | Open source requires a pre-processor. | All geometry variables. | Forces and moments. No derivatives. |
| Tornado | VLM | Matlab | open source Requires Matlab | All geometric variables. | Forces and moments . Aerodynamic and stability derivatives. |
| Apame | Panel | FORTRAN | Free | limited suite of airfoils. | Forces and moments. No derivatives. |

freely available but cannot model aerodynamic twist, nor complex geometries with many sections. PANAIR is a higher order panel method for supersonic and subsonic aerodynamics analysis of complex 3-dimensional geometries. The code is freely available and could be remotely operated but it has only few aerofoils in its suite. Consequently, it cannot be used to investigate the effect of aerodynamic twist. Furthermore, a commercial pre-processor (geometric modelling tool) needs to be procured in order to model flight control surfaces as this feature is not available in the open source software.

XFLR5 is an open source aerodynamic suite containing VLMs and 3D panel method. XFLR5 is capable of modelling geometric and aerodynamic twists as well as dihedral at different angles of attack. However, it requires complicated geometric manipulation in order to model control surfaces on a BWB aircraft. Additionally, the XFLR5 does not explicitly provide the derivatives required for stability and control analysis.

The AVL method was developed by Mark Drela at the MIT. It uses VLM for the aerodynamic analysis of simple and complex geometry at subsonic condition. The program is freely available, supports remote operation which is essential for automation and it is

capable of investigating geometry and aerodynamic twists as well as effect of control surface deflection on aerodynamic forces and moments. Furthermore, AVL provides stability and control derivatives without requiring further manipulation.

In view of the superior characteristics of the AVL over the other VLMs surveyed, the AVL was selected as the most suitable aerodynamic analysis solver for the GENUS Multi - variate Design Synthesis Optimisation (GMDSO) tool. This is because, just like the XFLR5, it is fast and provides remarkable insights into wing aerodynamics and component interactions which are essential in the conceptual design synthesis and exploration of the design space of a BWB. Equally important and unlike the XFLR5, the AVL easily models control surfaces and provides linear stability analysis without requiring complicated geometric manipulations.

The AVL is a legacy code programmed in FORTRAN, in order to integrate it into the GMDSO Tool design environment, it needs to be modified and recompiled for automated operation on WINDOWS Operating System (OS) without graphics. The steps to accomplishing this are explained in Appendix B.

**Procedure for Modifying AVL for Automated Operation Without an External Text File**

Being able to recompile the AVL source code to operate on WINDOWS operating system without a graphics provides the capability to manipulate it to perform intended objectives. The AVL source code contains 37 FORTRAN files. However, in order to enable automated operation from the JAVA environment without an input file only AVL.f, AINPUT.f, AOPER.f, and the ASETUP.f files needs to be to be modified. The AVL.f is the main file. It contains the 'Program' statement used at the start of every FORTRAN program to indicate the main file. In modifying the file for automated operation, the 'Program' keyword is replaced with the 'Subroutine' keyword thus allowing the AVL to be initiated from outside FORTRAN. The edited AVL.f thus becomes a subroutine where all relevant flight conditions and subroutines required to model and analyse the aircraft geometry are defined and invoked.

The 'subroutine input' within the AINPUT.f file is also edited to accept arguments directly from JAVA by replacing the read statement requesting for user intervention with direct substitution of required variables. With the input arguments and parameters set, the AINPUT.f creates the aircraft geometry ready for aerodynamic analysis in the OPER.f.

The 'subroutine OPER' found within the OPER.f file is used for processing and aerodynamic analysis of the geometry. Usually, it consists of a series of commands which are usually triggered via an interactive prompt from a FORTRAN Compiler. However, in order to allow for remote operation, the interactive process is edited to directly trigger the execution of commands required to calculate the required aerodynamic forces and moments as well stability and control derivatives. Subsequently, once the 'call OPER' is invoked from the AVL.f file, it will perform all necessary analysis, select and determine the stability axis and derivatives as well as sends relevant output to the JAVA environment without user intervention or input.

Critical to the execution of commands within the 'subroutine OPER' are 'call exec' and the 'call DERMATS' commands. These commands activate the processes for the aerodynamic analysis. Additionally, they initiate the transfer of aerodynamic forces and moments as well as stability derivatives to the design environment. Originally, the forces and moments are sent to a text file outside the operating environment. However, following the modifications made to the source code, the desired outputs are relayed to the JAVA programming environment via C++.

**Integrating AVL into the Multi - variate Design Synthesis Optimisation Framework**

Integrating AVL aerodynamic analysis software into the multi - variate design synthesis optimisation framework involves adapting AVL subroutines to allow for direct aerodynamic analysis without request for an external geometry input file. This involves linking the FORTRAN written AVL codes with the JAVA developed multi - variate conceptual design synthesis models. Since, JAVA has no direct interface to FORTRAN, they are linked through the Java Native Interface (JNI) using C++ programming language interface as shown in Figure 3.12. The JNI is a set of tools/code used to call native methods from JAVA [127].

Data, variables and arguments are transferred from JAVA to FORTRAN in the order GUI → JavaCode → JNI → C++Code → FORTRANCode. The result from FORTRAN is returned to JAVA environment in the reverse order. To permit interaction between the codes, the JAVA code must contain a native method with a static call to a shared library through the "System.loadLibrary ("system library name")" command. The "system library name" of shared library is platform dependent. In Windows, it is the name given to the compiled and linked C++/FORTRAN file without the .dll extension. For instance, given a compiled and linked C++/FORTRAN shared object file named "cppFor-

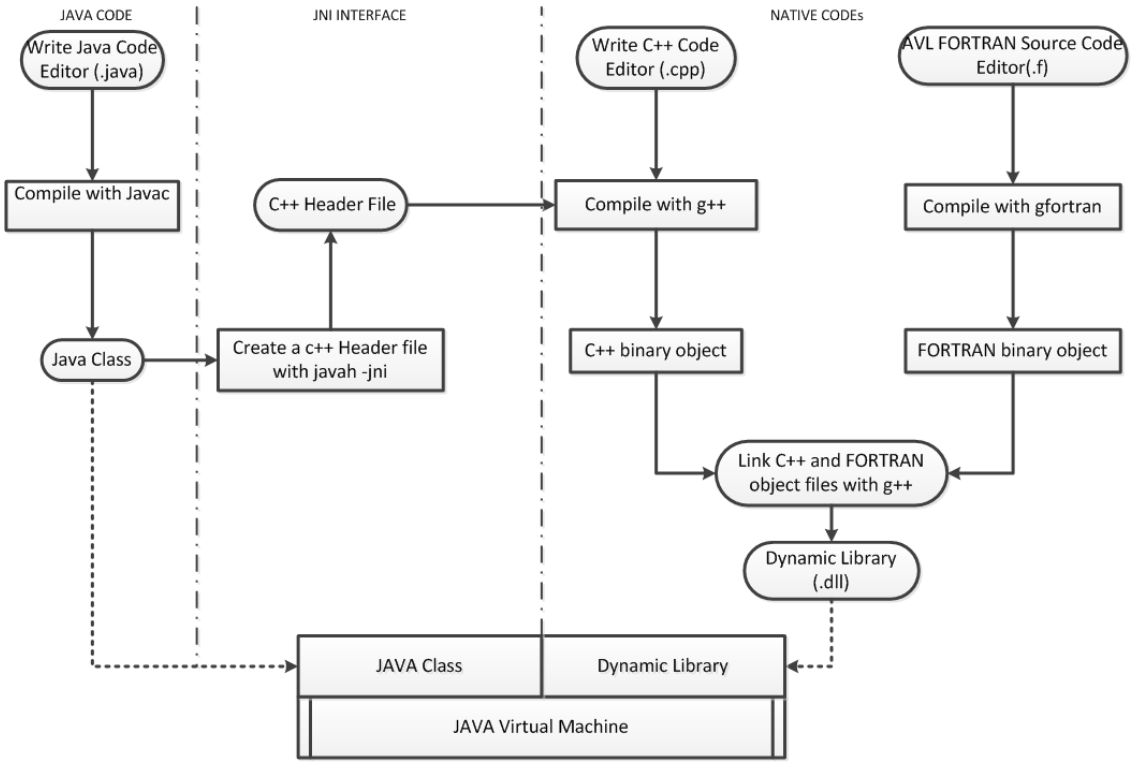


**Figure 3.12:** Framework for Integrating AVL into JAVA Using the JNI.

tranLinked.dll", the "system library name" defined above would be "cppFortranLinked". The process of creating a shared object file for JAVA and FORTRAN codes are detailed in Appendix C.

### Determining Lift and Drag Coefficient Increments

Total drag consists of the profile and friction drag, wave drag and lift induced drag. The AVL can only predict lift induced drag. Additionally, manipulating the AVL source code to calculate lift and drag increments due to flap deflections at different phases of flight is not trivial. Hence, a means of calculating zero - lift drag and increments to aerodynamic forces due to deployments of the aircraft control surfaces needs to be provided. This is required in order to accurately estimate the aerodynamic forces needed for performance analysis. The aerodynamic forces determined in this way are the zero lift drag, wave drag due to compressibility effects as well as the lift and drag increments due to deployment of leading and trailing edge devices in different phases of flight.

According to Howe [110], zero lift drag, consisting of the profile, friction and wave drag due to the volume of the aircraft, is a function of the Mach number and geometric parameters such as the quarter chord sweep, aspect ratio and wing reference area. Accordingly, the

zero lift drag is calculated from Equation 3.77.

$$C_{dz} = 0.005\left(1 - \frac{2c_l}{R_w}\right)\bar{\tau}\left[1 - 0.2M_N + 0.12\left\{\frac{M_N\left(\cos\Lambda_{o.25}\right)^{0.5}}{(A_f - t/c)}\right\}^{20}\right]R_w T_f S^{-0.1} \quad (3.77)$$

Where:
$A_f$ is the aerofoil factor which depends on the design of the aerofoil. Howe[110] estimates this value to be approximately equal to 0.93 for specially designed advanced aerofoil and 0.75 for aerofoil designed for incompressible flow conditions.
$M_N$ is the Mach number.
$c_l$ is the fraction of chord over which the flow is laminar.
$S$ is the reference area of the wing.
$\Lambda_{0.25}$ is the sweep of the quarter chord.
$t/c$ is the thickness to chord ratio.
$R_w$ is the ratio of weighted area to reference area. Howe[19] estimate it to be 5.5 for airliners.
$T_f$ is the type factor which provides for the departure of the shape from the ideal. It ranges between 1.1 - 1.2 [110] for jet airliners and executive jets.
$S^{0.1}$ ranges from 0.5 - 0.58 for airliners.
$\bar{\tau}$ is the wing thickness correction factor. $\bar{\tau}$ is determined from Equation 3.78.

$$\bar{\tau} = \left[\frac{(R_w - 2)}{R_w} + \frac{1.9}{R_w}\left\{1 + 0.526\left(\frac{t}{c}/0.25\right)^3\right\}\right] \quad (3.78)$$

$\bar{\tau}$ is often close to unity [110].

Wave drag is divided into two component, zero lift wave drag and wave drag due to lift. Zero lift wave drag is already estimated in Equation 3.77, leaving only wave drag due to lift. Wave drag due to lift is given by Equation 3.79.

$$C_{w_L} = 0.12M^6 C_{d_i} \quad (3.79)$$

Here $C_{d_i}$ is the induced drag.
$C_{w_L}$ is lift dependent wave drag.

Drag and lift increments due to deployments of the control surfaces depends on the flight profile and the extension and retraction of control surfaces and landing gears. With the landing gears retracted and high lift devices deployed in take off setting, the drag

increment due to the deployment of high lift devices in take off setting, $C_{dt}$, is obtained from Equation 3.80.

$$C_{dt} = (0.03F_F - 0.004) / A^{0.33} \tag{3.80}$$

Here:
$F_F$ depends on the type of trailing edge device employed. According to Howe [110].
$F_F$=1.0 for single slotted trailing edge flaps.
1.2 for double slotted trailing edge flaps.
1.5 for triple slotted or fowler flaps.
and 0.133 when there are no flaps. The drag increment for an extended landing gear is 0.03. For flaps at landing setting, the drag coefficient is estimated from Equation 3.81.

$$C_{dland} = 0.15F_F / A^{0.33} \tag{3.81}$$

Similarly, maximum lift coefficient is approximated by adding empirically derived lift increments due to the deployment of leading and trailing edge devices in landing and take - off setting to the AVL produced lift coefficient of the clean configuration. The lift increments in the landing setting is derived from Equation 3.82.

$$C_{Lmax} = C_{LAVL} + (\Delta_{LEL} + \Delta_{TEL}) \cos \Lambda_{0.25} \tag{3.82}$$

$C_{LAVL}$ is the lift coefficient derived from AVL at the landing speed.

$\Delta_{LEL}$ is the lift increment due to the deployment of leading edge device in the landing setting. It is typically taken as 0.65 when leading edge devices are deployed and zero in the absence of leading edge devices [110].

$\Delta_{TEL}$ is the lift increment due to the deployment of trailing edge devices in the landing setting. Its value depends on the type of trailing edge device deployed. Typical values are listed in Table 3.4.

In the landing approach condition, the total lift coefficient is estimated from Equation 3.83 by adding the lift increments, due to the deployment of leading and trailing edge devices in the landing setting, to the lift coefficient obtained from the AVL with a clean configuration of the aircraft at a speed 1.3 times the stalling speed.

$$C_{Lapp} = C_{LAVLapp} + 0.6 (\Delta_{LEL} + \Delta_{TEL}) \cos \Lambda_{0.25} \tag{3.83}$$

**Table 3.4:** Typical Lift Increments from Deploying Leading and Trailing Edge Flaps [110]

| Type of Flap | Lift Coefficient Increments | |
|---|---|---|
| | $\Delta_{TET}$ | $\Delta_{TEL}$ |
| Plain | 0.3 | 0.6 |
| Single slotted | 0.5 | 1.0 |
| Double slotted and Fowler | 0.7 | 1.35 |
| Triple slotted | 0.8 | 1.55 |

Similarly, in the take-off configuration, the total lift coefficient in take - off, $C_{LTO}$, is calculated from Equation 3.84.

$$C_{LTO} = C_{LAVLTO} + 0.8\,(\Delta_{LET} + \Delta_{TET})\cos\Lambda_{0.25} \tag{3.84}$$

Where:
$C_{LAVLTO}$ is the lift coefficient derived from AVL at the take - off speed.

$\Delta_{LET}$ is the lift increment due to the deployment of leading edge devices in take - off setting.

Typical value of $\Delta_{LET}$ is 0.4 when leading edge devices are deployed in take-off setting and zero when there are no leading edge devices [110].

$\Delta_{TET}$ is the increment due to the deployment of trailing edge devices in the take of setting. Typical values of $\Delta_{TET}$ are given in Table 3.4.

### 3.3.6 Packaging Module

Packaging is an essential module in the conceptual design synthesis of the BWB. It is necessary for the determination of the centre of gravity of an aircraft which subsequently affects the stability and control of the configuration and to ensure that internal object are well contained within the geometry. Ensuring items are completely contained within the geometry is critical in the design of the BWB due to the configuration's non - uniform cross - section. Packaging ensures there is sufficient internal space to fit all components

within the confines of the geometry. The packaging module consists of sizing, estimation of the centre of gravity, geometry parameterization and volume constraint handling.

### Sizing

Sizing models determine the dimensions of major aircraft components. The aircraft components sized in this thesis are the cabin, engines, landing gear and baggage compartment. The cabin is sized from the Bradley cabin sizing method while the engine(s) is/are rubber-scaled from selected nominal engine based on the desired thrust. Landing gear sizes were developed from the maximum landing weight while the baggage compartments is derived from the standard dimensions of conventional unit loading devices.

**Cabin Sizing.** The BWB passenger cabin is sized following the Bradley [63] sizing method. This method first calculates the total length required as if to fit everything into one bay before determining the appropriate number of bays. The Bradley [63] sizing method proposes for lateral expansion of the BWB centre-body in order to maximise the number of passengers that could be airlifted with minimal increase in root chord length. In developing this methodology, Bradley selected a $3 \times 3$, $3 \times 2$ and $2 \times 2$ seating arrangement in tourist, business and first class respectively. This arrangement was chosen in order to maximise the number of passengers with the least width. Now, assuming a nominal bay width of 12ft, to allow for wider seats and aisle widths beyond the current maximum seat and aisle widths of approximately 18 inches and 20 inches respectively, the total length required is determined from Equation 3.85.

$$l_{req} = (n_{frws} \cdot f_{pch}) + (n_{brws} \cdot b_{pch}) + (n_{trws} \cdot t_{pch}) + ((n_{gly} + n_{lav})36) + (n_{clst} \cdot 12) \quad (3.85)$$

Where:
$l_{req}$ is length required $[in]$ .
$f_{pch}$ is the pitch of first class seats $[in]$.
$b_{pch}$ is the pitch of business class seats $[in]$.
$t_{pch}$ is pitch of tourist class seats $[in]$.

The the number of seat rows in the first class, $n_{frws}$, is calculated from Equation 3.86.

$$n_{frws} = \frac{n_{fpax}}{n_{fabr}} \quad (3.86)$$

$n_{fpax}$ is the number of passengers in the first class.
$n_{fabr}$ is the number of seats abreast in the first class.

Similarly, the number of seat rows in the business and tourist classes are determined from Equation 3.87 and Equation 3.88 respectively.

$$n_{brws} = \frac{n_{bpax}}{n_{babr}} \tag{3.87}$$

$n_{bpax}$ is the number of business class passengers.
$n_{babr}$ is the number of seats abreast in the business class.

$$n_{trws} = \frac{n_{tpax}}{n_{tabr}} \tag{3.88}$$

$n_{tpax}$ is the number of passengers in the Tourist/Economy class passengers.
$n_{tabr}$ is the number of seats abreast in the Tourist class.

The number of galleys, $n_{gly}$, number of lavatory, $n_{lav}$, and number of closets, $n_{clst}$, are given by Equation 3.89, Equation 3.90 and Equation 3.91.

$$n_{gly} = 1 + \frac{n_{fpax} + n_{bpax} + n_{tpax}}{100} \tag{3.89}$$

$$n_{lav} = \left(1 + \frac{n_{tpax}}{100}\right) + \left(1 + \frac{n_{fpax} + n_{bpax}}{60}\right) \tag{3.90}$$

$$n_{clst} = 1 + \frac{n_{fpax}}{30} + \frac{n_{bpax}}{45} + \frac{n_{tpax}}{60} \tag{3.91}$$

In determining the appropriate number of bays, the maximum length of the cabin outer wall needs to be estimated. Knowing a BWB cabin blends into the outer wing, the root chord of outer wing must be equal to the minimum chord of the outer ribs enclosing the passenger compartment. Assuming a maximum thickness to chord ratio of $15 - 17\%$ in order to provide sufficient cabin height as well as ensure acceptable transonic performance, a minimum outer rib chord length of $55ft(16.764m)$ is specified [63]. This yields a depth of $8.2ft(2.5m)$. This depth provides sufficient internal space to accommodate the upper and lower skin surfaces, passenger decks, internal furnishings and more than 95th percentile of standing height of male passengers [63].

The BWB cabin extends from the leading edge to about 70% chord as shown in Figure 3.13. Hence, the specified minimum outer rib chord of $55ft$ would provide a useful cabin

length of $38.5ft$. Taking the centre - body as a linearly ruled surface, every $6ft$ increase in length creates a correspondingly $12ft$ increase in span or an additional bay as shown in Figure 3.14. Though this lateral expansion could be continued indefinitely, Bradley [63] limits the number of bays in a single deck to 5 and set the maximum length of cabin outer wall to $44.5ft$. This is necessary in order to ensure that the resulting aircraft fits within the 80 $m$ limit for Class VI airport.

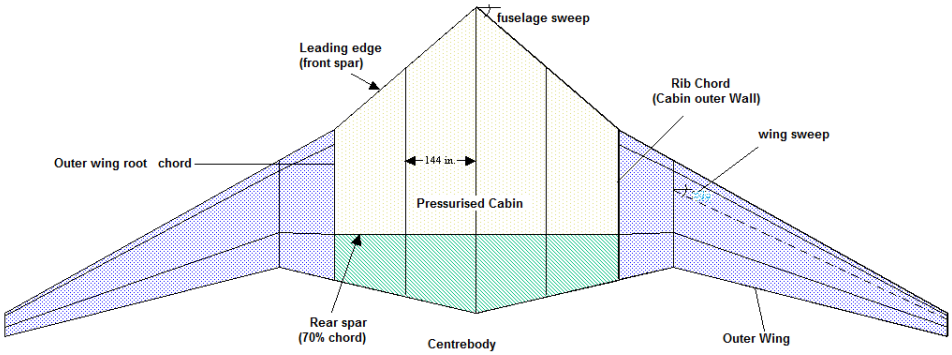


**Figure 3.13:** Planform View of BWB Geometry showing the Parameters used in Cabin Sizing

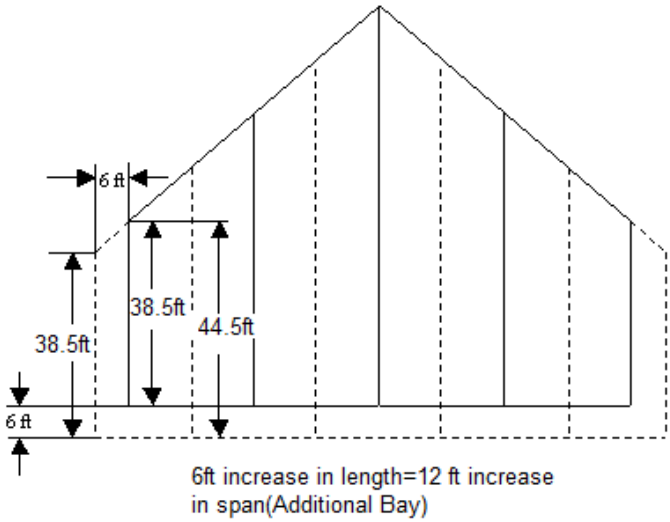


**Figure 3.14:** The BWB Cabin as a Ruled Surface

With the basic dimensions of the cabin determined, the maximum length for various number of bays at any given sweep angle can be calculated from Equation 3.92.

$$l_{tot} = nl_w + \frac{w}{2}\tan\Lambda_{fuse}\sum_{i=1}^{n}(i-1) \quad [63] \tag{3.92}$$

Where:
$i$ is the number of bays.
$l_w$ is the maximum length of the outermost wall = 44.5ft.
$\Lambda_{LE}$ is the sweep angle of centre - body leading edge.

For instance for a cabin with a sweep angle of 45°, the calculated maximum useful length for various number of bays is listed in Table 3.5.

**Table 3.5:** Maximum Useful Length for Certain Number of Bays

| Number of Bays | Maximum Length (ft) |
|---|---|
| 1 | 44.5 |
| 2 | 95.5 |
| 3 | 151.5 |
| 4 | 214.0 |
| 5 | 282. 5 |

Matching the values of total length required to the maximum length for various number of bays, the appropriate number of bays is determined. From the number of bays and the nominal width of each bay, the width of cabin is calculated as given in Equation 3.93.

$$w_{cabin} = w_{bay} \cdot n_{bay} [63] \tag{3.93}$$

Where:
$w_{cabin}$ is the width of cabin .
$w_{bay}$ is the width of each bay .
$n_{bay}$ is the number of bays.

The actual length of the outermost wall of the pressurised cabin is derived by replacing $l_{tot}$ in Equation 3.92 with $l_{req}$ and solving for $l_w$. This yields Equation 3.94.

$$l_{w_{actual}} = \left( \frac{l_{req} - \frac{w_{ca}}{2}\tan\Lambda_{fuse}\sum_{i=1}^{n}(i-1)}{n} \right) \quad [63] \tag{3.94}$$

Where:
$l_{w_{actual}}$ is the length of the outermost wall of the pressurised cabin.

The walls of each bay are of different length. Breaking each bay into 2 columns, the length of each column represents the length of the outboard wall of each bay. Since there are always 2 columns of equal length by symmetry, columns of equal lengths can be re-combined into equivalent bays as shown in Figure 3.15. Subsequently, the lengths of the centreline and outer - walls of each column are calculated.

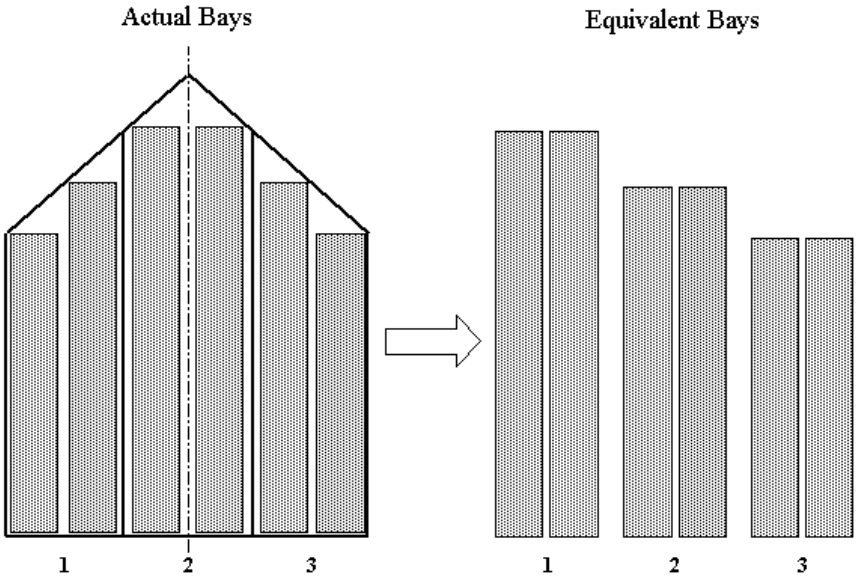


**Figure 3.15:** Converting Seating Areas into Equivalent Bays. [63]

The length of BWB cabin centreline is a function of the number of bays, leading edge sweep angle of the centre - body, length of outer - wall and the width of each bay. It is determined from Equation 3.95.

$$xl_p = l_{w_{actual}} + \frac{w_{ea}}{2} \tan \Lambda_{fuse} n_{bays} [63] \tag{3.95}$$

Now, assuming the outer walls of the columns are numbered consecutively from the centreline, $q = 0$ to $q = n_{fuse}$ outwards, the length of the outer wall of each column $xl_{ea}$, is obtained from Equation 3.96.

$$xl_{ea} = xl_p - q \left( \frac{w_{ea}}{2} \cdot \tan \Lambda_{fuse} \right) \tag{3.96}$$

**Engine Sizing.** The engine is rubber scaled from a reference engine to determine the dimensions required to provide the desired thrust. Rubber scaling involves calculating the thrust required for efficient performance of the aircraft and then scaling an already existing engine by a scale factor to dimensions required to provide the desired thrust [107]. Scale factor is obtained from Equations 3.97.

$$T_{SF} = \frac{T_{req}}{n_{eng} \cdot T_{engRef}} \quad [128] \tag{3.97}$$

Where:
$T_{SF}$ is the thrust scale factor.
$n_{eng}$ is the number of engines.
$T_{req}$ is the thrust required.
$T_{engRef}$ is the reference engine thrust.

Length and diameter of engines are calculated from Equations 3.98 and 3.99 respectively.

$$l_{eng} = l_{engRef} \cdot T_{SF}^{0.4} \quad [128] \tag{3.98}$$

Where:
$l_{eng}$ is the length of engines.
$l_{engRef}$ is the length of reference engine.

$$dia_{eng} = dia_{engRef} \cdot T_{SF}^{0.5} \quad [128] \tag{3.99}$$

Where:
$dia_{eng}$ is the diameter of engines.
$dia_{engRef}$ is the diameter of reference engine.

**Landing Gear Bay.** The landing gear is another very important component affecting the packaging of BWB. The landing gear is sized as a function of the MLM as given in Equation 3.100.

$$l_{LG} = \left(\frac{MLM}{k_{c2LG}}\right)^{kexp_{c2LG}} \tag{3.100}$$

Where:
$MLM$ is the Maximum Landing Mass.
$l_{LG}$ is the total length of landing gear.

$k_{c2LG}$ is a constant in correlation to landing gear length.
$kexp_{c2LG}$ is the exponential constant in relation to landing gear length.

Subsequently, the length of nose gear, $l_{NG}$, and main landing gears $l_{MG}$ are determined as a function of statistically determined ratios of nose gear to main gear and main gear to nose gear as given in Equations 3.101 and 3.102 respectively.

$$l_{NG} = \frac{(lt_{LG} \cdot r_{NG2MG})}{(r_{NG2MG} + 2)} \tag{3.101}$$

Where:
$r_{NG2MG}$ is the ratio of nose gear to main gear.

$$l_{MG} = 0.5 \cdot (lt_{LG} - l_{NG}) \tag{3.102}$$

The diameter and width of main and nose wheel are important parameter in the estimation of the length, height and width of landing gear bays. The diameter of main and nose wheel is estimated by Equations 3.103 and 3.104.

$$dia_{mwl} = f_{c2mwl} \cdot MLM + k_{c2mwl} \tag{3.103}$$

Where:
$dia_{mwl}$ is the diameter of main wheel.
$f_{c2mwl}$ is the factor in correlation to main wheel.
$k_{c2mwl}$ is constant in correlation to main wheel.

$$dia_{nwl} = f_{c2nwl} \cdot MLM + k_{c2nwl} \tag{3.104}$$

Where:
$dia_{nwl}$ is the diameter of nose wheel.
$f_{c2nwl}$ is factor in correlation to nose wheel.
$k_{c2nwl}$ is the constant in correlation to nose wheel.

The width of nose wheel is taken as $0.432m$, while the width of main wheel is determined from Equation 3.105.

$$w_{mwl} = f_{c2mwl} \cdot MLM + k_{c2wmwl} \tag{3.105}$$

Where:
$w_{mwl}$ is the width of main wheel.
$f_{c2mwl}$ is factor in correlation to main wheel.
$k_{c2wmwl}$ is the constant in correlation to width of main wheel.

The length of main bay, $l_{mbay}$, and nose bay, $l_{nbay}$, are determined from Equations 3.106 and 3.107 respectively.

$$l_{mbay} = 0.5 \cdot dia_{mwl} + l_{MG} \tag{3.106}$$

Where:
$dia_{mwl}$ is the diameter of main wheel.
$l_{MG}$ is the length of main gear.

$$l_{nbay} = 0.5 \cdot dia_{nwl} + l_{NG} \tag{3.107}$$

Where:
$dia_{nwl}$ is the diameter of nose wheel.
$l_{NG}$ is the length of nose gear.

Similarly, the width of main bay, $w_{mbay}$, and nose bay, $w_{nbay}$, could be determined by Equations 3.108 and 3.109 respectively.

$$w_{mbay} = f_{mwlwklr} \cdot w_{mwl} \tag{3.108}$$

Where:
$f_{mwlwklr}$ is the clearance factor in relation to main wheel.
$w_{mwl}$ is the width of main wheel.

$$w_{nbay} = f_{nwlwklr} \cdot w_{nwl} \tag{3.109}$$

Where:
$f_{nwlwklr}$ is the clearance factor in relation to nose wheel.
$w_{nwl}$ is the width of nose wheel.

The height of the main bay, $h_{mbay}$, and nose bay, $h_{nbay}$ are then determined by Equations 3.110 and 3.111.

$$h_{mbay} = f_{mwldklr} \cdot dia_{mwl} \tag{3.110}$$

Where:
$f_{mwldklr}$ is the main wheel diameter clearance factor.
$dia_{mwl}$ is the diameter of main wheel.

$$h_{mbay} = f_{nwldklr} \cdot dia_{nwl} \tag{3.111}$$

Where:
$f_{nwldklr}$ is the nose wheel diameter clearance factor.
$dia_{nwl}$ is the diameter of nose wheel.

### 3.3.7 Determination of the Aircraft Centre of Gravity

In order to determine the centre of gravity of the whole aircraft, the location of the centre of gravity of major aircraft components needs to be calculated. For most components, the centre of gravity is located at the centre of the component. However, the mass of the structure of the BWB is assumed to act at the centre of volume of the wing [129]. The centre of volume is defined as the distance aft of the x - position of the mean quarter chord point, $\bar{\bar{x}}_{1/4}$, as a fraction of the MAC.

According to Lovell [130], the centre of gravity location as a fraction of the wing root centre - line chord, for each panel of a multi - crank wing, is determined from Equation 3.112.

$$cg_p = \left[\frac{1}{56}\left\{13 - \frac{\left(27\lambda^2 + 1.75AR(1-\lambda^2)\left(1+4\lambda+\lambda^2\right)\tan\Lambda_{0.25}\right)}{\left(1+\lambda+\lambda^2\right)^2}\right\}\right] \tag{3.112}$$

Where :
$cg_p$ is the centre of gravity location of each panel in a multi - kinked wings.
For a multi - kinked wing, this fraction is combined with the weighted area of each panel as given in Equation 3.113 to obtain the location of the centre of gravity of a multi - kink wing.

$$cg_w = \sum_{i=1}^{m+1} \frac{S_i cg_{p_{i-1}}}{S_i} \tag{3.113}$$

Where: $cg_w$ is the location of the centre of gravity of a multi - cranked wing.
$S_i$ is the total surface area of each trapezoidal panel.

$i$ is the index of panels, starting from the outer panel.
$m$ is the number of kinks.

Converting the location of the wing centre of gravity location to a fraction of the MAC gives Equation 3.114.

$$cg_{mac} = \frac{(cg_w \times c_r) - \bar{\bar{x}}_{1/4}}{\bar{\bar{c}}} \tag{3.114}$$

With the masses and sizes of major aircraft components determined, the centre of gravity of the complete aircraft is estimated by dividing the pitching moment with relevant weights of the aircraft. However, the pitching moment can only be determined when the positions of items within the geometry are known. The 3 common internal arrangements proposed for the BWB commercial passenger transport is shown in Figure 3.16.

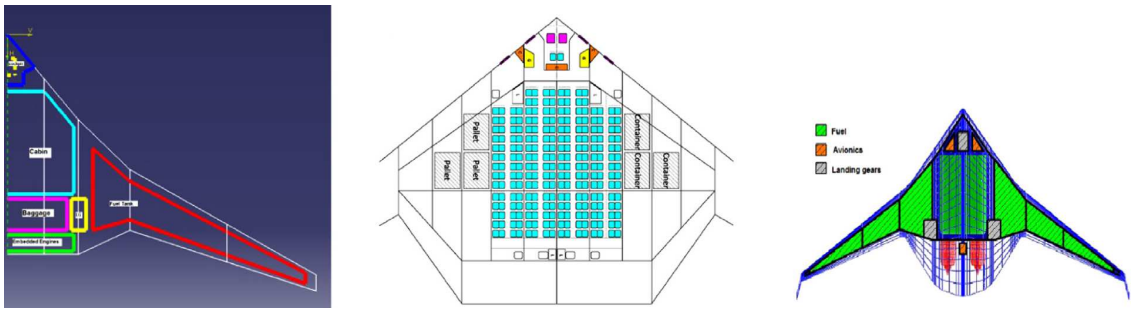


**Figure 3.16:** Common Internal Arrangements of a BWB Commercial Passenger Transport Aircraft

With the foregoing arrangements, the total pitching moment from aircraft nose with empty mass is found as given in Equation 3.115.

$$\begin{aligned} MOM_{mtom} = (m_{eng} \times [0.65c_0 + 0.5 \times l_{eng}]) + \left((m_{fuse} + m_{wing}) \left[\bar{\bar{x}}_{1/4} + (cg_{mac} \times \bar{\bar{c}})\right]\right) + \\ ((m_{LG} + m_{hydr}) [0.6 \times \bar{\bar{c}}]) + (m_{payload} [0.25c_0 \times (0.5 \times l_{cabin})]) + \\ ([m_{IAE} + m_{API} + m_{APU} + m_{fltcon}] \times (0.5 \times 0.25c_0)) + \\ ((m_{ops} + m_{furn}) \times [0.25c_0 + 0.5l_{cabin}]) + (m_{elec} \times [0.25 \times c_0]) + \\ (m_{fuel} \times [0.25c_0 + 0.5l_{cabin}]) \end{aligned} \tag{3.115}$$

$c_0$ is the wing centre - line chord.

Hence, the distance of the aircraft centre of gravity from the aircraft nose with MTOM

is given by Equation 3.116.

$$cg_{mtom} = \frac{MOM_{mtom}}{MTOM} \tag{3.116}$$

Similarly, the the distance of the aircraft centre of gravity from the aircraft nose with OEM is given by Equation 3.117.

$$cg_{oem} = \frac{MOM_{oem}}{OEM} \tag{3.117}$$

The total pitching moment from the aircraft nose with OEM, $MOM_{OEM}$ is obtained from Equation 3.115 by removing contributions from payload and fuel. This leads to the expressions in Equation 3.118.

$$\begin{aligned} MOM_{oem} = (m_{eng} \times [0.65c_0 + 0.5 \times l_{eng}]) + \left((m_{fuse} + m_{wing}) \left[\bar{\bar{x}}_{1/4} + (cg_{mac} \times \bar{\bar{c}})\right]\right) + \\ ((m_{LG} + m_{hydr}) [0.6 \times \bar{\bar{c}}]) + \\ ([m_{IAE} + m_{API} + m_{APU} + m_{fltcon}] \times (0.5 \times 0.25c_0)) + \\ ((m_{ops} + m_{furn}) \times [0.25c_0 + 0.5l_{cabin}]) + (m_{elec} \times [0.25 \times c_0]) \end{aligned} \tag{3.118}$$

The aircraft centre of gravity from the nose with zero fuel mass is derived from Equation 3.119.

$$cg_{zfm} = \frac{MOM_{zfm}}{ZFM} \tag{3.119}$$

The moment from the nose of the aircraft with ZFM is derived from Equation 3.118 by adding the contributions of the total pitching moment of the payload. This yields the expression given in Equation 3.120.

$$\begin{aligned} MOM_{oem} = (m_{eng} \times [0.65c_0 + 0.5 \times l_{eng}]) + \left((m_{fuse} + m_{wing}) \left[\bar{\bar{x}}_{1/4} + (cg_{mac} \times \bar{\bar{c}})\right]\right) + \\ ((m_{LG} + m_{hydr}) [0.6 \times \bar{\bar{c}}]) + \\ (m_{payload} [0.25c_0 \times (0.5 \times l_{cabin})]) + \\ ([m_{IAE} + m_{API} + m_{APU} + m_{fltcon}] \times (0.5 \times 0.25c_0)) + \\ ((m_{ops} + m_{furn}) \times [0.25c_0 + 0.5l_{cabin}]) + (m_{elec} \times [0.25 \times c_0]) \end{aligned} \tag{3.120}$$

The results from Equations 3.116, 3.117 and 3.119 gives the centre of gravity range for

the aircraft with the minimum being the forward CG and the maximum value being the aft CG.

### Geometry Parameterisation

Geometry parameterisation provides a mathematical description of the aircraft geometry. Parameterisation is used in the conceptual design synthesis of the BWB in order to generate a polynomial representation of the geometry. This permits the detection and avoidance of interference between internally placed components and the external geometry early in the conceptual design phase. According to Kulfan [131, 132], a good parameterisation technique must provide smooth and physically realisable shapes using computationally efficient and numerically stable process that is accurate and consistent. The technique should also be intuitive to permit the manipulation of a geometry using few design variables [131, 132].

Kulfan and Bussoletti [131] reviewed several parameterisation techniques for shape design optimisation including the discrete, polynomial and spline, Bezier curve, orthogonally derived basis function and free-form deformation techniques. The study finds neither of these methods appropriate for a shape design optimisation because they are either computationally expensive or incapable of smoothly modelling complex geometries. Consequently, they developed the Class Shape Function Transformation (CST) [131–133] technique. The CST parameterisation technique consists of 2 functions; the Class function and the Shape function. The class function defines the general class of geometry while the shape function ensures an analytically well - behaved mathematical function [132].

The Class function is defined by Equation 3.121.

$$c \begin{matrix} N1 \\ N2 \end{matrix} (\psi) = (\psi)^{N1}(1-\psi)^{N2} \tag{3.121}$$

Where $N1 = 0.5$ and $N2 = 1$ for the round nose and aft pointed airfoil [131–133].
$\psi$ is the non dimensional airfoil coordinate.
$\psi$ ranges from 0 to 1.

The shape function can be implemented using either the Bernstein polynomial or B-spline functions. Using Bernstein polynomial, the shape function is a product of the summation of unknown coefficients, $A_i$, and Bernstein polynomial terms. For a 2 - Dimensional (2D)

airfoil with upper and lower curves, the shape function for the upper curve , $Su_i$, is defined by Equation 3.122.

$$Su_i(\psi) = \sum_{i=1}^{N} Au_i \cdot S_i(\psi) \tag{3.122}$$

Where:
$S_i$ is the Bernstein polynomial terms given by Equation 3.123 as:
$Au_i$ is the upper curve coefficient.

$$S_i = k_i \psi^i (1-\psi)^{N-i} \tag{3.123}$$

Where:
$N$ is the order of the Bernstein polynomial,
and $k_i = \frac{N!}{i!(N-i)!}$ [131].

Combining the class and shape function, the equation for the upper curve of a 2D airfoil is given in Equation 3.124.

$$\zeta_u(\psi) = c \begin{matrix} N1 \\ N2 \end{matrix} (\psi) Su_i(\psi) + \psi \Delta\zeta_{upper} \tag{3.124}$$

where $\zeta_{upper}$, is the upper curve trailing edge thickness defined by $\frac{\Delta zu_{TE}}{c}$.

The CST for a 3 - Dimensional (3D) wing is derived from the 2D form by distributing airfoil sections across the wing span [132] and supplementing the class and shape functions for 2D airfoil with twist and local wing shear variables. The parameters used in deriving the CST of a 3D wing are shown in Fig 3.17.

The parameters are applied to the design of an arbitrary wing upper surface by Equation 3.125.

$$\zeta_u(\psi,\eta) = c \begin{matrix} N1 \\ N2 \end{matrix} (\psi) \sum_{i}^{Nx} \sum_{j}^{Ny} [Bu_{i,j} Sy_j(\eta) Sx_i(\psi)] + \psi [\zeta_T(\eta) - \tan\alpha_T(\eta)] + \zeta_N(\eta) \tag{3.125}$$

Where:
The stream - wise shape function $Sx_i(\psi)$ is defined by:

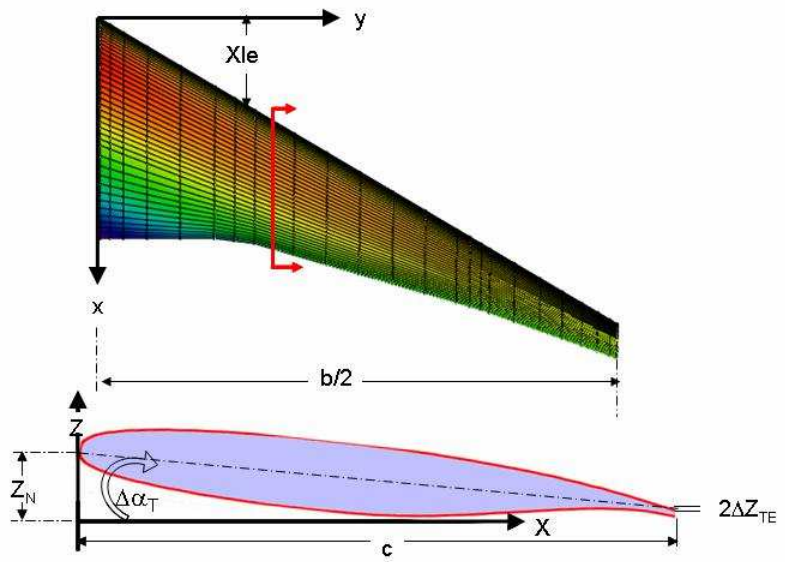


**Figure 3.17:** Parameters used in 3D Wing CST Derivation. [132]

$Sx_i(\psi) = kx_i\psi^i(1-\psi)^{Nx-i}\ for\ i = 0\ to\ Nx$

$Nx$ is the order of the Bernstein polynomial in the stream - wise direction.

$kx_i$, the stream - wise binomial coefficient, is given by:
$kx_i = \frac{Nx!}{i!(Nx-i)!}$.

The span - wise shape function, $Sy_j(\eta)$ is derived from:
$Sy_j(\eta) = ky_j\eta^j(1-\eta)^{Ny-j}\ for\ j = 0\ to\ Ny$

With $ky_j$, the span - wise binomial coefficient given by:
$ky_j = \frac{Ny!}{j!(Ny-j)!}$,

and $Bu_{i,j}$, the matrix of upper surface coefficient.

Similarly, the wing lower surface is defined by Equation 3.126.

$$\zeta_L(\psi,\eta) = C \begin{matrix} N1 \\ N2 \end{matrix} (\psi) \sum_i^{Nx} \sum_j^{Ny} [Bl_{i,j} Sy_j(\eta) Sx_i(\psi)] + \psi\left(\zeta_T(\eta) - \tan\alpha_T(\eta)\right) + \zeta_N(\eta) \quad (3.126)$$

These matrices of upper and lower surface coefficients are used as design variables which are determined from optimisation routines.

Where :
$Bl_{i,j}$ is the matrix of lower surface coefficients.
$\psi$ is the wing non - dimensional local chord x-coordinate derived from Equation 3.127.
$\psi$ ranges from 0 to 1.

$$\psi = \frac{x - x_{LE}(\eta)}{c(\eta)} \tag{3.127}$$

Where:
$x_{LE}(\eta)$, is the local leading edge coordinate at each span - station.
and $c(\eta)$, is the local chord length at each span - station.
$\eta$, the non - dimensional half - span station which also ranges from 0 to 1.

$\eta$ is determined from Equation 3.128.

$$\eta = \frac{2y}{b} \tag{3.128}$$

Non - dimensional upper surface coordinate, $\zeta_u(\eta)$ is defined by Equation 3.129.

$$\zeta_u(\eta) = \frac{z_u(\eta)}{c(\eta)} \tag{3.129}$$

While, $\zeta_N(\eta)$, the non - dimensional local wing shear is obtained from Equation 3.130.

$$\zeta_N(\eta) = \frac{z_N(\eta)}{c(\eta)} \tag{3.130}$$

$\zeta_T(\eta)$, is the local wing trailing edge thickness.

$\alpha_T(\eta)$, is the local wing twist angle.

To ensure the continuity of surface around the leading edge, Kulfan[132] proposed that $Bl_{0,j} = Bu_{0,j}$.

The physical x, y and z - ordinates of a wing are subsequently obtained by:

$y = \frac{b\eta}{2}$
$x = \psi c_{loc}(\eta) + x_{le}(\eta)$
$z_u(x, y) = \zeta_u(\psi, \eta) c_{loc}(\eta)$
$z_l(x, y) = \zeta_l(\psi, \eta) c_{loc}(\eta)$

**Volume Constraint Handling**

Volume constraint can be handled either by interference detection and correction or by curve fitting.

**Interference detection and correction.** The interference detection method detects collision by comparing the physical $z - coordinates$, $z_i(px_i, py_i)$, of the CST curves obtained using the $x$ and $y$ vertices, $(px_i, py_i)$, of internal objects with the $z - coordinate$, that is the $pz_i$ of the object.

Assuming internal objects are enclosed in a rectangular bounding box to reduce complexity, interference detection is implemented by converting physical coordinates, $px_i$, $py_i$, of all vertices of the bounding boxes into its non - dimensionalised values $\psi$, $\eta$. These values are then used to generate the CST polynomial functions $\zeta_i(\psi, \eta)$ of the upper and lower surfaces. The $\zeta_i(\psi_{px_i}, \eta_{py_i})$ representing the wing surfaces at all span stations are subsequently converted into the physical $z - coordinate$, $z_i(x_i, y_i)$, and compared with corresponding objects $z - coordinates$, $pz_i$ to assess interference. If the CST derived upper surface physical $z - coordinates$, $z_i(x, y)$, is greater than the objects $z - coordinate$, $pz_i$, the item is inside the geometry, otherwise it is interfering with the boundaries of the external geometry at such position(s). The reverse is the case with the lower surface.

For instance, given an object with vertices $(px_i, py_i, pz_i)$, the object is properly enclosed if $zupper_i(px_i, py_i)$ is greater than $pz_i$ at the point of interest on the surface of the geometry and less than $zlower_i(px_i, py_i)$. Conversely, objects are outside the geometry if $zupper_i(px_i, py_i)$ is less than $pz_i$ at determined point on the surface of the geometry and greater than $zlower_i(px_i, py_i)$.

It is imperative to note that the interference detection described here detects only internal objects violation on the vertical or normal axis $z - axis$. Longitudinal(stream-wise) and lateral(span-wise) interference detection is done using the chords and span of the airplane respectively. Additionally, since it would be computationally expensive to parametrically define all curves at every possible span stations on the wing, intersection of objects lying between 2 span stations are determined by interpolating the curves bounding the affected

span station. Notwithstanding, in order to improve accuracy, it is essential for the greatest distance between parameterised span stations to be less than the least width of internal objects within the geometry. In this way only one side of any object can lie between 2 span stations at any time rather than the complete object.

Interpolation between 2 span stations is implemented by determining the physical z-coordinate of the bounding span stations $z_i(px^*, py_i)$ and $z_{i+1}(px^*, py_{i+1})$ and then applying the linear interpolation theorem stated in Equation 3.131 to determine the overlapping object, $z^*$. The $z^*$ obtained is then compared with the actual z-coordinate of the object, $pz^*$ to determine if object interferes with geometry or is well enclosed.

$$z^* = z_i + \frac{(z_{i+1} - z_i)(y^* - y_i)}{y_{i+1} - y_i} \tag{3.131}$$

Knowing that a CST parameterisation is given in terms of $\psi$ and $\eta$, the physical coordinates or vertices of internal objects is converted to the non - dimensionalised form required for CST parameterisation by first converting $py_i$ and $px_i$ into $\eta$ and $\psi$ using Equations 3.132 and 3.133 respectively.

$$\eta = \frac{2py_i}{b} \tag{3.132}$$

$$\psi = \frac{px_i - x_{LE}(\eta)}{c_{local}(\eta)} \tag{3.133}$$

where :
The local leading edge x-coordinate is a function of the sweep angle and obtained as:
$x_{LE}(\eta) = \eta \times \tan \Lambda_{LE}$
$b$ is the wing span.

The $\eta$ and $\psi$ obtained are subsequently substituted into Equations 3.134 and 3.135 to determine the physical upper and lower surface $z - coordinates$, $zupper_i(x_i, y_i)$ and $zlower_i(x_i, y_i)$, respectively required for interference detection.

$$z_u(x, y) = \zeta_u(\psi, \eta) c_{loc}(\eta) \tag{3.134}$$

$$z_l(x, y) = \zeta_l(\psi, \eta) c_{loc}(\eta) \tag{3.135}$$

**Curve fitting.** Curve fitting is performed by scaling a curve with the right shape to ensure that it goes through the vertices of the bounding boxes of the internal geometry. Generating a curve with the right shape could be done by either the variation method or the use of coefficients. Assuming the coordinates of the 2 upper vertices of a bounding box enclosing an internal object are given by ($\psi_1$,$\zeta_1$) and ($\psi_2$,$\zeta_2$), the method of variation involves varying the $N1$ exponent of the class function and keeping the $N2$ exponent constant to obtain Equation 3.136.

$$\psi_1{}^{N1_{fit}}(1-\psi_1) = \frac{\zeta_1}{\zeta_2}\psi_2{}^{N1_{fit}}(1-\psi_2) \tag{3.136}$$

Solving for $N1_{fit}$ gives Equation 3.137.

$$N1_{fit} = \frac{\log\left[\frac{\zeta_1(1-\psi_2)}{\zeta_2(1-\psi_1)}\right]}{\log\left(\frac{\psi_1}{\psi_2}\right)} \tag{3.137}$$

Applying the value obtained from Equation 3.137 gives the generalised class function given in Equation 3.138. This generalised class function is then used to creates a curve with the right shape.

$$(\psi_1)^{N1_{fit}}(1-\psi_1)^{N2} \tag{3.138}$$

The method of coefficients involves scaling the class function with two coefficients $a$ and $b$ as given in the simultaneous equations in Equation 3.139.

$$\begin{cases} (\psi_1)^{N1}(1-\psi_1)^{N2}\cdot[a(1-\psi_1)+b\psi_1] = \zeta_1 \\ (\psi_2)^{N1}(1-\psi_2)^{N2}\cdot[a(1-\psi_2)+b\psi_2] = \zeta_2 \end{cases} \tag{3.139}$$

Solving the simultaneous equations and applying the obtained coefficients to a generalised class function, creates a curve with the right shape using Equation 3.140.

$$(\psi)^{N1}(1-\psi)^{N2}\cdot[a(1-\psi)+b\psi] \tag{3.140}$$

Having obtained the curves with the right shape, the curves are made to go through the vertices of the bounding box by scaling it using $\zeta_{bb}/zeta_{gen}$.

Where:
$\zeta_{bb}$ is the non - dimensionalised value of z at the vertices of the box bounding the internal objects.

$\zeta_{gen}$ is the non - dimensionalised value derived from the generalised form of the curve fitting equation.

This research applied the curve fitting volume constraint handling method for packaging because they directly ensure that internal objects are well contained without first checking for interference detection.

## 3.4 Chapter Summary

This Chapter describes the theories of disciplinary models used in the developed synthesis and optimisation tool. The GMDSO Tool couples a Class II component weight estimation method incorporating the Bradley and Howe BWB structural mass estimation models with a vortex lattice aerodynamic analysis model and CST parameterisation packaging module to create a synthesis model for the fast, accurate design and analysis of the BWB. This ensures that items are well fitted and positioned within the confines of the geometry to provide an appropriate centre of gravity.

# Chapter 4

# Performance and Stability Analysis

The performance and stability analysis are conducted to investigate the stability, controllability and flying qualities as well as assess if an aircraft is sufficiently able to fulfil the mission for which it was designed. The stability analysis implemented in this research evaluates the static margin and trim characteristics of the aeroplane. The performance analysis on the other hand consists of point and mission performance. The point performance assesses the ability of the aircraft to perform required manoeuvres during its mission. Point performance calculations performed in the GMDSO Tool includes field performance, climb gradients and thrust required at various mission segments. Mission performance on the other hand determines the bulk fuel as well as the ability of the aircraft to achieve a specific range. The mission performance is used to determine the distance travelled during a mission, duration required and the fuel burnt during that mission. This Chapter will discuss the algorithms employed in calculating various performance and stability characteristics of a BWB in the development of the multi - variate design synthesis tool.

## 4.1 Performance Analysis

A typical mission profile for a commercial air transport consists of the main mission and a reserve mission. The main mission consists of the take-off, climb, cruise, descent and landing as shown in Figure 4.1. The main mission is the typical mission profile of a commercial aircraft under normal conditions without delays or any incidents. However, due to unforeseen circumstances, traffic congestion or weather related incidents, etc, a commercial flight may deviate from its intended mission to an alternate aerodrome. The

reserve mission profile comprises all the flight phases described in the main mission, however, the cruise range is limited and its often flown at 10000 ft. In this thesis, the reserve mission consist of missed approach, climb to diversion cruise altitude of 10000 ft, cruise for a range of 200 nm, hold at 5000 ft, descent to 1000 ft, approach and landing as shown in Figure 4.2.

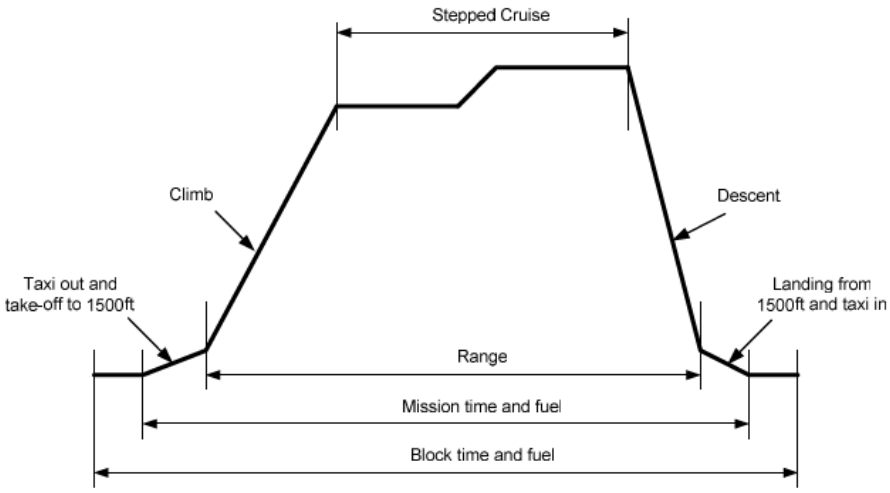


**Figure 4.1:** Typical Main Mission Profile of a Commercial Transport Aircraft

The reserve mission profile determines the reserve and regulatory fuel need

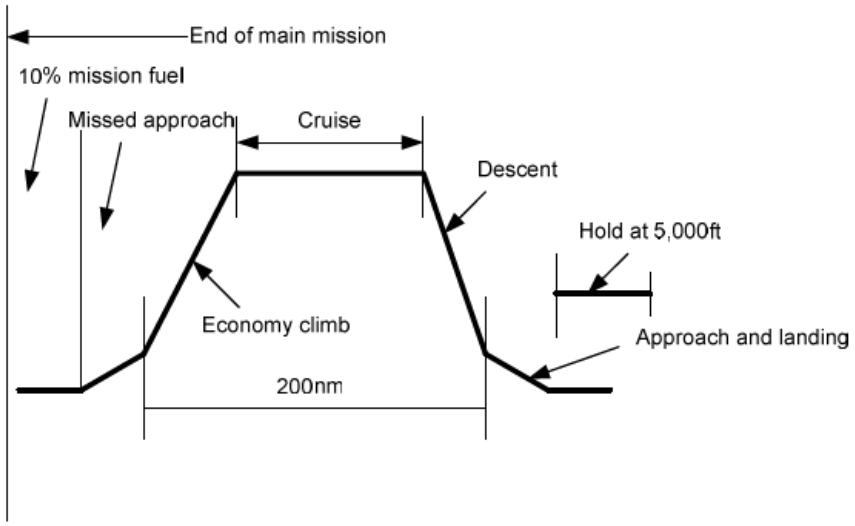


**Figure 4.2:** Typical Reserve Mission Profile of a Commercial Transport Aircraft

### 4.1.1 Take-off

In analysing the field performance, the mass of fuel consumed, time spent and distance travelled within each phase are determined. The manoeuvres during take - off consists of the ground roll, transition to climb and climb to 1500 $ft$. The ground roll measures the distance from the start of take - off to the point of lift - off. It is estimated by Equation 4.1.

$$s_g = \frac{1}{2gK_A} \ln\left[\left(K_T + K_A \times V_{LOF}^2\right)/K_T\right] \qquad [115] \tag{4.1}$$

Where :
$g$ is the acceleration due to gravity in $m/s$.
$K_A = \frac{\rho\left(-(a+bC_L{}^2)+\mu C_L{}^2\right)}{2MTOM/S_{ref}}$ [115]
$K_T = \frac{T}{MTOM \times g} - \mu$ [115]
$\mu$, the runway coefficient of friction.
$\mu = 0.02$ for paved runway. [115]
$\rho$ is the density in $kg/m^3$.
$V_{LOF}$ is the lift off speed in $m/s$. $V_{LOF} = 1.1V_{stall}$.
$(a + bC_L{}^2) = C_D$.
$C_L$ is the lift coefficient.
$T$ is the thrust in $N$.

The transition to climb refers to the portion of the take-off manoeuvre during which the aircraft accelerates from lift - off speed($V_{LOF}$) to the Take - off Climb Speed($V_2$) [115].

The transition speed($V_t$) is given as the average of lift-off speed and the take-off climb speed. This is expressed mathematically in Equation 4.2.

$$V_t = 0.5 \times (V_{LOF} + V_2) \qquad [115] \tag{4.2}$$

The aircraft is assumed to fly with a lift coefficient equal to $0.9 \times C_{Lmax}$ and a load factor ($n$), given by Equation 4.3.

$$n = 1 + \frac{V_t^2}{rg} \qquad [115] \tag{4.3}$$

The radius of arc($r$) is determined from Equation 4.4.

$$r = \frac{V_t^2}{[g(n-1)]} \qquad [115] \tag{4.4}$$

The height at the end of transition($h_t$) is calculated from Equation 4.5.

$$h_t = r \times \gamma^2/2 \qquad [115] \tag{4.5}$$

where:
$\gamma$ is the flight path angle.

If the $h_t$ is greater than the screen height($h_s$) then the distance to the screen height ($s_s$), is calculated from Equation 4.6.

$$s_s = \left[(r + h_s)^2 - r^2\right]^{0.5} \qquad [115] \tag{4.6}$$

Where:
subscript s is the screen height.
subcript t denotes transition height.

Subsequently, the total distance required for take-off($dist_{TO}$) is obtained from Equation 4.7. The factor of 1.15 is included in the equation to account for pilot and operational variations [115].

$$dist_{TO} = 1.15 \times (s_g + s_s) \qquad [111] \tag{4.7}$$

If $h_t$ less than the $h_s$, then the total take-off distance is derived from the summation of the ground roll distance, distance in transition and climb distance multiplied by a factor of 1.15 as given in Equation 4.8.

$$dist_{TO} = 1.15 \times (s_g + s_t + s_c) \qquad [111] \tag{4.8}$$

The ground distance to transition height($sg_t$) is calculated from Equation 4.9.

$$sg_t = r \times \gamma \tag{4.9}$$

The ground distance from end of transition to screen height ($sg_s$) is determined from Equation 4.10.

$$sg_s = \frac{(h_s - h_t)}{\tan\gamma} \qquad [115] \tag{4.10}$$

Where:
$h_t$ is greater than $h_s$, then the $t_s$ is given by Equation 4.11.

$$t_s = \frac{2s_s}{V_{LOF} + V_2} \qquad [115] \tag{4.11}$$

After transition, the aircraft enters the take - off climb also known as the initial climb. The take-off climb profile is often split into 4 main segments. These are the 0 - 35 ($ft$), 35 - 400$ft$, 400$ft$, 400+$ft$ and 1500 $ft$. The definition of the various segments including the operating conditions and required gradients are given in Table 4.1.

**Table 4.1:** Definition of Climb Segments

| | | | | | Gradient (%) number of engines | | |
|---|---|---|---|---|---|---|---|
| Segment | Height(ft) | Flap | LG | Ratings | 2 | 3 | 4 |
| 1st | 0-35 | TO | Down | TO | +ve | 0.3 | 0.5 |
| 2nd | 400 | TO | Up | TO | 2.4 | 2.7 | 3.0 |
| 3rd | 400+ | variable | Up | Max. cont. | | level acceleration | |
| 4th | 1500 | En-route | Up | Max. cont. | 1.2 | 1.5 | 1.7 |

The take-off climb of civil transport aircraft is often defined by the second segment climb requirements. In the second segment climb, the aircraft must demonstrate the the ability to achieve the minimum climb rate specified in Table 4.1 at a speed equal to or greater than 15 percent above the stall speed with one engine inoperative.

### 4.1.2 Take-off One Engine Inoperative

Take-off performance analysis in the one engine inoperative condition is undertaken to asses the runway length required for safe manoeuvre of the aircraft in the case of engine failure during take-off. Usually, pilot could, subject to the time of occurrence of the failure, either continue the take-off and fly away on the remaining engines or apply emergency braking and bring the aircraft to a stop. These are the 'accelerate - go' and 'accelerate - stop'. The common distance at which the 'accelerate - go' distance equals the 'accelerate - stop' distance is referred to as the Balanced Field Length (BFL).

The BFL is calculated using exactly same equations as the all engine operative condition up to the point of engine failure. Subsequently, using a pilot reaction time of two seconds and accounting for the expected increase in drag due to the failed engine in the 'accelerate - go' condition as well as the performance and limitations of the braking system in the 'accelerate - go' condition, the BFL is calculated from a range of speeds at which the engine fails.

In this research, the engine failure speed used ranged from $V_1$ to $V_2$. The critical engine failure speed ($V_1$), is taken as $v_1 = 0.8V_S$ while $V_2 = 1.2V_S$. Applying Equation 4.1 to the engine failure speed range, the distances to each engine failure speed are determined. Giving a typical pilot reaction time of $2s$, the distance travelled in the reaction time is obtained through the relationship given in Equation 4.12.

$$s_{2s} = V_1 \times 2 \tag{4.12}$$

Next, the distance from the end of reaction time to lift off speed is calculated. This is obtained by first estimating the mean speed during transition for each of the assumed critical engine speed using Equation 4.13.

$$V_{mean} = (V_1 + V_{LOF})/2 \tag{4.13}$$

The $am$ is obtained from Equation 4.14.

$$am = (T/W - \mu) + (\rho/(2MTOM \times g/S_{ref})) \left[(C_D - \mu C_L) \times {V_{mean}}^2\right] \quad [115] \tag{4.14}$$

Where:

The drag coefficient ($C_D$) consists of the asymmetric and wind - milling drag in addition to the induced and profile drag. The profile drag must account for the increments in take-off configuration.

The asymmetric drag coefficient or windmill drag, $cd_{assy}$, is obtained from Equation 4.15.

$$cd_{assy} = \frac{0.3 \times (0.0254 \times ((0.037 \times (m_{flow} \times 2.21)) + 32.2))}{S_{ref}} \quad [115] \tag{4.15}$$

Now, dividing the difference between lift - off speed and each of the critical engine speeds

by the associated aircraft acceleration, as given in Equation 4.16, the change in time is obtained.

$$dt = (V_{LOF} - v_1)/am \tag{4.16}$$

The distance travelled within this time, $dt$, is calculated from Equation 4.17.

$$\Delta_s = dt \times V_{mean} \tag{4.17}$$

The distance covered during transition from lift - off to climb and from transition to screen height are determined in the same way as the all engine condition.

The accelerate - go distance($s_{accgo}$) is thus given by Equation 4.18.

$$s_{accgo} = s_{goei} + s_{2s} + \Delta_+ s_{Toei} + s_{soei} \tag{4.18}$$

The subscript, *oei* denotes one engine inoperative. This indicates that the variable is determined in the one engine inoperative condition using the specific engine failure or mean speed as required.

The accelerate - stop distance ($s_{accstop}$) is derived from Equation 4.1 for the different critical speeds within the chosen failure speed range.

Having determined the 'accelerate - stop' and 'accelerate - go' distances, the BFL is obtained by plotting these distances against the square of the engine failure speeds. The point where the 2 curves intersects gives the BFL on the distance axis and the critical speed on engine failure speeds axis.

Other variables determined in take-off analysis are the time used and mass of fuel consumed. The time used for take-off is determined from Equation 4.19.

$$t = dist/speed \tag{4.19}$$

$t_g$ is given by $t_g = \frac{2s_g}{V_{LOF}}$.
$t_t$ is given by $t_t = \frac{2s_t}{V_{LOF}}$.
$t_c$ is given by $t_c = \frac{2s_c}{V_{LOF}+V_2}$.

The mass of fuel used for take - off ($m_{fuelTO}$), is determined from Equation 4.20.

$$m_{fuelTO} = T \times SFC \times t \tag{4.20}$$

Where:
$T$ is the thrust at the given condition.
$SFC$ is the specific fuel consumption.
$t$ is time used in seconds.

### 4.1.3 En-route Climb

Aircraft rarely climb directly from take-off to cruise altitude due to air traffic control restrictions and to enable a good rate and gradient of climb. Often, climb is split into several parts. The main parts are the 1500 - 10000 $ft$ and from 10000 $ft$ to the cruise altitude. In this research, the en-route climb is extended to include climb to the following segments: 35 - 1500 $ft$, 1500-5000 $ft$, 5000 - 15000 $ft$ calculated at a mean height of 10000 $ft$, 15000 - 25000 $ft$ calculated at a mean height of 20000 $ft$ and 25000$ft$ - cruise altitude. The flight characteristics during the take - off and each segment of the en -route climb phase are shown in Figure 4.3.

Within each of the climb segment, the time, distance and mass of fuel used are calculated. The distance travelled during climb($s_{ec}$) is determined from Equation 4.21.

$$s_{ec} = V_{TAS} \times t_{cl} \tag{4.21}$$

Where:
$t_{ec}$ is calculated from $t_{cl} = \frac{h_{cl}}{ROC}$.
$h_{cl}$ is the climb height.
ROC is estimated from $ROC = V_{TAS} \times \sin\gamma$.
$V_{TAS}$ is the true airspeed.
$\gamma$ the climb gradient is derived from:
$\gamma = \frac{T}{MTOM \times g} - \frac{C_D}{C_L}$

The thrust at maximum continuous setting($T_{maxCont}$) is calculated from Equation 4.22.

$$T_{maxCont} = T \times \sigma^{0.8} \tag{4.22}$$

Where:
The subscript, $maxCont$, denotes maximum continuous rating.

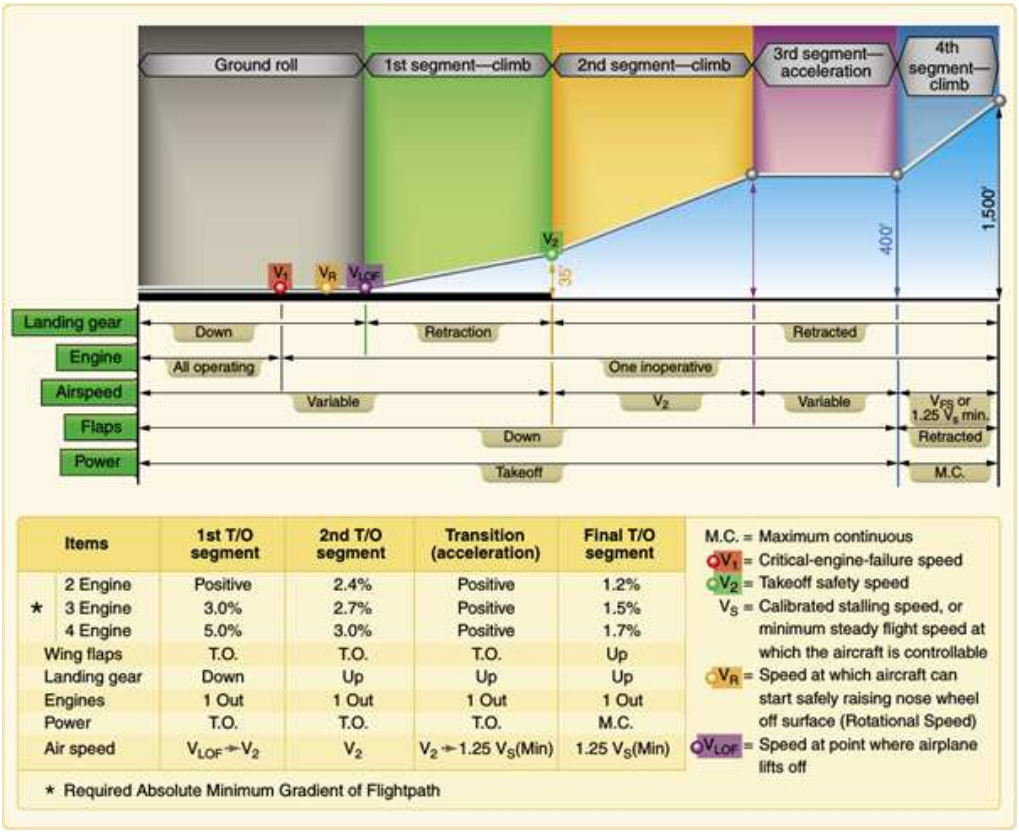


| | Items | 1st T/O segment | 2nd T/O segment | Transition (acceleration) | Final T/O segment |
|---|---|---|---|---|---|
| | 2 Engine | Positive | 2.4% | Positive | 1.2% |
| ★ | 3 Engine | 3.0% | 2.7% | Positive | 1.5% |
| | 4 Engine | 5.0% | 3.0% | Positive | 1.7% |
| | Wing flaps | T.O. | T.O. | T.O. | Up |
| | Landing gear | Down | Up | Up | Up |
| | Engines | 1 Out | 1 Out | 1 Out | 1 Out |
| | Power | T.O. | T.O. | T.O. | M.C. |
| | Air speed | $V_{LOF}$ → $V_2$ | $V_2$ | $V_2$ → 1.25 $V_S$(Min) | 1.25 $V_S$(Min) |

★ Required Absolute Minimum Gradient of Flightpath

M.C. = Maximum continuous
$V_1$ = Critical-engine-failure speed
$V_2$ = Takeoff safety speed
$V_S$ = Calibrated stalling speed, or minimum steady flight speed at which the aircraft is controllable
$V_R$ = Speed at which aircraft can start safely raising nose wheel off surface (Rotational Speed)
$V_{LOF}$ = Speed at point where airplane lifts off

**Figure 4.3:** Flight Characteristics in the Different Segments of the Enroute Climb Phase

$\sigma$ is the relative density.
$T$ is the static thrust.

The mass of fuel at any flight condition is determined from the product of static thrust, specific consumption and time as given in Equation 4.23.

$$m_{fuelcon} = T \times SFC \times t \tag{4.23}$$

### 4.1.4 Cruise

The cruise phase is a crucial part of an civil transport aircraft mission profile. This is because the aircraft usually spends the most time in cruising flight. The ability to assess the cruise performance of an aircraft is therefore vital to assessing the performance of an aircraft.

Aircraft can cruise in 3 different ways. These are the constant angle of attack - constant Mach number cruise; constant angle of attack - constant altitude cruise; and the constant

altitude - constant Mach number cruise. The constant angle of attack - constant Mach number cruise, also known as the cruise - climb technique, requires the aircraft to climb during the cruise in order to maintain the power/thrust to weight ratio. The cruise - climb method gives the best range for a given mass of fuel [134]. However, due to Air Traffic Control (ATC), constraints and the need to provide vertical separations between aircraft in different directions, aircraft cannot be allowed to change direction indiscriminately in flight [134].

Cruising at constant angle of attack, constant altitude gives maximum range but increases the need to continuously reduce the airspeed to compensate for the decrease in aircraft weight [134]. This cruise approach tends to increase the time of flight which could nullify any advantage the method may have [134]. Nonetheless, this method is suitable for surveillance operation where endurance is more important than distance travelled [134].

In the constant altitude, constant Mach number cruise, the angle of attack is decreased with decrease in weight in order to maintain the weight to lift ratio. This is the preferred method for commercial airline operation. The range flown by aircraft using this method is derived from Equation 4.24.

$$R = \left[\frac{V_{mdi}}{SFC} E_{max}\right] 2u_i \left\{\tan^{-1}\left[\frac{1}{{u_i}^2}\right] - \tan^{-1}\left[\frac{1}{\omega {u_i}^2}\right]\right\} \qquad [134] \qquad (4.24)$$

Where:
$R$ is the cruise range.
$E_{max}$ is the maximum endurance.
$u_i$ is the relative speed.

The relative speed, $u_i$, is the ratio of the cruise speed to the minimum drag speed as expressed in Equation 4.25.

$$u_i = \frac{V_{cr}}{V_{mdi}} \qquad (4.25)$$

Where:

$V_{mdi}$ is the minimum drag speed.
$V_{cr}$ is the cruise speed.

Hence, taking an optimum relative speed of 1.316 [134], the minimum drag speed is calculated from Equation 4.26.

$$V_{mdi} = \frac{V_{cr}}{1.316} \tag{4.26}$$

Maximum endurance, $E_{max}$ is derived from Equation 4.27.

$$E_{max} = \frac{1}{2(C_{d0}K)^{\frac{1}{2}}} \tag{4.27}$$

Where:

$C_{d0}$ is the zero lift drag coefficient.
$K$ is the induced drag correction factor.

The induced drag correction factor, $K$, is inversely proportional to the wing aspect ratio, AR, and the Oswald efficiency factor,$(e)$. The induced drag corrector, $K$, is obtained from Equation 4.28.

$$K = \frac{1}{\pi e AR} \tag{4.28}$$

The Oswald efficiency factor, $e$, varies with the AR and the leading edge sweep angle. According to Sadraey [135], the $e$ is determined from Equation 4.29.

$$e = 4.61\left(1 - 0.045AR^{0.68}\right)\left[\cos\left(\Lambda_{LE}\right)\right]^{0.15} - 3.1 \tag{4.29}$$

Substituting into Equation 4.24, the fuel weight ratio, $\omega$, in cruise is estimated in terms of the range function, $(R_f)$, by Equation 4.30.

$$\omega = \frac{1}{\tan\left[\tan^{-1}\left[\frac{1}{{u_i}^2}\right] - \frac{R}{R_f \times 2u_i}\right]{u_i}^2} \qquad [134] \tag{4.30}$$

The range function, $R_f$, is obtained from Equation 4.31.

$$R_f = \frac{V_{mdi}E_{max}}{SFC} \tag{4.31}$$

According to Eshelby [134], $\omega$ equal 1.5 for very long range aircraft, 1.3 for medium range aircraft and 1.1 for short range aircraft. Knowing the fuel weight ratio, $\omega$, and the mass of

the aircraft at the beginning of cruise, $wi_{cr}$, the mass of the aircraft at the end of cruise, $mf_{cr}$, is calculated from Equation 4.32.

$$w_f = \frac{w_i}{\omega} \tag{4.32}$$

Subsequently, the weight of fuel consumed in cruise is derived from Equation 4.33.

$$w_{fcr} = w_i - w_f \tag{4.33}$$

The time required for cruise is calculated from Equation 4.34.

$$t = R/V_{TAS} \tag{4.34}$$

### 4.1.5 Descent

The descent from cruise to landing consists of 3 phases. The en-route descent, descent in the terminal area and the final approach. A requirement in descent is that the aircraft must not descend at a rate that could increase cabin pressure beyond 300 $ft/min$ [134].

Consequently, given that the cabin of a civil transport aircraft is pressurised to 8000 $ft$ pressure height. Assuming the pressure is increased from 8000 $ft$ in cruise to 1000 $ft$ at the terminal boundary, the minimum time in descent is determined from Equation 4.35 to obtain 23.3 $min$.

$$t_{mintd} = \frac{8000 - 1000}{300} \tag{4.35}$$

Therefore, the average Rate of Descent (ROD), from cruise altitude to 25000 $ft$ calculated at the mean altitude is given by Equation 4.36.

$$ROD = \frac{dH}{t_{mintd}} \tag{4.36}$$

Given the descent speed and knowing the ROD and aircraft mass in that stage of descent, the gradient of descent is obtained from Equation 4.37.

$$\sin\gamma = \frac{dH/dt}{V_{TAS}} \tag{4.37}$$

The $T_{desc}$ is derived from Equation 4.38.

$$T_{desc} = \left(\frac{C_D}{C_L} + \sin\gamma\right) \times m_h \times 9.81 \qquad [134] \tag{4.38}$$

$m_h$ is the mass at the given height.

The time required for descent is subsequently determined from Equation 4.39.

$$t_{desc} = \frac{dH}{ROD} \tag{4.39}$$

Distance flown in the descent stage is determined from Equation 4.40.

$$s_{desc} = V_{TAS} \times t_{desc} \times \cos\gamma \qquad [134]. \tag{4.40}$$

The mass of fuel required for descent, $mfuel_{desc}$, for each stage of the descent phase is determined from Equation 4.41.

$$mfuel_{desc} = T_{desc} \times t_{desc} \times SFC \tag{4.41}$$

This is done for all stages within the en-route descent phase.

In the descent phase of the Terminal Manoeuvring Area (TMA), an aircraft is flown on ATC speed of 165 KEAS with flaps in the landing setting, landing gear extended and engine thrust adjusted to provide the rate of descent required necessary to maintain the flight path to the final approach.

Given the distance from the TMA to the touchdown point, $s_{TMA}$, the distance to the start of final approach, $s_{FA}$, and the descent gradient, $\gamma_{desc}$, the height at the start of final approach,$h_{FA}$, is calculated by Equation 4.42.

$$h_{FA} = s_{FA} \times \tan\gamma_{desc} \tag{4.42}$$

Assuming the height at the entry to the TMA, $h_{TMA}$, is known, the mean gradient at the TMA, $grad_{mean}$, is determined from Equation 4.43.

$$grad_{mean} = \frac{h_{TMA} - h_{FA}}{s_{TMA} - s_{FA}} \tag{4.43}$$

Taken the $h_{TMA}$ to be 5000 $ft$ (1524 $m$), an aircraft needs to decelerate from a certain deceleration speed, $V_{TMA5000}$, to a suitable speed of $V_{TMA}$ at the $h_{FA}$. This phase of the flight is performed with flap in the take-off setting and the landing gear extended. The distance covered to decelerate, $s_{desc}$, from $V_{TMA5000}$ to $V_{TMA}$ is determined from Equation 4.44.

$$s_{desc} = \frac{m_{TMA}}{2F_{mean}} \left( \frac{{V_{TMA}}^2 - {V_{TMA5000}}^2}{\sigma} \right) \tag{4.44}$$

Where :
$F_{mean} = T - D + (MTOM \times g \sin\gamma)$ .
$m_{TMA}$ is the mass of the aircraft at the entry of the TMA.

The time expended in the TMA, $t_{TMA}$, is obtained from Equation 4.45.

$$t_{TMA} = \frac{2s_{desc}\sigma^{\frac{1}{2}}}{V_{e1} + V_{e2}} \tag{4.45}$$

Where: $V_{e1}$ is the equivalent airspeed at the entry to the TMA at a height of 5000 $ft$.
$V_{e2}$ is the equivalent airspeed at the start of the final approach in the TMA.

Equivalent airspeed (EAS), is derived from true airspeed (TAS), by the relation given in Equation 4.46.

$$V_{EAS} = V_{TAS} \times \sigma^{\frac{1}{2}} \tag{4.46}$$

### 4.1.6 Landing

The landing phase of flight includes descent from the screen height of 50 $ft$(15 $m$) at idle thrust until touch down. The touch down speed is estimated to be slightly above the stall speed. In this research, touch - down speed is derived from $V_{td} = (V_s + 5)\ m/s$. Idle thrust, $(T_{id})$, is assumed to be $1000N$ [134]. The total landing distance is the sum of the air and ground distance covered during landing.

The air distance in landing $(sa_{land})$, is calculated from Equation 4.47.

$$sa_{land} = -\frac{-MTOM \times g}{([T_{id} \times n_{eng}] - D)_{av}} \left\{ \frac{{V_{app}}^2 - {V_{td}}^2}{2g} + 15 \right\} \qquad [134] \tag{4.47}$$

Where:
subscript land designates variable in landing phase.
subscript id designates variable in idle mode.
$n_{eng}$ is the number of engines.
subscript eng represents engine.
subscript cr denotes variable in the cruise phase.
$V_{app}$ is the approach speed.$V_{td}$ is the touch down speed.$g$ is acceleration due to gravity-
subscript td represent the given variable in touch down.
subscript app denotes approach.

The ground run distance in landing ($sg_{land}$) is estimated from Equation 4.48.

$$sg_{land} = \frac{1}{2gB} \ln\left(BV^2 + A\right) \text{[134]} \tag{4.48}$$

Where:
$BV^2 + A = \left[\frac{\rho S_{ref} C_L}{(2\times MTOM\times g)}\left(\frac{C_D}{C_L} - \mu\right) V^2 \left\{[\mu + \sin\gamma] - \frac{T}{(MTOM\times g)}\right\}\right]$ [134].

The ground run is evaluated at $0.7V_{td}$.
$B = \frac{\rho S C_L}{(2\times MTOM\times g)}\left(\frac{C_D}{C_L}\right)$ [134].
$A = \mu - \frac{T}{(MTOM\times g)}$ [134].

### 4.1.7 Diversion and Reserves

Diversion is included in the mission performance analysis in order to provide for unlikely diversion to an alternative airfield due to destination airfield being unavailable for landing. The Diversion phase involves climb to the decision height from the final approach, cruise and descent to the alternate airfield. The diversion fuel and time are thus calculated in the same way as corresponding segments of the main flight phases.

Reserve fuel includes regulatory and contingency fuel. Regulatory fuel is fuel for 45 minutes cruise calculated with landing weight and best endurance speed [134]. Contingency reserve is usually determined by the aircraft operator as a percentage of the trip fuel required for flight between departure and destination. In this research contingency fuel is taken as 10 % of the trip fuel [134].

Knowing the landing weight, the mass of regulatory fuel($mfuel_{reg}$) is determined from

Equation 4.49.

$$mfuel_{reg} = T_{reg} \times SFC \times 45 \times 60 \tag{4.49}$$

The regulatory thrust ($T_{reg}$), is calculated from Equation 4.50.

$$T_{reg} = \frac{MLW \times g}{(C_L/C_D)_{max}} \tag{4.50}$$

In this research, the diversion schedule involve cruise of 200 nm to the diversion airfield at an altitude of 10000 $ft$. Consequently, the diversion phase involves climb from the decision height to the diversion altitude, cruise to the diversion airfield, descent to 5000 $ft$ in the TMA and subsequently to the final approach for landing. The mass of fuel, distance travelled and time expended in this phase is calculated in the same way as the corresponding segment of main flight phase.

## 4.2 Stability

The BWB has good aerodynamic potentials but fairly complicated stability challenges arising from the low moment arm and poor trim characteristics. This research assesses the longitudinal static stability of a BWB by determining the static margins and trim characteristics.

### 4.2.1 Static Margin

Static margin is a concept used to characterise the degree of static stability and controllability of the aircraft. Static margin is defined as the distance between the center of gravity and the neutral point of the aircraft. Applying classical stability theory to the free - body diagram shown in Figure 4.4, the pitching moment of a tailless aircraft in a trimmed, quasi- steady flight at constant mass, normal atmosphere and without compressibility effects for small angles of attack, assuming moments due to power plant and the centre of gravity due to normal displacement are negligible, is given by Equation 4.51.

$$C_{m_{cg}} = C_{m_0} + C_L(h - h_0) = 0 \tag{4.51}$$

Taking $h = x_{cg}$ and $h_0 = x_{ac}$, Equation 4.52 is derived.

$$C_{m_{cg}} = C_{m_0} + C_L(x_{cg} - x_{ac}) = 0 \tag{4.52}$$

Where :
$C_{m_{cg}}$ is the coefficient of moment about the centre of gravity.
$C_{m_0}$ is the zero lift pitching moment.
$x_{cg}$ is the cg position on the mean aerodynamic chord.
$x_{ac}$ is the aerodynamic centre location on the mean aerodynamic chord.

Differentiating Equation 4.52 with respect to $\alpha$ gives Equation 4.53.

$$\frac{\delta C_{m_{cg}}}{\delta \alpha} = (x_{cg} - x_{ac}) \frac{\delta C_L}{\delta \alpha} \tag{4.53}$$

Rewriting Equation 4.53 in terms of static stability derivatives gives Equation 4.54.

$$C_{m_\alpha} = C_{L_\alpha} (x_{cg} - x_{ac}) \tag{4.54}$$

But $x_{ac} - x_{cg}$ is also known as stability margin, $K_n$. Making $K_n$ the subject leads to Equation 4.55.

$$K_n = -\frac{C_{m_\alpha}}{C_{L_\alpha}} \tag{4.55}$$

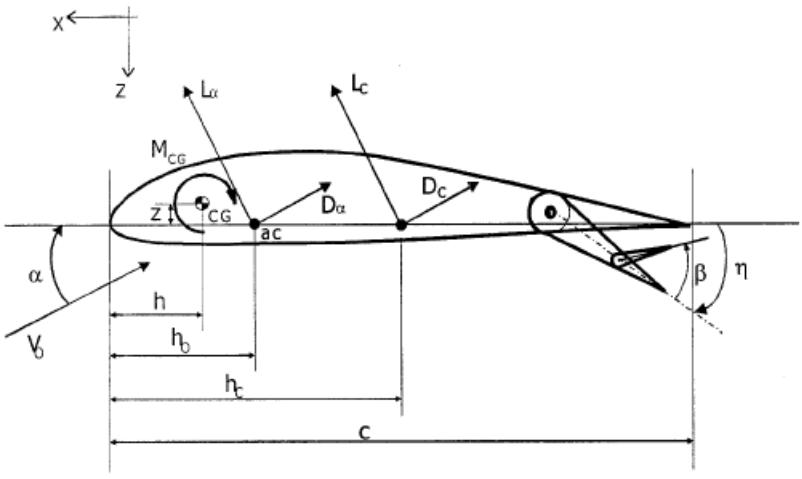


**Figure 4.4:** Forces and Moments acting on an Aircraft

To guarantee good stability, it is essential for an aircraft to be longitudinally static stable. An aircraft is longitudinally static stable if it has a positive static margin $K_n$ [136, 137].

This implies from Equation 4.55, therefore, that longitudinal static stability is achieved when the design satisfies Equation 4.56.

$$\frac{C_{m_\alpha}}{C_{L_\alpha}} < 0 \tag{4.56}$$

### 4.2.2 Trim Characteristic

Trim characteristics determines the elevon deflections necessary to trim an aircraft in operating flight envelope. This criterion is particularly expedient for a BWB design due to its short moment arm and tailless nature. According to Castro [138, 139], a BWB aircraft trim characteristics is assessed by its trim angle of attack and the elevon deflection angle for trim. Castro [138, 139] defined the trim angle of attack, $\alpha_{trim}$ by Equation 4.57 and elevon deflection for trim by Equation 4.58.

$$\alpha_{trim} = \frac{C_K C_{L_{\delta_e}} - C_B C_{m_{\delta_e}}}{Det} \tag{4.57}$$

$$\delta_{e_{trim}} = \frac{C_B C_{m_\alpha} - C_{L_\alpha} C_K}{Det} \tag{4.58}$$

Where:
$C_K = -C_{m0} - C_{m_\beta}\beta$
$C_B = C_{L_{trim}} - C_{L0} - C_{L_\beta}\beta$
$Det = C_{L_{\delta_e}} C_{m_\alpha} - C_{L_\alpha} C_{m_{\delta_e}}$

$C_{m0}$ is the basic pitching moment at zero degree angle of attack.
$C_{m_\beta}\beta$ is the pitching moment due to elevon trim tab deflections.
$C_{L_\beta}\beta$ is the lift coefficient derivative due to elevon trim tab deflections.
$C_{L_{\delta_e}}$ is the lift coefficient derivative due to elevon deflections.
$C_{m_\alpha}$ is the pitching moment coefficient derivative with respect to angle of attack.
$C_{L_\alpha}$ is the lift coefficient derivative with respect to angle of attack.
$C_{L0}$ is the lift coefficient at zero degree angle of attack.
$C_{L_{trim}}$, the trim lift coefficient, is obtained from Equation 4.59.

$$C_{L_{trim}} = \frac{W}{\frac{1}{2}\rho V^2 S} \tag{4.59}$$

$W$ is the weight of the aircraft [N] at the given flight phase.

Assuming no trim tabs are used, since tailless aircraft rarely have them [140], then:

$$C_K = -\bar{C}_{m0}$$
$$C_B = C_{L_{trim}} - C_{L0}$$

### 4.2.3 Framework for Design Synthesis and Optimisation

The models developed in this chapter and the preceding chapter are coupled for the conceptual design synthesis of a BWB according to the flow-chart shown in Figure 4.5. Subsequently, the design synthesis and analysis models are combined with an optimiser, as shown in Figure 4.6, to permit the exploration of the BWB design space.

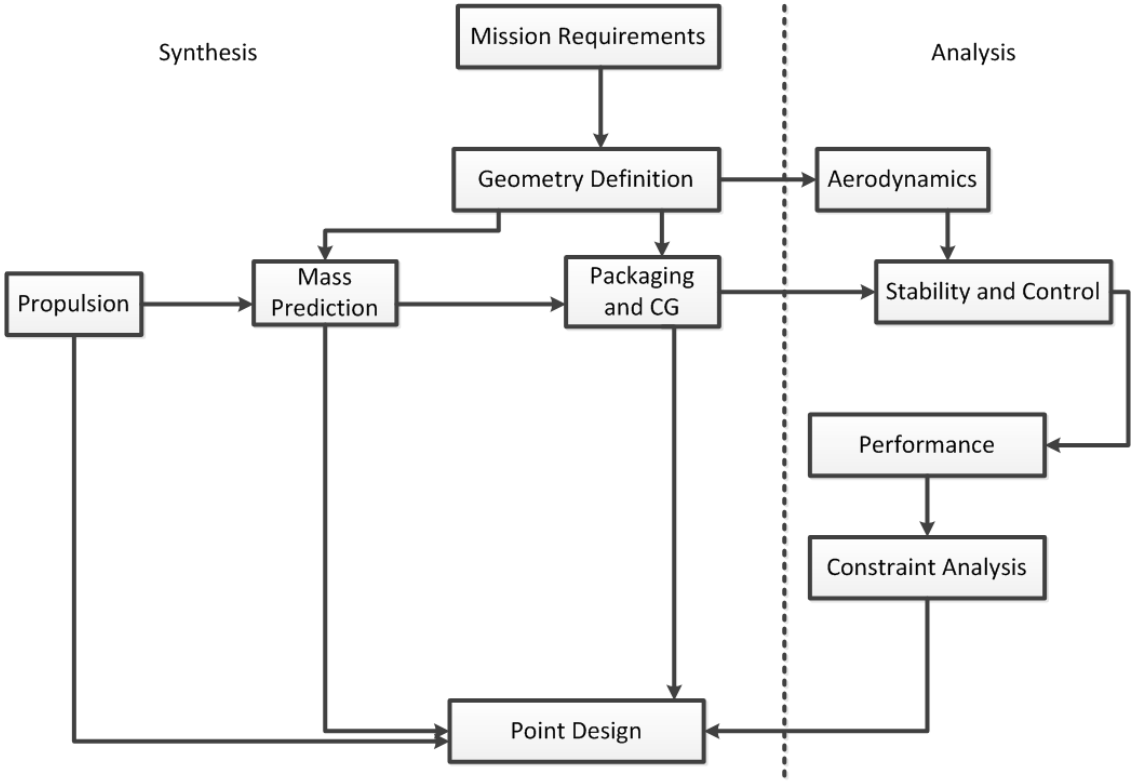


**Figure 4.5:** Flow - Chart for a Conceptual Design Synthesis and Analysis of a BWB Aircraft.

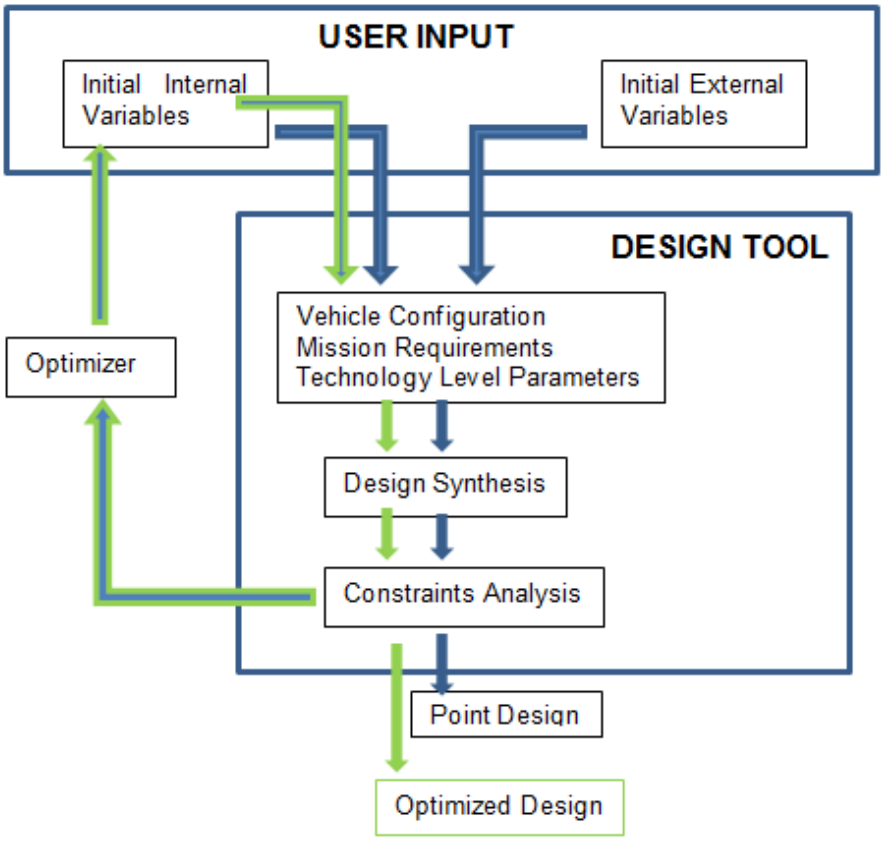


**Figure 4.6:** Framework for the Design Synthesis and Optimisation of a BWB Aircraft.

## 4.3 Chapter Summary

This Chapter describes the implementation of the stability and performance analysis modules of the design synthesis tool as well as the framework for coupling developed disciplinary models. The 2 modules are treated separately from the methodology Chapter because they are analysis module which depends on the disciplinary modules implemented in the preceding Chapter for its action. The performance module estimate the mission and point performance in full engine operative and one engine - inoperative conditions. The stability module on the other hands assesses the static margin, trim characteristics and the ride quality.

# Chapter 5

# Structure of the Multi-variate Design Synthesis Tool

This Chapter presents an overview of the synthesis and optimisation process for the developed GMDSO Tool. The tool is implemented through a large JAVA code containing various isolated modules. The modules are integrated with an optimiser which manipulates design variables to ensure constraints are met and optimal objective function is realised. The arrangement of modules, data flow and operation of the tool are explained in the following sections.

## 5.1 Top Level Requirements for GENUS Aircraft Design Software

The need to develop computational design synthesis tool that permits the re - use of design processes led to the development of the multi - variate design synthesis optimisation software code-named 'GENUS'. The GENUS Multi - variate Design Synthesis Optimisation Tool integrates disciplinary models in a modular, expandable, flexible and independent arrangement.

The modularity arrangement ensures disciplinary modules are implemented in a self - contained, independent, clearly - separated blocks of code. This reduces debugging difficulties and enables the efficient modification of any module without recourse to the whole program. Additionally, it allows the use of more than one technique in any disciplinary

module. For example one can have different ways to predict aerodynamic coefficients. One module could implement empirical method or integrate a physics based code. A knowledgeable user could then select either of the different techniques to meet the requirements of the design synthesis.

The program's expandability is intended to ensure the number of modules could be increased to any desired number with the requisite level of detail or fidelity for the intended aircraft design phase. Though the software is designed primarily to be used for conceptual design, with expandability, relevant parts of the software could be modified accordingly to support preliminary or even the detailed design phase depending on the available computational power. Further to the foregoing, the JAVA programming languages can handle dynamic memory allocation thus providing infinite expandability as opposed to legacy languages such as Fortran 77, where the whole program has to be loaded into the memory before execution.

Flexibility entails the ability of the tool to be used for the design of any aerospace vehicle. This requires high levels of abstraction towards representation and implementation. For this reason, lifting surfaces are used to define all aerospace systems with lifting surface geometric parts rather than wings which could restrict the application of the tool. Furthermore, the use of JAVA programming language which supports abstraction and polymorphism also helps the tool to achieve sufficient flexibility.

Independence and sustainability are also important requirements for the GENUS software. This is derived from the need to avoid any dependency on proprietary software. Proprietary software is expensive and require manufacturer's permission to modify any aspect of the code. Any form of dependency on proprietary software increases the cost of development and exposes GENUS to the risk of becoming obsolete in the case of the proprietary software being discontinued. In order to avoid this, the GMDSO Tool was developed in a well established programming language that is freely distributed with great potential for future growth.

## 5.2 Selection of a Suitable Programming Language for GMDSO Tool

A wide range of programming language is available for the development of the GMDSO tool. Generally, there are two main categories of programming languages; the compiler and interpreter languages. A compiler language refers to programming language, where

the typed instructions are assembled, linked and subsequently converted into machine code which the computer can execute directly from the host Central Processing Unit (CPU). Interpreter languages are not compiled into an object code but rather rely on interpreter programs or virtual machines to interpret and execute the commands one after the other. Generally compiled languages tend to run faster, as they can be directly executed and do not have the "interpretation overhead".

There are several programming languages that could be used in the development of the GMDSO Tool. According to the Institute of Electrical and Electronics Engineers (IEEE), the 2015 Top 10 programming language in order of their popularity are shown in Table 5.1. Although, generally regarded as the language of technical computing, FORTRAN is not listed in the top 10 programming language for 2015. Nonetheless, it is expedient that any program chosen for the implementation of GENUS should be able to interface with FORTRAN. This is because several legacy programs which could enhance the capacity and capability of the developed tool are written in FORTRAN. These includes NASA and U.S Air Force codes as well as such other codes like the AVL and DATCOM amongst others.

Based on the requirements for the GMDSO Tool, the programming language adopted is JAVA. JAVA was chosen because its a general purpose programming language that is easy to learn with good potential for future growth and longevity. Additionally, JAVA easily interfaces with several other programming languages in the top 10 such as Python, C/C++/C as well as with Fortran through the C/C++ interface using the JNI. Also, JAVA is platform independent and benefits from a wide range of support resources from several programming communities such as the StackOverflow and CodeRanch amongst others. Most notably, JAVA is an object oriented program with dynamic memory allocation. It is free to use and considerably faster than most interpreter language. The JAVA programming language also supports abstraction and polymorphism.

JAVA was implemented in the Netbeans Integrated Development Environment (IDE). The NetBeans IDE is a text editor that enables quick and easy development of JAVA applications. It consists of editors, code analysers and a converter to enable smart editing and rapid search through multiple applications at the same time. NetBeans IDE facilitates efficient project management by providing different views of data, from multiple project windows to helpful tools for setting up applications. Additionally, the NetBeans IDE enables rapid Graphic User Interface (GUI) development through the use of editors and the drag - and - drop tools in the IDE. Furthermore, NetBeans provides static analysis tools for identifying and fixing common problems in JAVA code.

**Table 5.1:** 2015 Top 10 Programming Languages

| Rank | Name | Properties | Introduction |
|---|---|---|---|
| 1 | JAVA | Compiler<br>General purpose, concurrent,<br>class-based, object oriented, | 1995 |
| 2 | C | Compiler<br>General Purpose, imperative | 1972 |
| 3 | C++ | Compiler<br>General purpose, imperative,<br>object -oriented, generic features | 1983 |
| 4 | Python | Interpreter<br>High level, general-purpose,<br>object-oriented, imperative<br>functional | 1991 |
| 5 | C# | Compiler<br>Multi-paradigm programming, involves much typing<br>imperative, declarative, functional<br>generic,object-oriented, component-oriented | 2000 |
| 6 | R | Interpreted<br>object oriented, supports matrix arithmetic,<br>procedural programming,generic | 1993 |
| 7 | PHP | Interpreter<br>Server-side scripting language,<br>General purpose | 1995 |
| 8 | JavaScript | Interpreter<br>Dynamic language,<br>mainly used as part of a web browser | |
| 9 | Ruby | Interpreter<br>Dynamic, reflective, object-oriented,<br>general purpose | 1995 |
| 10 | Matlab | Interpreter<br>Multi paradigm, numerical computing environment | 1984 |

## 5.3 Overview of GMDSO Tool

The GMDSO Tool consist of 9 essential disciplinary modules. These modules are the mission specification, geometry, propulsion specification, mass breakdown, aerodynamics, propulsion, packaging and centre of gravity, performance, stability and control. In addition to the essential modules, the design program can have any number of "special modules". The special modules represent modules that are unique and specific to a given aircraft type. This includes, for instance, modules used in calculating solar radiation intensity for solar powered aircraft, but are not required for the design of any other aerospace vehicles.

The essential modules and any special module are integrated with an optimiser to create a GMDSO Tool with nice interactive GUI. An outline of the data flow between the GUI, the modules and the optimizer is shown in Figure 5.1.

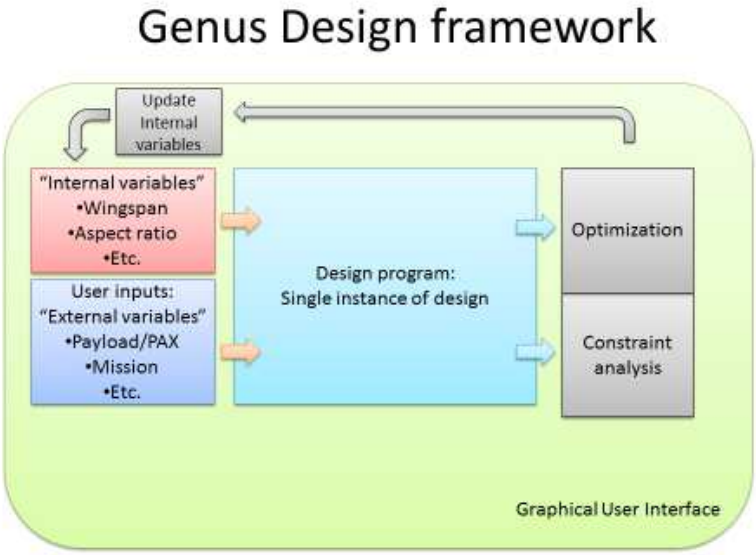


**Figure 5.1:** Data Flow for the GMDSO Tool.

The Figure 5.1 shows the exchange of data between the various modules in the design synthesis framework and the Optimiser. From Figure 5.1, it could be seen that the GMDSO Tool is designed to enable users to input and extract values as well as set up optimization processes through a GUI. The GUI also offers users the ability to select an objective function and define the constraints and design variables. Based on the objective and the constraints, the user could set up the external variables and define the internal variable for the optimiser. Internal variables are those variables which the optimiser can control while external variable are variable that are pre-set by the programmer or entered as inputs.

## 5.4 The Design Program

The GMDSO Tool is created around a set of internal and external variables, INPUTS, OUTPUTS and RESULTS and models. Internal variables are those sets of variables that directly controls the behaviour of a model. As stated earlier, internal variables are often the design variables in an optimisation process. External variables on the other hand are

parameters used to interact with the operation of the program.

INPUTS refer collectively to the variables used to control the behaviour of a module. Inputs could be integers like the number of passengers or power - plants; double precision real numbers; or a list which enables the user choose from a selection of pre-defined options.

OUTPUTS are the responses synthesised from the input variables within a disciplinary module. Outputs are available to be used during optimisation, either as the objective function or as constraints.

RESULTS, just like outputs, are derived from the manipulation of inputs within the disciplinary modules. They are available to the user for post - processing or analysis. It could be in the form of numbers, text, images or videos amongst others. Unlike outputs, RESULTS have no effect on the optimization process. However, they can be further processed by the user to create plots or analysed in their raw forms for reports. A module can write out its OUTPUTS as part of the RESULTS.

Models are the blocks of codes within a module used to describe physical processes. A model could range from a few lines of code to tens of thousands of lines. While models could be self-contained it could also contain method(s) that call(s) or invoke some external program(s). A model could also be blank module without performing any computation. Blank models are however implemented only when other modules do not rely on its results.

It worthy to note that a model must not require direct input from the user or optimizer nor provide outputs or results. This is often the case with aerodynamics module using empirical equations that are based on geometry and require no special settings. Such module would not have an input. Nonetheless, there needs to be outputs or results from such models otherwise the user will not have any information from the given module. Unless, such modules are created to support the function of another module, they are not desirable.

The structure of the design modules in the GMDSO Tool showing data interactions between the 9 essential modules is shown in Figure 5.2. The GMDSO Tool is designed to produce a single instance of aerospace vehicle design using its current set of inputs (both internal and external). Consequently, the GMDSO Tool is made to be robust in order to be able to produce a design for all potential combinations of input variables. The

colouring is consistent with Figure 5.1 to aid the identification of the module location within the GMDSO framework. The arrows show the direction of data flow within the design program.

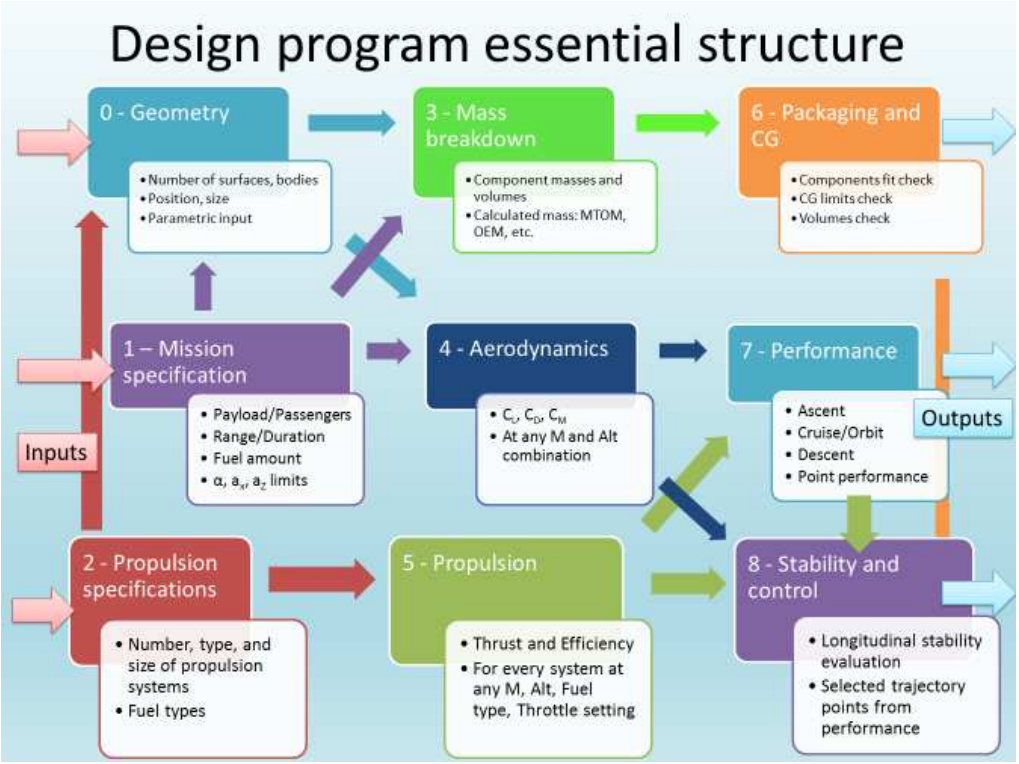


**Figure 5.2:** Interaction Between Modules in the GMDSO Tool

Generally, aircraft design is an inverse process. This implies that the desired outcome is known ahead of the design process, but not the inputs. However, it is quite difficult to reverse engineer a design due to the coupling between disciplines and the non - linear relationships between desired outputs and inputs. Though, human ingenuity could estimate the desired output, computers often produce a desired design through the process of assume inputs, synthesis, evaluate and iterate until the desired output is obtained. Computers are able to do this because of the increase in computing power which enables modern computers to perform about $177 \times 10^9$ floating point operations per second [141]. A diagrammatic comparison of human vs computer design process is shown in Figure 5.3.

The 'iterate' task in Figure 5.3 is performed by an optimiser in the Computer-based design process. The optimiser iterates and prescribe new sets of inputs for the design. These new inputs, set within reasonable bounds determined by a knowledgeable user, are used by the design program to produce several outputs for any single instance of the design. In order to ensure results are always generated, the design program must be robust, otherwise the optimizer will not be able to drive the process. This involves some form of fail safe option

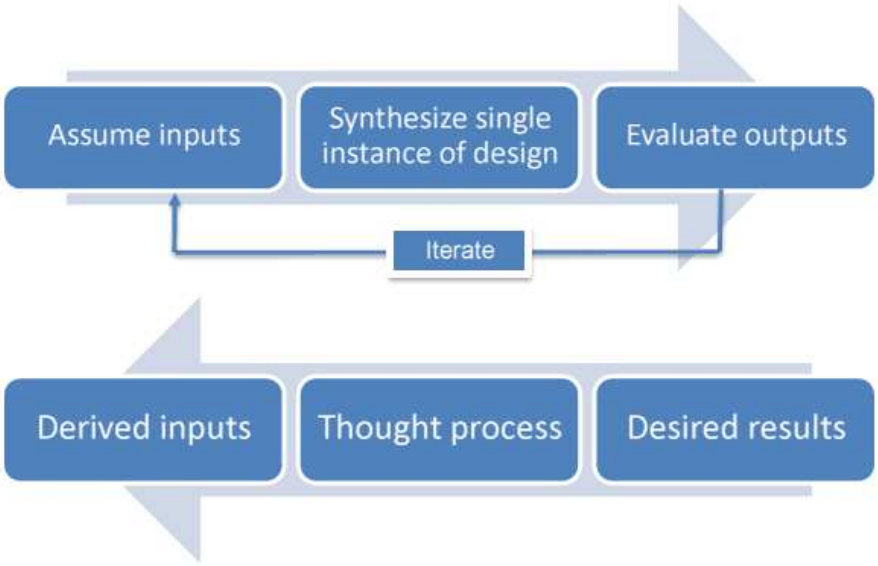


**Figure 5.3:** Computer-based (top) vs Human Intuitive Design Process(bottom)

within the program to ensure that careless or wrong inputs, does not crash the program. For instance, if an indiscriminate input combination results in an infeasible aircraft, it is required that this does not stop the program from completing the design process, even if the result is rather meaningless.

Despite the robustness of a program, it is absolutely necessary to constrain the design to yield a feasible or acceptable product. Constraint analysis routines is used to determine if a constraint is satisfied and if not, by what extent it is from the desired value. Due to the different tolerance required for different outputs within the GMDSO Tool, constraints are analysed by Equation 5.1. The Equation 5.1 scales the constraint to ensure an acceptable tolerance is obtained with different category of constraints.

$$Constraint_i = \frac{value_{target_i} - value_{calculated_i}}{value_{target_i}} \tag{5.1}$$

## 5.5 The GMDSO Tool GUI

The GMDSO GUI is created with the JAVA native Swing GUI. The GUI enables a knowledgeable user select the modules, set the inputs, select internal variables, objective function and constraints. The GUI could be used to trigger single and optimisation run and view results in text format. The various parts of a GUI are shown in Figures 5.4, 5.5, 5.6 and 5.7.

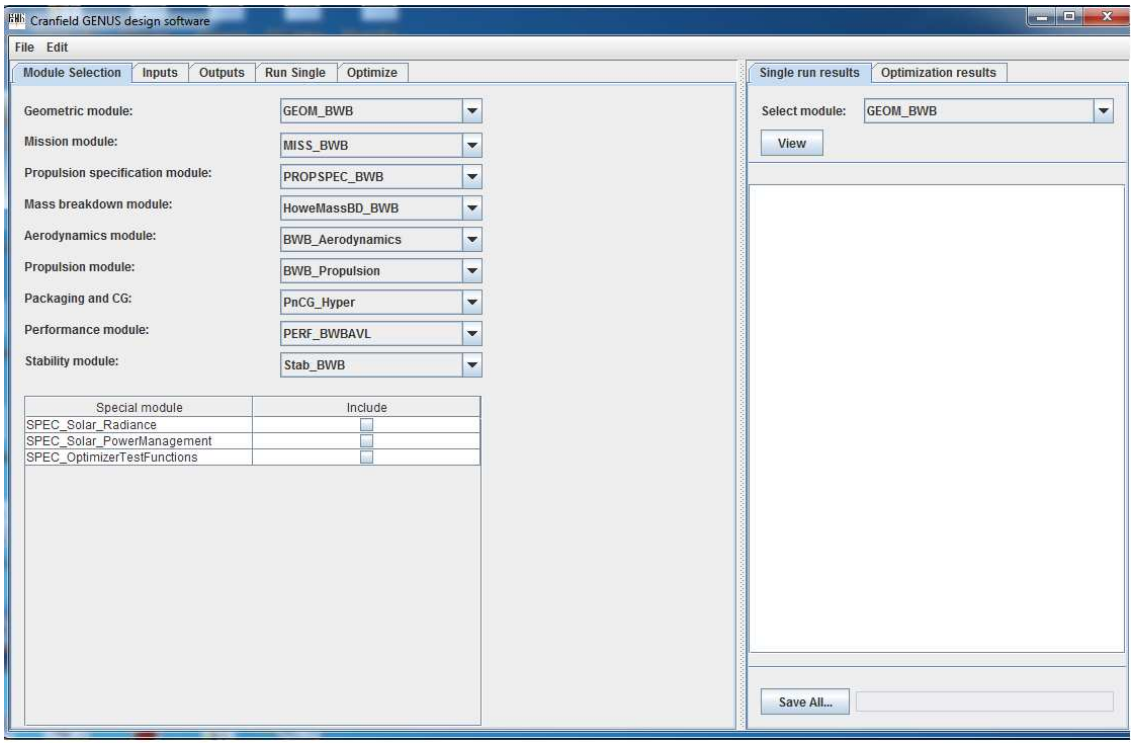


**Figure 5.4:** Selection of Modules in the GMDSO Tool.

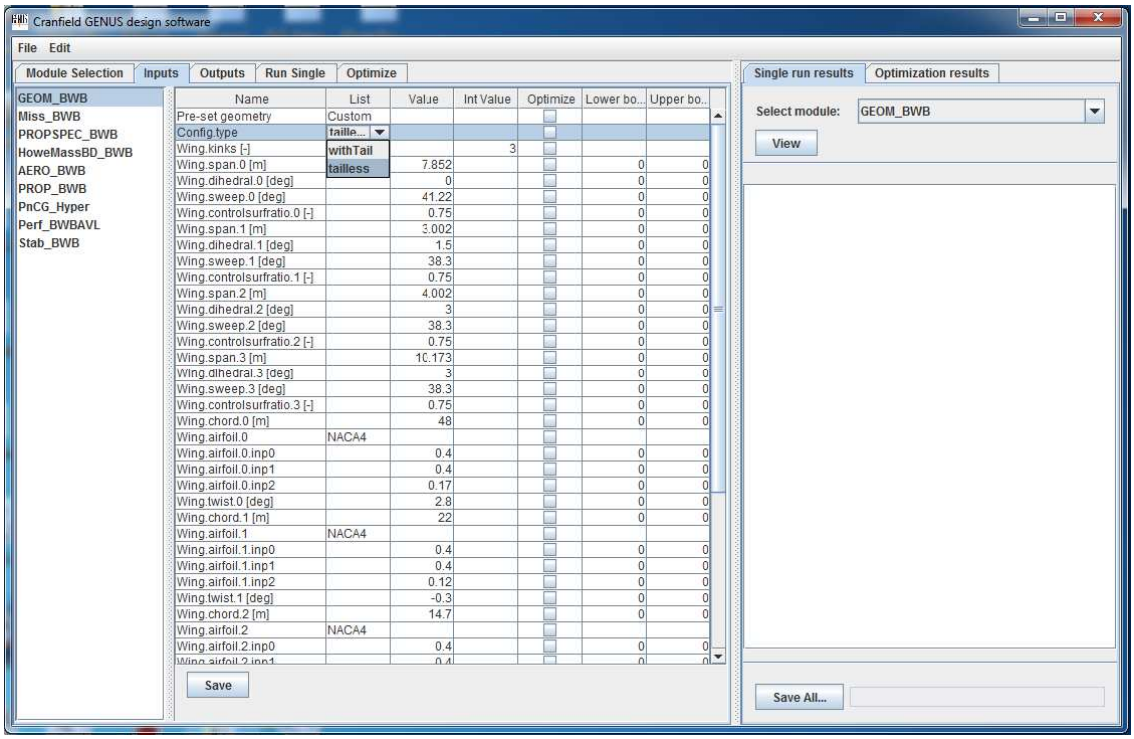


**Figure 5.5:** Setting Inputs in the GMDSO Tool.

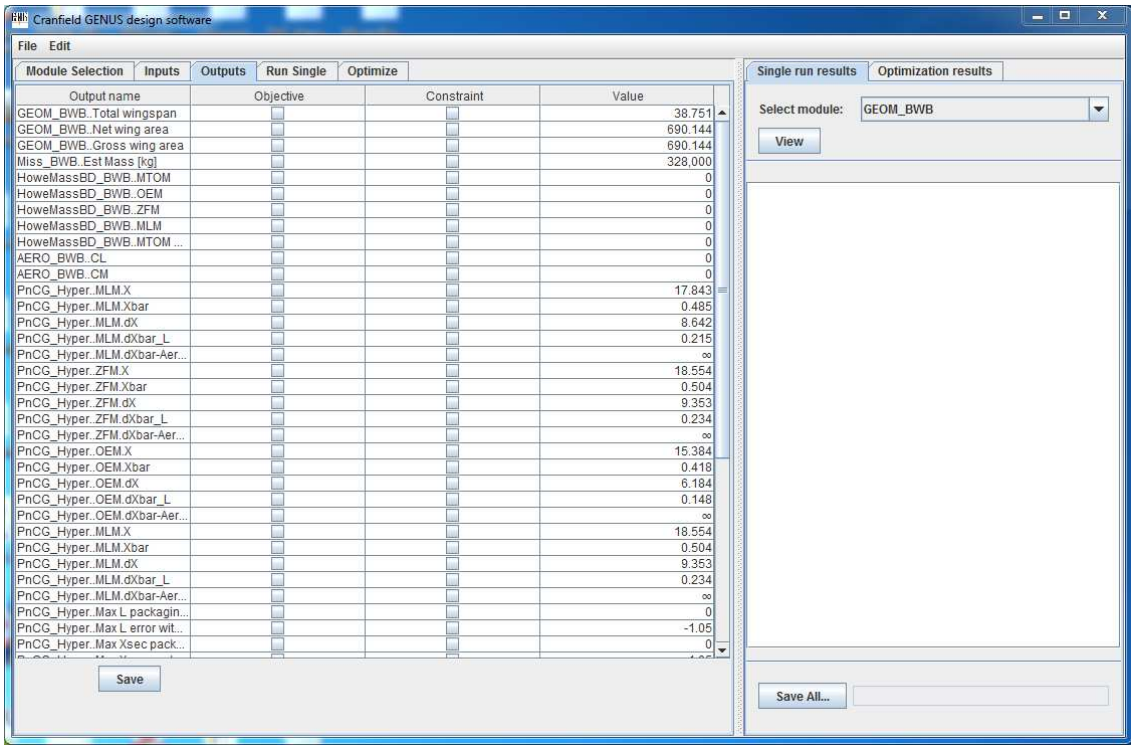


**Figure 5.6:** Output Frame Showing Selection of Objective Function and Constraints for Optimisation.

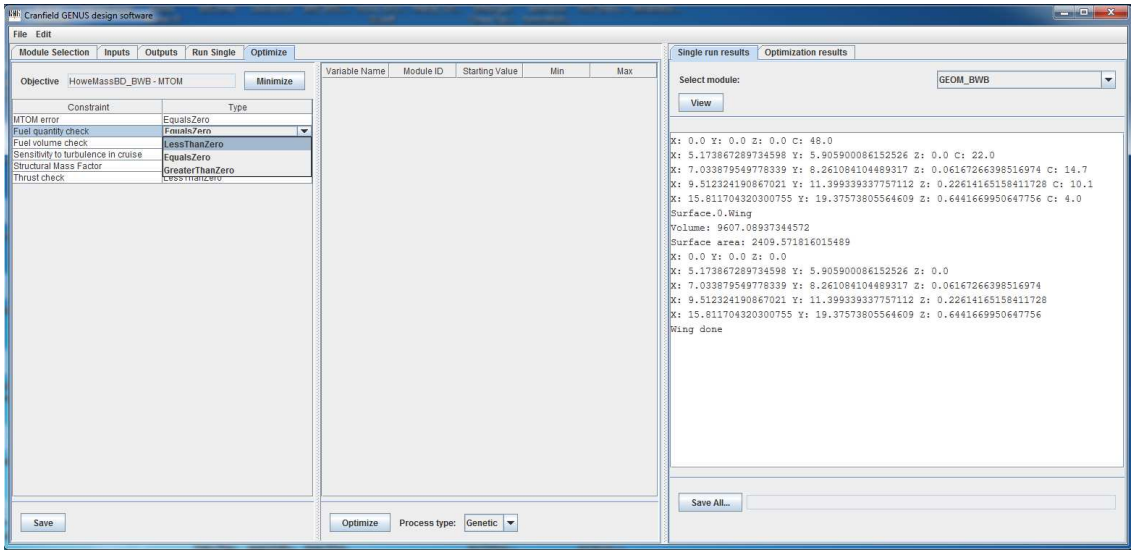


**Figure 5.7:** Optimisation Frame Showing Constraint Definition.

## 5.6 Data Flow in the GMDSO Tool

In the development of the GMDSO Tool, a standard format is created to ensure uniform coding and eliminate time programmers might have spent developing their own format.

The standard format to which all modules must conform to include features such as the method to write inputs to be displayed in the GUI called 'writeInputArray' and another method for setting the module from the GUI inputs known as the 'setModule'.

The inputs to modules within the GMDSO Tool are chosen by the programmer. However, these inputs must be methodically defined to allow optimisers vary them without human intervention. Additionally, the modules could be executed during a single instance of design to perform its function without an optimiser. The single instance of the program determines the OUTPUT and provides RESULTS of the modules from the default values of inputs set in the constructor. For example, single instance of the program could be initiated to determine the aerodynamic coefficients from the initial geometry specified in the geometry module.

In addition to the methods mentioned, each module must include the following features:

Name: Name is the identifier that enables a user select the appropriate module from the module selection pane. The name does not have to be unique.

ID: ID refers to the numerical identifier, denoting the position of a module in the 'selectedModules' array. It has to be unique and conform with the numbering for the 9 essential modules.

Besides, 'Name and ID', every module must contain the following boolean variables:

hasInputs: 'hasInput' is a Boolean variable that specifies if the GUI has to display and set inputs for this module.

hasOutputs: 'hasOutputs' is Boolean variable describing whether the module has any outputs to be used by the optimizer.

hasResults: Similarly, 'hasResults' is a Boolean, describing whether the module is expected to produce text result for the user.

isExecutable: 'isExecutable' is a Boolean variable used to specify whether the module has to be executed during a single instance of design or not. A module is executable if it provides OUTPUTs that used in subsequent parts of the program or RESULTS. However,

if the module does not calculate anything nor produce OUTPUTs, such module need not be executed. In this case all the changes to the model occurs when the module is set from the GUI.

Both execution and setting are sequenced in the order of conceptual design synthesis in the 'selectedModules' array. The modules are ordered from 0 to 8, with the geometry executed first, given order 0 and stability executed last given order number 8 as shown in Figure 5.8. The Figure 5.8 also shows the flow of data within the 9 essential modules. Detailed description of individual modules is given in Appendix D.

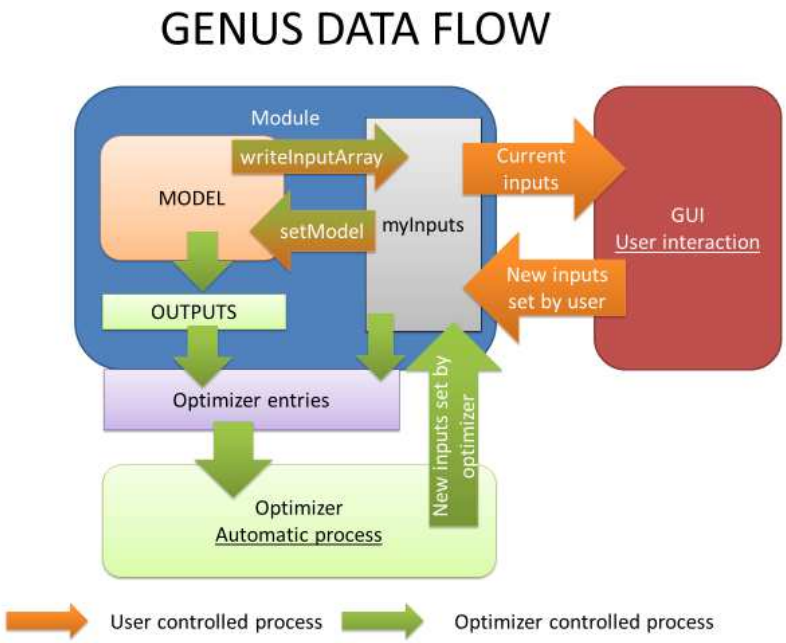


**Figure 5.8:** Flow of Data in the GMDSO Tool.

## 5.7 Chapter Summary

In this Chapter, the overall structure of the developed GMDSO Tool showing the selection and data flow between modules are described. The GMDSO Tool consists of 9 essential modules applicable to all designs irrespective of the configuration. The design of the GMDSO Tool also allows for the integration of special modules which are only applicable to certain categories or designs of aircraft. For instance, power management module in solar - powered aircraft. All modules comprise a set of INPUTS, OUTPUTS and RESULTS. INPUTS are user defined or set by default. INPUTS drives the synthesis or act as design variables in the optimisation routine. OUTPUTS are used as objective

functions or constraints in optimisation process while RESULTS are data presented for the purpose of reports and analysis.

# Chapter 6

# Results, Discussions and Analysis

In this Chapter, the results obtained from various applications of the developed GMDSO tool in the conceptual design synthesis and analysis of a BWB is presented. These results includes a quasi-validation to verify the accuracy of the developed models, design improvements using the multi - variate optimisation capability of the GMDSO Tool and sensitivity analysis to explore the design space of the BWB aircraft.

## 6.1 Quasi - validation of the GMDSO Tool

The developed tool is validated to ensure the integrity and establish a measure of reliability on the techniques and models implemented in the GMDSO tool. In the absence of any commercial passenger transport BWB aircraft and paucity of verified data, only a partial validation using available data from studies by notable research institutions is possible. This is termed quasi-validation because there is no means of ascertaining the accuracy of the data from such researches. In this research, data used for validation is obtained from the 2011 Cranfield University [32], Aerospace Vehicle Design (AVD), Group Design Project specification of a BWB aircraft. The aircraft developed from this Cranfield study is referred to as the BW-11 [32].

### 6.1.1 Geometry Module

The BW - 11 is designed to airlift 555 passengers in a 3 class seating arrangement over a range of 7620 nautical mile (14,167.8 km) at a cruising speed of M 0.85. The Geometry

Module of the GMDSO Tool defines the configuration using body component and lifting surface geometry parts. The lifting surface geometry parts is used to describe lifting surfaces such as wings, horizontal and vertical tails as well as canards while the body component parts specify fuselage, tail boom and nacelles amongst other. In order to validate the GMDSO Tool, the Geometry Module models a tailless BWB configuration, the BW - 11 [32], with the specifications given in Table 6.1. The BW-11 as described in the project specification [32] consists of 8 kinked sections. However, in order to reduce modelling complexities, the Geometry Module implements the BW - 11 with only 5 sections by eliminating 3 superfluous kinks.

**Table 6.1:** BW - 11 Semi - span Geometry Specification

| Section [-] | y[m] | Chord [m] | $\Lambda$[°] | $\Gamma$ [°] | twist [°] | t/c[-] |
|---|---|---|---|---|---|---|
| 1 | 0 | 48 | 63 | 0 | 2.7 | 0.165 |
| 2 | 13 | 22 | 38.3 | 0 | -0.3 | 0.12 |
| 3 | 17.5 | 14.69 | 38.3 | 1.5 | 0.5 | 0.09 |
| 4 | 23.5 | 9.95 | 38.3 | 3 | 0.9 | 0.08 |
| 5 | 38.75 | 4.23 | 38.3 | 3 | -2.7 | 0.08 |

The model derived from the geometry specification in Table 6.1 is visualised using the free plotting software, gnuplot, embedded in the GMDSO tool. The plot obtained is given in Figure 6.1.

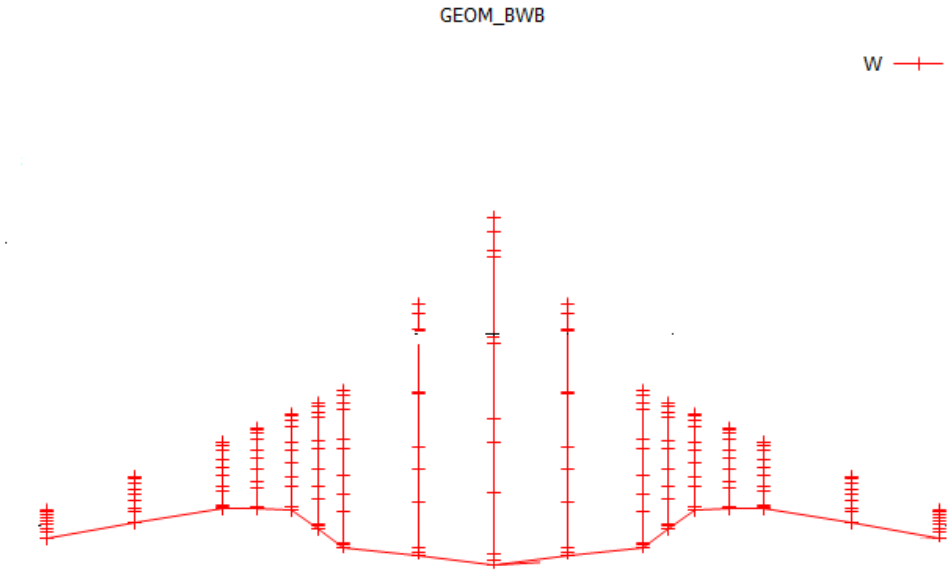


**Figure 6.1:** BW -11 Tailless Aircraft Pre - coded in the GMDSO Tool Geometry Module.

Running a half span of the test geometry through the GMDSO tool geometry module

yields the geometric properties which are compared with similar outputs from the AVL, the XFLR5 and the data from the BW - 11 project specification handbook [32] in Table 6.2. An analysis of the data shows that the GMDSO Tool Geometry Module produces results that are consistent with the other modelling tools investigated except for the reference area. The reason for the difference in reference area could be due to modelling imperfections arising from the fact that the implemented geometry data were derived from a picture rather than any actual data or probably due to round - off errors. Nonetheless, the GMDSO tool generates more outputs than the other geometry modelling tools. In addition to the standard geometry outputs of span and reference surface area, the GMDSO tool also provides total surface volume. These quantities are invaluable quantities in the packaging module for conventional aircraft.

**Table 6.2:** Comparison of the GMDSO Tool Geometry Results with the AVL, XFLR5 and Test Data

| Variables [-] | BW - 11 Specification | GMDSO | XFLR5 | AVL |
|---|---|---|---|---|
| Reference Area $[m^2]$ | 1390.6 | 1439.2 | 1439.2 | 1439.2 |
| Span $[m^2]$ | 77.5 | 77.5 | 77.5 | 77.5 |
| Volume $[m^3]$ | - | 10712 | - | - |

The GMDSO Tool's geometry module is designed to enable a knowledgeable user, through the GUI, create any BWB configuration by selecting and inputting the dimensions of the required geometry parts. In addition to the customised option, the Geometry Module also provides 3 pre - defined configurations. Besides the tailless BW - 11 used for validating the design tool, the Module also generates a BWB aircraft with winglets and a conventional tube and wing aircraft. These pre - defined configurations were included to allow for fast rapid analysis of the design and enable comparison across platforms in order to explore the design space. The gnuplot representation of the pre - defined configuration showing a BWB with winglets and a conventional A320 aircraft are shown in Figures 6.2 and 6.3 respectively.

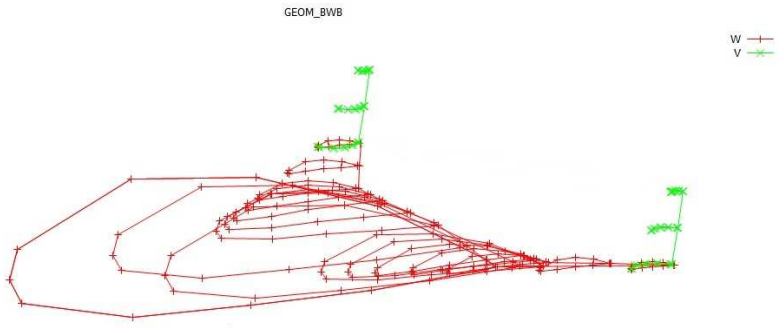


**Figure 6.2:** BWB Geometry with Winglets Pre - coded in the Geometry Module.

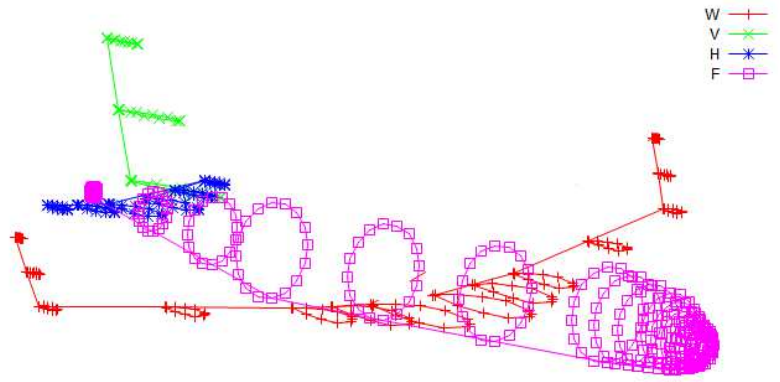


**Figure 6.3:** A Conventional A320 Class of Aircraft Pre -coded in the Geometry Module.

### 6.1.2 Mass Module

To validate the mass models implemented in the GMDSO tool, the module is decoupled from the aerodynamic, performance and stability analysis models. This is necessary in order to reduce the run - time of the program. Most components masses were estimated as a function of the MTOM. Thus, in order to determine the MTOM and hence the masses of the various components, a mini optimisation problem is created. The objective of this mini optimisation problem is to minimise the calculated MTOM by varying the estimated MTOM while ensuring that the difference between the estimated and the calculated MTOM is zero.

Two structural or airframe mass estimation methods and 3 optimisers were implemented in the GMDSO Tool. The structural mass prediction methods are the Bradley and Howe methods while the optimisers are the gradient based LSGRG2, the non - gradient based Genetic Algorithm (GA)and a combined gradient and non-gradient optimiser referred to as the Hybrid optimiser. The Bradley method distinguishes between the masses of the

wing and centre - body (fuselage). However, this distinction is not very clear in the the Howe method. The Howe method estimates the structural mass from the masses of the inner and outer wings together with penalty factors for departure from the ideal and allowance for the secondary structure [19]. Though, it is reasonably expected that the inner wing performs fuselage function, the different characterisation between the 2 methods could affect their prediction of component masses.

Since, the wing is clearly defined in both methods, the challenge is to determine the mass of the fuselage in the Howe method in order to provide a consistent breakdown of masses to enable the assessment of the component masses. Hence, assuming the mass of the fuselage, in the Howe method, is the sum of the masses of the inner wing and fuselage function mass penalty, the results obtained using the LSGRG2 optimiser for mass estimation with Howe structural mass method is shown in Figure 6.4. The Figure 6.4 is the GMDSO Tool's GUI presentation of the optimisation routine for the determination of the MTOM. It shows the problem set, the design variable as well as the variations of the objective function with number of iterations until an optimum is achieved.

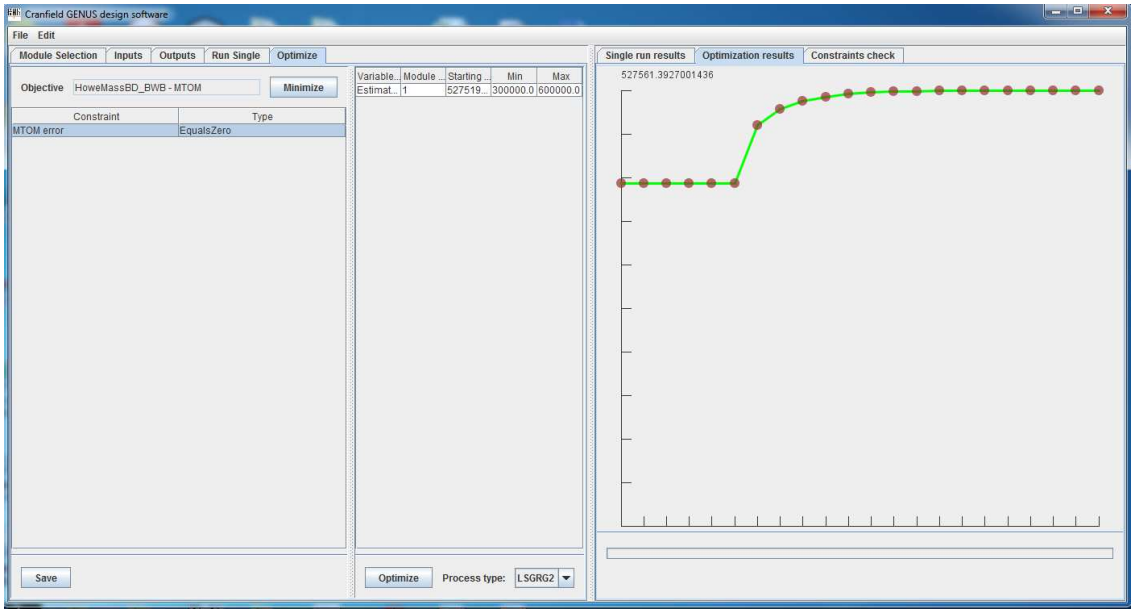


**Figure 6.4:** LSGRG2 Optimisation for Mass Estimation with the Howe Structural Mass Method

Similar results are obtained using the LSGRG2 optimiser for mass estimation with the Bradley structural masses. However, in order to highlight the multi - features of the GMDSO Tool, a different view of the result is shown in Figure 6.5. The view shows the selection pane to the left and the results pane on the right. The selection pane is where

the user selects the appropriate module, sets the inputs and specifies design variables, objective functions and constraints. It is the panel where all inputs are selected and problem is set up. The right hand pane on the other hand shows the result from the different modules as well as the variation of the objective function from an optimisation run. The Figure 6.5 shows the selected mass breakdown module as well as the change in the objective function from 328000 $kg$ to 481148 $kg$ in 18 iterations.

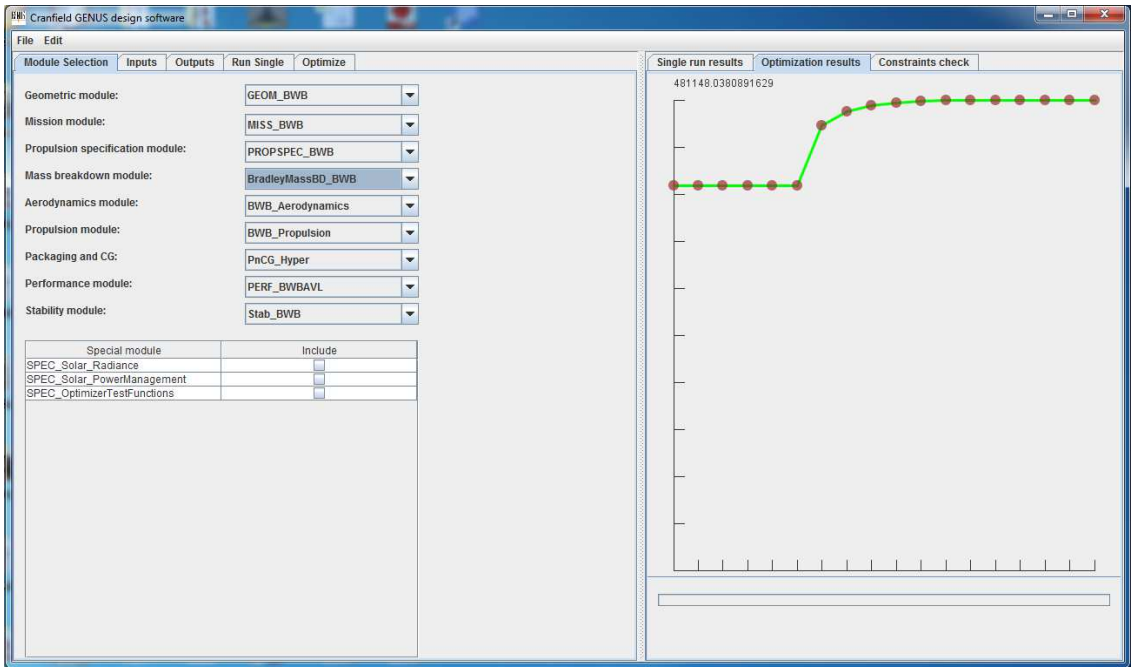


**Figure 6.5:** LSGRG2 Optimisation for Mass Estimation with the Bradley Structural Mass Method.

The differences in the results of the LSGRG2 optimisation for the determination of the MTOM using the Howe and Bradley structural mass models can be seen from the plot of the variation of the objective function with number of iterations given in Figure 6.6. The Figure shows that using the Howe model requires an increased number of iterations to achieve an optimum result. Additionally, using the Howe structural mass estimation model yields a higher MTOM compared to the Bradley method. According to Figure 6.6, the Howe Model requires 22 iterations to achieve an optimum MTOM of over 527000 kg compared to 18 iterations required by the Bradley method to generate a MTOM of 481148 kg.

A breakdown of the component masses obtained with either structural estimation methods when the LSGRG2 optimiser is selected compared with the BW - 11 estimates is given

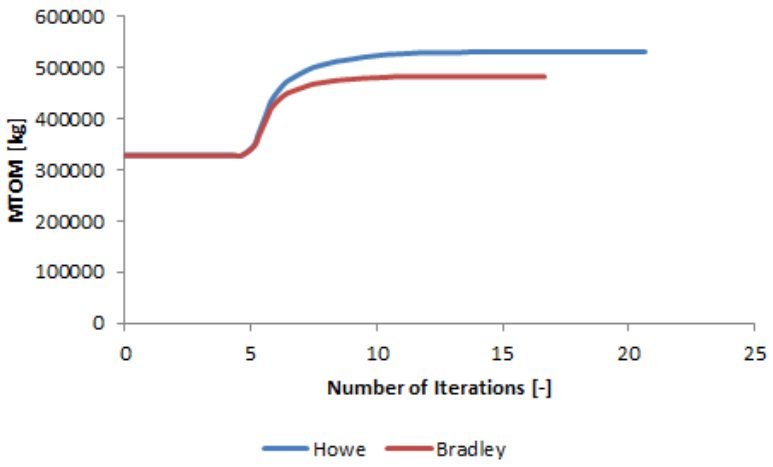


**Figure 6.6:** Comparison of Mass Variation with Number of Iteration Using the LSGRG2 Optimiser.

in Table 6.3. The masses obtained with either the Bradley or Howe structural weight prediction methods are fairly consistent and of the same order of magnitude with the BW - 11 specifications except for the structural masses. The Bradley and Howe methods give significantly higher structural masses than the BW - 11. While the structural mass constitutes about 28 percent of the MTOM using the Bradley method, it takes about 31 percent when predicted with the Howe method. This is considerably higher than the 19 percent of the MTOM given for structures in the BW - 11 specification document [32]. Nevertheless, the results obtained with the Howe and Bradley models are considered reasonable as they are still within the acceptable limits of 24 - 31.5% provided in the Cranfield University Lecture Note DAet 9317/30 [142].

Selecting the GA optimiser, the variations of the MTOM with number of iterations for the determination of the MTOM with the Howe and Bradley structural mass estimates are shown in Figures 6.7 and 6.8 respectively. The optimised values of $527615.3kg$ and $483366.5kg$ obtained for the Howe and Bradley methods respectively are similar to the values obtained using the LSGRG2 optimiser. This shows that the selected optimisation technique has negligible effect on the MTOM obtained. However, it does affect the efficiency of the process. It took 18 and 22 iterations with the LSGRG2 as against 14 and 11 runs using the GA, to obtain optimised values for the Howe and Bradley methods respectively.

From Figures 6.7 and 6.8, it could be argued that the GA is more efficient than the LSGRG2 due to the lower number of iterations required to achieve optimal result. However, this is not always the case. This is because the GA exploits random search algorithm to solve optimisation problems. Hence, the number of iterations and results obtained for any

**Table 6.3:** Comparison of the LSGRG2 Optimiser GMDSO Tool Weight Estimates with the BW -11

| Components | mass[kg] | | | $\%MTOW$ | | |
|---|---|---|---|---|---|---|
| | GMDSO | | Cranfield | GMDSO | | Cranfield |
| | Bradley | Howe | | Bradley | Howe | |
| Wing | 54501.4 | 16654.9 | | 11 | 3 | |
| Fuselage | 83759 | 147178.1 | 90412.3 | 17 | 28 | 19 |
| IAE | 5910.4 | 6478.5 | 7104.5 | 1 | 1 | 1 |
| Hydraulics | 2219.6 | 2324.2 | 172 | 1 | 0 | 0 |
| API | 1375.6 | 1375.6 | 4276.1 | 0 | 0 | 1 |
| Electrical | 2244.7 | 2387.6 | 2838.9 | 1 | 1 | 1 |
| APU | 481.1 | 527.5 | 400 | 0 | 0 | 0 |
| Flight Control | 2811.1 | 3026.1 | 2829.7 | 1 | 1 | 1 |
| Furnishing | 15271.6 | 15256 | 7903.1 | 3 | 3 | 2 |
| Payload | 65115 | 65115 | 64851.2 | 14 | 12 | 14 |
| Under-carriage | 21409 | 23474.6 | 25443.8 | 4 | 5 | 5 |
| Fuel | 183588.4 | 201301.4 | 193821.3 | 38 | 38 | 41 |
| Propulsion | 33071 | 33071 | 35798.8 | 7 | 6 | 8 |
| Operational Items | 9390 | 9390 | 32496 | 2 | 2 | 7 |
| MTOM | 481148 | 527561.4 | 468347.7 | 100 | 100 | 100 |
| ZFM | 297559.7 | 326260 | 274526.4 | 36 | 36 | 34 |
| OEM | 232444.7 | 261145 | 210469 | 28 | 28 | 26 |
| MLM | 297094.2 | 325753 | 321501 | 36 | 36 | 40 |

optimisation problem varies as shown in Figure 6.9 for other GA derived results of the same mass determination problem as addressed in this section. Despite these variations, the GA is able to converge over several generations towards a global optimum using a mixture of selection, crossover and mutation

A detailed breakdown of the masses of components obtained with the GA optimiser for the 2 structural mass prediction methods implemented in the GMDSO Tool is given in Table 6.4. The Table 6.4 supports the finding that there is only a negligible difference in optimised values regardless of the selected optimisation technique.

Combining the GA with the LSGRG2 optimiser creates the Hybrid optimiser. The results of mass estimation with the Hybrid optimiser for the implemented structural mass methods are shown in Figures 6.10 and 6.11. The values of the MTOM obtained with both the Howe and Bradley structural mass prediction methods are consistent with the values obtained with the LSGRG2 and the GA optimisers. However, the efficiency of the process is diminished. It took 25 and 53 iterations to obtain optimised results when the Hybrid optimiser is selected compared to 18 and 22 with the LSGRG2 and 11 and 14 with the GA for the Bradley and Howe structural mass methods respectively. This suggests that

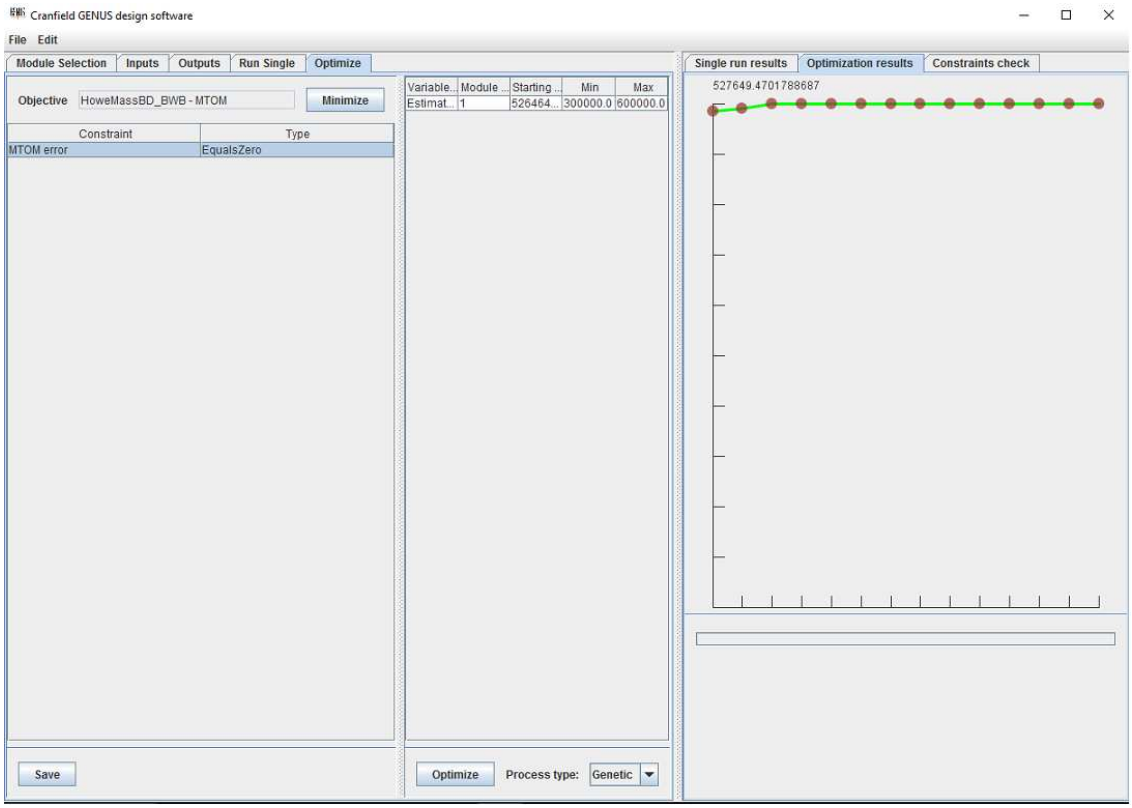


**Figure 6.7:** GA Optimisation for Mass Estimation with the Howe Structural Mass Method

the Hybrid method is the least efficient of the 3 optimisation methods implemented while the GA is the most efficient optimisation method for computing the MTOM of a BWB aircraft. However, as earlier highlighted, because the GA and the Hybrid optimisers are non - deterministic methods and exploits random search algorithms, the efficiency of the methods cannot easily be determined.

The masses of components obtained with the Hybrid optimiser is compared with those of the BW - 11 [32] in Table 6.5. This was necessary in order to ascertain the consistency of results with the other optimisers. Reviewing the results in Table 6.5 reveals that they are similar to the component mass breakdown obtained with the other optimisers. This further validates the assertion that selected optimisers have negligible impact on the MTOM and the masses of components. The variations of the MTOM with the number of iterations for mass estimation with the GA and Hybrid optimisers is shown in Figure 6.12. The plots are consistent with the trend observed with the LSGRG2 which establishes that employing the Howe structural mass estimation method leads to a higher MTOM and reduced computational efficiency.

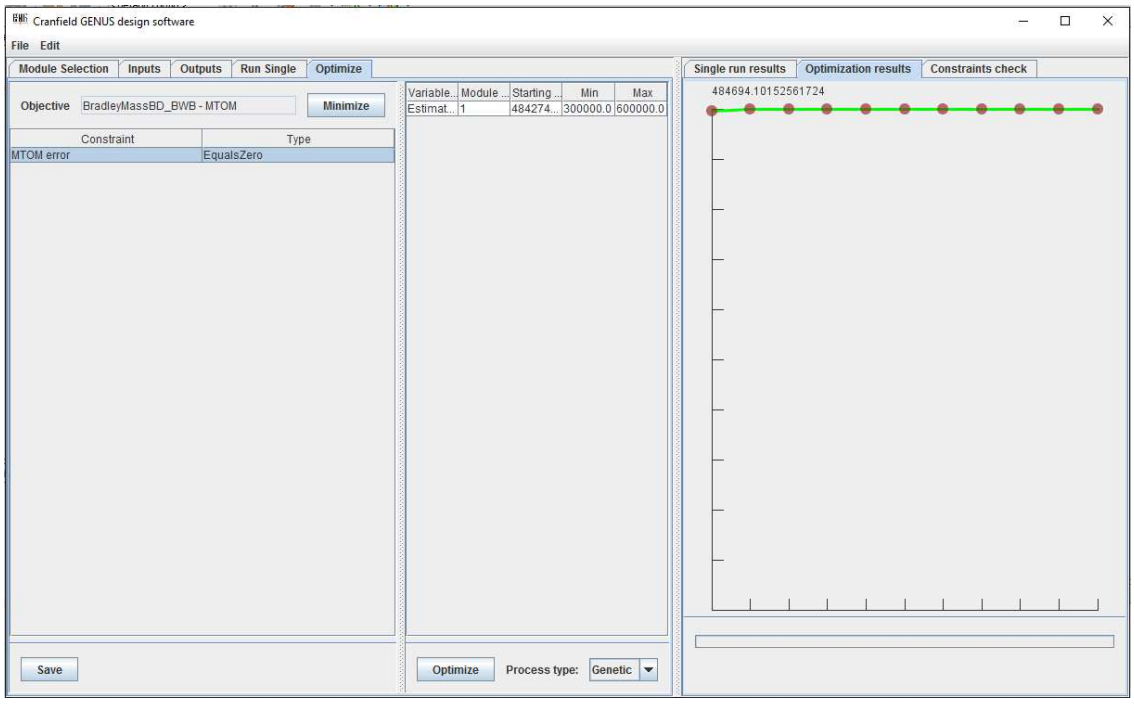


**Figure 6.8:** GA Optimisation for Mass Estimation with the Bradley Structural Mass Method

**Table 6.4:** Comparison of GMDSO Tool BW - 11 Weight Estimates Obtained with the GA Optimiser to Cranfield Study

| Components | mass[kg] | | | $\%MTOM$ | | |
|---|---|---|---|---|---|---|
| | GMDSO | | Cranfield | GMDSO | | Cranfield |
| | Bradley | Howe | | Bradley | Howe | |
| Wing | 56527.2 | 16626.5 | | 11 | 3 | |
| Fuselage | 83850.8 | 147087 | 90412.3 | 17 | 28 | 19 |
| IAE | 5958.6 | 6465.6 | 7104.5 | 1 | 1 | 1 |
| Hydraulics | 2228.6 | 2321.9 | 172 | 1 | 0 | 0 |
| API | 1375.6 | 1375.6 | 4276.1 | 0 | 0 | 1 |
| Electrical | 2254 | 2384.4 | 2838.9 | 1 | 1 | 1 |
| APU | 484.3 | 526.5 | 400 | 0 | 0 | 0 |
| Flight Control | 2826 | 3021.2 | 2829 | 1 | 1 | 1 |
| Furnishing | 15274 | 15256.8 | 7903.1 | 3 | 3 | 2 |
| Payload | 65115 | 65115 | 64851.2 | 14 | 12 | 14 |
| Under-carriage | 21550 | 23427.7 | 25443.8 | 4 | 5 | 5 |
| Fuel | 184799.7 | 200898.8 | 193821.3 | 38 | 38 | 41 |
| Propulsion | 33071 | 33071 | 35798.8 | 7 | 6 | 8 |
| Operational Items | 9390 | 9390 | 32496 | 2 | 2 | 7 |
| MTOM | 484694.7 | 528270.3 | 468347.7 | 100 | 100 | 100 |
| ZFM | 299895 | 326068.5 | | 36 | 36 | 34 |
| OEM | 234780 | 260953.5 | 210469 | 28 | 28 | 26 |
| MLM | 299283.8 | 325386.2 | 321501 | 36 | 36 | 40 |

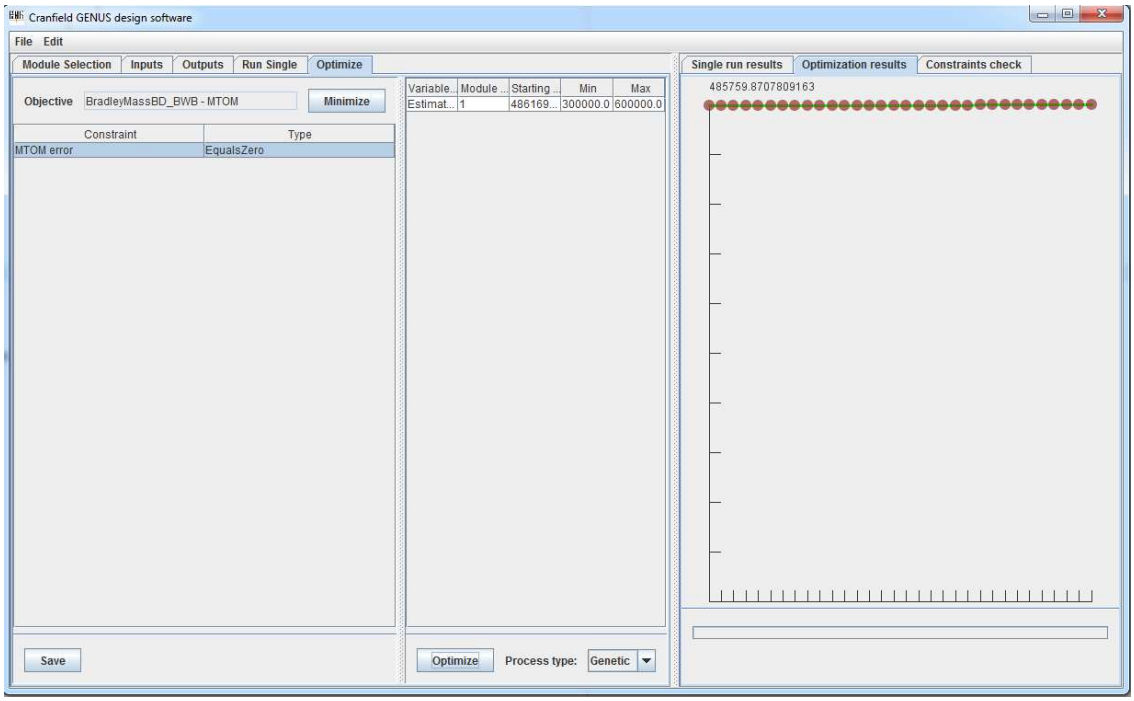


(a) Bradley

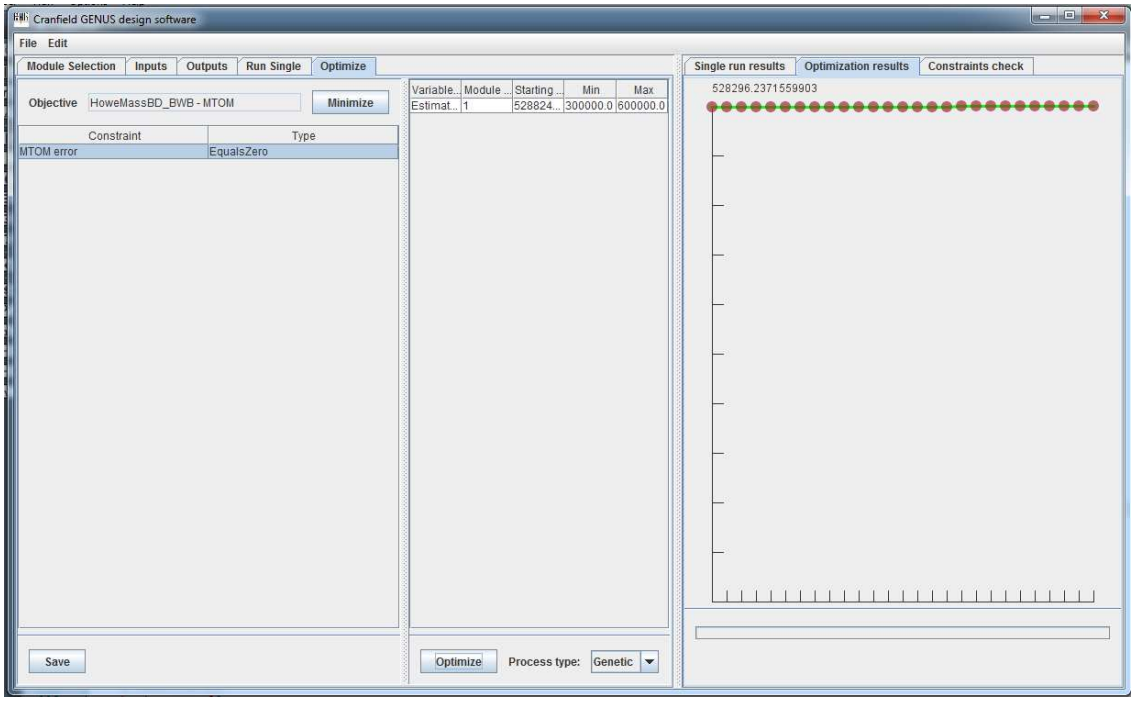


(b) Howe

**Figure 6.9:** GA Result for Design Case 1 Highlighting the Randomness of the Technique.

With negligible differences in the MTOM and the components mass breakdown obtained with the the various optimisation techniques, the results were compared on the basis of

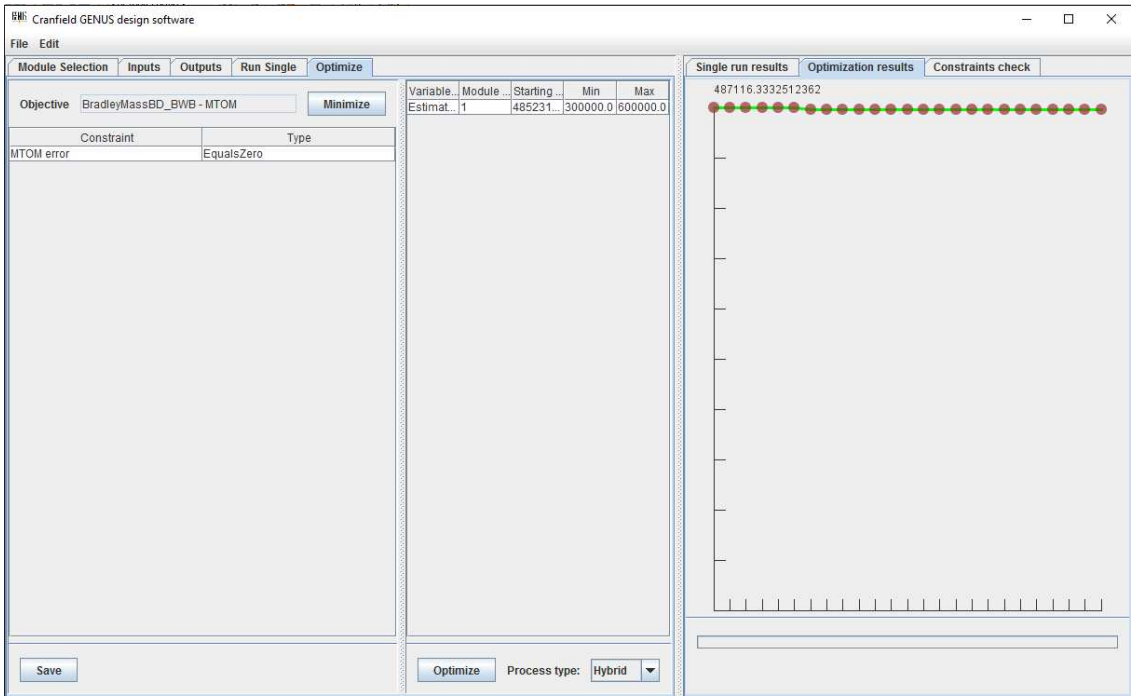


**Figure 6.10:** Hybrid Optimisation for Mass Estimation with the Bradley Structural Mass Method

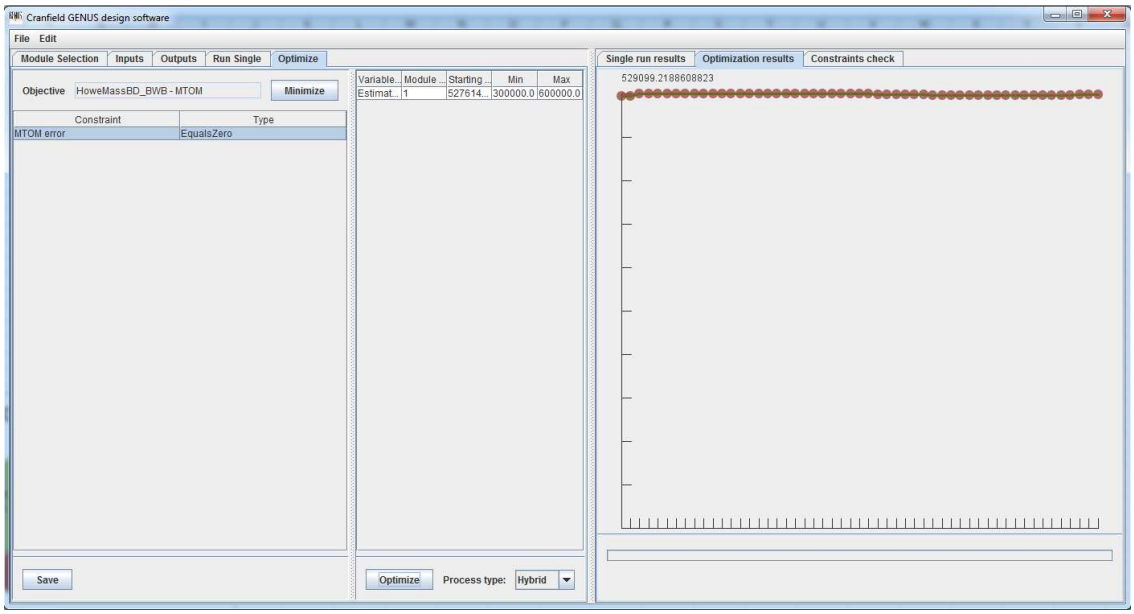


**Figure 6.11:** Hybrid Optimisation for Mass Estimation with the Howe Structural Mass Method

**Table 6.5:** Comparison of GMDSO Tool BW - 11 Weight Estimates Obtained with the Hybrid Optimiser to Cranfield Study

| Components | mass[kg] | | | $\%MTOM$ | | |
|---|---|---|---|---|---|---|
| | GMDSO | | Cranfield | GMDSO | | Cranfield |
| | Bradley | Howe | | Bradley | Howe | |
| Wing | 56607 | 16657.4 | | 11 | 3 | |
| Fuselage | 83878.4 | 147186.3 | 90412.3 | 17 | 28 | 19 |
| IAE | 5961 | 6479.7 | 7104.5 | 1 | 1 | 1 |
| Hydraulics | 2229 | 2324.4 | 172 | 1 | 0 | 0 |
| API | 1375.6 | 1375.6 | 4276.1 | 0 | 0 | 1 |
| Electrical | 2257.6 | 4801.6 | 2838.9 | 1 | 1 | 1 |
| APU | 485.2 | 527.6 | 400 | 0 | 0 | 0 |
| Flight Control | 2830.4 | 3026.5 | 2829 | 1 | 1 | 1 |
| Furnishing | 15274.8 | 15256.9 | 7903.1 | 3 | 3 | 2 |
| Payload | 65115 | 65115 | 64851.2 | 14 | 12 | 14 |
| Under-carriage | 21592.8 | 23478.8 | 25443.8 | 4 | 5 | 5 |
| Fuel | 185164.3 | 201337.6 | 193821.3 | 38 | 38 | 41 |
| Propulsion | 33071 | 33071 | 35798.8 | 7 | 6 | 8 |
| Operational Items | 9390 | 9390 | 32496 | 2 | 2 | 7 |
| MTOM | 485232.5 | 527614.9 | 468347.7 | 100 | 100 | 100 |
| ZFM | 300068.2 | 326277.3 | | 36 | 36 | 34 |
| OEM | 234953.2 | 261162.3 | 210469 | 28 | 28 | 26 |
| MLM | 299616.2 | 325786 | 321501 | 36 | 36 | 40 |

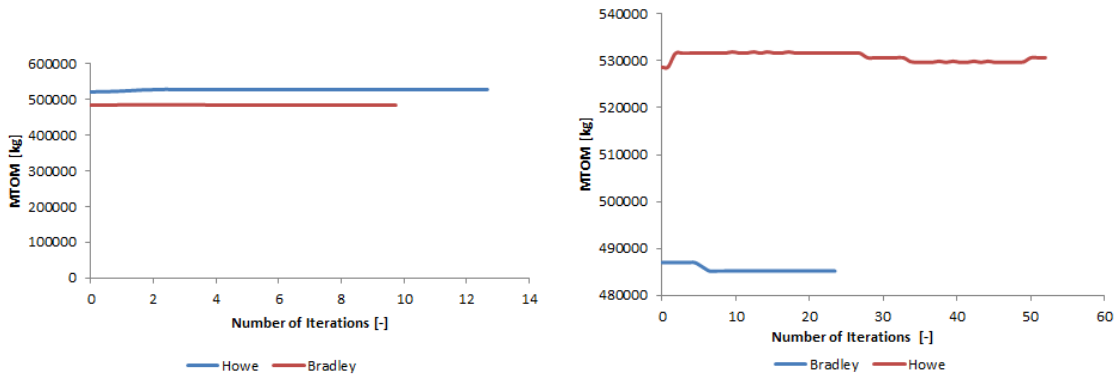


(a) GA (b) Hybrid

**Figure 6.12:** Variations of MTOM with Number of Iterations for Mass Estimation Using the GA and Hybrid Optimisers.

the differences between the estimated and derived MTOM. The margin of errors obtained with the different optimisers when the Bradley structural method is applied are shown in Table 6.6.

A chart of the data in Table 6.6 showing the margin of error and the computational costs

**Table 6.6:** Error Between Calculated and Estimated Masses for Bradley Method

| Method | Estimated Mass[kg] | Calculated Mass[kg] | Absolute Error[-] |
|---|---|---|---|
| LSGRG2 | 481119 | 481148 | 29 |
| GA | 484274 | 484694 | 420 |
| Hybrid | 485231 | 485232 | 1 |

of the implemented optimisers when the Bradley structural mass estimation is used can be found in Figure 6.13. The chart shows that the GA optimisation generates the most error between the estimated and calculated mass with a difference of $420kg$ compared to $29kg$ and $1kg$ for the LSGRG2 and the Hybrid optimisers respectively.

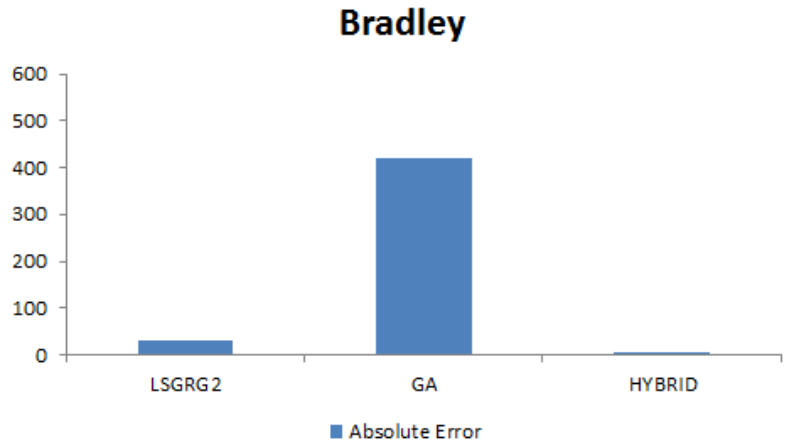


**Figure 6.13:** Absolute Error Obtained with the Bradley Method.

Similarly, comparing the performance of the different optimisation techniques when the Howe structural mass estimation technique is applied, in terms of the difference between the estimated and calculated mass gives the results in Table 6.7.

**Table 6.7:** Error Between Calculated and Estimated Masses for the Howe Method

| Method | Estimated Mass [kg] | Calculated Mass [kg] | Absolute Error[-] |
|---|---|---|---|
| LSGRG2 | 527519 | 527561 | 42 |
| GA | 526464 | 526967 | 503 |
| Hybrid | 527614 | 527615 | 1 |

An analysis of the data in Table 6.7 as shown in Figure 6.14 indicates that the GA method gives the most margin of error between the calculated and estimated mass while the Hybrid optimisation technique provides the least margin of error. This is consistent with the result obtained when the Bradley structural method is applied. Hence, even though all the optimisers generate results which are within permitted tolerance limit, the

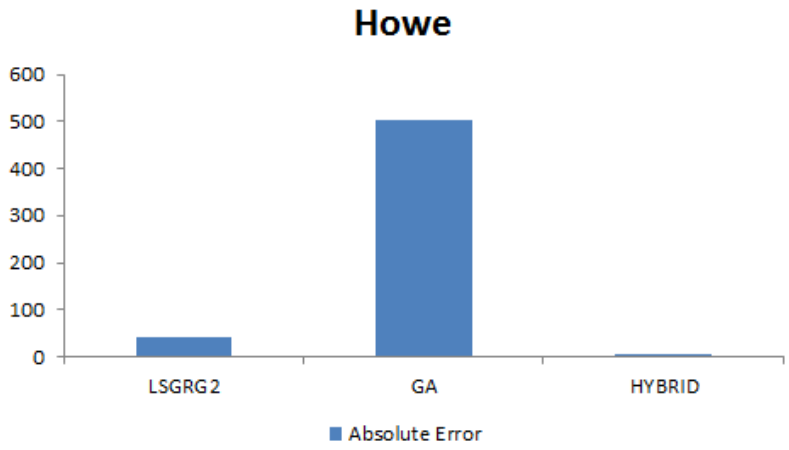


**Figure 6.14:** Absolute Error Obtained with the Howe Method.

most accurate result is that provided by the Hybrid method. Nevertheless, a trade - off needs to be made between accuracy and speed in order to determine the most suitable optimiser for any aspect of the design.

Reviewing the 2 structural mass estimation methods viz - a - viz the BW -11 mass estimates, the Bradley method is adjudged to be the most appropriate method for conceptual design of the BWB because it consists of fewer number of variables compared to the Howe method. Additionally, these variables are readily available at the conceptual design stage. The Howe method, on the other hand, requires several variables that are not easily determined at the onset of design. Also, while the Howe method tends to over - estimate the structural mass, the Bradley structural provides masses which are very close to the values given for BW-11 in the specification handbook [32]. Because, the Bradley method shows a higher degree of consistency and consists of few easily available variables, it is the preferred mass prediction model for the design synthesis of BWB Aircraft in the GMDSO Tool.

### Centre of Gravity

In estimating the centre of gravity of a complete aircraft, the locations of individual components centre of gravity needs to be determined. Given that the BWB is defined as a wing, the centre of gravity of the structure is assumed similar to that of a flying wing which lies between 15 - 25% of the MAC. Additionally, to simplify the process, the CG of aircraft systems are taken to be located close to the avionics bay on the wing centreline. This is necessary in order to provide sufficient volume to contain these systems. Additionally, this location enables systems to be used for controlling the entire aircraft. The location of the centre of gravity of the engine is taken at the mid - span of its length

while the landing gear is positioned between 55 - 60%$\bar{\bar{c}}$ [143]. Other components have their centre of gravity at the centre of the length of the components.

Now taking the location of the centre of gravity of the structure to be equal to $0.2\bar{\bar{c}}$ and the landing gear to be located at $0.6\bar{\bar{c}}$, the complete aircraft centre of gravity values with OEM, MZFM and MTOM are determined. The result which is given in Table 6.8 were obtained with a MAC of 24.7m and an x - position of the quarter chord of 30.7m. The Table 6.8 shows the results are very similar with those of BW - 11 which were obtained with a MAC of 27.3m. The similarity of results and negligible percentage difference between the calculated and BW - 11 specifications validates the accuracy of the methodology employed in the CG calculation.

**Table 6.8:** Validation of Aircraft Centre of Gravity in Cruise

| CG | BW - 11 | GMDSO | Percentage Error |
|---|---|---|---|
| CG at MTOM | 29.1m | 28.1m | 3.4 |
| CG at MZFM | 31.9m | 32.1m | -0.6 |
| CG at MOEM | 32.7m | 35m | -7 |

### 6.1.3 Propulsion Module

The propulsion module determines the SFC and thrust available at given altitudes and Mach numbers within the aircraft flight profile. It is a tripartite module consisting of the power - plant, propulsion specification and propulsion modules. The power - plant module models the specific type of propulsion system, whether it is turbojet, turbofan or the ramjet used in the design. The power - plant type employed for the design synthesis of the BWB is the Turbo - fan engine. The engine is modelled on the Howe's empirical engine performance method. The propulsion specification model specifies the operating characteristics of the selected power - plant. These characteristics include the BPR, static thrust, number of power - plant, fuel fraction and fuel types amongst others. The propulsion component creates methods that compute the SFC and available thrust at different altitudes and Mach numbers.

The BW - 11 propulsion system consist of 2 turbo - electric project engines driving 14 fans. The engine designated the BW - 11 - 627 - TE, has a Sea Level Static (SLS) thrust rating of 627.15kN and an assumed SFC of 0.468lb/lbf/h. However, because it is a project engine, it is not possible to validate the accuracy of these specifications. Subsequently, a standard turbo - fan engine was selected to validate the developed propulsion model.

The turbo - fan engine selected for this process is the the Rolls Royce Trent 900 [144].

The Trent 900 is a powerful cost - effective power - plant designed for the Airbus A380 aircraft. Besides, the fact that it is currently been used in an aircraft of similar operating capacity, the Trent 900 was selected for this validation because it has impressive SFC and excellent environmental attributes. In order to obtain approximately the total static thrust specified for the project engine, a 4 - engined design is assumed. The engines have a BPR of 8.5 and a SLS thrust rating of 350 kN. Computing the engine performance based on the given specification, the variation of thrust with Mach numbers at different altitudes is determined as shown in Figure 6.15.

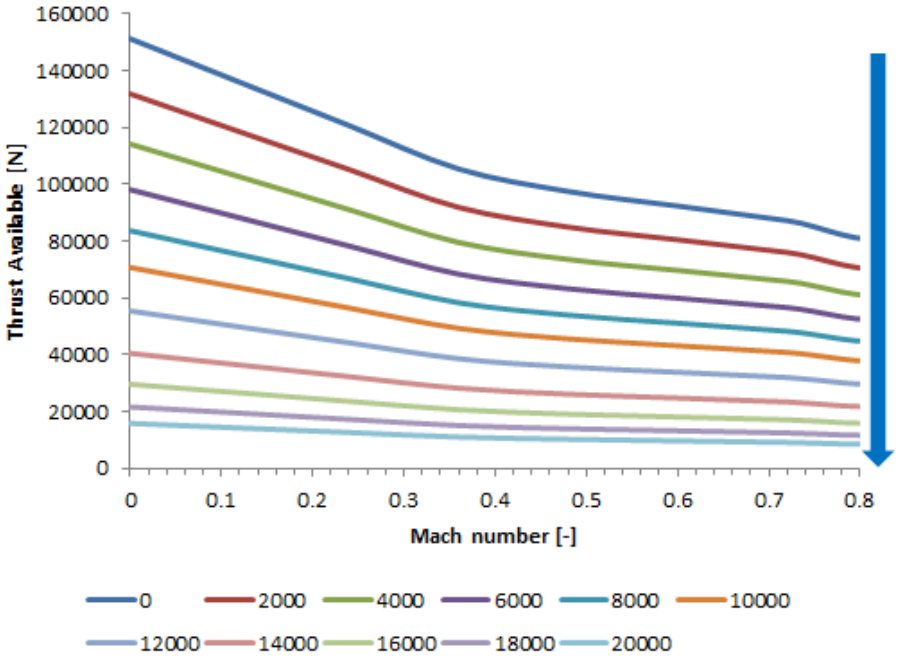


**Figure 6.15:** Variation of Thrust with Mach Numbers at Various Altitudes.

The plot shows a decreasing available thrust with Mach numbers and altitude until about M0.84. Subsequently, there is a sharp increase in available thrust between M0.84-0.96 and then the thrust decreases subsequently. This suggests that the cruising speed of M0.85 would provide near optimum thrust value for the aircraft performance. However, choosing the operating altitude and Mach numbers based only on the thrust without consideration for fuel burn is not advisable. Due to environmental considerations and the fact that fuel constitutes about 35 - 45% of the total take - off weight, there is the need to select operating point at which fuel burn is minimal. Consequently, the plots of SFC at different Mach numbers and altitudes using Kerosene fuel is generated as shown in Figure 6.16.

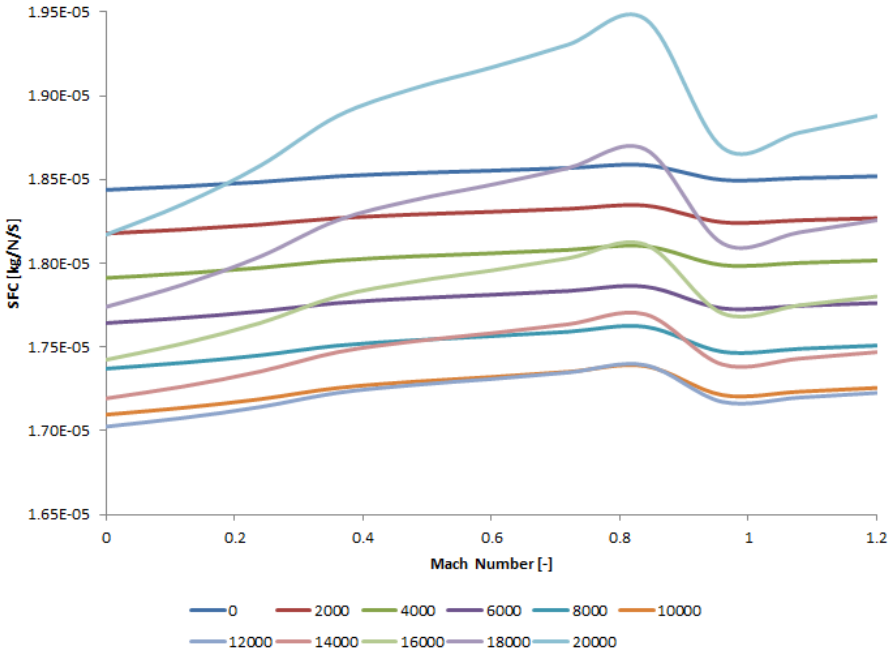


**Figure 6.16:** Variation of SFC with Mach Numbers and Altitudes

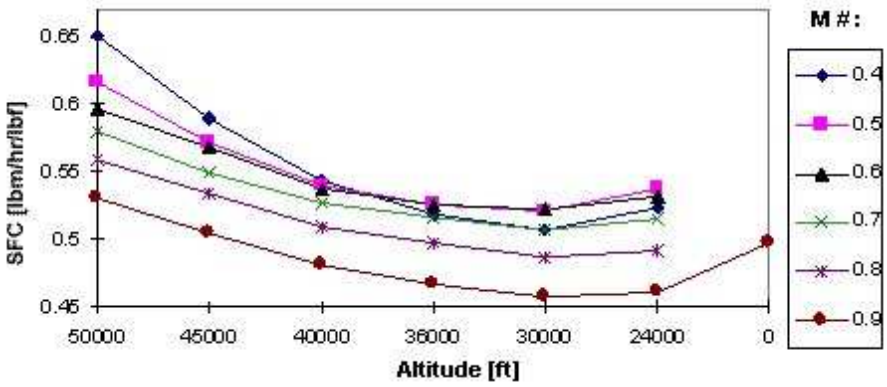


**Figure 6.17:** Variation of SFC with Mach Numbers and Altitudes for the FJ442-A Turbofan Engine [145]

The plots show that the SFC increases with Mach number but decreases with increasing altitude up to the limit of the troposphere culminating in the lowest fuel consumption at 12000m and then rising subsequently with increasing altitude as could be seen in the plots in Figure 6.18. This is similar to the to the variation of SFC with altitude at different Mach number for the FJ44-2A engine provided by the manufacturer [145] and shown in Figure 6.17. The reason for this behaviour is because increasing airspeed increases the mass flow rate of air passing through the engine. This subsequently forces more fuel to

be introduced into the flow in the combustion chamber in order to ensure an optimum air/fuel mixture. On the other hand, increasing altitude will cause a decrease in temperature and hence in the pressure and density of air up to the troposphere. Decreased air density reduces the air mass flow rate thereby lowering the fuel flow needed to ensure optimum fuel/air mixture. However, temperature beyond the troposphere remains constant up till 20km. This phenomenon causes the air pressure and hence density to remain constant. Consequently, changes in the engine air mass flow rate would therefore only be influenced by variations in Mach number. Since, increasing Mach numbers causes an increase in mass flow rate and hence the fuel consumption, this explains the reversal in the relationship between SFC and altitude from 12km to 20km.

It is also worthy to state that even though the SFC increases with Mach number, it drops sharply between M0.84 and M0.96 and then begins to rise again. This suggests that in order to lower fuel consumption, the selected engine should be flown at 12000m with a cruising speed between M0.84 and M0.96. There is also a negligible difference between the SFC at 10000m and 12000m. These suggests that M0.85 and 12000m are the optimum Mach number and altitude respectively, also known as he sweet spot, for an aircraft operating a high BPR turbo - fan engine. This is the reason why most airlines cruise at M0.85 and between 10 - 12km.

Efforts to find thrust performance data of the Trent - 900 engine at various altitude proved particularly challenging. The only turbo - fan engine performance data found was a plot of the combined effects of velocity and altitude on the thrust of the JT15D - 4C. The JT15D - 4C is a Pratt and Whitney turbofan engine with a static thrust of 2500Ib and a BPR of 2.6. The plots of the JT15D - 4C thrust variation with Mach numbers at different altitudes alongside that of Trent - 900 engine obtained with the GMDSO Tool is given in Figure 6.19.

A quick comparison of the plots shown in Figure 6.19 indicates similar pattern and trends of variations. The reasons for observed pattern of behaviour could be deduced from the effects of altitude and speed on thrust of a turbofan engine. The net thrust of a jet engine is derived from the difference between the outgoing exhaust momentum and the ram drag as given in Equation 6.1. As altitude increases, the pressure and density decrease. Hence, according to Equation 6.1, the available thrust also reduces. But temperature decreases with increasing altitude and decreased temperature increases the available thrust [146]. Nevertheless, the pressure and density of the outside air decrease at a much faster rate than the temperature, so an engine produces less thrust as the altitude increases.

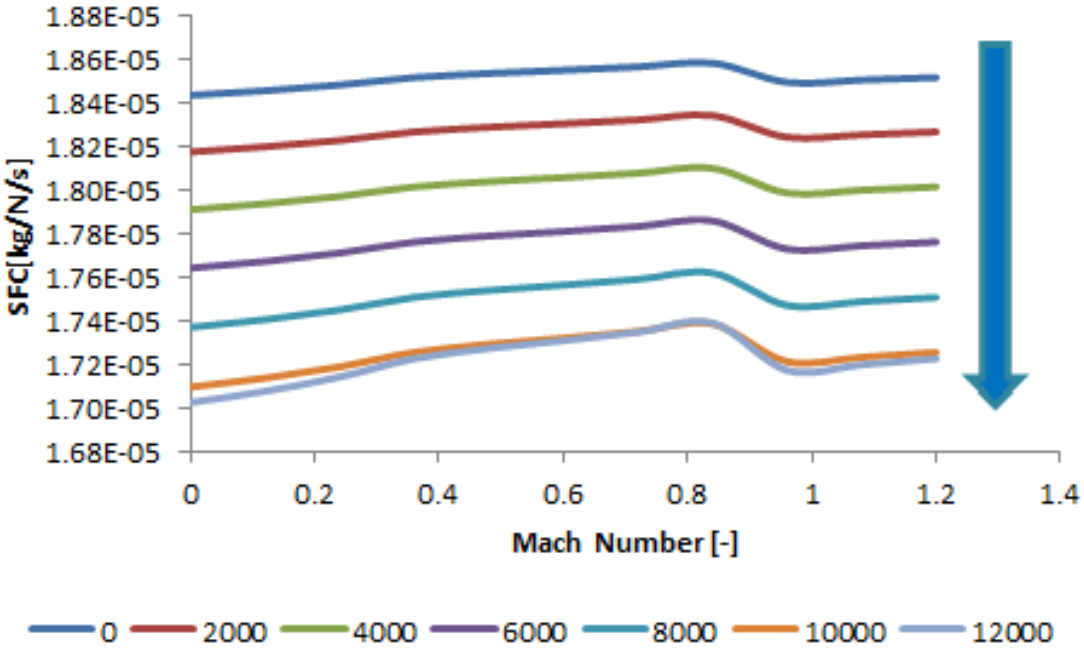


(a) 0 - 12000m

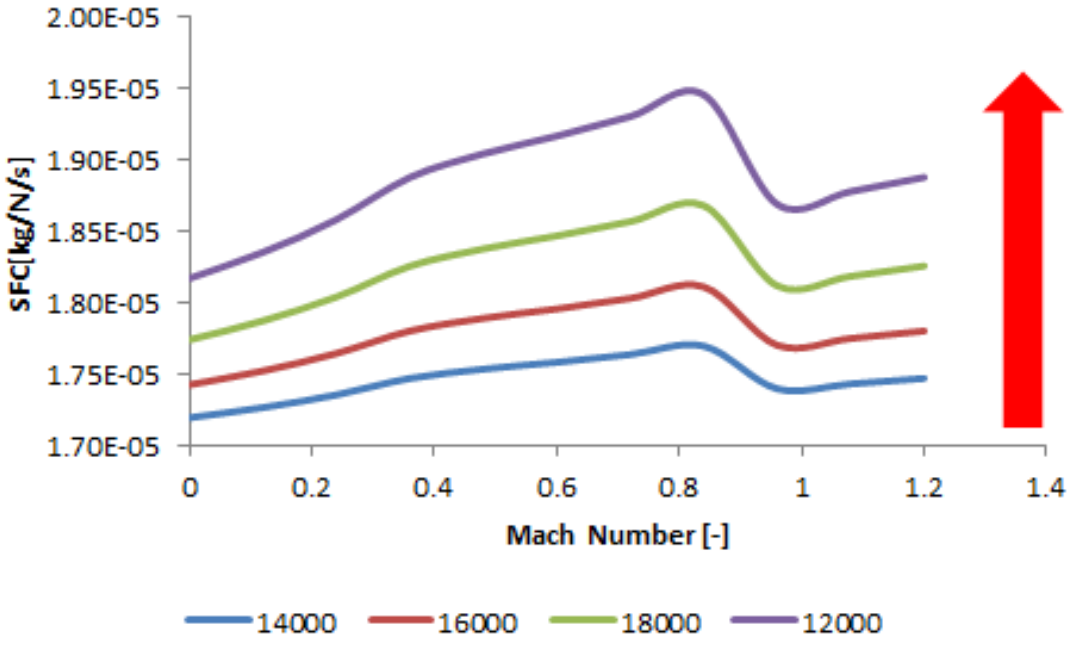


(b) 14000 - 2000m

**Figure 6.18:** GA Result for Design Case 1 Highlighting the Randomness of the Technique.

$$T = [\dot{m}V_j + A_j (P_j - P_{am})] - \dot{m}V_i \tag{6.1}$$

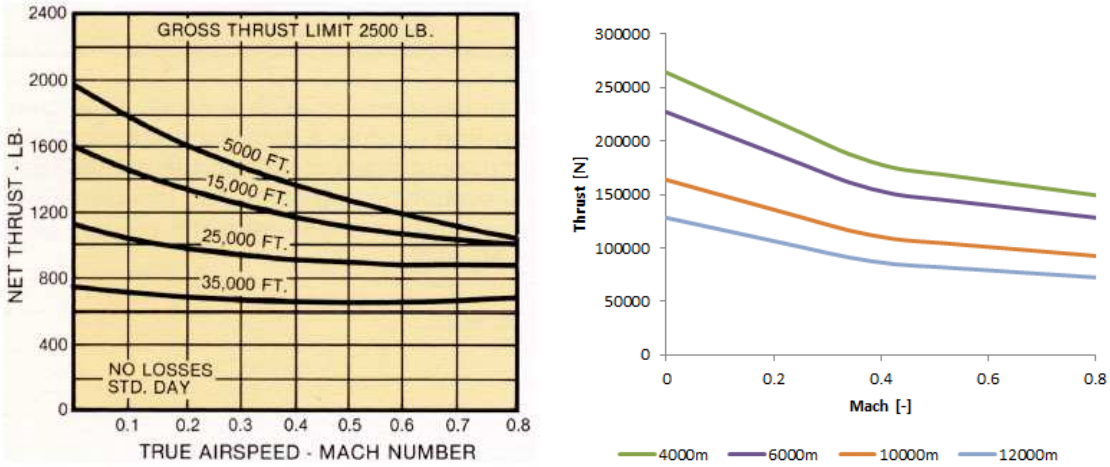


(a) JT15D - 4C (b) Trent - 900

**Figure 6.19:** Comparison of the Combined Effect of Velocity and Altitude on Selected Turbo - Fan Engines.

Where:

$\dot{m}$ is the mass flow rate.
$V_i$ is the incoming air velocity.
$P_{am}$ is the atmospheric pressure.
$V_j$ is the exhaust gas velocity.
$A_j$ is the area of jet nozzle.

The effect of speed on the thrust of an engine is due to the velocity difference variations in the intake and exhaust, and ram effects. When the engine is been run - up prior to take - off, the momentum drag is zero because the intake velocity is zero. However, as the aircraft begins to move, the intake velocity increases thereby decreasing the difference between the intake velocity and the exhaust velocity and hence minimising the available thrust. Furthermore, increase in airspeed also increases the compression of air in the inlet duct arising from the forward motion. This phenomenon popularly referred to the ram effect increases the air mass flow to the engine and the intake pressure and consequently increases the available thrust as shown in Figure 6.20. However, ram pressure is not significant at lower speeds, thus it cannot offset the effect of velocity difference and hence the thrust decreases with increasing airspeed. This is reflected in Figure 6.15 where the thrust decrease to velocity increase is more pronounced at lower altitude than at a higher altitude as seen from a flattening of the curve from 14000m onwards. In addition, the sharp rise in thrust with increase in airspeed could be due to the reversal in the sign of the difference between intake and exhaust velocity at higher speed.

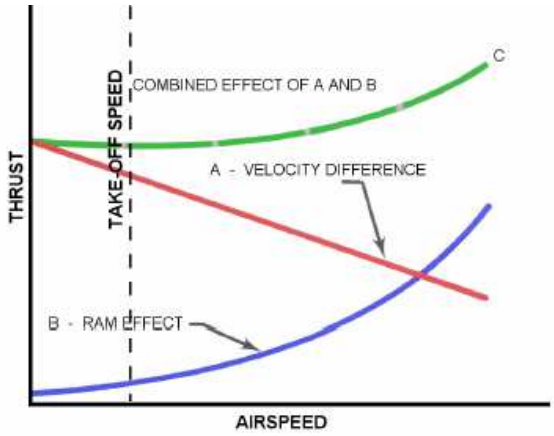


**Figure 6.20:** Effect of Speed on Jet Engine Thrust.

### 6.1.4 Aerodynamic Analysis Module

Creating the aerodynamic analysis module involves the selection of the most appropriate code between the XFLR5 and AVL VLMs and the subsequent integration of the selected code into the GMDSO environment. In this research, the BWB is modelled as a wing. Creating a wing with complex trailing edge profile involving non-uniform kink sections, in the XFLR5, requires the intelligent use of the offset feature which is not trivial. Hence, without the use of the offset feature, the geometry derived with the XFLR5 from the specifications in Table 6.1 is shown in Figure 6.21. The XFLR5 analysis of the obtained geometry generates the polar curves in Figure 6.22.

With the AVL, the complex trailing edge profile and control surfaces are easily modelled, as shown in Figure 6.23, using the leading edge coordinate parameter and the 'add control' function respectively. Despite the geometry modelling differences between the 2 VLMs, it was found that the AVL and XFLR5 provided similar aerodynamic forces at M0.02, as shown in Table 6.9, using NACA 4 digit airfoils with the specified thickness to chord ratio. However, there is relatively, a significant difference in the pitching moment coefficient. This could be due to the difference in the trailing edges of the geometries from XFLR5 and the AVL models.

Besides, the geometry modelling complications, it was discovered that the XFLR5 cannot handle the high subsonic Mach numbers required for the BW - 11 analysis. Hence only the AVL was used to analyse the test geometry at M0.85. AVL is able to handle high subsonic Mach numbers by implementing the classical Prandtl Glauert transformation.

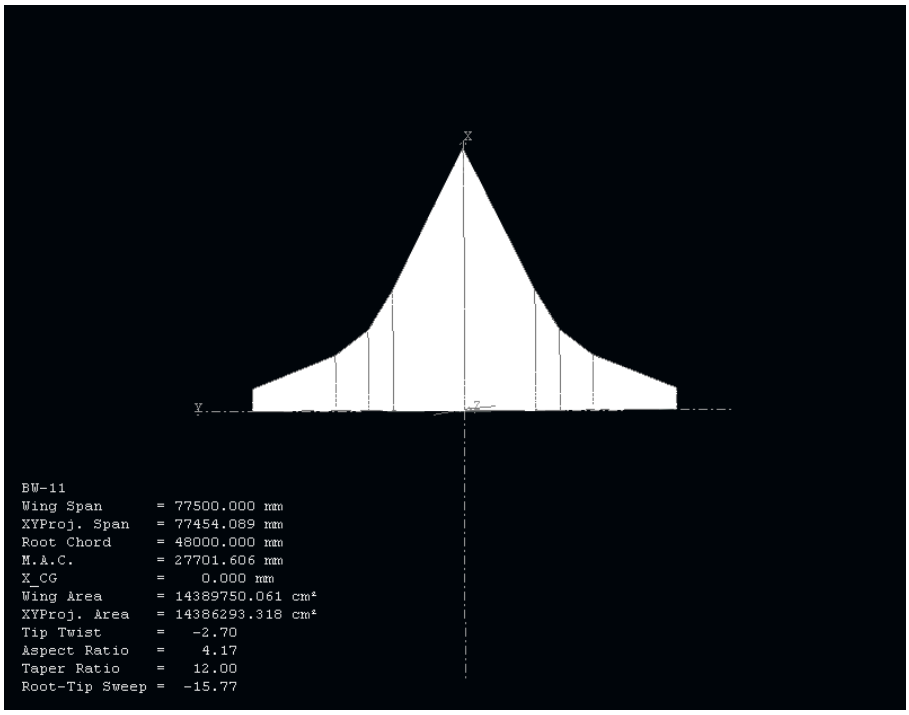


**Figure 6.21:** Geometry Model obtained with the XFLR5.

**Table 6.9:** Comparison of Aerodynamic Forces and Moments from AVL and the XFLR5 at M0.02

| Coefficients | AVL | XFLR5 |
|---|---|---|
| CL | 0.265 | 0.262 |
| CD | 0.006 | 0.008 |
| CM | -0.247 | -0.135 |

To ensure uniformity in the validation process, the NACA airfoils used for low speed analysis are replaced with the airfoil provided in the project specification handbook [2]. A comparison of the results obtained from the AVL analysis with data in the project specification handbook [32] is presented in Table 6.10. The coefficients are very similar with the same order of magnitude thus validating the aerodynamic analysis module of the GMDSO tool. Consequently, with the enhanced geometry modelling capability, ability to analyse geometries at high subsonic Mach number and the relatively consistent results compared with the XFLR5 and the data in the project specification handbook [32], AVL is considered a reliable and suitable choice for the aerodynamic analysis module of the GMDSO Tool.

It is imperative to state that even though the AVL stand - alone programme permits the

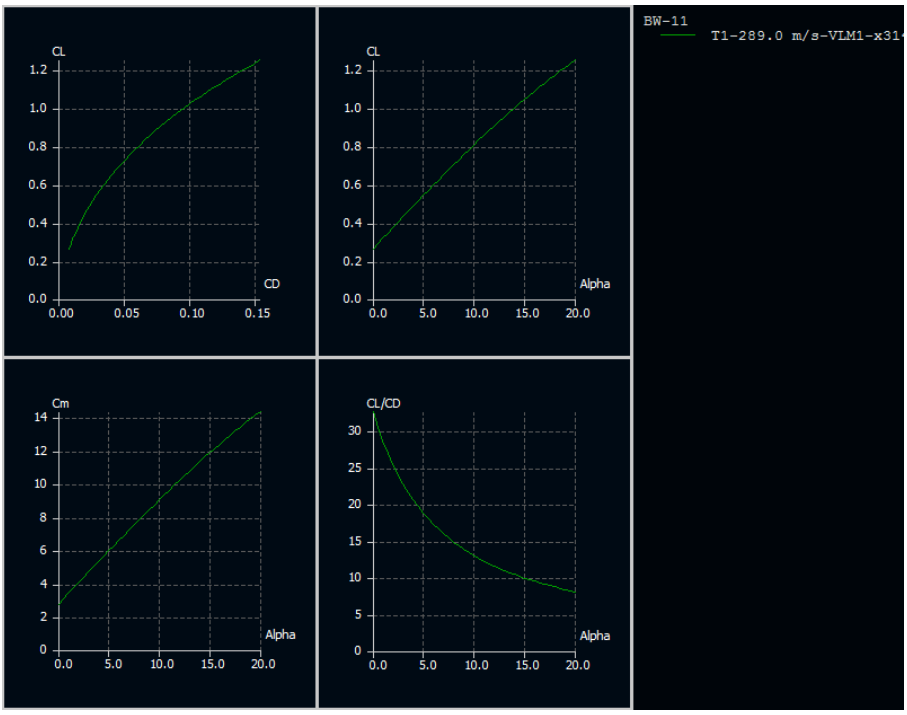


**Figure 6.22:** Polar Plots from XFLR5 Aerodynamic Analysis of Test Geometry.

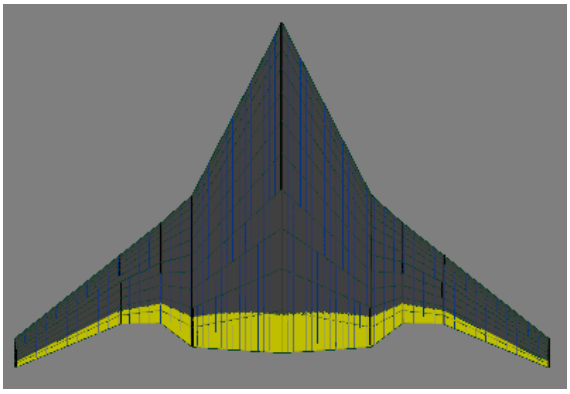

**Figure 6.23:** Geometry Model Obtained with the AVL.

**Table 6.10:** Comparison of Aerodynamic Forces and Moments from AVL and the BW-11 at M 0.85

| Coefficients | AVL | BW-11 |
|---|---|---|
| CL | 0.243 | 0.236 |
| CD | 0.0055 | 0.0033 |
| CM | -0.052 | 0 |

use of externally generated airfoils, this feature has not been implemented in the GMDSO tool. Subsequently, the test geometry was analysed using NACA 4 digit airfoil of required thickness. The result obtained are given in Table 6.11.

**Table 6.11:** Result of the AVL Analysis of Test Geometry with NACA 4-digit Airfoils Sections

| Coefficients | AVL |
|---|---|
| CL | 0.440 |
| CD | 0.015 |
| CM | -0.08 |

A single instance of the AVL VLM, as currently being distributed, can perform the aerodynamic analysis of a geometry at only one angle of attack and Mach number. However, the modified code integrated in the GMDSO tool has been extended to enable batch analysis of multiple angles of attack and Mach numbers at any instance of the module during a design synthesis. This multi-speed and angle of attack feature ensures the accurate prediction of aerodynamic forces for the different phases of flight. This is especially useful in the performance and stability analysis modules as well as for the exploration of the design space within a multivariate design synthesis optimisation framework.

To investigate the validity of the multi-speed/angles feature, the test geometry was analysed for a range of Mach numbers within the operating envelope of the aircraft at angles of attack between -5 and 20°. The relationships between the lift, drag and pitching moment coefficients with angles of attack at low and high subsonic Mach numbers are shown in Figure 6.24.

The plots show an increase in aerodynamics coefficients with angles of attacks except for the pitching moment coefficient which increases in a negative sense with increasing angles of attack. This phenomenon conforms to established trends. The linear nature of the plot is because the AVL uses linear VLM which assumes an incompressible, irrotational, inviscid flow. Hence, the AVL cannot determine viscous effects of a fluid or simulate flow separation. The accuracy of the AVL is thus limited to small angles of attack where there is little or no flow separation.

Similar trend is observed with the polar plots at low (M0.2) and high subsonic Mach numbers (M0.85) as shown in Figure 6.25. The plots show an increasing drag and lift coefficients with increases in angles of attack. This is expected because the AVL generates only induced drag which is directly proportional to the lift produced.

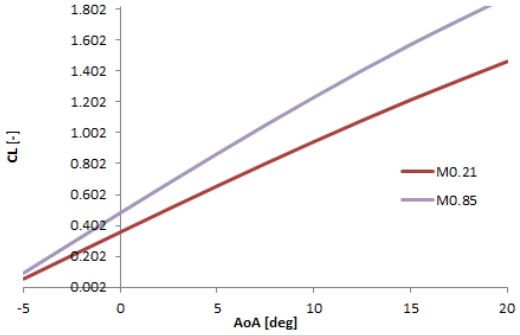


(a) CL vs AoA

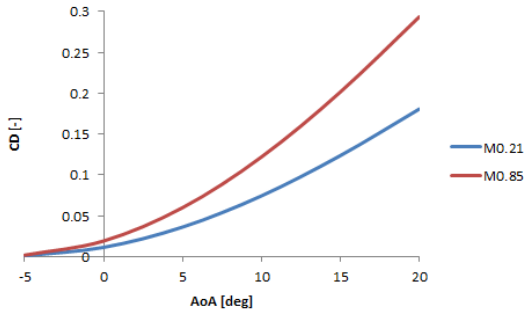


(b) CD vs AOA

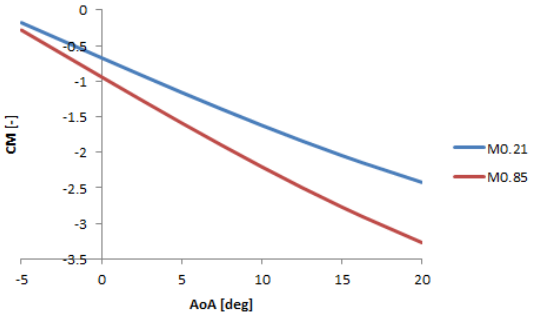


(c) CM vs AOA

**Figure 6.24:** Graphical Relationship Between Aerodynamic Forces and Moments at Low and High Subsonic Mach Numbers.

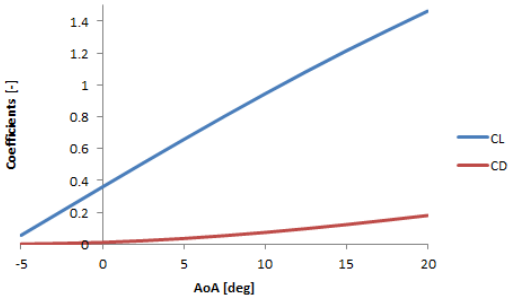


(a) CL vs CD at M0.21

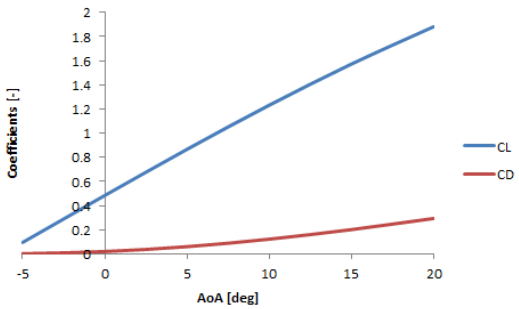


(b) CL vs CD at M0.85

**Figure 6.25:** Polar Plots of Lift and Drag Coefficients at Low and High Subsonic Mach Numbers.

Earlier, it was established that a single point aerodynamic analysis at zero degree angle of attack using the AVL provides a satisfactory result. It suffices to say, therefore, that the results from a multi-speed/angle aerodynamic analysis should be equally reliable thus validating the aerodynamics module of the GMDSO tool. In addition to the foregoing, the sensitivity of aerodynamic coefficients to Mach numbers was investigated. The results, which are shown in Figure 6.26, indicates a direct proportional relationship between the

coefficients and Mach number.

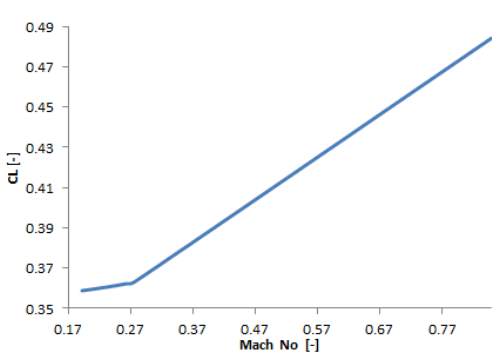


(a) CL vs Mach Number

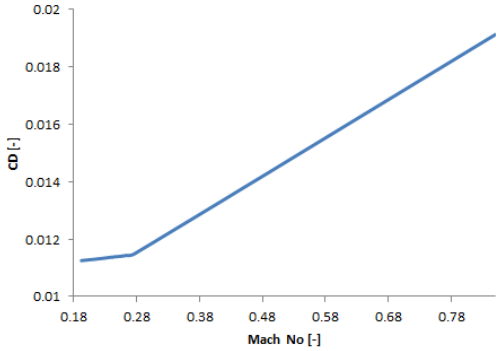


(b) CD vs Mach Number

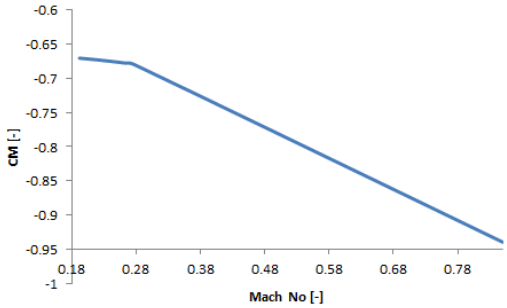


(c) CM vs Mach Number

**Figure 6.26:** Sensitivity of Aerodynamic Forces and Moments to Mach Numbers.

### 6.1.5 Stability Module

The stability module of the GMDSO Tool assesses the control fixed, longitudinal static stability of the BWB using static margin and trim characteristics. The static margin is defined as the distance between the center of gravity and the neutral point of the aircraft as a percentage of the MAC. Given the centre of gravity of the test aircraft as 31.9m [32], the aerodynamic forces and moments were derived from the aerodynamic modules.

Applying the relevant forces and moments into Equation 4.55, the stability margin was determined to be -0.02 or -2%. This is exactly the same value (-2%) specified for the BW - 11 in the specification hand - out thus validating the implemented process and methodology. Additionally, the result indicates that the aircraft is marginally statically unstable. While this is not ideal, it does not reflect a bad design as it could ensure the aircraft is trimmable which is a more stringent requirement for tailless aircraft.

According to Sadraey [147], acceptable elevon deflection angle for trim must lie between $\pm 20 - 25°$ [10, 25, 147]. This is because elevon deflection above 20 - 25° causes flow separation which could lead to loss of control effectiveness. For the test case, the elevon deflection and trim angles of attack were determined at cruise, take - off and landing. The results obtained are given in Table 6.12.

**Table 6.12:** Trim Characteristic for the Test Aircraft in Different Flight Conditions

| Phase | Speed [m/s] | Mass[kg] | Trim AOA[deg] | Elevon Deflection[deg] |
|---|---|---|---|---|
| Take-off | 1.2Vs | MTOM | 1.2 | -13.7 |
| Landing | 1.3Vs | MLM | 3.74 | -16.2 |
| Cruise | Cruise speed | MTOM | 5.45 | -4.37 |

Plots of the trim characteristics at take-off, landing and cruise are given in Figure 6.27.

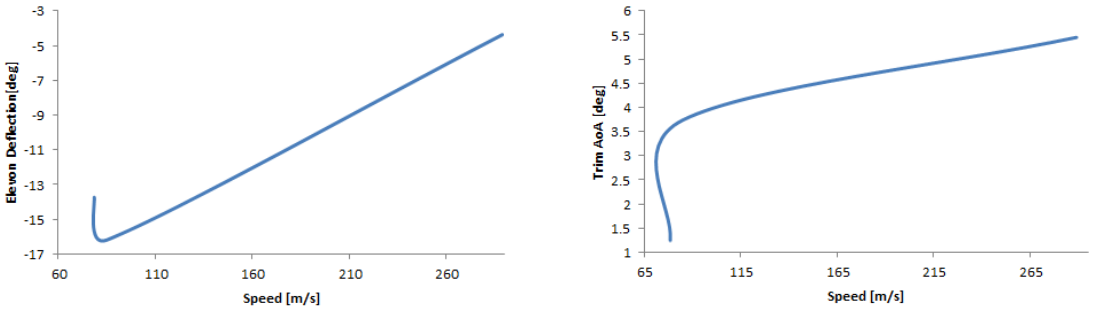


(a) Elevon Deflection vs Speed

(b) Trim Angle of Attack vs Speed

**Figure 6.27:** Plot of Trim Characteristic at Take-Off, Cruise and Landing.

The plots show that the aircraft can be trimmed in the operating flight conditions assessed. This is because the elevon deflection angles obtained (-4 to -17°) and angles of attack required (1.2 to 5.4°) lie within the acceptable limits. The plots also show that the critical region for trim is the low speed phases of take off and landing. This is evidenced from the relatively large elevon deflection(-13.7 and -16.2°) needed to trim the BWB aircraft as against the -4.4° required in cruise. A BWB tailless aircraft must therefore be designed to be trim-able in all flight conditions and most especially at the critical landing and take-off phase of flight.

The foregoing stability results were obtained with the MAC and CG given in the BW - 11 specification document. With the MAC and CG derived from the GMDSO Tool, the stability and trim characteristics with forward and aft CG is detailed in Table 6.13.

**Table 6.13:** Trim and Stability Characteristics with GMDSO Tool Derived CG and $\bar{\bar{c}}$

| Characteristics [deg] | CG MTOM | CG MZFM | CG OEM |
|---|---|---|---|
| Static Margin [-] | 0.13 | -0.031 | -0.15 |
| Elevon Deflection to Trim [cruise] | -2.3 | -1.67 | -1.1 |
| Elevon Deflection to Trim [Take - off] | -2.95 | -0.31 | 2.3 |
| Elevon Deflection to Trim [Landing] | -4.3 | -1.35 | 1.5 |
| AoA to Trim[cruise] | 3.9 | 3.5 | 3.1 |
| AoA to Trim[TO] | 4.02 | -5.8 | -7.5 |
| AoA to Trim[Land] | 1.61 | 0.8 | 0.1 |

### 6.1.6 Performance Module

The performance module assesses the mission and field performance of the test geometry using the GMDSO Tool. The mission performance includes both point and path performances. The point performance determined consists of climb gradient, climb rate and thrust required at different ceilings. Path performance includes range with different load profiles used in the payload range diagram. Airfield performance include take - off and landing distance as well as the balanced field length.

#### Take off and Landing

The take - off and landing performance of the BW - 11 with all 4 engines operational as derived from the GMDSO Tool are summarised in Table 6.14.

**Table 6.14:** Take - off and Landing Performance of the BW - 11 Aircraft

| | | Field Length [m] | Time [s] | Fuel Burn [kg] |
|---|---|---|---|---|
| Take-off | AEO (unfactored) | 1791 | - | |
| | AEO (factored) | 2059 | 46 | 3617 |
| Landing | Flare | 207.6 | - | - |
| | Free - roll | 165.6 | - | - |
| | Approach | 281.8 | - | - |
| | Brake - roll | 858.2 | - | - |
| | AEO (unfactored) | 1419 | - | 608.4 |
| | AEO (factored) | 2355 | 360 | 608.4 |

The field lengths are not given in the specification document. However, comparing the factored field performance value obtained from the GMDSO Tool with the the A380 specification. It was found that the BW - 11 has a comparatively similar take off field length of 2059m compared to 2050m for the A380 - 800 and a shorter landing distance of 2355m as against 2900 m specified for the A380 - 800 [148]. The improved BW - 11 field performance over the A380 - 800 conventional aircraft is expected since the BWB has a

lower wing loading compared to conventional aircraft. Low wing loading reduces the take - off and landing speeds hence leading to shorter take - off and landing field lengths.

### One Engine Inoperative Condition

Details of take - off performance in the OEI condition is required to determine the balanced field length. Assuming a critical engine speed ranging from 0.8 -1.0 $V_s$, the accelerate stop distance, $s_{accstop}$, and accelerate go distance, $s_{accgo}$, are calculated and presented in Table 6.15. On engine failure during take - off run, the $s_{accstop}$ is the distance required to accelerate an aircraft to a specified speed and then bring the airplane to a stop on the remaining runway. The $s_{accgo}$ is the total distance required to accelerate to the take - off safety speed and climb the $35ft$ obstacle after an engine failure on take - off.

**Table 6.15:** Balanced Field Length Calculations

| BFL Parameters | Multiples of Stall Speed [m/s] | | | | | | |
|---|---|---|---|---|---|---|---|
| | $0.74V_s$ | $0.79V_s$ | $0.83V_s$ | $0.88V_s$ | $0.93V_s$ | $0.97V_s$ | $V_s$ |
| $v1$ | 57.6 | 61.2 | 64.8 | 68.4 | 72 | 75.6 | 77.8 |
| $v1^2$ $[m^2/s^2]$ | 3317.8 | 3745.4 | 4199 | 4678.6 | 5184 | 5715.4 | 6046.6 |
| $s_{accstop}$ $[m]$ | 3175.5 | 3368.9 | 3579 | 3807.1 | 4054.7 | 4323.6 | 4496.0 |
| $s_{accgo}$ $[m]$ | 4116.0 | 3955.5 | 3755.4 | 3506.8 | 3197.4 | 2809.9 | 2530.4 |

Plotting the accelerate go distance, $s_{accgo}$, and accelerate stop distance, $s_{accstop}$, against the square of the critical engine speed, $v1^2$, as shown in Figure 6.28 give the balanced field length of 3650m and a critical engine failure speed of $66.2m/s$. The balanced field length is well within the existing runway lengths of major airports. For instance, the length of the Northern runway at Heathrow is 3902m, while the Southern runway is 3660m long [149].

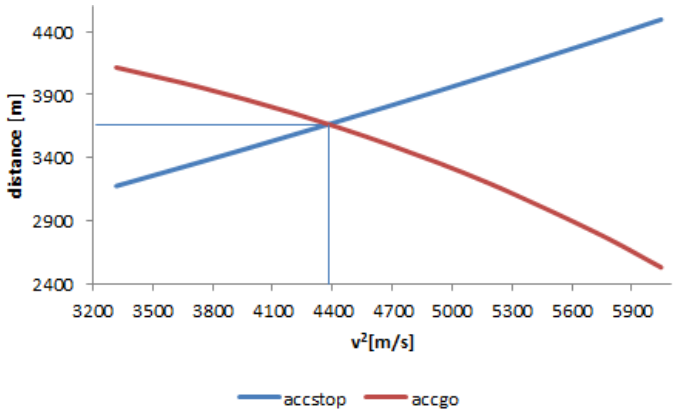


**Figure 6.28:** Determination of Balanced Field Length

### Enroute Performance

The enroute performance consists of the climb, cruise and descent phase. The climb and descent are flown in several segments as detailed in the methodology chapter. The distance, time and fuel burn in each phase of the en - route mission is listed in Table 6.16.

**Table 6.16:** En - route Performance of the BW - 11 Aircraft

| | Distance[m] | Time [s] | Fuel Burn [kg] |
|---|---|---|---|
| Climb | 345372 | 1040.2 | 14391.3 |
| Cruise | 14800 | 56042.7 | 228119 |
| Descent | 262246 | 1592.5 | 26974.8 |
| Diversion | 370400 | 2366.2 | 66682 |

### Climb Gradients

The CS 25.117 details the required climb gradient for various number of engines in the critical engine in - operative flight phase. It specifies climb gradients of not less than 0.5, 3 and 1.7 per cent for a four - engined airplane in the first, second and third segment climb respectively. Consequently, analysing the test aircraft climb gradients performance indices using the GMDSO tool, the results in Table 6.17 were obtained. The results given in Table 6.17 indicate that the BW - 11 meets the climb gradient requirement.

**Table 6.17:** Climb Gradients of the BW - 11 Aircraft for a 4 -engined Propulsion System Arrangement

| Segments | Gradients in percentages |
|---|---|
| First Segment | 12.5 |
| Second segment | 14.9 |
| Third Segment | 14.1 |

The Table 6.17 shows quite high climb gradients relative to a conventional aircraft. Though the order of magnitude in relation to conventional configuration cannot be verified due to lack of data, the BWB is expected to have a higher climb gradient compared to a conventional tube and wing aircraft. This is because the BWB has a low wing loading. This gives it a superior climb rate. Given that climb gradient is derived from Equation **??**, superior climb rate leads to a higher climb gradient when compared to a conventional aircraft.

$$climb_{gradient} = \frac{climb_{rate}}{Airspeed} \tag{6.2}$$

### Thrust Requirement

The thrust requirement analysis is used to assess the thrust needed to accomplish different phases of flights. This is necessary in order to evaluate the propulsion system capacity to power the aircraft through its mission. Details of thrusts required for different flight conditions are given in Table 6.18.

**Table 6.18:** Thrust Required at Different Flight Condition

| Condition | Thrust Required [N] |
|---|---|
| Climb to Absolute Ceiling | 883391.7 |
| Maximum ROC | 129067 |
| Climb to Cruise Ceiling | 452462.5 |
| Climb to Initial Climb | 391197.8 |
| Service Ceiling | 574887.9 |
| Maximum Velocity | 40018.6 |
| Landing | 79702.7 |

The table shows that the maximum thrust is required in climb to absolute ceiling. Consequently, it is expedient to ensure that the propulsion system is capable of providing this amount of thrust.

### Payload Range Diagram

The payload range diagram evaluates the trade - off between the aircraft range and disposable loads. The typical payload range diagram consists of 3 critical points. These are the maximum payload, maximum fuel and the maximum ferry range. The maximum payload range is determined with the full payload of the 555 passengers. Maximum fuel range determines the range obtained from decreasing the number of passengers. In this thesis, the maximum fuel range is obtained by reducing the number of passenger to 325 while maximum ferry range assumes there is no payload. Subsequently, applying this assumptions to the GMDSO tool performance analysis module, the payload range characteristics given in Table 6.19 is obtained.

A plot of the payload and range combinations for the 3 critical points is given in Figure 6.29.

### Other Performance Indices

Other performance indices calculated in the GMDSO tool are the sensitivity to turbulence, structural parameter and the regulatory and reserve fuel. The sensitivity to turbulence

**Table 6.19:** Critical Payload Range Characteristics of the BW - 11 Aircraft

| Critical Points | Maximum Payload | Maximum Fuel | Maximum Ferry Range |
|---|---|---|---|
| Number of Passengers [-] | 555 | 325 | 0 |
| Payload [kg] | 65115 | 39125 | 0 |
| Total Fuel [kg] | 183588 | 209578 | 209578 |
| Total trip fuel[kg] | 112956 | 138946 | 138946 |
| Trip fuel available[kg] | 86203 | 112193 | 112193 |
| Cruise fuel available[kg] | 41220 | 67210 | 67210 |
| MTOM [kg] | 481148 | 481148 | 442023 |
| Range[m] | 14172728 | 17933358 | 18046252 |

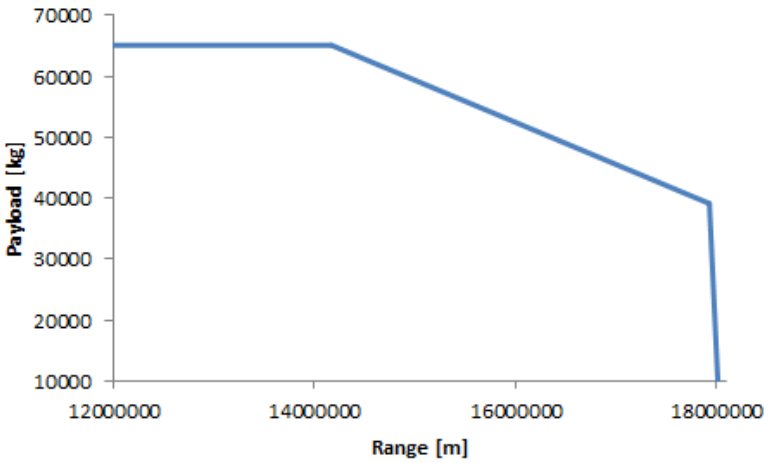


**Figure 6.29:** Payload Range Diagram for the BW - 11 Mission.

factor is included in the GMDSO Tool to enhance passenger comfort and ensure a good ride quality. The sensitivity to turbulence in cruise is derived from a simple discrete gust analysis.

According to Agenberg and Theron [150], tailless aircraft have turbulence handling challenges because of their low damping ratio and pitch inertia. This challenge led Monnich and Dalldorf [151] to develop a criteria that assesses tailless aircraft turbulence handling quality. The criteria states that for a tailless to have good turbulence handling quality, it must satisfy Equation 6.3.

$$\frac{C_{m\alpha}}{C_{mq}} < (C_{L\alpha} + C_D) \frac{\rho S_{ref} \bar{\bar{c}}}{2MTOM} \tag{6.3}$$

Equation 6.3 expressed differently gives Equation 6.4.

$$\frac{C_{m\alpha}}{C_{mq}} - \left[ (C_{L\alpha} + C_D) \frac{\rho S_{ref} \bar{\bar{c}}}{2MTOM} \right] < 0 \tag{6.4}$$

Here:
$C_{m\alpha}$ is the pitching moment due to change in angle of attack.
$C_{mq}$ is the pitching moment due to changes in dynamic pressure.
$S_{ref}$ is the reference surface area.
$\bar{\bar{c}}$ is the mean aerodynamic chord.
$MTOM$ is the maximum take off mass.
$C_D$ is the drag coefficient which includes profile drag, zero lift drag, wave drag and lift induced drag.
$C_L$ is the lift coefficient.

The Structural Parameter (SP) is provided to resolve any potential conflicts between the aerodynamic and structural requirements in aircraft design. It is established to indicate any likely structural limitations with the design [110]. The SP is derived from the expression in Equation 6.5.

$$SP \leq \sec \Lambda_E \left[ \frac{NAR^{1.25}}{(t/c)^{0.5}} \right]^{0.5} \tag{6.5}$$

Where :
$N$ is the normal acceleration factor.
$\Lambda_E$ is the effective structural sweep. It is approximated by the quarter chord sweep $\Lambda_{0.25}$.
$t/c$ is the thickness to chord ratio.

The regulatory fuel refers to the 45 minutes mandatory fuel required by regulation while the reserve fuel refers to the 10% contingency fuel.

The result of the GMDSO Tool prediction of other performance indicators are given in Table 6.20. According to Howe [110], SP for a commercial passenger aircraft lies between 15 to 16. From the performance analysis with the GMDSO tool, the SP was found to be equal to 16.2. Consequently, it could be inferred that the BW - 11 is aero - structurally efficient. Additionally, the BW - 11 is found to have good turbulence handling quality because the calculate value of -0.12 satisfies Agenberg and Theron [150] condition given in Equation 6.4.

**Table 6.20:** Fuel Reserves for the BW - 11 Aircraft

| | Fuel Mass [kg] |
|---|---|
| 45 minutes Regulatory | 3952 |
| 10% Contingency | 26753 |
| Sensitivity to Turbulence | -0.12 |
| Structural Mass Factor | 16.22 |

## 6.2 Packaging

The packaging module comprises the sizing and volume constraint handling models. It estimates the size of the cabin and internal components as well as ensures that the internal object are well enclosed within the BWB geometry. The packaging model can be used for sizing all major components including the engine, landing gear and cabin. However, only cabin dimensions are validated in the packaging module as it is the only information found in the specification handbook [32].

The cabin is sized to carry 555 passengers in 3 class seating arrangement with a leading edge sweep of 63°. The passengers are seated in $2 \times 2$, $2 \times 3$ and $3 \times 3$ arrangement in the first, business and tourist class respectively. The number of passengers and dimension of seat pitches in the various class are given in Table 6.21.

**Table 6.21:** Seat Pitch and Number of Pax in the Different Classes

| Class of Seats | Number of Passengers [ - ] | Seat Pitch [$in$] |
|---|---|---|
| First Class | 9 | 81 |
| Business Class | 80 | 55 |
| Economic Class | 466 | 32 |

Inserting these values into the packaging module of the GMDSO Tool, the cabin is sized using the Bradley sizing model. A comparison of the results from the process with the specifications of the test geometry is given in Table 6.22.

**Table 6.22:** Comparison of GMDSO Cabin Size With Test Geometry

| Parameters | GMDSO Cabin | BW - 11 Test Geometry |
|---|---|---|
| Length of Cabin Centre Line [m] | 47.86 | 48 |
| Length of Cabin Outer - wall [m] | 12 | 22 |
| Half Width of the Cabin [m] | 10.97 | 13 |

The results of the sizing module correlates closely with the specifications of the test geometry in terms of the length of the cabin centre - line and the cabin width. However, they differ markedly in the length of cabin outer walls. This difference could be due to the positioning of the baggage compartment behind the passenger cabin in the test configuration.

Volume constraint handling is integrated in the GMDSO Tool packaging module using the CST Parameterization technique. The technique generates airfoil - like cross - sections which are distributed across the span, according to chosen geometric variables such as sweep, dihedral, twist and trailing edge thickness, to create the wing. In order to demonstrate the implementation of the volume constraint feature of the packaging module, the ability of the CST parameterisation technique to model geometry with different combinations of twist, sweep and dihedral is demonstrated.

The project handbook [32] specifies a cabin with a leading edge sweep angle of 63°, a zero degree twist angle and no dihedral. A 2D airfoil of the root section of the BW - 11 cabin generated using the CST method is shown in Figure 6.30. The upper and lower curves of the airfoil are created independent of each other, as suggested by their different colours, but with a condition that ensures closure and continuity from the leading to the trailing edge. In the Figure 6.30, the upper and lower curves are coloured blue and red respectively. The airfoil shown in Figure 6.30 is the root section of the BW - 11 geometry with zero twist and dihedral.

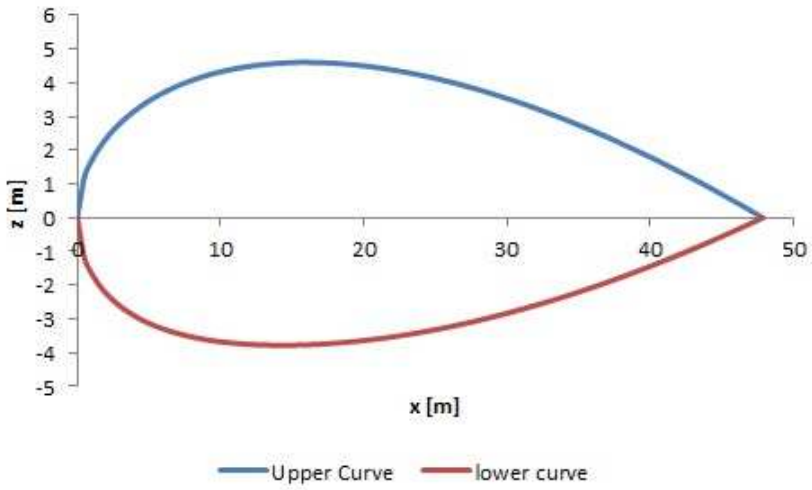


**Figure 6.30:** An Airfoil Obtained with the CST Parameterisation Technique.

Besides creating an airfoil for analysis, the GMDSO Tool also calculates the maximum camber and thickness of the generated geometry as given in Table 6.23. The Table 6.23 indicates that the airfoil has the recommended 17% thickness to chord ratio providing a maximum thickness of 8.6 $m$. However, as will be shown later, this does not always guarantee that volume constraint is satisfied at all points due to the non - uniform cross - section of the airfoils.

**Table 6.23:** Properties of the Obtained CST - Airfoil

| Properties | Values |
|---|---|
| Maximum Thickness [m] | 8.38 |
| Maximum Camber [m] | 0.43 |
| Thickness to Chord Ratio [%] | 0.175 |
| Camber to Chord Ratio [%] | 0.009 |

Further, to the foregoing the test cabin is modelled with different twist and dihedral combinations as shown in Figure 6.31. In Figure 6.31a, the upper and lower curves of the root section are coloured blue and green respectively while the cabin outer - wall section curves are shown in red and purple colours as shown in Figure 6.31.

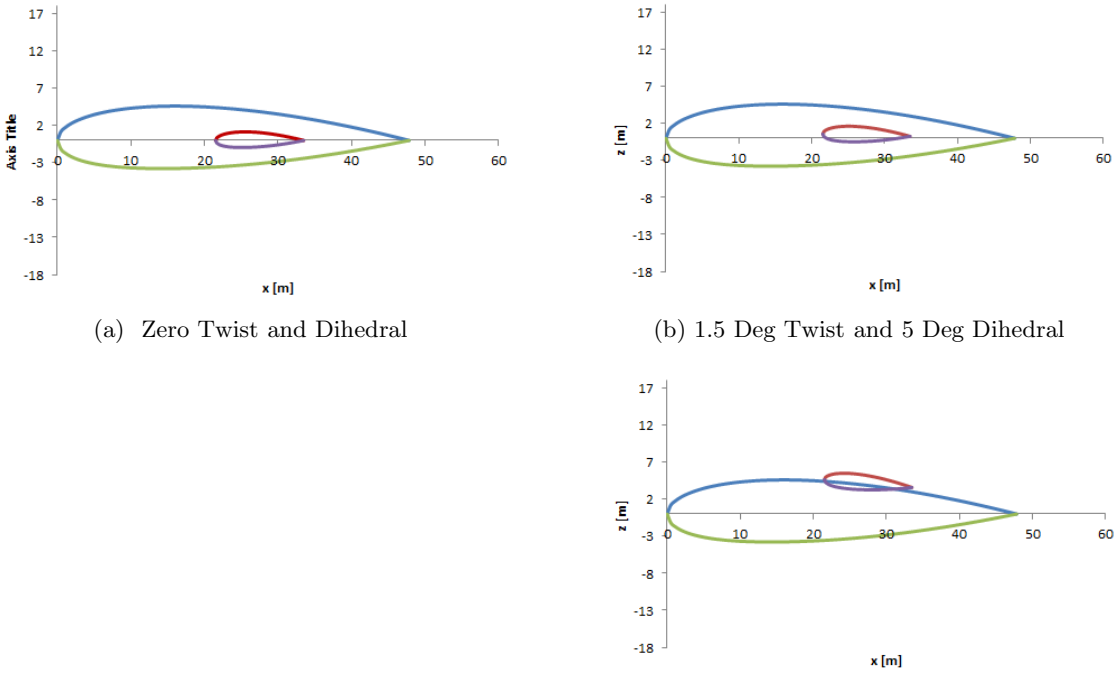


(a) Zero Twist and Dihedral

(b) 1.5 Deg Twist and 5 Deg Dihedral

(c) 5 Deg Twist and 25 Deg Diheral

**Figure 6.31:** CST Description of the Test Geometry With Different Twist and Dihedral Combinations.

Having established the capabilities of the CST as a geometry parameterisation tool, the aircraft is checked to ensure there is sufficient space to enclose internal objects. Volume constraints could be implemented by either the method of logarithms or by the use of coefficients. In order to select the most suitable method for use in the handling volume constraint, the methods were applied to curve fitting of a wing section.

Assuming a thickness constraints of $2.5m$ for an internal objects lying between $x = 2.87m$ and $x = 38.76m$ and using the logarithmic and coefficient methods, Figure 6.32 was derived. The Figure 6.32 shows the initial wing cross - section in brown colour with the modified upper curves of the section in purple and green. From the original Figure 6.32, it could be seen that the internal bounding box, represented by the red dashed and solid lines, fits properly within the cross - section at $x = 2.87m$ but stuck out at the $x = 38.76m$ point.

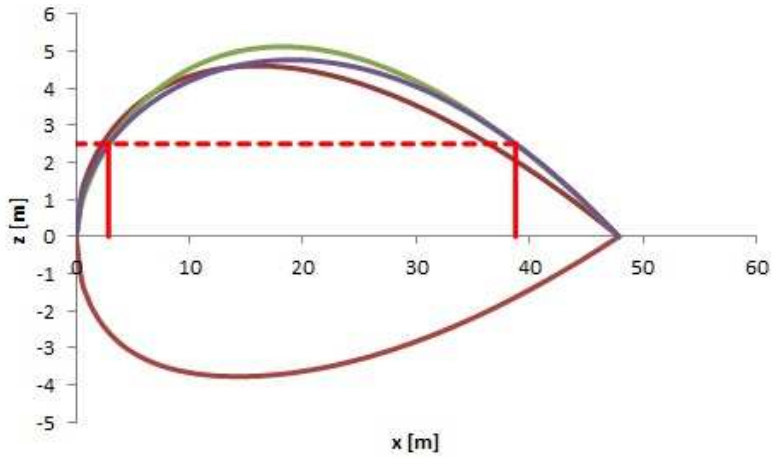


**Figure 6.32:** Comparison of Volume Constraint Handling with the Logarithmic and Coefficient Methods.

However, by applying scaling function to the upper curve using the logarithmic method (Green curve) and the coefficient method (blue curve), the internal object is found to be properly enclosed at all points. Nonetheless, the logarithm method (Green curve) leaves a much larger unused space compared to the method of coefficient. Consequently, in order to avoid such redundant space and ensure efficient utilization of space within a BWB cross - section, the Method of Coefficient is selected as the most appropriate option for volume constraint handling feature of Packaging Module.

According to Bradley [63], a minimum thickness of $2.5m$ is required to accommodate a standing height of passengers including furnishing and the skins of the upper and lower deck. It has been estimated that a 15 - 17% thickness to chord ratio provides the required depth. However, as shown in this preceding discourse, there is no guarantee that the depth would be maintained through the chord of the section. Consequently, to ensure the required depth is obtained, the packaging module is essential.

The ratio of the internal object to the length of the chord as well as its size presents different sets of challenges in the packaging of a BWB. Figure 6.33 shows a selection of possible fitting cases that could be encountered in the conceptual design synthesis of the BWB. In the Figure, the original curve is shown in brown while the volume constraint fitting curves, implemented using the method of coefficients, are shown in blue and green colours on the plots. The bounding boxes representing internal objects of different sizes are represented in red with the dashed portion provided to connect the upper vertices of the boxes to the $2.5m$ mark on the z - axis.

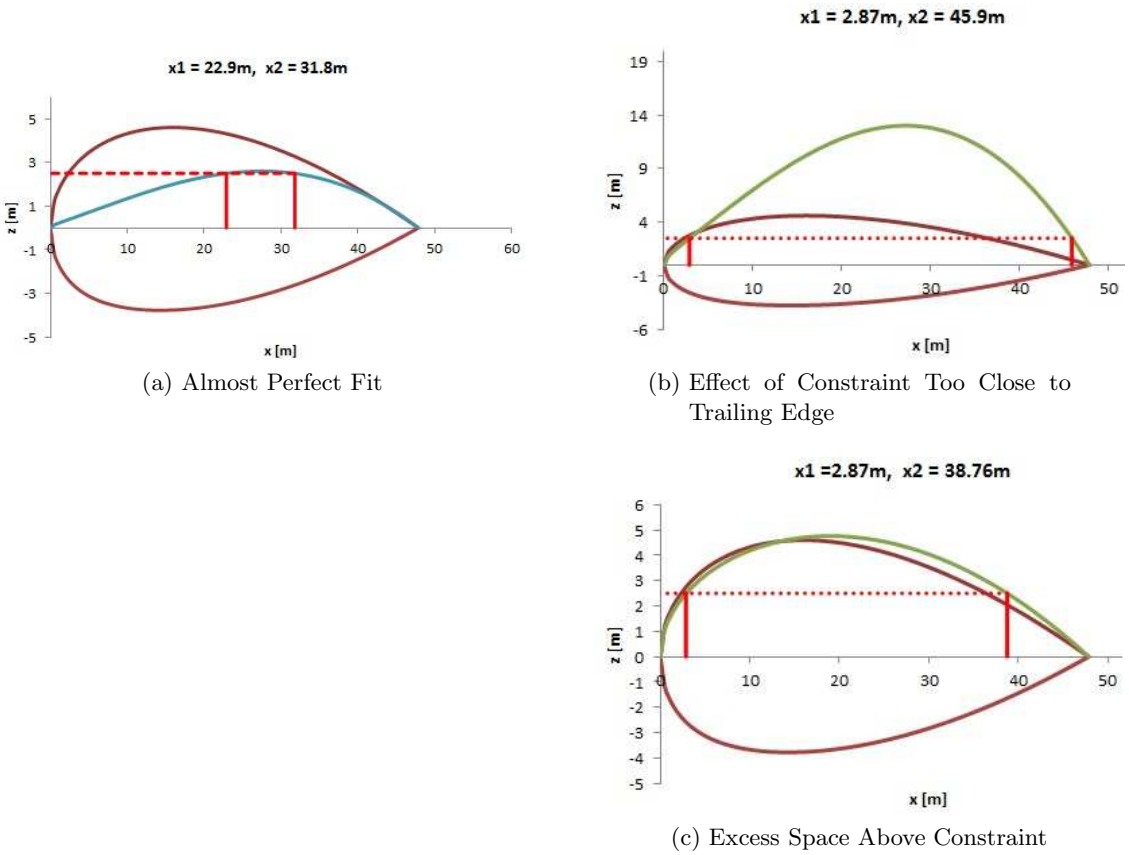


(a) Almost Perfect Fit

(b) Effect of Constraint Too Close to Trailing Edge

(c) Excess Space Above Constraint

**Figure 6.33:** Volume Constraint Handling Using CST Parameterisation Technique.

In the Figure 6.33, the bounding boxes are placed at different locations along the chord. In the first case, the box was positioned between $x = 22.9m$ and $x = 31.8m$. The second case placed the box between $x = 2.87m$ and $x = 45.9m$. The third case located the box between $x = 2.87m$ and $x = 38.76m$.

In Figure 6.33a, the internal object is found to be well contained within the initial geometry but at the cost of redundant space. The volume constraint fitting curve (blue)

minimises the excess space thereby allowing for efficient space utilization within the cabin but distort the leading edge radius of the geometry. In Figure 6.33b, the object is found to be sticking out from the geometry. The volume constraint curve in green is subsequently provided to enclose the object. However, it has been found to generate so much redundant space which could create aerodynamic problems. The case given in Figure 6.33c encloses only one of the vertices of the bounding box. The volume constraint handling curve(green) modifies the initial curve to enclose the internal object but could not minimise the redundant space. Consequently, from the Figure 6.33, it is evident that volume constraint fitting using the method of coefficient works nicely for any potential packaging problem thus establishing the robustness of the method. However, it exposes some challenges that still needs to be mitigated. Among the challenges discovered are poor space utilization arising from redundant space and the distortion of the leading edge radius with potential consequence on aerodynamic performance.

Distortion of the leading edge radius could easily be resolved by incorporating a variable for the leading edge radius in the formulation of the CST function. Redundant space, however, is not easily amenable. Redundant space occurs because the Bernstein polynomial used in the CST functions provides global control rather than local control of the geometry. Consequently, Michiel Straathof [152] proposed the addition of a B-Spline polynomial function to the CST Method to obtained a modified function known as the Class Shape Refinement Transformation (CSRT). The CSRT method minimises the redundant space within the geometry by ensuring local control of the geometry in addition to the global control provided by the Bezier polynomial in the CST method.

## 6.3 Design Improvements

The quasi - validation section of the GMDSO Tool assesses individual models in isolation in order to establish a measure of the level of confidence that could be placed on the results. The sensitivity analysis section would combine modules to explore the design space in order to understand the effect of different variables on the characteristics of a BWB aircraft. This section is used to demonstrate the ability of the GMDSO Tool to create design improvements using the optimisation techniques integrated into the tool.

The design space of the BWB is infinitely wide. Hence, while the GMDSO Tool enables a wide range of applications, due to limited computational resources and time, only a selection of the possibilities is presented in this research.

### 6.3.1 Design Case 1 - Mass Minimisation Subject to Geometric Constraint

The first sensitivity analysis problem investigated is the effect of the variations of geometric and mission variables on the reduction of the MTOM of the BWB. Using the 3 kinked BW - 11 geometry, defined in Table 6.1, as the baseline and selecting the Bradley structural weight estimation method, an optimisation problem is formulated. The objective of the optimisation problem is to minimise the $MTOM$ by varying geometry and mission variables subject to an equality constraint. The problem was assessed using both the LSGRG2 and the GA optimisers. The design problem showing specified upper and lower bounds is given in Table 6.24.

**Table 6.24:** Design Variables and Constraints for Design Case 1

| Variables | lower bounds | Baseline | Upper bounds |
|---|---|---|---|
| Fuselage Sweep [deg] | 45 | 63 | 72 |
| Wing Sweep[deg] | 32 | 38.3 | 45 |
| Dihedral section 0[deg] | 0 | 1.5 | 5 |
| Dihedral section 1[deg] | 0 | 3 | 5 |
| Dihedral section 2[deg] | 0 | 3 | 5 |
| Twist section 0 [deg] | -3 | 2.8 | 3 |
| Twist section 1 [deg] | -3 | -0.3 | 3 |
| Twist section 2 [deg] | -3 | 0.5 | 3 |
| Twist section 3 [deg] | -3 | 0.9 | 3 |
| Twist section 5 [deg] | -3 | -2.7 | 3 |
| Cruise Altitude [m] | 10000 | 11227.6 | 20000 |
| Cruise Mach Number [-] | 0.85 | 0.85 | 0.95 |
| Initial MTOM Estimate[kg] | 300000 | 481148 | 700000 |

#### LSGRG2 Design Case 1

With the LSGRG2 optimiser, the MTOM was reduced from 481148$kg$ to 469293$kg$. The design case and optimisation result is shown in Figure 6.34. A comparison of the initial geometric and mission variables to the optimised values is given in Table 6.25.

The results in Table 6.25 retained most of the geometry and mission variables of the baseline BW - 11 except for the slight increase in the fuselage leading edge sweep angle from 63° to 64.8° and a reduction in wing sweep angle from 38.3° to 32°. The increase in fuselage sweep angle and corresponding decrease in the wing sweep angle leads to a 4.7% reduction in the structural mass from 138260.4$kg$ to 131769 $kg$. However, the fuselage sweep angle is tied to the size of the cabin and hence the number of passengers. In order to accommodate the required number of passengers, the decrease in the cabin width

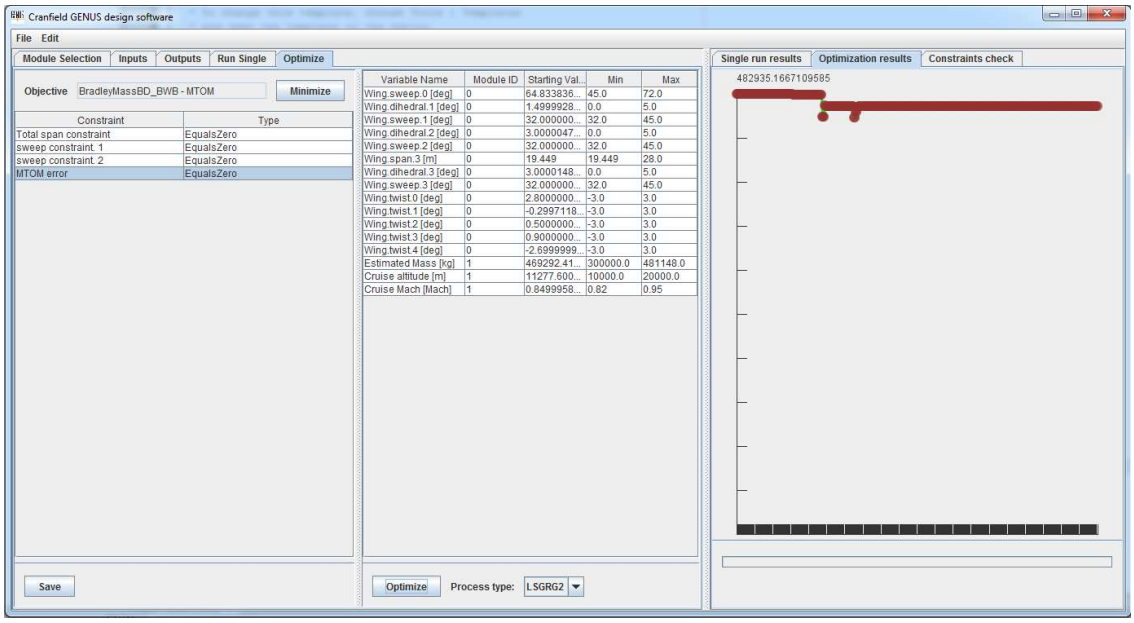


**Figure 6.34:** Evolution of MTOM with Design Optimisation Iterations.

**Table 6.25:** Variation of Geometric Variable for Design Case 1

| Variables | Baseline BW - 11 | LSGRG2 |
|---|---|---|
| Fuselage Sweep [deg] | 63 | 64.8 |
| Wing Sweep[deg] | 38.3 | 32 |
| Dihedral section 0[deg] | 1.5 | 1.5 |
| Dihedral section 1[deg] | 3 | 3 |
| Dihedral section 2 [deg] | 3 | 3 |
| Twist section 0 [deg] | 2.8 | 2.8 |
| Twist section 1 [deg] | -0.3 | -0.3 |
| Twist section 2 [deg] | 0.5 | 0.5 |
| Twist section 3 [deg] | 0.9 | 0.9 |
| Twist section 5 [deg] | -2.7 | -2.7 |
| Cruise Altitude [m] | 11227.6 | 11227.6 |
| Cruise Mach Number [-] | 0.85 | 0.85 |
| MTOM [kg] | 481148 | 469338 |

resulting from increase in the fuselage sweep angle is compensated for by an increase in the root chord. This is likely to have an adverse effect on the aerodynamic efficiency of the design. Consequently, it is essential to consider the aerodynamics and productivity implications of any increase in fuselage sweep angles viz - a - viz the weight reduction before deciding on the appropriate sweep angle for the centre - body (fuselage) of the BWB.

Similarly, though the reduction in wing sweep decreases the structural mass, it could lead

to an increase in the drag rise Mach number. Therefore, in view of the tight inter - disciplinary couplings on the BWB, geometric modifications should only be made with due considerations for the other characteristics affecting the performance of the BWB. This requires the implementation of a suitably designed optimisation case with appropriate objective function and constraints within defined limits.

The limited variations in design variables highlights the weakness of the gradient based LSGRG2 optimiser to being locked in a local minima and not being able to obtain a global optimum. The implementation of both the gradient and non - gradient optimisation technique in the GMDSO Tool is therefore a smart decision as it allows for the use of appropriate option in different design scenario.

The plot of the resulting geometry from the mass minimisation problem of design case 1 is given in Figure 6.35.

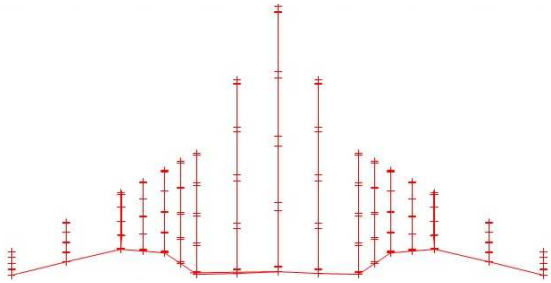

**Figure 6.35:** Geometry Obtained from the Minimisation of MTOM

### GA - Design Case 1

The GA is a non - deterministic (random) optimisation technique. Using the GA optimiser, greater variations of the design variables are observed. This is due to the ability of the GA to obtain global optima and not to be locked in a local minima. Nevertheless, due to the randomness of the process, there is no definite solution to the design problem rather several solutions consisting of different combinations of geometry and mission variables producing various magnitudes of reductions in the $MTOM$ of the BWB were generated. A comparison of the design solutions with the geometry and mission variables of the baseline BW - 11 is given in Table 6.26.

A typical GMDSO Tool output for the Design Case 1 is shown in Figure 6.36. The greater variations of design variables seen in Table 6.26 compared to the results obtained using the LSGRG2 (Table 6.25) demonstrates the strength of the non - gradient GA in being

**Table 6.26:** Variation of Design Variables for Case 1 Using the GA Optimiser

| Variables | Baseline | GA 1 | GA 2 | GA 3 | GA 4 | GA 5 | GA 6 |
|---|---|---|---|---|---|---|---|
| Fuselage Sweep [deg] | 63 | 72 | 69.6 | 72 | 69.5 | 72 | 68.9 |
| Wing Sweep[deg] | 38.3 | 32 | 32 | 32 | 32 | 32 | 32 |
| Dihedral section 1[deg] | 1.5 | 5 | 5 | 5 | 3.5 | 0 | 0 |
| Dihedral section 2[deg] | 3 | 5 | 5 | 5 | 3 | 0 | 0 |
| Dihedral section 3 [deg] | 3 | 5 | 1.04 | 4.02 | 5 | 2.3 | 0 |
| Twist section 0 [deg] | 2.8 | 0.09 | 1.26 | -0.84 | 0.48 | 0.07 | -0.15 |
| Twist section 1 [deg] | -0.3 | -1.5 | -1.18 | 0.46 | -2.2 | 0.95 | -1 |
| Twist section 2 [deg] | 0.5 | -1.3 | -0.49 | -0.27 | -3 | -0.07 | 0.38 |
| Twist section 3 [deg] | 0.9 | -1.5 | -0.42 | 0.12 | -0.58 | 0.62 | 1.96 |
| Twist section 4 [deg] | -2.7 | -1.4 | 0.70 | 2.62 | -1.32 | 1.66 | -0.76 |
| Cruise Altitude [m] | 11227.6 | 12611 | 10958 | 17021 | 13155 | 20000 | 10000 |
| Cruise Mach Number [-] | 0.85 | 0.82 | 0.86 | 0.82 | 0.82 | 0.95 | 0.82 |
| MTOM [kg] | 481148 | 420281 | 440818 | 423121 | 438692 | 424840 | 441865 |

able to obtain a global optimum. However, the GA is a random technique and may require several computationally expensive runs to generate significant result. In the design case under consideration, the best objective obtained is a 12.7% decrease in the $MTOM$ from 481146$kg$ to 420281$kg$. This reduction requires the aircraft to fly at a reduced cruise Mach number of 0.82 and a slightly higher cruise altitude of 12611$m$ compared to the baseline cruise Mach number of 0.85 and altitude of 11227.6$m$. The reduced cruise Mach number and higher cruise altitude minimise fuel burn due to reduced thrust. Reduced thrust arises from an improved flight efficiency caused by the lower air density at higher flight altitude. Consequently, the reduced fuel burn lowers the mass of mission fuel which subsequently reduces the MTOM.

All reductions in MTOM is accompanied by a higher fuselage sweep angle, a lower wing sweep angle and random variations in twist distributions and dihedral angles. Reduced wing sweep angle minimises tip loading due to the reduction in structural span. This subsequently reduces the structural weight and hence the MTOM. Twist modifies the moment distribution over the wing thereby affecting structural weight, pitching moment, stalling and induced drag characteristics for wings with additional highly weighted load distributions at the wing tips.

The combined effect of these geometry features coupled with the increased flight altitude and reduced Mach number helps to minimise the MTOM. Nevertheless, while a decrease in wing sweep angle reduces the structural weight and hence the MTOM, it could potentially increase the drag rise Mach number, thereby reducing the ability of the aircraft to operate efficiently at higher Mach number. Though, this may be offset with the high fuselage sweep

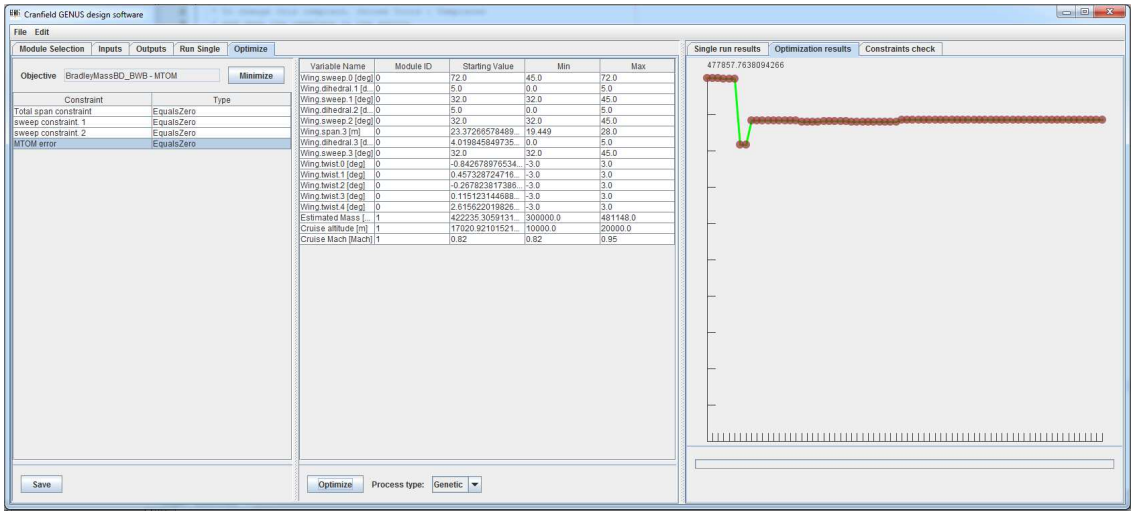


**Figure 6.36:** Typical GMDSO Tool Output for the GA Optimisation of Design Case 1.

angle, it is worthy to note that the fuselage sweep angle is linked to the size of the cabin and hence the number of passengers. Hence, it is imperative to ensure that the lengthening of the root chord, in order to accommodate the required number of passengers, following the increase in the fuselage sweep angle does not deteriorate the aerodynamic efficiency of the configuration. Additionally, since the twist distribution also affects the pitching moment and trim drag, there is the need for to conduct a multivariate optimisation of the configuration in view of the interconnected disciplines to ensure that a reduction in the MTOM does not adversely affect the aerodynamic and stability characteristics of the aircraft.

### 6.3.2 Design Case 2 - Mass Minimization Subject to Stability Constraint

Design Case 2 combines the mission, geometry, aerodynamic and stability modules to create a BWB with reduced MTOM and a positive static margin from the Baseline. It is implemented to investigate the ability of the GMDSO Tool to perform multi - module, multi - constraints design synthesis and optimisation involving aerodynamic analysis. Like design case 1, design case 2 is also a mass minimisation problem set up as given in Table 6.24 but subject to a positive stability margin. The stability margin is a function of the position of the c.g and the aerodynamic centre. The c.g depends on the geometry and the locations of major components. The aerodynamic centre on the other hand is a function of the aerodynamic characteristics of the aircraft.

Earlier in the quasi - validation of the GMDSO Tool stability module, it was found that

the BW - 11 with NACA 4-series airfoil sections generated a negative stability margin of -0.02. By varying the shape variables, it is expected that there will be some changes in the centre of gravity of the aircraft and hence the static margin. To investigate this phenomenon, design case 2 was formulated to determine the changes in design variables necessary to obtain a positive static margin. Using the Bradley structural mass models and applying the Hybrid method and the gradient based LSGRG2 optimisers integrated in the GMDSO Tool, the BW - 11 geometry is manipulated to obtain the results presented in the the next 2 sections.

### GA - Design Case 2

A comparison of the baseline mission and geometry variables with the results obtained using the GA optimiser is given in Table 6.27. The resulting geometry from GA optimisation for design case 2 is given in Figure 6.37.

**Table 6.27:** Comparison of the Baseline with Results Obtained Using GA for Design Case 2

| Variables | Baseline | GA |
|---|---|---|
| Fuselage Sweep [deg] | 63 | 72 |
| Wing Sweep[deg] | 38.3 | 32 |
| Dihedral section 1[deg] | 1.5 | 0 |
| Dihedral section 2[deg] | 3 | 1.13 |
| Dihedral section 3 [deg] | 3 | 0 |
| Twist section 0 [deg] | 2.8 | -0.36 |
| Twist section 1 [deg] | -0.3 | 0.7 |
| Twist section 2 [deg] | 0.5 | 3 |
| Twist section 3 [deg] | 0.9 | 1.02 |
| Twist section 4 [deg] | -2.7 | 2.43 |
| Cruise Altitude [m] | 11227.6 | 10000 |
| Cruise Mach Number [-] | 0.85 | 0.88 |
| MTOM [kg] | 481148 | 437742 |
| Stability Margin [-] | -0.02 | 0.13 |

The result presented in Table 6.27 shows wide variations between the baseline BW - 11 specifications and the obtained results. This demonstrates the GA's ability to perform a global search of feasible space. Furthermore, similar to design case 1, the result shows an increase in the fuselage sweep angle and a reduction of the wing sweep angle from the baseline. Additionally, there was a reduction in the dihedral of corresponding span stations. Combining the effect of these variables with the manipulation of the twist distribution leads to a 9% reduction in the MTOM and a change in the static margin from -2% to 13%. The change in static margin is due the effect of twist distribution on the centre of gravity of the structure and pitching moment of the configuration.

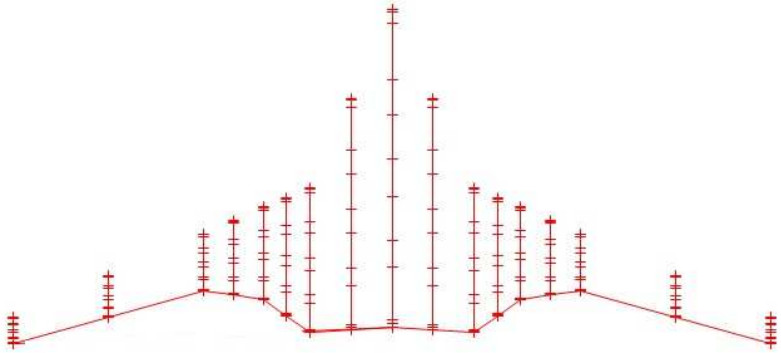

**Figure 6.37:** Geometry Obtained from Design Case 2 Using GA.

### LSGRG2 Design Case 2

Using the gradient based LSGRG2 for design case 2, the MTOM of the baseline BWB was reduced from 481148 kg to 440589 kg creating a BWB with static margin of 0.11. A comparison of the baseline and the result from the LSGRG2 is given in Table 6.28. Similar to the GA results, the results obtained from the LSGRG2 for design case 2 shows an increase in the fuselage sweep angle and a decrease in the leading edge sweep angle of the optimised geometry. With various combinations of twist, dihedral and mission variables, the MTOM decreases by about 8% while providing a positive stability margin of 11%. Consequently, it could be concluded that higher fuselage sweep angle, a reduced wing sweep and the intelligent combination of twist, dihedral and mission variables would provide a BWB aircraft with a reduced MTOM. The geometry of the BWB obtained from the LSGRG2 optimisation for design case 2 is given in Figure 6.38.

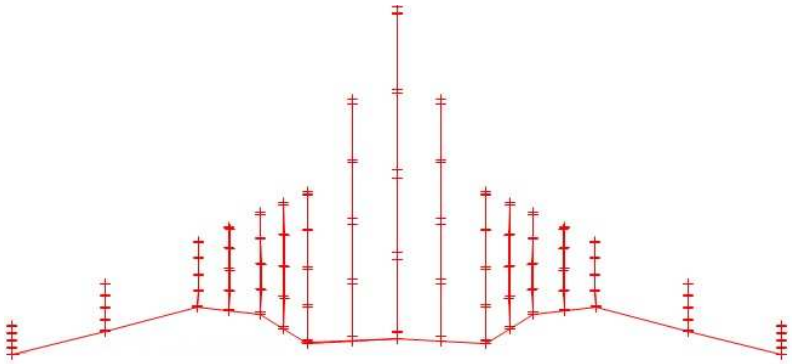

**Figure 6.38:** Geometry Obtained from Design Case 2 Using LSGRG2.

The design cases presented in this thesis were based on the NACA 4 - series airfoil. However, studies have shown that the BWB will require careful aerodynamic shaping of the centre - body using different combinations of appropriately cambered supercritical airfoil in order to satisfy conflicting aerodynamic, cruise deck angle and trim requirements

**Table 6.28:** Comparison of the Baseline with Results Obtained Using LSGRG2 for Design Case 2

| Variables | Baseline | LSGRG2 |
|---|---|---|
| Fuselage Sweep [deg] | 63 | 71 |
| Wing Sweep[deg] | 38.3 | 32.3 |
| Dihedral section 1[deg] | 1.5 | 2.17 |
| Dihedral section 2[deg] | 3 | 2.17 |
| Dihedral section 3 [deg] | 3 | 2.17 |
| Twist section 0 [deg] | 2.8 | -1.85 |
| Twist section 1 [deg] | -0.3 | -1.85 |
| Twist section 2 [deg] | 0.5 | 2.78 |
| Twist section 3 [deg] | 0.9 | -1.85 |
| Twist section 4 [deg] | -2.7 | -1.85 |
| Cruise Altitude [m] | 11227.6 | 10000 |
| Cruise Mach Number [-] | 0.85 | 0.89 |
| MTOM [kg] | 481148 | 440589 |
| Stability Margin [-] | -0.02 | 0.11 |

of the BWB. Hence, there is the need to introduce supercritical and other airfoil suite into the GMDSO Tool. This will expand the design space allowing for the investigation of the effects of different airfoils on the various characteristics of the aircraft.

## 6.4 Exploration of the Design Space

In this section the effects of different phenomena affecting the design of the BWB will be investigated and analysed. The aim of this, is to provide a design with relevant data needed to make informed design decisions in the synthesis of the BWB. Among the phenomena investigated in this research are the effects of Mach number and productivity, sensitivity of airfoil types to aerodynamic efficiency, productivity and the MTOM, effects of the camber and its position on the aerodynamic efficiency and stability of the BWB amongst several other possibilities like turbulence handling, stability characteristics as well as the field and mission performance of the BWB.

### 6.4.1 Sensitivity of Mach Number to Productivity, Aerodynamic Efficiency and Turbulence

Commercial airline operates for the purpose of conveying passenger safely to their destinations at the least cost and most profits. This is the basis for the term productivity in commercial aviation. Liebeck [1] states that it might be better to design for productivity rather than aerodynamic efficiency. Productivity and aerodynamic efficiency are defined

in terms of the Mach number by Equation 6.6 and Equation 6.7.

$$Productivity = \frac{MP}{D} \tag{6.6}$$

Where:
$M$ is the Mach number.
$P$ is the payload in $N$. $D$ is the aerodynamic drag in $N$.

$$Eff = \frac{ML}{D} \tag{6.7}$$

Similarly,
$M$ is the Mach number.
$L$ is the lift in $N$.
$D$ is the aerodynamic drag in $N$.

Applying the foregoing equations to the BW - 11 test aircraft with NACA 4 digit airfoil profiles having 4 percent camber located at the 40 percent chord position and appropriate thickness and varying the Mach number from M0.8 to M0.92 in steps of 0.02 using the GMDSO Tool, the plot shown in Figure 6.43 is obtained. The Figure 6.43 shows the variations of Mach number with productivity and aerodynamic efficiency. It could be seen from the plot that productivity decreases linearly with increasing Mach number while the aerodynamic efficiency showed a non - linear variation with increasing Mach number. Maximum productivity of 1.5 was obtained at M0.8 while maximum aerodynamic efficiency of 1.82 was derived at M0.87.

Maximum productivity implies low fuel consumption due to low drag and hence increased range or payload capacity. This indicates that the maximum aerodynamic efficiency might not always be economically beneficial. Consequently, while the BWB is well suited to fly at high Mach number due to the natural area ruling of the configuration, high speed might not necessarily be the best option. This is due to the reduced productivity and lower efficiency at very high speeds. Hence, design decisions about speed must not only be based on aerodynamics efficiency but also on productivity considerations, stability and turbulence handling. Also, the plot shows that the best aerodynamic performance is obtained between M0.84 and 0.88 as observed from the increase in $ML/D$. The reduced aerodynamic efficiency beyond Mach 0.88 could be due to wave drag rise resulting from transonic effects.

Now, applying Agenberg and Theron [150] criteria to the BW - 11, the variations of tur-

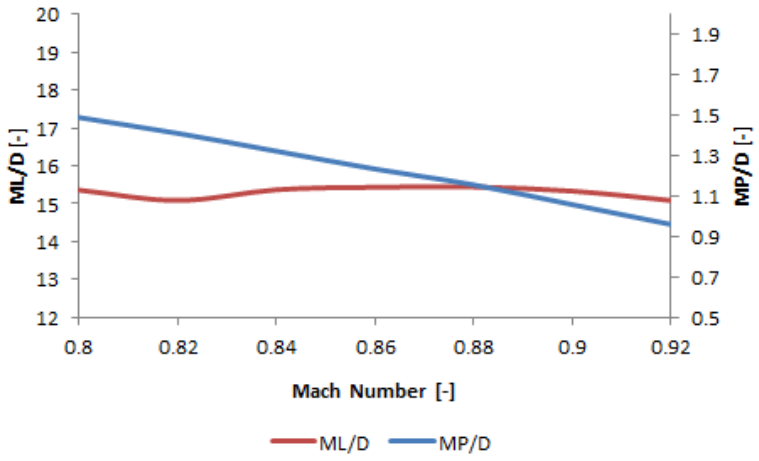


**Figure 6.39:** Sensitivity of Mach Number to Productivity and Aerodynamic Efficiency.

bulence handling characteristics with Mach number is obtained as given in Figure 6.40. The plot shows a decreasing negative value and hence a reduction in turbulence handling capacity with increase in Mach number. This implies that high speed will increase the sensitivity of the aircraft to turbulence and subsequently minimises passenger comfort and ride quality.

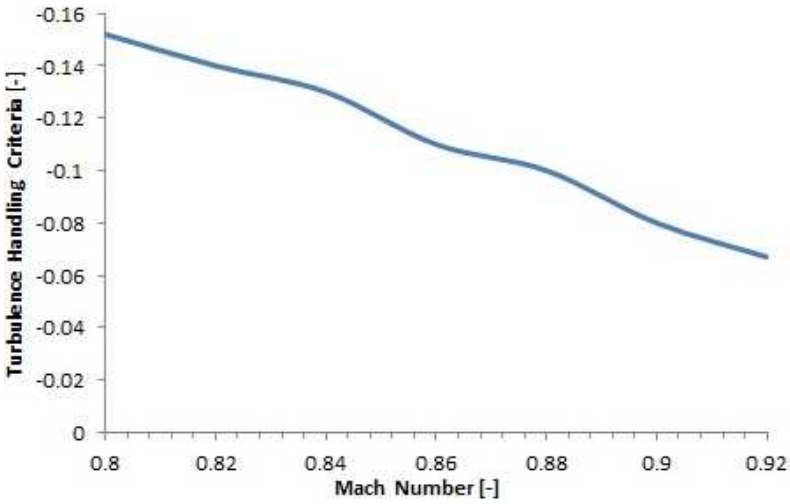


**Figure 6.40:** Sensitivity of Mach Number to Turbulence Handling

The test geometry was subsequently assessed for effects of speeds on the static margin. The result shows an improvement in static margin with increasing Mach number as shown in Figure 6.41. This is due to the increased lift coefficient derived with increase in Mach number causing a rearward shift in the aerodynamic centre of the aircraft thus improving the static margin or making it more positive. This behaviour is corroborated by a com-

parison of the static margin of F - 14A and the F - 111 shown in Figure 6.42. The result shows an increase in static margin with Mach number in the subsonic region as obtained for the BW - 11.

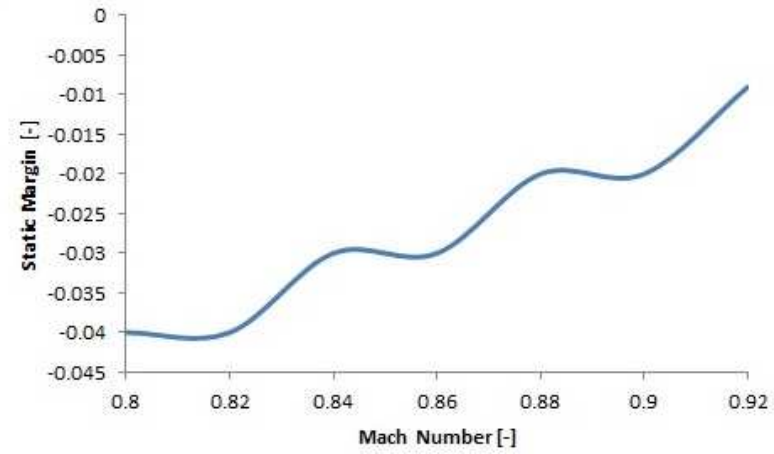


**Figure 6.41:** Sensitivity of Mach Number to Static Margin

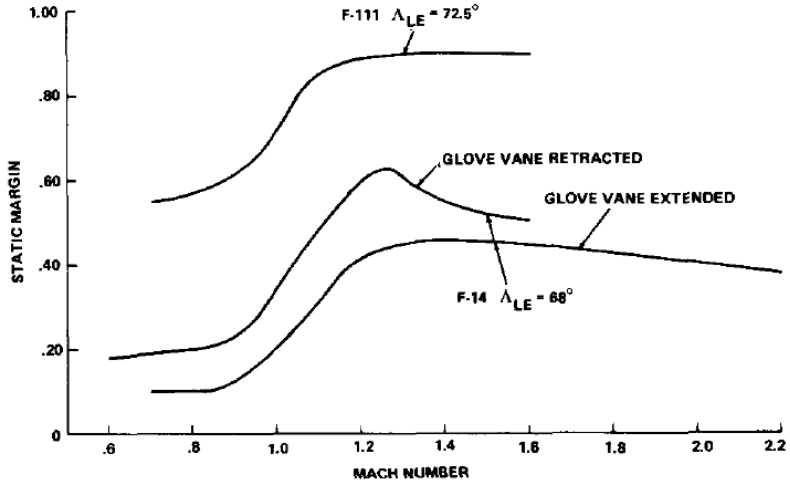


**Figure 6.42:** Comparison of the Static Margin of the F -14 A and F - 111

A review of the sensitivity of Mach number to productivity, aerodynamic efficiency, turbulence handling and static margin highlights the strong interdisciplinary coupling on the BWB aircraft and the need for a multi - variate optimisation in the design synthesis. It is envisaged that the integration of multi - variate optimisation techniques in the GMDSO Tool will enable a knowledgeable users create the desired BWB that is commercially profitable as well as provides good stability with reduced sensitivity to turbulence.

### 6.4.2 Sensitivity of Maximum Camber to Productivity, Aerodynamic Efficiency, Static Margin and Turbulence

The GMDSO Tool contains a suite of NACA 4 digit airfoils. In the NACA four digit numbering system, the first digit represents the maximum camber in percentage of chord, the second digit is the position of the maximum camber from the leading edge in tenths of chord while the third and fourth digit refers to maximum thickness in percentage of chord. The airfoil profile affects the aerodynamic efficiency, stability, turbulence handling and productivity of the BWB aircraft. Consequently, it was necessary to investigate how the various features of the 4 digit NACA airfoil affects the relevant characteristics of the BWB airfoil. The thickness of the airfoil is set by the volume requirements of the aircraft, though it could be manipulated in the packaging module. Consequently, maintaining the given thickness to chord ratio and positioning the airfoil maximum camber at the 40% chord position from the airfoil leading edge, the maximum camber is varied from 0 - 9 percent in increments of 1%. The results obtained from this sensitivity study is given in Table 6.29.

**Table 6.29:** Effect of Variations in Maximum Camber

| Max. Camber [% Chord] | ML/D | MP/(D) | Static Margin [-] | Turbulence Handling [-] |
|---|---|---|---|---|
| 0 | 7.99 | 4.62 | -0.034 | -0.13 |
| 1 | 15.45 | 3.60 | -0.033 | -0.125 |
| 2 | 17.58 | 2.56 | -0.033 | -0.124 |
| 3 | 17.01 | 1.8 | -0.032 | -0.122 |
| 4 | 15.57 | 1.3 | -0.032 | -0.122 |
| 5 | 14.38 | 0.98 | -0.032 | -0.121 |
| 6 | 12.61 | 0.73 | -0.031 | -0.11 |
| 7 | 10.15 | 0.45 | -0.030 | -0.12 |
| 8 | 10.25 | 0.46 | -0.030 | -0.12 |
| 9 | 9.37 | 0.37 | -0.030 | -0.12 |

Plotting the values of the maximum camber against the aerodynamic efficiency (ML/D) and the productivity (MP/D) gives Figure **??**. The Figure **??** shows a decreasing productivity with increase in camber. Maximum productivity is obtained with a symmetric airfoil or 0% camber while the aerodynamic efficiency is highest at 2% camber. Subsequently, the aerodynamic efficiency and productivity decreases as maximum camber increases. Hence, it could be seen that 2% provides the most gains in terms productivity and aerodynamic efficiency.

In terms of stability and turbulence handling, the plot of the static margin and the measure of turbulence handling against maximum camber is shown in Figure 6.44. The Figure

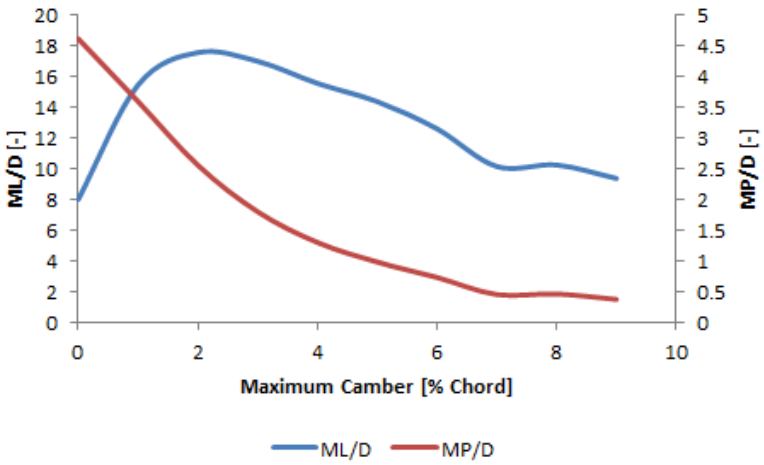


**Figure 6.43:** Sensitivity of ML/D and MP/D to Maximum Camber

indicates that the aircraft have good turbulence handling characteristics irrespective of the airfoil's maximum camber. Additionally, the 4 - digit NACA airfoil applied on the BWB tailless aircraft yields unstable aircraft at all cambers as variations of the camber always give a negative static margin. The static margin is improved with increasing camber as the static margin tends towards positive value with increasing camber, levelling off at the 7% camber onwards.

The turbulence handling characteristics on the other hand is marginally deteriorated as it becomes less negative with increase in maximum camber. Also just like in the case of static margin, the turbulence handling characteristic is diminished until the 7% camber position where it remains steady at -0.12. There is therefore only a negligible change in static margin and turbulence handling with increase in maximum camber. It could thus be concluded that the maximum camber of NACA 4 - digit airfoil, positioned at 40 percent chord position from the airfoil leading edge has only a minimal impact on the turbulence handling characteristics and static margin.

Having investigated the effect of the airfoil's maximum camber on the BWB aerodynamic efficiency, productivity as well as the stability and turbulence handling, it was necessary to vary the positions of the maximum camber in order to establish if they have any effect on the investigated aerodynamic and stability characteristics. Consequently, varying 2% maximum camber from 10 - 90% chord position, the results given in Table 6.30 is obtained.

The Table 6.30 shows that all camber positions give unstable aircraft with good turbulence handling characteristics. There is also a negligible difference in the static margin

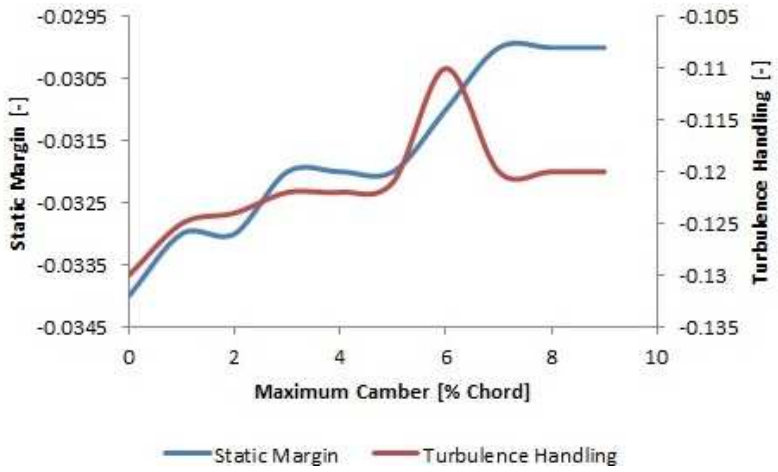


**Figure 6.44:** Sensitivity of Static Margin and Turbulence Handling Characteristics to Maximum Camber

**Table 6.30:** Effect of Variations in the Position of 2% Maximum Camber

| Position of Max. Camber [% Chord] | ML/D | MP/D | Static Margin [-] | Turbulence Handling [-] |
|---|---|---|---|---|
| 0.1 | 13.69 | 2.43 | -0.033 | -0.125 |
| 0.2 | 17.18 | 2.89 | -0.033 | -0.124 |
| 0.3 | 17.35 | 2.74 | -0.033 | -0.124 |
| 0.4 | 17.36 | 2.53 | -0.033 | -0.124 |
| 0.5 | 17.34 | 2.31 | -0.033 | -0.124 |
| 0.6 | 16.95 | 2.01 | -0.033 | -0.123 |
| 0.7 | 16.20 | 1.67 | -0.032 | -0.123 |
| 0.8 | 14.83 | 1.24 | -0.032 | -0.123 |
| 0.9 | 11.77 | 0.70 | -0.031 | -0.120 |

and turbulence handling characteristics of the aircraft with increasing maximum camber position. However, this is not the case with productivity and aerodynamic efficiency of the aircraft. A plot of the positions of 2% maximum camber against the aerodynamic efficiency and productivity is given in Figure 6.45.

The Figure 6.45 shows that maximum aerodynamic efficiency is obtained when maximum camber is positioned at 40%. However, maximum productivity occurs with the maximum camber at the 20% chord position. Nonetheless, both characteristics tended to decrease after first rising to their maximum values. It could therefore be concluded that minimal aft camber is necessary to obtaining maximum productivity and higher aerodynamic efficiency with the 2% maximum camber NACA 4 - digit airfoil.

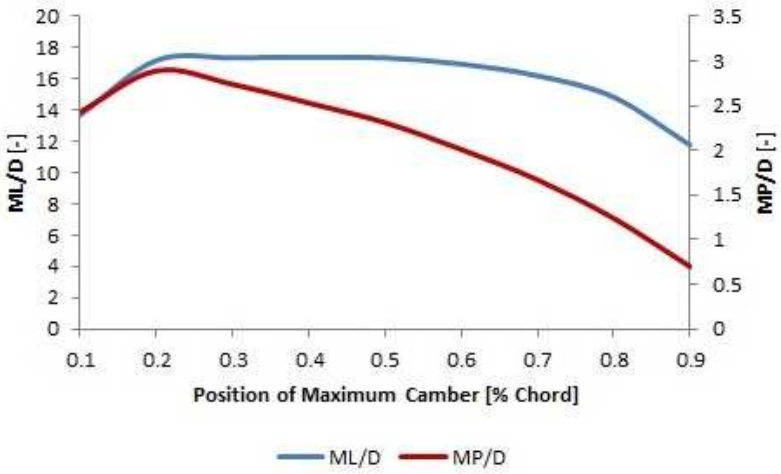


**Figure 6.45:** Sensitivity of the Position of Maximum Camber on Aerodynamic Efficiency and Aircraft Turbulence Handling Characteristic

### 6.4.3 Effect of Centre -Body Sweep on Aerodynamic Characteristics of the BWB Centre - Body

Siouris and Qin [45] studied the effect of outer wing sweep on the aerodynamic performance of the BWB but did not consider the effect of the sweep of the centre - body. Since, the BWB is often modelled as a wing, it was considered necessary to also investigate the effect of sweep of the centre - body(fuselage) on the aerodynamic characteristics of the BWB aircraft. Consequently, varying the centre - body sweep angles from 45 to 75° in steps of 5° while keeping the outer wing sweep angle constant at 38.3 ° and maintaining a constant cruise Mach number of 0.85, the aerodynamic characteristics of the BW - 11 (test aircraft) were determined at zero degree AoA. The results of the study is shown in Figures 6.46, 6.47, and 6.48.

The plots show that the lift and drag coefficients decrease with increase in the centre - body sweep angles, but the aerodynamic efficiency $ML/D$ increases. This trend favours the use of higher sweep angles on the centre - body thus explaining the usual high sweep angles observed on BWB centre - body. However, it ought to be noted that increase in centre - body sweep angles is accompanied with corresponding extension in the length of the centre - body, in order to accommodate the given number of passengers. Consequently, decision on the appropriate sweep angle for the centre - body needs to be made with due assessment of the impact of the resultant increase in length on the desired aircraft performance indicators.

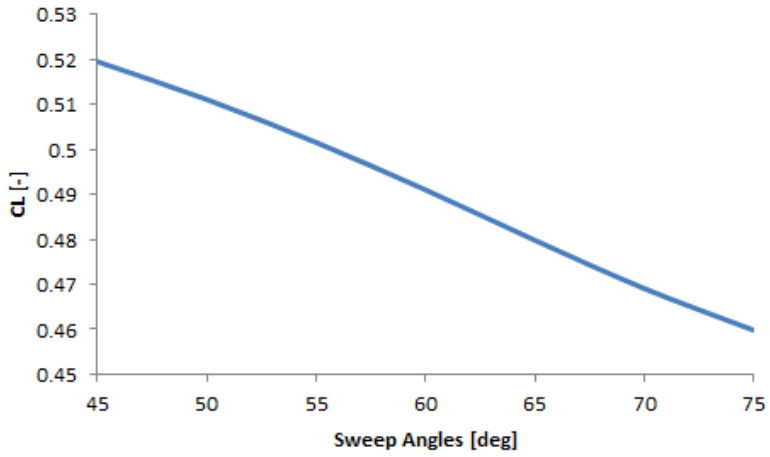


**Figure 6.46:** Variation of Lift Coefficients with Sweep Angles at M0.85 and 0° AoA.

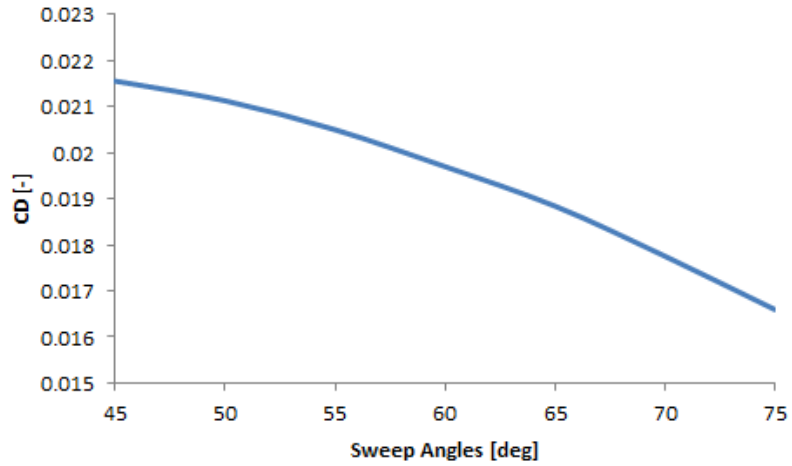


**Figure 6.47:** Variation of Drag Coefficients with Sweep Angles at M0.85 and 0° AoA.

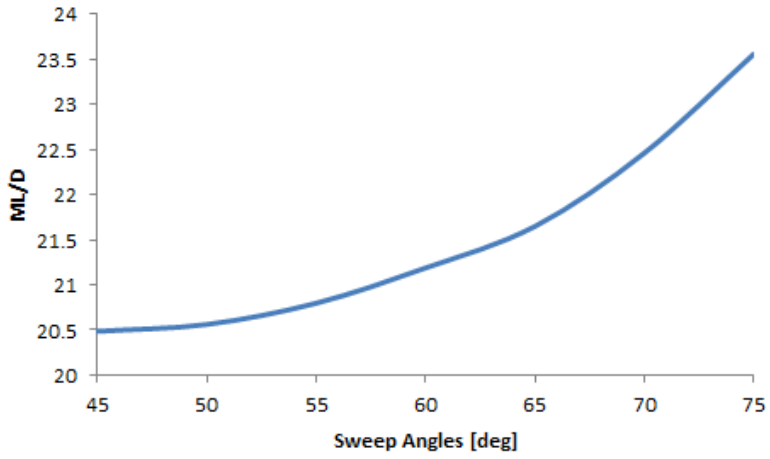


**Figure 6.48:** Variation of $\frac{ML}{D}$ with Sweep Angles at M0.85 and 0° AoA.

## 6.5 Chapter Summary

This chapter presents some of the applications of the developed GMDSO Tool in the design synthesis, optimisation and exploration of the design space of the BWB. The first sets of applications isolated and tested individual modules and compared the results with a test aircraft, the BW - 11, to ascertain the degree of accuracy of its results. This is the quasi - validation of the developed tool. The results obtained from this process compares closely with the data given in the BW -11 specification document and validates the accuracy of the models implemented in the GMDSO Tool. Subsequently, some test cases with different objective functions, design variables and constraint(s) were implemented in a multivariate optimisation to demonstrate the capability and robustness of the design tool. The exploration of the design space was performed next through various sensitivity studies to understand the impact of different design drivers on the characteristics of the BWB aircraft. The results maintained a high level of consistency with the test aircraft and other results from different studies.

# Chapter 7

# Conclusions and Recommendations for Further Work

This research develops a flexible user driven tool for the conceptual design synthesis and optimisation of the BWB aircraft. The GMDSO Tool couples a geometry parameterisation packaging model, vortex lattice aerodynamic model and a Class II Component weight estimation methods incorporating BWB - specific structural mass model to create a multivariate design synthesis optimisation tool nicknamed GENUS. The GMDSO Tool enables a knowledgeable user to rapidly perform the conceptual design synthesis and exploration of the design space of the BWB aircraft. Though, the complete GMDSO tool is created by a team of researchers, the author is wholly responsible for the development and integration of all modules involving the BWB. Additionally, the author is solely responsible for extending the functionalities of the AVL and the creation of the parametric based packaging module. However, the development of the GENUS framework on which the individual aircraft synthesis is performed is a group effort, with the author making significant contribution in shaping the platform. This Chapter presents the principal findings from the research objectives, the research's contributions to knowledge, limitations of the study and recommendations for future work followed by the author's publications.

## 7.1 Principal Findings From the Research Objectives

### 7.1.1 Develop Algorithms for the Estimation of Several Variables within an Aircraft Design Synthesis

In order to develop a design synthesis tool, algorithms for the estimation of disciplinary variables and enabling inter - disciplinary interactions were developed. These algorithms were developed from a mixture of legacy codes and JAVA coded analytical and empirical models. The systematic integration of these algorithm enables the creation of the BWB aircraft and the investigation of coupled effects on the design. Additionally, the algorithm allows for the estimation of several variables rather than the usual assumption used in conceptual design. The algorithms developed in the GMDSO Tool include BWB specific structural mass estimation, physics - based aerodynamic analysis , stability and performance evaluation and packaging incorporating volume constraint handling. The algorithm allows for the design synthesis and exploration of the design space of the BWB.

### 7.1.2 Incorporate Packaging Module Early in the Conceptual Design Process

Packaging module was incorporated into the GMDSO Tool using the CST parameterisation technique and geometry scaling. The need to integrate packaging early in the conceptual design stage was necessary due to the non - uniform cross - section of the BWB aircraft. This increases the requirements to ensure there is sufficient space within the BWB geometry to prevent interference and accommodate internal objects. Additionally, packaging enables the creation of an aircraft with realistic and acceptable static margin to improve controllability and reduce pilot workload. Furthermore, integrating packaging into the design tool eliminates interference between internal objects and the geometry thereby minimising costly geometry redesign later in the design process. However, it highlights the need for aerodynamic shape design optimisation and the need to extend the airfoil suite of the aerodynamic model to include CST derived airfoils.

### 7.1.3 Create a multi-variate optimisation tool to rapidly perform the conceptual design synthesis and analysis of the BWB commercial passenger aircraft

The research set out to create a multi - variate optimisation tool to perform the conceptual design synthesis and analysis of the BWB. This task is accomplished by integrating 3 optimisers into the GMDSO Tool. These optimisers are the gradient based LSGRG2, the non - gradient GA and the internally coded Hybrid gradient/non - gradient PDGenetic

optimiser. The computational efficiency and accuracy of the optimizers varies. The gradient - based LSGRG2 optimiser is the only deterministic method while the others are based on a random search process. However, the GA and the Hybrid both yields global optima while the LSGRG2 has a tendency of being locked in a local minima. Nevertheless, the Hybrid optimiser is the most accurate method with the least margin of error while the GA produces results with the most absolute difference between the design variable and the set objective. Using these optimisers, design improvements can be made to a BWB through a careful definition of design problems involving appropriate objective function and relevant constraints.

### 7.1.4 Explore the design space of a BWB aircraft configuration

This research explores the BWB design space by sensitivity analysis investigating the impact of design drivers on different aircraft characteristics. The results obtained highlights the highly coupled nature of the BWB and the non - linear behaviour of different design drivers to different aircraft characteristics. This consolidates the application for the application of a multi - variate design optimisation technique in the synthesis of the BWB aircraft. With an infinite design space of the BWB configuration, only a limited number of cases to demonstrate the capability and application of the developed tool were explored.

## 7.2 Contributions to Knowledge

This research provides the following significant contributions to knowledge:

1. A novel, robust, flexible conceptual design software to support the iterative and unique process of the design of a Blended Wing Body aircraft. This tool couples physics based vortex lattice aerodynamics analysis model with BWB - specific structural mass module and the CST parameterisation packaging into a multivariate conceptual design synthesis tool for the rapid design and exploration of the design space of the BWB aircraft.

2. Algorithms for the accurate estimation of several variables within a design synthesis rather than relying on assumed values thus providing a more realistic design.

3. Expanded physics based vortex lattice software, AVL, with added functionality for automated multi - speed, multi - angles of attack aerodynamic analysis of aircraft in a multivariate design environment.

4. A compendium of evolving trends in the design of the BWB aircraft to provide handy reference that will enable designers to quickly understand and select the most appropriate concepts and systems in the design synthesis of the BWB, without reviewing large volumes of literatures.

5. An easy to use design environment which enables interaction between a knowledgeable user and the design process while allowing for extension to other aircraft class.

## 7.3 Limitations of the Research

The absence of any reliable data of a BWB commercial passenger transport aircraft limits the validation of the developed Tool to quasi - validation using information from the Cranfield BWB research project. Though the result obtained from the Tool compares favourably with the Cranfield designed BW - 11, it needs to be subjected to real or near - real life conditions in order to fully affirm its validity. The development of a scaled model subjected to wind - tunnel test will provide a more reliable data for validation of modules within the GMDSO Tool.

Also, this research involves a lot of coding and integration of 3 different programming languages, JAVA, FORTRAN and C++. In the design and development of the GMDSO, efforts have been made to ensure the tool meets a very high standard. Nevertheless, it is envisaged that it could still fall short of the standard of a professional programmer which could affect the efficiency and program runtime. It might thus be useful if a programmer is recruited to arrange the codes and program design in a most efficient way.

## 7.4 Recommendations for Future Work

The GMDSO Tool is developed as a design suite for the conceptual design synthesis of the BWB Aircraft. Though it is reasonably equipped with most of the models appropriate for conceptual design synthesis, there is still room for improvement. Potential modification that could enhance the applications of the GMDSO Tool are:

- Extension of the airfoil suite to include airfoils created from the CST geometry parameterisation implemented in the packaging module, supercritical airfoils and other tailless non - NACA airfoils.

- Modification of the the physics - based aerodynamics tool to integrate or accept non - NACA airfoils. This modification extends the design space and allow for better assessment of the stability of the aircraft.

- Couple the aerodynamics and packaging modules with the optimisers to perform aerodynamic shape design optimisation.
- At the moment only one core is running, and the program can easily be overwhelmed by a complex optimization task. Hence, there is the need for the program to be run on parallel cores to reduce computational time. This will increased the number of design cases that could be investigated therefore enabling better exploration of the design space.
- The GUI could be significantly improved to include some form of analytics for the optimiser including number of runs, plots of variations of constraints and objective functions, number of iterations and duration of the optimisation.
- The GMDSO Tool employs a free plotting software, the gnuplot. The gnuplot is integrated in the GMDSO Tool as a geometry viewer. Currently, the viewer displays the geometry by wireframes. This could be updated to display polygons in order to enable better displays. Additionally, the geometry could be linked to the CATIA software to provide additional functionalities in geometry representation.
- The GMDSO Tool permits only the implementation of single objective optimisation using continuous variables. Multi-objective optimization should be implemented to increase the options of design cases that could be investigated. Additionally, the optimiser could be improved to enable discrete optimisation.
- Incorporate advanced technologies to the design synthesis tool.
- Consider the impact of technology reduction factors on mass models.

## 7.5 Publications

### 7.5.1 Journal Paper

1. P. Okonkwo and H. Smith, Review of Evolving Trends in Blended Wing Body Aircraft Design, Progress in Aerospace Sciences (2016), http://dx.doi.org/10.1016/j.paerosci.2015.12.002i.

### 7.5.2 Conference Paper

1. P. Okonkwo and H. Smith, Packaging in a Multivariate Conceptual Design Synthesis of the Blended Wing Body Aircraft, International Journal of Mechanical, Aerospace, Industrial and Mechatronics Engineering Vol:8 No:6, 2014.

# References


[1] RH. Liebeck. Design of the Blended Wing Body Subsonic Transport. *Journal of Aircraft*, 41(1):10–25, 2004.

[2] H Smith. College of Aeronautics Blended Wing Body Development Programme. *ICAS Congress*, pages 1–10, 2000.

[3] S Mistry. *A Novel Airframe Design Methodology for Novel Aircraft*. PhD thesis, Cranfield University, 2009.

[4] Al Bowers. Blended Wing Body: Design Challenges for the 21st Century. *The Wing is the Thing(TWITT) Meeting, NASA Dryden Flight Research Center. September 2000.*, 2000.

[5] R Martinez-Val, C Cuerno, E Perez, and HH Ghigliazza. Potential Effects of Blended Wing Bodies on the Air Transportation System. *Journal of Aircraft*, 47 (5):1599–1604, September 2010. ISSN 0021-8669. doi: 10.2514/1.C000214.

[6] R Martinez-Val, Perez J Perez, E and, and JF Palacin. Optimising Flying Wings. In *25th International Congress of the Aeronautical Sciences (ICAS)*, 2006.

[7] TA Zang and LL Green. Multidisciplinary Design Optimization Techniques: Implications and Opportunities for Fluid Dynamics Research. In *30th AIAA Fluid Dynamics Conference*, 1999.

[8] R Martinez-Val. Flying Wings . A New Paradigm for Civil Aviation ? *Acta Polytechnica*, 47(1), 2007.

[9] R Martinez-Val, E Pérez, P Alfaro, and J Pérez. Conceptual Design of a Medium Size Flying Wing. *Proceedings of the Institution of Mechanical Engineers, Part G: Journal of Aerospace Engineering*, 221(1):57–66, January 2007. ISSN 0954-4100. doi: 10.1243/09544100JAERO90.

[10] A Ko, LT Leifsson, WH Mason, JA Schetz, and B Grossman. MDO of a Blended-Wing-Body Transport Aircraft with Distributed Propulsion. In *AIAA's 3rd Annual Aviation Technology Integration and Operations (ATIO) Technical Forum, Denver, Colorado*, number 6732, pages 1–11, 2003.

[11] RM Wood and Bauer SXS. Flying Wing/Flying Fuselage. Number AO1-16217, 2001.

[12] M Statzer, B Williams, and M Zauberman. Flying Wing. 2003.

[13] NU Rahman. *Propulsion and Flight Controls Integration for the Blended Wing Body Aircraft*. PhD thesis, School of Engineering, Cranfield University, 2009.

[14] JM Bruce. Dunne D.8 at Farnborough 11 March 1914. Technical report, Aeroplanes of the Royal Flying Corps, 1992.

[15] AH Lukins. Westland Pterodactyl V. In *The Book of Westland Aircraft*. http://www.aviastar.org/air/england/west_pterodactyl5.php, 1943.

[16] T Ikeda. Aerodynamic Analysis of a Blended-Wing-Body Aircraft. Master's thesis, School of Aerospace, Mechanical and Manufacturing Engineering, Science and Technology, RMIT University, Melbourne Australia, 2006.

[17] E Torenbeek. *Advanced AircrafAirplane: Conceptual Design, Analysis and Optimisation of Subsonic Civil Airplanes, First Edition*. John Wiley and Sons Limited, 2013.

[18] T Wan and B Song. Aerodynamic Performance Study of a Modern Blended-Wing-Body Aircraft Under Severe Weather Situations. In *49th AIAA Aerospace Sciences Meeting Including the New Horizons Forum and Aerospace Exposition*, pages 1–10, 2011.

[19] D Howe. Blended Wing Body Airframe Mass Prediction. *Proceedings of the Institution of Mechanical Engineers, Part G: Journal of Aerospace Engineering*, 215(6): 319–331, 2001. ISSN 0954-4100. doi: 10.1243/0954410011533329.

[20] L.T. Leifsson. *Multidisciplinary Design Optimization of Low-Noise Transport Aircraft*. PhD thesis, Virginia Polytechnic Institute & State University Blacksburg, VA 24061-0203, 2005.

[21] M D Guynn, JE Freh, and ED Olson. Evaluation of a Hydrogen Fuel Cell Powered Blended-Wing-Body Aircraft Concept for Reduced Noise and Emissions. *NASATM2004212989*, (February), 2004.

[22] M Kozek and A Schirrer, editors. *Modelling and Control for a Blended Wing Aircraft - A Case Study*. Springer, 2015.

[23] A Morris, P Arendsen, G LaRocca, M Laban, R Voss, and H Honlinger. MOB - A European Project on Multidisciplinary Design Optimisation. In *24th International Congress of the Aeronautical Sciences*, 2004.

[24] AJ Morris. MOB- A European Distributed Multi-Disciplinary Design and Optimisation Project . *Optimization*, (September):1–10, 2002.

[25] M Laban, P Arendsen, WFJA Rouwhorst, and WJ Vankan. A Computational Design Engine for Multidisciplinary Optimisation with Application to a Blended Wing Body Configuration. Technical Report NLR-TP-2003-193, NLR, 2002.

[26] NACRE. Final Activity Report 2005 -2010. Technical report, Sixth Framewirk programme Priority 4 Aeronautics and Space, 2011.

[27] JI Hileman, ZS Spakovszky, and M Drela. Airframe Design for Silent Aircraft. *AIAA paper*, pages 1–15, 2007.

[28] ZS Spakovszky. Toward a Silent Aircraft Goals. In *22nd Symposium on Aviation Noise and Air Quality*, 2007.

[29] J.J. Lee, S.P Lukachko, I.A. Waitz, and A. Schafer. Historical and Future Trends in Aircraft Performance, Cost and Emissions. *Annu. Rev. Energy Environ., Vol. 26, pp. 167200*, 2001.

[30] D Paulus, T Salmon, B Mohr, C Roessler, F Stroscher, Baier H, and M Hornung. Configuration Selection for a 450 Passenger Ultra -Efficient 2020 Aircraft. *Progress in Flight Dynamics, GNC and Avionics 6*, 2013.

[31] YA Ko. *The Multidisciplinary Design Optimisation of a Distributed Propulsion Blended-Wing-Body Aircraft.* PhD thesis, Virginia Polytechnic Institute and State University, 2003.

[32] H Smith. Advanced Blended Wing Body High Capacity Airliner BW-11 Project Specification. Technical report, Cranfield Universiy, Department of Aerospace Engineering, Aerospace Design Group, 2011.

[33] T Wan and H Yang. Aerodynamic Performance Investigation of a Modern Blended-Wing-Body Aircraft Under the Influence of Heavy Rain Condition. In *27th International Congress of the Aeronautical Sciences*, pages 1–11, 2010.

[34] N Qin, A Vavalle, A Le Moigne, M Laban, K Hackett, and P Weinerfelt. Aerodynamic Studies for Blended Wing Body Aircraft. In *9th AIAA/ISSMO Symposium on Multidisciplinary Analysis and Optimization 4-6 September 2002, Atlanta, Georgia*, number AIAA-2002-5448, pages 1–11, 2002.

[35] Y Staelens, R Blackwelder, and M Page. Novel Pitch Control Effectors for a Blended Wing Body Airplane in Takeoff and Landing Configuration. *AIAA paper*, pages 1–13, 2007.

[36] L.A Moreno, R.S Palma., and L.P Pascual. Aerodynamic Study of a Blended Wing Body; Comparison With A Conventional Transport Airplane. In *ICAS 2006 25TH INTERNATIONAL CONGRESS OF THE AERONAUTICAL SCIENCES*, 2006.

[37] A Valiyff. An investigation into the Aerodynamic Efficiency of Tailless Aircraft. *AIAA Aerospace Sciences*, pages 1–9, 2009.

[38] JI Hileman, ZS Spakovszky, and M Drela. Aerodynamic and Aeroacoustic Three-Dimensional Design for a a Silent Aircraft. *44th AIAA Aerospace*, pages 1–15, 2006.

[39] JI. Hileman, ZS. Spakovszky, M. Drela, MA Sargeant, and A Jones. Airframe Design for Silent Fuel-Efficient Aircraft. *Journal of Aircraft*, 47(3):956–969, May 2010. ISSN 0021-8669. doi: 10.2514/1.46545.

[40] NB Kuntawala. Aerodynamic Shape Optimization of a Blended-Wing-Body Aircraft Configuration. Master's thesis, Department of Aerospace Engineering, University of Toronto, 2011.

[41] PF Roysdon and K Mahmood. Lateral-Directional Stability Investigation of a Blended-Wing Body. In *10th AIAA Aviation Technology, Integration and Operation Conference*, 2010.

[42] RH Liebeck. Blended Wing Body Design Challenges. *AIAA*, (AIAA 2003-2659): 1–12, 2003.

[43] D Roman, R Gilmore, and S Wakayama. Aerodynamics of High Subsonic Blended-Wing-Body Configurations. *AIAA*, (AIAA 2003-554):1–9, 2003.

[44] JE Green, JP Fielding, J McClarty, K Mitchel, KDR Manns, PJ Newton, J Lee, CJ Hume, WN Dawes, M Davies, and RV Cottington. Greener by Design-The Technology Challenge. 2002. doi: http://dx.doi.org/10.1108/aeat.2001.12773fac.001.

[45] S Siouris and N Qin. Study of the Effects of Wing Sweep on the Aerodynamic Performance of a Blended Wing Body Aircraft. *Proceedings of the Institution of Mechanical Engineers, Part G: Journal of Aerospace Engineering*, 221(1):47–55, January 2007. ISSN 0954-4100. doi: 10.1243/09544100JAERO93.

[46] D Crichton, ED Blanco, TR. Law, and JI. Hileman. Design and Operation for Ultra Low Noise Takeoff. In *45th AIAA Aerospace Sciences Meeting and Exhibit.*, volume 456, pages 1–18, 2007.

[47] M Stettner and R Voss. Aeroelastic, Flight Mechanics and Handling Qualities of the MOB BWB Configuration. *9th AIAA/ISSMO Symposium and Exhibit on Multidisciplinary Analysis and Optimization, Atlanta, GA, USA, 4-6 September*, (2002-5449):1–10, 2002.

[48] RL Campbell, MB. Carter, OC. Pendergraft Jr, DM. Friedman, L Serrano, and BP. Works. Design and Testing of a Blended Wing Body with Boundary Layer Ingestion Nacelles at High Reynolds Numbers. In *Proc Conference of the 43rd AIAA Aerospace Sciences Meeting*, pages 1–27, 2005.

[49] GA. Hill and RH. Thomas. Challenges and Opportunities for Noise reduction through Advanced Aircraft Propulsion Airframe Integration and Configurations. In *8th CEAS Workshop: Aeroacoustics of New Aircraft and Engine Configurations, Budapest, Hungary*, pages 1–13, 2004.

[50] DJ. Thompson, J Feys, DF. Michael, S. Abdel-Magid, D Dalli, and F Goto. The Design and Construction of a Blended Wing Body UAV. In *49th AIAA Aerospace Sciences Meeting Including the New Horizons Forum and Aerospace Exposition*, pages 1–11, 2011.

[51] M Voskuijl, G La-Rocca, and F Dircken. Controllability of Blended Wing Body Aircraft. *28th International Congress of the Aeronautical Sciences, 2008*, 2008.

[52] RK Nangia and ME Palmer. Flying Wings ( Blended Wing Bodies ) With Aft And Forward Sweep, Relating Design Camber and Twist to Longitudinal Control. *AIAA Journal*, (August):1–12, 2002.

[53] YD Staelens. *Study of Belly-flaps to Enhance Lift and Pitching Moment Coefficient of a Blended Wing-body Airplane in Landing and Takeoff Configuration.* PhD thesis, Faculty of the Graduate School University of Southern California, 2007.

[54] A Wildschek, T Havar, and K Plötner. An All-composite, All-Electric, Morphing Trailing Edge Device for Flight Control on a Blended-Wing-Body Airliner. *Proceedings of the Institution of Mechanical Engineers, Part G: Journal of Aerospace Engineering*, 224(1):1–9, January 2010. ISSN 0954-4100. doi: 10.1243/09544100JAERO622.

[55] SH. Cho, C Bil, and J Bayandor. BWB Military CargoTransport Fuselage Design and Analysis. In *26th Congress of the international Council of the Aeronautical Sciences (ICAS)*, pages 1–7. International Council of the Aeronautical Sciences, 2008.

[56] SH. Cho, C Bil, and J. Bayandor. Structural Design and Analysis of a BWB Military Cargo Transport Fuselage. In *RMIT University, AIAA-2008-165, 46th AIAA Aerospace Sciences Meeting and Exhibit, Reno, Nevada*, pages 1–10, 2008.

[57] DW Jung and MH Lowenberg. Stability and Control Assessment of a Blended-Wing-Body Airliner Configuration. In *AIAA Atmospheric Flight Mechanics Conference and Exhibit*, pages 1–19, 2005.

[58] LU Hansen, W Heinze, and P Horst. Blended Wing Body Structures in Multidisciplinary Pre-design. *Structural and Multidisciplinary Optimization*, 36(1):93–106, 2008. ISSN 1615147X.

[59] SH Cho, C Bil, and J. Bayandor. Design and Analysis of BWB Military Cargo Centre Body Structure. *AIAA*, pages 1–9, 2011.

[60] V Mukhopadhyay, I Kosaka, G Quinn, and C Charpentier. Analysis, Design and Optimization of Non-cylindrical Fuselage for Blended-Wing-Body ( BWB ) Vehicle . In *9th AIAA / ISSMO Symposium on Multidisciplinary Analysis and Optimization Atlanta , GA*, number AIAA 2002-5664, pages 0–9, 2002.

[61] V Mukhopadhyay. AIAA 2005-2349 Blended-Wing-Body ( BWB ) Fuselage Structural Design for Weight Reduction 46th AIAA / ASME / ASCE / AHS / ASC Structures , Structural Dynamics and Materials Conference. *Design*, pages 18–21, 2005.

[62] N Qin, A Vavalle, A Lemoigne, M Laban, K Hackett, and P Weinerfelt. Aerodynamic Considerations of Blended Wing Body Aircraft. *Progress in Aerospace Sciences*, 40(6):321–343, 2004. ISSN 03760421. doi: 10.1016/j.paerosci.2004.08.001.

[63] KR Bradley. A Sizing Methodology for the Conceptual Design of Blended Wing Body Transports. Technical report, NASA, 2004.

[64] CL Nickol. Silent Aircraft Initiative Concept Risk Assessment. Technical Report February, 2008.

[65] AJ Diedrich, J Hileman, D Tan, K Willcox, and Z Spakovszky. Multidisciplinary Design and Optimization of the Silent Aircraft. In *44th AIAA Aerospace Sciences Meeting and Exhibit, Reno, Nevada, 9-12 January*, number 1323, pages 1–12, 2006.

[66] CA. Hall and D Crichton. Engine and Installation Configurations for a Silent Aircraft. *ISABE*, 1164, 2005.

[67] AK Noor and S.L Venneri, editors. *Future Aeronautical and Space Systems*. American Institute of Aeronautics and Astronautics, Inc., 1997.

[68] HJM Kok, M Voskuijl, and MJL van Tooren. Distributed Propulsion featuring Boundary Layer Ingestion Engines for the Blended Wing Body Subsonic Transport. *AIAA paper*, pages 1–12, 2010.

[69] CA Hall, D Crichton, and P Freuler. Integration of the Silent Aircraft Propulsion System. *8th Aeroacoustics Workshop*, pages 1–22, 2004.

[70] J Protz. *Engine Models*. Massachusetts Institute of Technology, Cambridge, MA, USA, 2004.

[71] Q Yang, Y Zheng, and Streit T. Aerodynamic Design for Wing Body Blended and Inlet. *ICAS*, pages 1–6, 2006.

[72] H.D Kim, G.V Brown, and J.L Felder. Distributed Turboelectric Propulsion for Hybrid Wing Body Aircraft. In *International Powered Lift Conference, London-England, July 22-24*, 2008.

[73] GA Hill, SA Brown, and KA Geiselhart. Integration of Propulsion-Airframe-Aeroacoustic Technologies and Design Concepts for a Quiet Blended-Wing-Body Transport. *AIAA paper*, pages 1–20, 2004.

[74] LT Leifsson, A Ko, WH Mason, JA Schetz, RT Haftka, and B Grossman. Multidisciplinary Design Optimization for a Blended Wing Body Transport Aircraft with Distributed Propulsion. Technical Report 2005-05-01, Virginia Polytechnic Institute & State University Blacksburg, VA 24061-0203, 2005.

[75] E De La-Rosa Blanco and C Hall. Challenges in the Silent Aircraft Engine Design. *AIAA Paper*, pages 1–20, 2007.

[76] E. Natarajan, R. Anusha, and S. Srinath. Design of Transport Aircraft for the Future. Technical report, National Aeronautics and Space Administrations (NASA) Fundamental Aeronautics Contest 2007/2008, 2008.

[77] S.I D'souza. An analysis of the developments in blended wing body aircraft for sustainable aviation. *University of Toronto Institute for Aerospace Studies*, 2012.

[78] MSc Aerospace Vehicle Design 2011-2012. BW-11 Eagle Ray Blended Wing Body Airliner. Technical report, Cranfield University, Department of Aerospace Engineering, September 2011.

[79] ER Galea, L Filippidis, Z Wang, PJ Lawrence, and Ewer J. Evacuation Analysis of 1000+ seat Blended Wing Body Aircraft Configurations: Computer Simulations and Full-Scale Evacuation Experiment. In *PED 2010, NIST, Maryland USA , March 8-10*, pages 1–10, 2010.

[80] J Ehlers, D Niedermeier, and D Leiß ling. Verification of a Flying Wing Handling Qualities Analysis by Means of In-Flight Simulation. *AIAA*, pages 1–15, 2011.

[81] S Wakayama. Blended-Wing-Body Optimization Problem Setup. In *8th AIAA/USAF/NASA/ISSMO Symposium on Multidisciplinary Analysis and Optimisation,Long Beach, CA*, 6-8 September 2000.

[82] I Kroo. The Effect of Aircraft Size on Performance. *Aircraft Aerodynamics and Design group, Department of Aeronautics and Astronautics, Stanford University, Stanford California*, 1995.

[83] D. H Allen. *How Mechanics Shaped the Modern World.* Springer International Publishing Switzerland, 2014.

[84] V.J Rossow. Lift - Generated Vortex Wake of Subsonic Transport Aircraft. *Progress in Aerospace Sciences, vol. 35, No. 6, pp. 507 -660*, 1997.

[85] H.H Ghigliazza. Wake of Transport Flying Wing. *Journal of Aircraft, vol.44, No. 2, March - April*, 2007.

[86] NE Antoine. Aircraft Optimization for Minimal Environmental Impact. *AIAA*, pages 1–8, 2002.

[87] J Markish and K Willcox. Multidisciplinary Techniques for Commercial Aircraft System Design. In *9th AIAA/ISSMO Symposium on Multidisciplinary Analysis and Optimization*, volume 2, pages 1–9. Citeseer, 2002.

[88] McMasters J.H. and Cummings R.M. Rethinking the Airplane Design Process An Early 21st Century Perspective. In *AIAA 2004-693, 42nd AIAA Aerospace Sciences Meeting and Exhibit, Reno, NV, USA*, Jan. 2004.

[89] S.A Brandt, R.J Stiles, J. J. Bertin, and R. Whitford. *Introduction to Aeronautics: A Design Perspective (2nd ed.).* Reston, Virginia: AIAA Education Series, 2004.

[90] D. Ferreri. *Marketing and Management in the High-Technology Sector: Strategies and Tactics in the Commercial Plane Industry.* Westport, USA: Praeger Publishers, 2003.

[91] J.P Fielding. *Introduction to Aircraft Design*. Cambridge: Cambridge University Press, 1999.

[92] R Pradeep. Requirements for Effective Use of CFD in Aerospace Design. In *Surface Modeling, Grid Generation and Related Issues in Computational Fluid Dynamic (CFD) Solutions : Proceedings of a Workshop / Sponsored by NASA Steering Committee on Surface Modeling and Grid Generation held at NASA Lewis Research Center, Cleveland, Ohio, May 9-11*, 1995.

[93] C Bil. *Development and Application of a Compuuter-based System for Conceptual Aircraft Design*. Delft University Press, 1988.

[94] J.S Robinson and J. G Martin. An Overview of NASA's Integrated Design and Engineering Analysis (IDEA) Environment . In *Joint Army-Navy-NASA-Air Force (JANNAF) 6th Modeling and Simulation / 4th Liquid Propulsion / 3rd Spacecraft Propulsion Joint Subcommittee Meeting Orlando, Florida December 8-12, 2008*, 2008.

[95] DARcorporation. Advanced aircrafpropulsion computer program. http://www.darcorp.com/Software/AAA/, 2015. Accessed 15 August 2015.

[96] Stanford University. Program for aircraft synthesis studies (pass). http://adg.stanford.edu/aa241/pass/pass1.html, 2012. Accessed 15 August 2015.

[97] A Azamatov, J Lee, and Y Byun. Comprehensive aircraft configuration design tool for integrated product and process development. *Advances in Engineering Software*, 42(1 - 2):35–49, January - February 2011.

[98] B.E Magrab, K.S Gupta, F.P McCluskey, and P Sandborn. *Integrated Product and Process Design and Development: The Product Realisation Process, Second Edition (Environmental and Energy Engineering)*. CRC Press;, 2009.

[99] K.G Bowcutt. A Perspective on the Future of Aerospace Vehicle Design. In *12th AIAA International Space Planes and Hypersonic Systems and Technologies15 - 19 December 2003, Norfolk, Virginia,USA*, 2003.

[100] C.B Chapman and M. Pinfold. Design Engineering A Need to Rethink the Solution using Knowledge Based Engineering. *Journal of Knowledge Based System,, Vol. 12, Issue 5-6, pp. 257-267*, 1999.

[101] De Weck O.and Agte J.and Sobieszczanski-Sobieski J.and Arendsen P.and Morris A. and Spieck M. State-of-the-Art and Future Trends in Multidisciplinary Design Optimization. In *AIAA 2007-1905, 48th AIAA/ASME/ASCE/AHS/ASC Structures, Structural Dynamics & Material Conference, Honolulu, HI, USA*, 2007.

[102] Giesing J.P. and Barthelemy J-F.M. A Summary of Industry MDO Applications and Needs. In *AIAA 1998-4737, AIAA/USAF/NASA/ISSMO Symposium on Multidisciplinary Analysis and Optimization, St. Louis, MO, USA*, 1998.

[103] J.H Vadenbrande, Grandine T.A., and Hogan T. The Search for the Perfect Body: Shape Control for Multidisciplinary Design Optimization. In *AIAA 2006-928, 44th Aerospace Sciences Meeting and Exhibit, Reno, NV, USA*, 2006.

[104] JJ Doherty and SC. McParlin. Generic Process for Air Vehicle Concept Design and Assessment. In *42nd AIAA Aerospace Sciences Meeting and Exhibit 5 - 8 January 2004, Reno, Nevada*, 2004.

[105] NASA. US Standard Atmosphere 1976. http://ccmc.gsfc.nasa.gov/modelweb/atmos/us_standard.html, October 1976. Accessed 7 August 2015.

[106] Geometrical Properties of Cranked and Straight Tapered Wing Planforms. Technical Report 76003, Engineering Science Data Units (ESDU), October Issued January 1976, Amendment A, October 1981.

[107] DP Raymer. *Aircraft Design: A Conceptual Approach, Fourth Edition*. AIAA Education Series, Blacksburg, Virginia, 2006.

[108] MCY Niu. *Airframe Structural Design*. Technical Book Company, California, 1988.

[109] KK Ajoy. *Aircraft Design*. Cambridge University Press, Cambridge, 2010.

[110] D Howe. *Aircraft Conceptual Design Synthesis*. Professional Engineering Publishing Limited, London and Bury ST Edmunds,Uk, 2000.

[111] Acceptable Means of Compliance for Large Aeroplanes, Certification Specification-25. Technical Report. Amendment 16, March 2015.

[112] American Institute of Aeronautics and Inc Astronautics. *AIAA Aerospace Design Engineers Guide*. Professional Engineering Publishing Limited, London and Bury ST Edmunds,Uk, IP326BW,UK, 2003.

[113] M.D Ardema, A.P Chambers, M.C.and Patron, H Hahn, A.S.and Miura, and M.D. Moore. Analytical Fuselage and Wing Weight Estimation of Transport Aircraft. Technical report, NASA Technical Memorandum 1 10392, 1996.

[114] D Howe. The Prediction of Aircraft Wing Mass. *Proc. Instn Mech. Engrs, Part G, Journal of Aerospace Engineering*, 210(G3):135–145, 1996.

[115] L.R Jenkinson, P Simpkin, and D Rhodes. *Civil Aircraft Design*. Butterworth Heinemann Publications, 2003.

[116] E Torenbeek. *Synthesis of Subsonic Airplane Design*. Kluvwer Academic Publishers, Dordrecht, The Netherlands, 1982.

[117] AK Kundu. *Aircraft Design*. Cambridge University Press, New York, 2010.

[118] DJ Roskam. *Airplane Design - Part V: Component Weight Estimation*. Roskam Aviation and Engineering Corporation, 1989.

[119] Powerplants, systems and equipment mass (daet 9218).

[120] Flight Standard Service. Aircraft weight and balance control, October 2005. URL http://www.faa.gov/documentLibrary/media/Advisory_Circular/AC120-27E.pdf. Washington, DC.

[121] Ali Elham. *Weight Indexing for Multidisciplinary Design Optimization of Lifting Surfaces*. PhD thesis, Delft University of Technology, The Netherlands, 2013.

[122] R.M Cummings, J.R Forsythe, S.A Morton, and K.D Squires. Computational Challenges in High Angle of Attack Flow Prediction. Technical report, Aerospace Engineering Department, California Polytechnic State University, San Luis Obispo, CA 93407, USA, 2003.

[123] A Jameson. Requirements and Trends of Computational Fluid Dynamics as a Tool for Aircraft Design. In *Proceedings 12th NAL Symposium on Aircraft Computational Aerodynamics*, 1994.

[124] D McLean. *Understanding Aerodynamics: Arguing from the Real Physics*. John Wiley and Sons Limited, 2013.

[125] B Chudoba. *Stability and Control of Conventional and Unconventional Aircraft Configurations: A Generic Approach*. Bernd Chudoba and Cranfield University, England, 2001.

[126] J Alonso. Computational Methods in Aircraft Design. Technical report, Aircraft Aerodynamics and Aircraft Design Group, Stanford University, USA, 2005.

[127] C. Hock-Chuan. Java Programming Tutorial:Java Native Interface (JNI), February 2014. URL http://www.ntu.edu.sg/home/ehchua/programming/java/JavaNativeInterface.html.

[128] A Turnbull. *A Preliminary Sizing Method for Unmanned Aircraft Using Multi-Variate Optimisation*. PhD thesis, Cranfield Institute of Technology, 1990.

[129] N Niyomthai. *Packaging and Configuration Design Aspects of UCAV Concept Synthesis and Optimisation*. PhD thesis, Cranfield University, 2002.

[130] D.A Lovell. The Application of Multivariate Optimisation to Combat Aircraft Design. Technical report, Cranfield Institute of Technology, 1988.

[131] MB Kulfan and JE Bussoletti. "Fundamental" Parametric Geometry Representations for Aircraft Component Shapes. In *11th AIAA/ISSMO Multidisciplinary Analysis and Optimization Conference: The Modeling and Simulation Frontier for Multidisciplinary Design Optimization*, number AIAA–2006-6948, 2006.

[132] MB Kulfan. Universal Parametric Geometry Representation Method. *Journal of Aircraft*, 45(1), 2008.

[133] BM Kulfan. CST Universal Parametric Geometry Representation Method With Applications to Supersonic Aircraft. In *Fourth International Conference on Flow Dynamics Sendai International Center Sendai, Japan*, 2007.

[134] M.E Eshelby. *Aircraft Performance Theory and Practice*. Arnold Publishers Euston Road, London NW1 3BH, 2000.

[135] M. Sadraey. *Aircraft Performance Analysis*. Saarbrucken VDM Verlag Dr. Muller, 2009.

[136] MV Cook. *Flight Dynamics Principles*. Butterworth Heinemann Publications, 2007.

[137] C Mader. Optimal Flying Wing. In *3rd AIAA/ASME/ASCE/AHS/ASC Structures, Structural Dynamics and Materials Conference*, 2012.

[138] H. V De Castro. The longitudinal static stability of tailless aircraft. *Cranfield University College of Aeronautic CU/COA-2000/0018/1*, 2000.

[139] H. V De Castro. *Flying and Handling Qualities of a Fly-by-wire Blended-wing-body Civil Transport Aircraft*. PhD thesis, School of Engineering, Cranfield University, 2003.

[140] M Carley. Some note on aircraft and spacecraft stability and control. Technical report, National Flying Laboratory Centre, Cranfield University, 2012.

[141] D Kinghorn. Haswell Floating Point Performance. http://www.pugetsystems.com/blog/2013/08/26/Haswell-Floating-Point-Performance-493/, August 2013. Accessed 5 August 2015.

[142] Aerospace Vehicle Design College of Aeronautics. Aircraft Mass Prediction of Structural Component. Technical report, Cranfield University.

[143] N.S Currey. *Aircraft Landing Gear Design: Principles and Practices*. AIAA Education Series Washington, 1988.

[144] Rolls Royce. Trent 900. http://www.rolls-royce.com/customers/civil-aerospace/products/civil-large-engines/trent-900.aspxoverview, October 2015. Accessed 1 November 2015.

[145] aerospaceweb.org. Propulsion. http://www.aerospaceweb.org/design/ucav/propulsion.shtml, 2012. Accessed 7 May 2016.

[146] M Cavcar. *Jet Engine*. Anadolu University, School of Civil Aviation, 2004. http://home.anadolu.edu.tr/~mcavcar/common/Jetengine.pdf.

[147] MH Sadraey. *Aircraft Design: A System Engineering Approach*. John Wiley and Sons Limited, 2012.

[148] Airlines Inform. Airbus a380 specifications. http://www.airlines-inform.com/commercial-aircraft/Airbus-A380.html, 2012. Accessed 12 February 2016.

[149] LHR Airports Limited. Heathrow our comapany : Facts and figures. http://www.heathrow.com/company/company-news-and-information/company-information/facts-and-figures, 2014. Accessed 12 February 2016.

[150] DS Agenberg and N Theron. *Investigation into the Longitudinal Handling Characteristics of a Gull Wing Planform Tailless Aircraft*. PhD thesis, Department of Mechanical and Aeronautical Engineering, University of Pretoria, South Africa, 2008.

[151] W. Mnnich and L. Dalldorf. A New Flying Qualities Criterion for Flying Wings. *AIAA*, 1993.

[152] MH Straathof, MJL van Tooren, and Koren B Voskuijl M and. Aerodynamic Shape Parameterisation and Optimisation of Novel Configurations. In *Proceedings of the RAeS Aerodynamic Shape Parameterisation and Optimisation of Novel Configurations Conference, London*, 2008.

[153] Oracle JAVA Documentation. Polymorphism. https://docs.oracle.com/javase/tutorial/java/IandI/polymorphism.html, 1995. Accessed 10 August 2015.

[154] R Carmichael. The NASA Langley Wireframe Geometry Standard. http://www.pdas.com/lawgs.html, March 2013. Accessed on 11 August 2015.

[155] The USAF Stability and Control Datcom, April 1979.

[156] D Adamczak and A A Bhungalia. Supersonic Hypersonic Arbitrary Body Program (S/HABP). In *Thermal & Fluids Analysis Workshop (TFAWS) AUGUST 18-22*, 2003.

[157] M Drela and H Youngren. AVL Aerodynamic Analysis Trim Calculation Dynamic Aircraft Configuration Development. http://web.mit.edu/drela/Public/web/avl/, November 2007. Accessed 5 August 2015.

[158] Oracle JAVA Documentation. Enum Types. https://docs.oracle.com/javase/tutorial/java/javaOO/enum.html, 1995. Accesssed 6 August 2015.

# Appendix A

# Atmospheric Model

Given that the temperature in the international standard atmosphere is derived from Equation A.1:

$$T = T_i + L_i(h - h_i) \tag{A.1}$$

$T$ is the temperature in Kelvin ,$(K)$.
$L$ is the temperature lapse rate in $K/m$.
$h$ is the geopotential altitude in $m$.
Subscript $i$ is the datum level for each segments of the atmosphere.

And knowing the temperature lapse rate in the various segments, then substituting into Equation A.1, the temperatures at the 3 segments are determined as follows:

$T = 288.15 - 0.0065h$ for $0 \leq h \leq 11000m$.
$T = 216.65$ for $11000 \leq h \leq 20000m$.
$T = 216.65 + 0.001(h - 20000)$ for $20000 \leq h \leq 32000m$.

The pressures at the different segments are determined as:

$p = 101325\,[1 - 0.000022558h]^{5.25588}$ in the troposphere.
$p = 22632\exp\left[-0.000157688\,(h - 11000)\right]$ in the lower stratosphere.
$p = 5474.9\,[1 + 0.000004616\,(h - 20000)]^{-34.1632}$ in the lower stratosphere.

Density is derived from the equation of state A.2 using the temperature and pressure obtained at the given altitude.

$$\rho = \frac{p}{RT} \tag{A.2}$$

Where:

$\rho$ is density in $kg/m^3$.
$R$ is the gas constant $= 287.05287Nm/kgK$.

The speed of sound $a$ is a function of temperature and is derived from Equation A.3.

$$a = \sqrt{401.87T} \tag{A.3}$$

The kinematic viscosity in $m^2/s$ is calculated from Equation A.4.

$$\nu = \frac{1.458 \times 10^{-5} T^{1.5}}{(T + 110.4)\, p} \tag{A.4}$$

# Appendix B

# Steps to Compiling the Athena Vortex Lattice for Operations on Windows

Though AVL is often distributed pre-compiled, the source code is also available for modification if need be. Pre - compiled AVL.exe file requires a geometry text file, to be loaded prior to analysis. However, because the design synthesis tool being developed requires automated operation, there was the need to modify the source code and recompile it accordingly. Generally, compiling a FORTRAN source code such as the AVL is pretty straight-forward. However, AVL source code just like most FORTRAN code is platform dependent and requires the X11 plot library which is not often available on windows.

The -X11 is a windowing support library used by Linux to make plots. Compiling the distributed AVL source code on windows therefore involves a complicated process of installing several programs which is not convenient. There is therefore the need to modify the AVL source code in order to bypass the requirement for the -X11 library which, nonetheless, is not necessary in a multivariate optimisation scheme.

The procedure described in this thesis assumes that the open source Minimalist GNU for Windows (MinGW) and Minimal System (MSYS) are installed on the system. After installing MinGW and MSYS, 'C:/MinGW/bin;' 'C:/MinGW/msys/1.0/local/bin;' and 'C:/MinGW/msys/1.0/bin' should be added to the end of the PATH system environment variable.

The AVL is then compiled according to the following steps:

1. Download the AVL source code from http://web.mit.edu/drela/Public/web/avl/.
2. Unzip the source code using any unzipping program.
3. Place the unzipped AVL folder in the path 'MinGW/msys/1.0/home/usr' . 'usr' in the path name refers to the login or user name.
4. Now open the plotlib folder located in the path: MinGW/msys/1.0/home/usr/AVL/plotlib.

5. Open and edit the file 'makefile.f' as follows:
   - Comment out PLTLIB=libPlt.a and uncomment PLTLIB=LibPltDp.a.
   - comment out Xwin.o in OBJ.
   - Change FC=f77 to FC=gfortran if using gfortran compiler or to the appropriate FORTRAN compiler installed on the system.
   - Change "CC=CC" to "CC=g++" or the appropriate C++ compiler installed on the system.
   - Uncomment and change "DP=r8" to "DP=-fdefault-real-8 -fdefault-double-8".
   - Comment out "include.config.make".
   - Comment out "Xwin.o:Xwin.c".
   - "$cc -c $ $(cflags) Xwin.c$".
6. Having completed the foregoing process, open MinGW shell or run terminal.
7. Do "cd c:/MinGW/msys/1.0/home/usr/AVL/plotlib".
8. Do "make" to generate the plot lib object file.
9. Open the eispack folder in the in the path MinGW/msys/1.0/home/usr/AVL/eispack and edit the edit the makefile.f as follows:
   - Comment out FC=f77.
   - Change fc=ifort to FC =gfortran or the appropriate fortran compiler.
   - Change "Fflags =-0" to "Fflags =-o -fdefault-real-8 -fdefault-double-8".
10. Open MinGW shell.
11. Change directory to eispack by typing "cd: c:/MinGW/msys/1.0/home/usr/AVL/eispack".
12. Create the eispack object file using "make" to generate eispack.o.
13. Open the bin folder in AVL directory i.e c:/MinGW/msys/1.0/home/usr/AVL/bin.
14. Edit the makefile as follows:
   - Comment out the plotOBj.
   - Change FC=f77 to FC=gfortran.
   - Change Fflags =-0 to Fflags =-o -fdefault-real-8 -fdefault-double-8.
   - Change PLTLIB=LX11 to PLTLIB=
   - Change SECOND=second_g77.f to SECOND =second.f
   - Comment out everything from "uncomment flags for desired machines" until and including "PLTLIB", "SECOND" and "FTNlib".
   - Ensure PltOBJ = ...../plotlib/libpltDP.a.
   - Comment out $cp(SRC) /$(SECOND) $ (SRC) /second.f$
15. Open the file gw_subs.f in the path c:/MinGW/msys/1.0/home/usr/AVL/src and delete contents of all subroutines within the file except the "return" and "end" commands. In other words creating an empty subroutine. This step is critical as it controls the process responsible for invoking the X11 library call.
16. Now open MinGW shell or run terminal again.
17. Change directory to c:/MinGW/msys/1.0/home/usr/AVL/bin.
18. Generate the executable file using the "make" command.

# Appendix C

# Process of Creating a Shared Library of FORTRAN Written AVL Codes and JAVA Disciplinary Models

In order to create a shared object file that allows for self contained JAVA execution of the aerodynamic analysis code, the JAVA code is first compiled by typing "javac JavaCodefilename.java" in the compiler to create a classfile named "JavaCodefilename.class". Subsequently, a JNI header file is generated by typing "javah JavaCodefilename" to create a header file with the same name as the class file but with a ".h" extension. Following the example in this thesis, this will create a file named "JavaCodefilename.h"

As JAVA can only be interfaced with Fortran through a C++, a C++ code to link the FORTRAN code to JAVA is created by inserting "#include" followed by the name of the header file at the top of the C++ document. Using the example in this thesis, this translates to writing "#include <JavaCodefilename.h.>" at the top of the C++ code. This will be followed by a declaration of the name of the C++ function invoked in the "native method" in JAVA together with the prototype interface from the header file. The term "Extern "C" " is used before the C++ function name in order to notify C++ compilers that the function(s) following should be compiled using Cs function naming convention instead of C++ naming protocol.

A "C" function naming convention is written as Java_package_ and _ classname _ {function _name { (JNI arguments, arguments of the C function). The JNI arguments are the JNIEnv* and jobject. JNIEnv refers to the JNI environment which provides access to all the JNI functions while the jobject argument refers to "this" java object.

Applying this convention to the example used so far in this chapter, the prototype declaration and subsequent C function would look like the following:

JNIEXPORT returntype JNICALL Java _ JavaCodefilename _ cppfunctionNameAsGiveninJava(JNIEnv *env, jobject thisobj, jargumenttype, argument..)
{ Describe what the C++ function is to written to accomplish;
}

The C++ code file generated from the foregoing process, assuming it is named "Cppcode.cpp", is then compiled, by typing:

"g++ -c Cppcode.cpp -m64"

This creates an object file "Cppcode.o". This object file is then linked with FORTRAN object files to create a Dynamic Link Library (DLL).

In this thesis, the FORTRAN codes that needs to be linked is the AVL source code. The AVL source codes comprises 37 files. A single library file is created from these 37 files by first creating an object file for each of the 37 files using the command :

"gfortran -c *.f -m64"

Subsequently, the object files are combined into a library file through the command:

"ar rcvf libAVLf.a *.o"

This creates a library file named libAVlf.a.

The C++ object file and the combined FORTRAN library file are then linked to create a DLL file using the command:

"g++ Cppcode.o -L. -lAVLf.a -o nameofDLL.dll -m64 -static -lgfortran -shared"

This generates a DLL file named "nameofDLL.dll". The generated DLL file is copied and placed in the same folder as the JAVA file. The JAVA program which now serves as the main program for the C++ and FORTRAN codes within the interface is then executed using the 'run' button in 'Netbeans' or by typing in 'java Javacode' in the compiler console.

# Appendix D

# Development of the GMDSO Tool

The GMDSO Tool is developed to ensure modularity by creating distinct disciplinary modules with sequentially defined forward interacting paths. The modules, which are created with the polymorphism feature of JAVA programming language, are the computational engines driving the functioning and operations of the GMDSO Tool. Polymorphism is an essential feature in the development of the GMDSO Tool due to the need for different aircraft configurations with different design models to utilise common features and conform to a set format. Polymorphism allows objects with different internal features to share the same external interface. Additionally, it enables subclasses of a class to define their own unique behaviour while still retaining or sharing some of the functionality of the parent class [153].

The organisation and hierarchy of the modules within the GMDSO Tool is shown in Figure D.1.

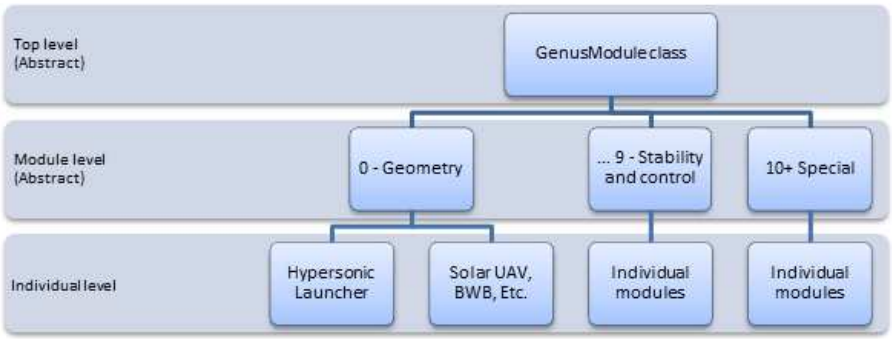


**Figure D.1:** Overview of the GENUS Module Class.

The GMDSO Tool is organised into 3 levels namely the top, module and individual level classes. The top level class termed the 'GENUSModule' and module level classes are implemented as Abstract classes. Abstract classes are used because of the need to share common top level codes among the different individual level modules. There are 10 individual level essential modules and an arbitrary number of special modules in the GMDSO Tool. The top level module specifies all the methods and fields that enable the GMDSO tool to function. These methods and fields are used:

- To display and acquire information from the GUI.
- To enable the modules to be updated as well and provide values to the optimizer(s) or other processes.
- For communicating between modules.
- For saving data to permanent storage as opposed to RAM.
- For writing output report to the hard disk.

## D.1 0 - Geometry

The Geometry Module defines the shape of the aircraft using geometric variables such as the span, sweep, twist, etc and store the generated data in an agreed common format. The organisation of the Geometry Module showing its constituent parts is given in Figure D.2.

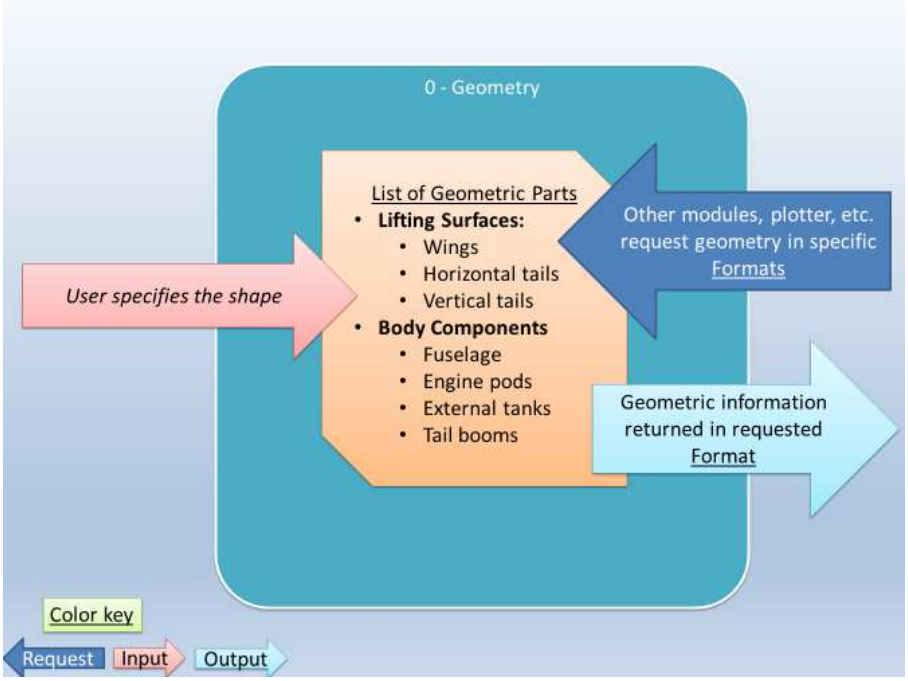


**Figure D.2:** A Layout of the Geometric Module.

The shape of an aircraft is defined in the Geometry Module using components of the GeometrycPart abstract class. The hierarchy of Geometrycpart is defined in Figure D.3.

The GeometrycPart is divided into the LiftingSurfaces and BodyComponents arrays. One of the arrays can be zero long but not both. Setting both arrays to zero long denotes absence of a geometry which is impracticable. A zero long BodyComponents array is used to describe a flying wing type aircraft, while zero long LiftingSurfaces is applicable to a space capsule.

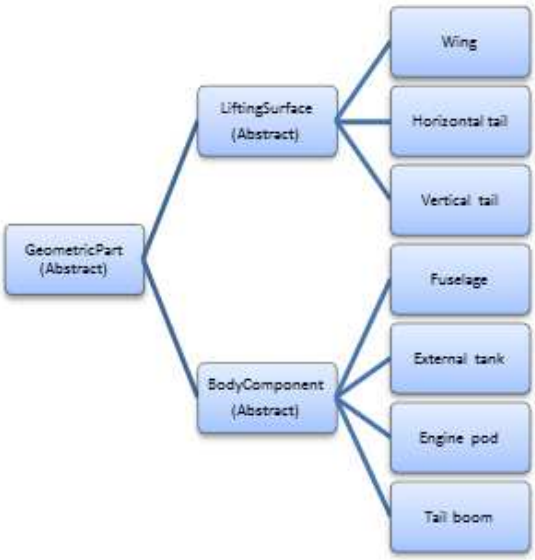


**Figure D.3:** Hierarchy of Geometric Parts in the Geometric Module.

### D.1.1 LiftingSurface

The LiftingSurface is used to describe elements that generate the aerodynamic forces and/or moments to lift and/or control the vehicle. LiftingSurfaces are used to define the wings, horizontal and vertical tails. The shape of a lifting surface is controlled by the number, arrangements and dimensions of cross-sections or kinks. In the GMDSO Tool, the number of kinks is denoted by the letter $m$. The location and arrangement of the kinks are governed by the Apex, section and cross-section properties.

Apex represents the xyz reference coordinates of the kink. Section properties refers to the section span[m], leading edge sweep[rad], dihedral[rad] and the area ratio of the control in surface meters. The area ratio of a control surface is the ratio of the portion of the section used for control function to the total length of the section. It is taken as 0 in the absence of control surfaces and 1 when the whole surface is used for control function. Nevertheless, when control surfaces are present, this ratio ranges from 0.1 -1, depending on the location of the control surface from the leading edge of the section. Each section property has an array length equal to $m + 1$.

Cross-section properties consist of the chord length [m], airfoil type and inputs specifying the thickness and camber of the airfoil, and the local incidence or twist in radians. Each cross-section properties has an array length equal to $m + 2$.

The XY, YZ and XZ - plane views of an arbitrary 4 - sections lifting surface as generated from the GMDSO Tool using the lifting properties are shown in Figures D.4, D.5 and D.6 respectively. The shape was splined and surfaced in CATIA from the outputs of the Geometry Module. The shape sections are coloured differently to aid identification of the different sections.

The span of a section in the GMDSO Tool is defined differently from the span normally used in aircraft design. Span as used in the Geometry Module of the GMDSO Tool refers to the true distance between the 2 leading edge points as shown in Figure D.5 rather than the usual projected distance in the XY - plane. This definition was adopted in order to be able to specify non-conventional wings such as winglets, box-wing, c - wings etc. Knowing the projected distance and provided none of the dihedral or sweep is 90°, the input span length can be calculated by Equation D.1.

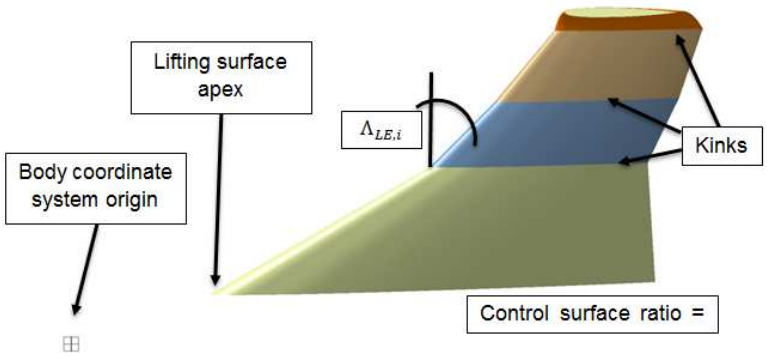


**Figure D.4:** XY - Plane View of a Lifting Surface Showing Definition of Properties.

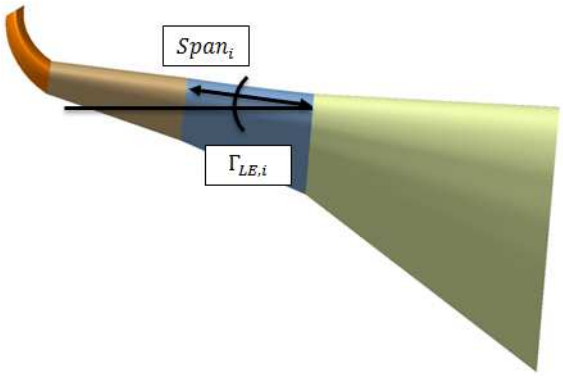


**Figure D.5:** YZ - Plane View of a Lifting Surface Showing Span Definition.

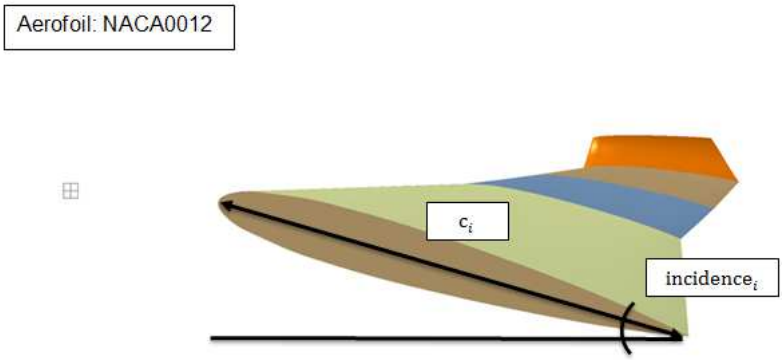


**Figure D.6:** XZ - Plane View of a Lifting Surface Showing Span Definition.

$$span_i = span_{projected,i}\sqrt{1 + \tan^2 \Gamma_i + \tan^2 \Lambda_{LE,i}} \tag{D.1}$$

### D.1.2 BodyComponent

BodyComponents define non-lifting surfaces such as the fuselage, tail boom, etc using apex, number of kinks, section and cross-section properties. The apex, number of kinks, $m$, and section properties are arrays with length equal to $m + 1$. They are defined in the same way as the LiftingSurface properties of same name.

The cross-sectional properties comprise the width [m], height [m], bottom distance[m] and the cross-section shape. The cross - section shape could be either oval or rectangular. Cross - section properties are arrays of length equal to $m + 2$.

In order to completely define a BodyComponent, the nose and/or end section of must also be specified. The nose and end sections are described by their radius [m] and length [m]. The variation of the length and radius of the nose determines its shape. Various definitions of the nose section are given in Figures D.7, D.8, and D.9.

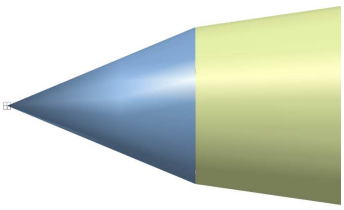

**Figure D.7:** Shape of the Nose Section with Zero Radius and Finite Length.

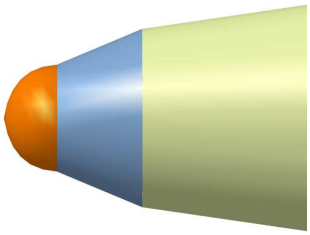

**Figure D.8:** Shape of the Nose Section with Finite Radius and Finite Length.

A 3 - dimensional view of a fuselage section together with a description of its properties are defined in Figures D.10, D.11 and D.12. It is pertinent to note the difference between the fuselage total length and its structural length. Th total length refers to the tip to tip length of the fuselage from the nose to the from the nose to the end of the rear section. The structural length refers to the length of the mid section or body of the fuselage without the nose and end sections of the body.

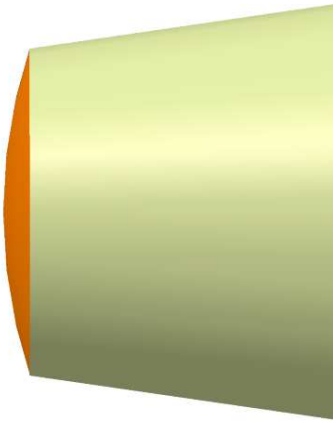

**Figure D.9:** Blunt Nose Section with Zero Length and $R > R_o$.

**Figure D.10:** XZ-Plane View of the Fuselage Section.

**Figure D.11:** XY-Plane View of the Fuselage Section.

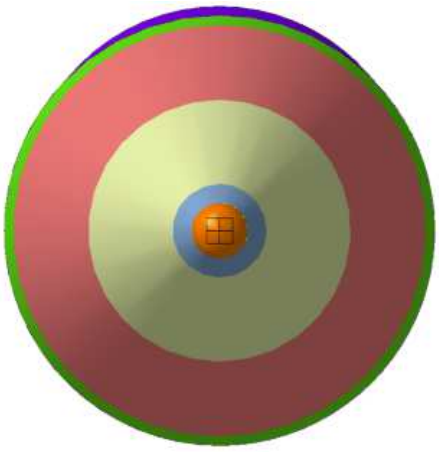

**Figure D.12:** YZ-Plane View of the Fuselage Section.

### D.1.3 Geometry Formats

The geometry format provides a common storage standard for the outputs of LiftingSurfaces and BodyComponents. The number of geometry formats implemented depends on the different aerodynamic analysis modules integrated into the GMDSO Tool. This is because geometry formats must conform to the geometry standards required by the aerodynamic analysis tool implemented. Consequently, 3 geometric formats are defined in the GMDSO Tool in line with the 3 aerodynamic analyses tools implemented. The geometry formats are the NASA Langley Wireframe Geometric Standard (LAWGS) [154], Digital Datcom [155] and the AVL geometry format.

The NASA LAWGS is a format that describes a configuration geometry with discrete points. It is implemented in the GMDSO Tool for use with the Supersonic/Hypersonic Arbitrary Body Program (SHABP) [156], and the built-in plotting in the GMDSO Tool. The Digital Datcom format defines the wing and tail surfaces as equivalent straight tapered plan - forms with only one kink, and the fuselage by a series of circular cross -sections with equivalent radius. The Digital Datcom format is developed for use with the Digital Datcom aerodynamic analysis tool. Similarly, the AVL geometry format is implemented for use in the AVL aerodynamic analysis tool. The AVL geometry format describes a surface by a mixture of the xyz leading edge coordinates, kinks, sections, spans, chords and airfoil. Though the AVL does not analyse bodies as it does not model thickness. However, bodies could be defined, for aesthetic reasons only, using series of circular cross - section [157].

All geometry formats generated during a single instance of the GMDSO Tool are stored. This is to enable them to be reused in other parts of the program when needed thereby avoiding duplication of effort. The process of generating, requesting for and transfer of geometry module within the GMDSO Tool Geometry Module are shown in Figure D.13.

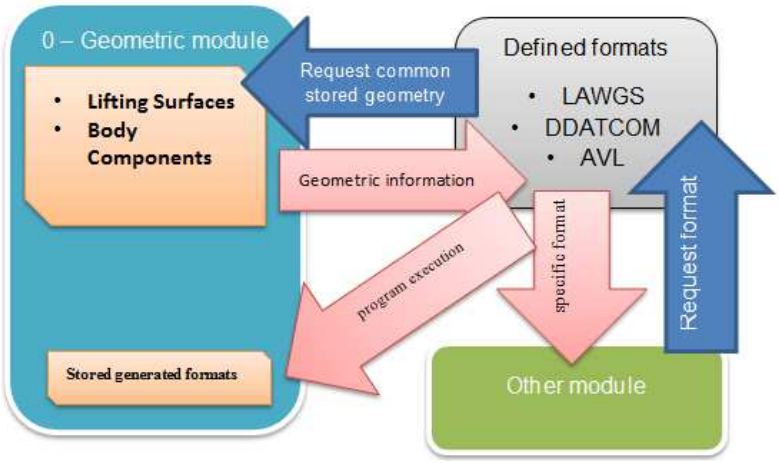


**Figure D.13:** The Process of Generating and Transfer of Geometry Formats Within the GMDSO Tool.

In addition to defining the shape of the aircraft, the Geometry Module also contains utility methods for modifying the shape and/or extracting information for use in other modules. The utility methods implemented in the GMDSO Tool are categorised into the common methods, BodyComponents methods and the LiftingSurfaces methods.

The common utility methods are applied to both the LiftingSurface and BodyComponents. Common methods are used to modify an aircraft shape or extract information for use in other modules. Common utility methods implemented in the GMDSO Tool are the:

- Add kinks.
- Remove kinks.
- Set Apex(origin).
- Set non-dimensional Apex.
- Count number of parameters.
- Get the total volume.
- Get the total surface area.
- Get section volume and surface area.
- Get cross-section area and circumference.
- Get the lowest z-coordinate.
- Get the highest z-coordinate.
- Get XYZ coordinate at $\bar{X}$ and $\bar{Y}$.

BodyComponents utility methods comprise:

- Copy object properties from other BodyComponent.
- Set body component.
- Calculate volume and surface area of nose and rear.
- Add/remove/set nose and rear.
- Get XYZ coordinate at $\bar{X}$ and $\bar{Y}$.
- Get end coordinate.
- Get planform area.

LiftingSurfaces utility methods are used to manipulate lifting surfaces elements or extract information for use in other modules. These include :

- Copy object properties from other LiftingSurface.
- Set LiftingSurface.zz
- Get XYZ coordinate at $\bar{X}$ and $\bar{Y}$ top or bottom surface.
- Get equivalent sweep at chord fraction.
- Get XYZ coordinate at p% of the Mean Aerodynamic Chord (MAC).
- Get XYZ coordinate at at p% of the Mean Aerodynamic Chord (MAC) at $\bar{Y}$.

LiftingSurfaces and BodyComponents use aerofoils and simple sections respectively to define their cross-section shapes. The fineness of the cross-section shapes, which are generated in planar XY coordinates form, is controlled by a division parameter. The division parameter sets the total number of points on the cross-section depending on the type of geometry. For a lifting surface, the number of points or fineness is derived from Equation D.2.

$$fineness_{LS} = 2 \cdot Divisions + 7 \tag{D.2}$$

For a BodyComponent, the number of points is determined from Equation D.3.

$$fineness_{BC} = 8 \cdot Divisions + 9 \tag{D.3}$$

BodyComponents and LiftingSurface cross - section must be defined in a clockwise direction to form a closed loop starting from the trailing edge of the lifting surface or bottom of the body section to the leading edge of the lifting surface or top of the section.

## D.2 1-Mission Specification Module

The mission module specifies the minimum requirement which a design is expected to satisfy. These requirements are derived from the market or customer specification. The mission module consists of the following common fields:

- cruiseAlt[m]: This is the assumed cruising/orbit altitude [m] used in the design of the aircraft.
- cuiseSpeed[m/s]: This is flight speed of the aircraft in the cruising phase of flight. It is also referred to as the Cruising/Orbital speeds.
- cruiseMach[-]: Cruising/orbital Mach number.
- tRange[m]: Target range determined from the cruising phase of flight.
- tEndurance[s]: Target Endurance also obtained from the cruising portion of the aircraft flight profile.
- pax [-]: Number of passengers.
- crew [-]: Number of crew on board.
- payload, payload _drop, payload_pick: These refer to mass of payload [kg].
- estMass [kg]: Estimated all up mass of the aircraft.
- nzmax: Allowable maximum z-acceleration as multiples of sea level g(+ and -) [-].
- cTake _ off _ Type, cLanding _Type: Take-off and landing method. In the GMDSO Tool, the methods implemented are the horizontal and vertical take-off and landing methods.

A block diagram showing the flow of data in the mission specification module is shown in Figure D.14.

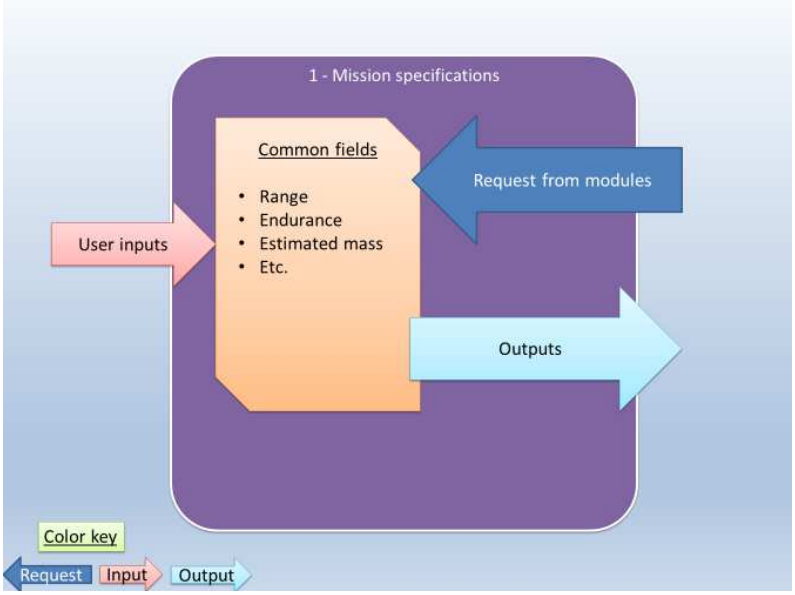


**Figure D.14:** Data Flow in the Mission Specification Module.

## D.3 2-Propulsion Specifications Module

The propulsion specifications module sets the static properties of the propulsion system in use. This includes the static thrust, number and type of power - plant and fuel properties for the propulsion system(s). Usually, most aircraft use one type of propulsion system with different number of power - plants. However, spacecraft often combine different types of propulsion systems in order to enable take - off and low speed flights. In the propulsion specification module, the list of power - plants is populated with objects of the power - plants abstract class as shown in Figure D.15.

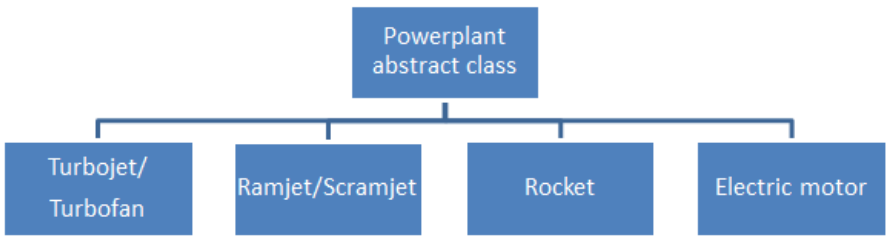


**Figure D.15:** Power - plant Types Implemented in the GMDSO Tool.

The data flow and operations within the propulsion specification module is given in Figure D.16.

Within the propulsion specification module, a method is developed to extract the available fuel and oxidizer stored on-board the aircraft based on an assumed specified fuel fraction.

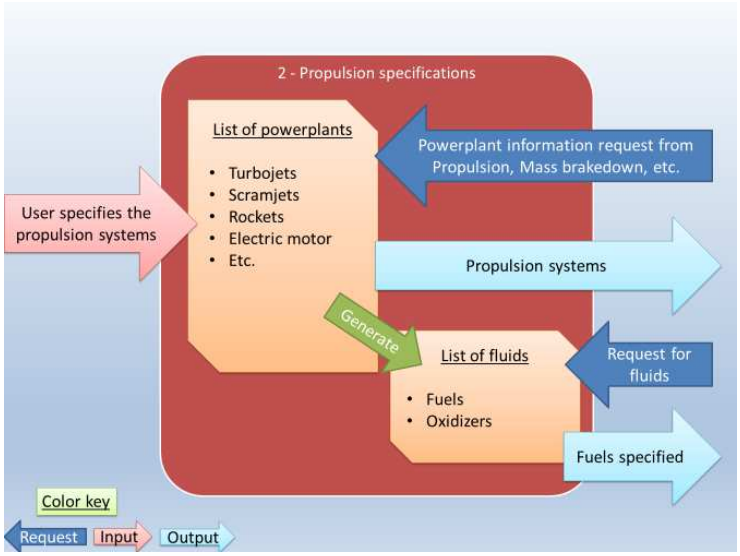


**Figure D.16:** Operations in the Propulsion Specification Module.

### D.3.1 Power - plant Class

The power - plant class calculates the thrust available, SFC and efficiency of the selected propulsion system type for every Mach number, altitude, fuel type and throttle setting. This information is subsequently used to asses the capacity of an aircraft to deliver the necessary thrust in any given flight regime. Consequently, the power - plant or propulsion class is designed to return a 2 dimensional array of doubles denoting the SFC and available thrust at any given flight condition.

The power - plant class also implements a set of methods that returns the type of oxidizer and fuel used, sends a list of inputs and updates inputs with the values from the GUI/optimiser. The operations within the power - plant class are given in Figure D.17.

Power - plants are assessed for the ability to deliver the needed thrust at the given flight condition and throttle settings using the logic described in Figure D.18.

The choice of fuel and oxidiser types are implemented with the 'Enum' [158] data type in JAVA. 'Enum' allows variables to be a set from a predefined constants or list.

The fuel types available in the GMDSO Tool are the Liquid Hydrogen(LH2), Kerosene, Liquid Methane (LMethane), Liquid Ethanol (LEthanol), Hydrazine, Unsymmetrical Dimethylhydrazine Liquid Ethanol (UDMH) and electricity. The GMDSO Tool consider electricity as fuel because it is the main source of energy in the solar powered UAV. The list of oxidisers available for selection include none, air, Liquid Oxygen (LOX), Hydrogen Peroxide (H2O2) and the Dinitrogen Tetroxide (N2O4).

For each fuel type, the following properties must be defined:

- Density $[kg/m^3]$.
- Constant specific heat of fuel, Cpfuel $[J/kg/K]$.
- Specific gas constant of fuel(gaseous form), $Rspec[J/kg/K]$.

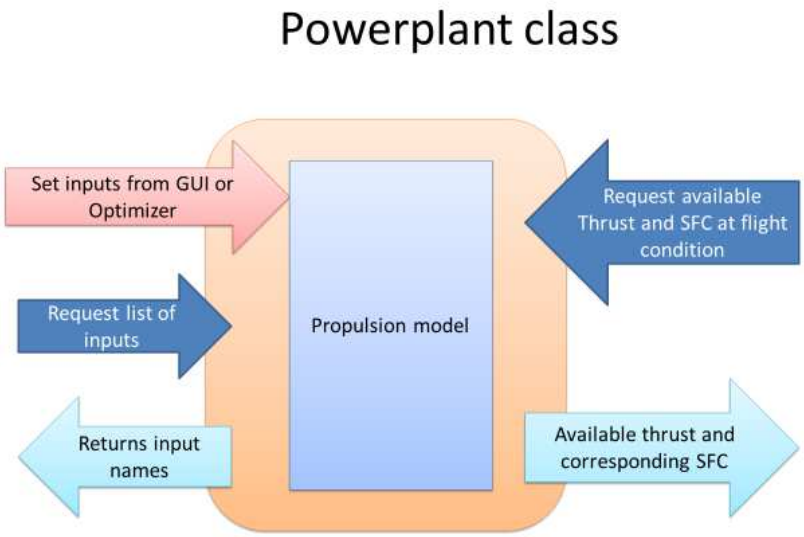


**Figure D.17:** Operations in the Power - plant/Propulsion Module.

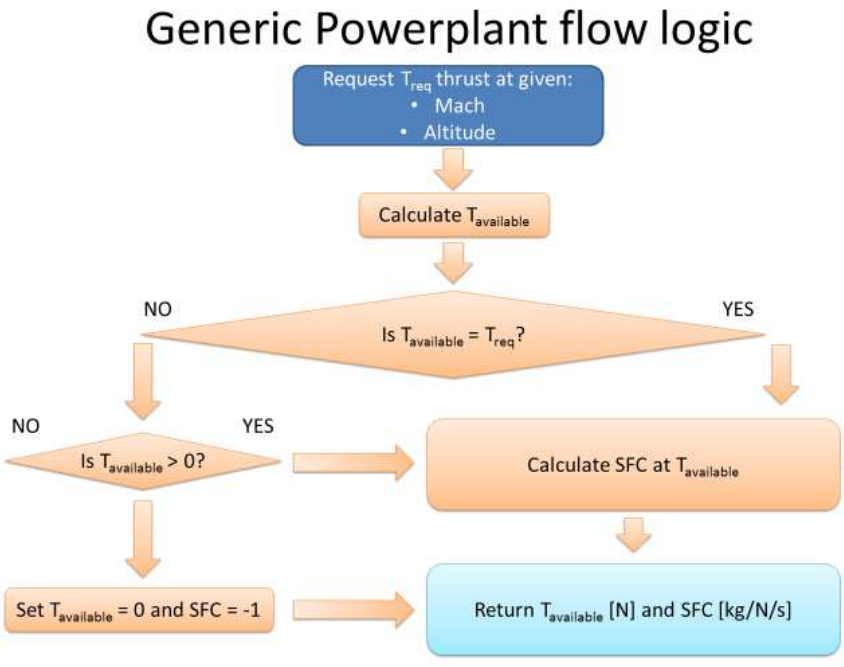


**Figure D.18:** Logic Employed in Power - plant Evaluation.

- Ratio of specific heats, $gamma[-]$.

- Temperature of fuel, $storageTemp[K]$.
- The boolean, *storable*, specifying whether the fuel has to be stored in a fuel tank or not.

For the oxidiser, the properties that must be the specified are:

- Density $[kg/m^3]$
- The boolean, $storable[-]$, specifying whether the fuel is stored in a tank or not.

It is important to note that the mono-propellant fuel 'UDMH' is only used when 'none' is selected as the oxidizer. Also, when the selected fuel is electricity, the density is set to zero.

### D.3.2 3 - Mass Breakdown

The mass - breakdown module provides a framework for estimating the mass of major components of an aircraft. It also decouples the mass components from the modules that generated them for use in the packaging module. The main operations within the mass breakdown module is given in Figure D.19.

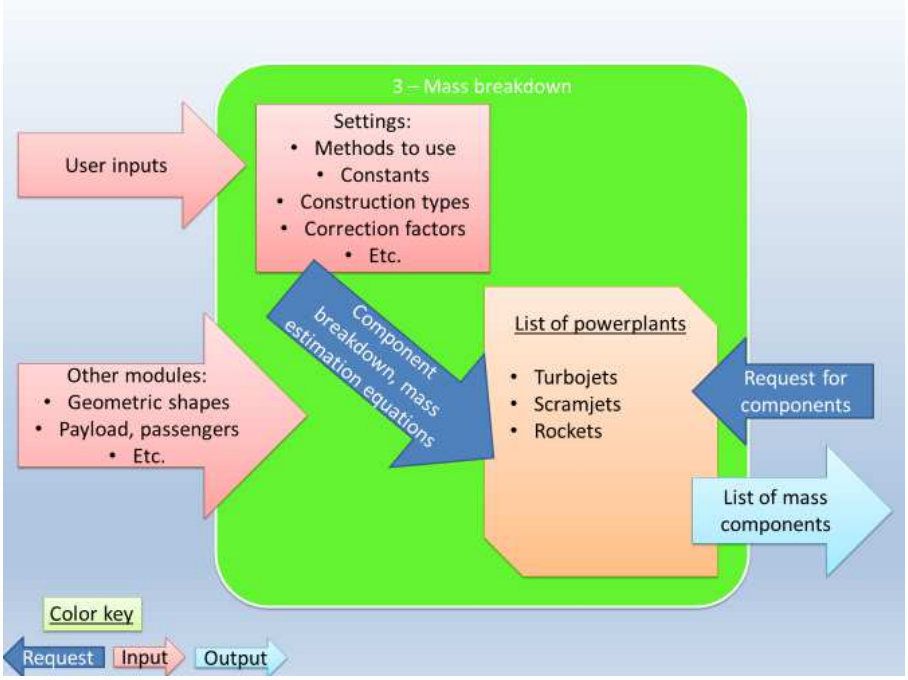


**Figure D.19:** Layout of the Mass Breakdown Module.

The mass - breakdown module generates an array of mass components. The mass component class is an abstract class with various sub - classes for the different components of the aircraft. The hierarchy of the mass components in the GMDSO Tool is shown in Figure D.20.

The properties of each mass component is defined by the following fields:

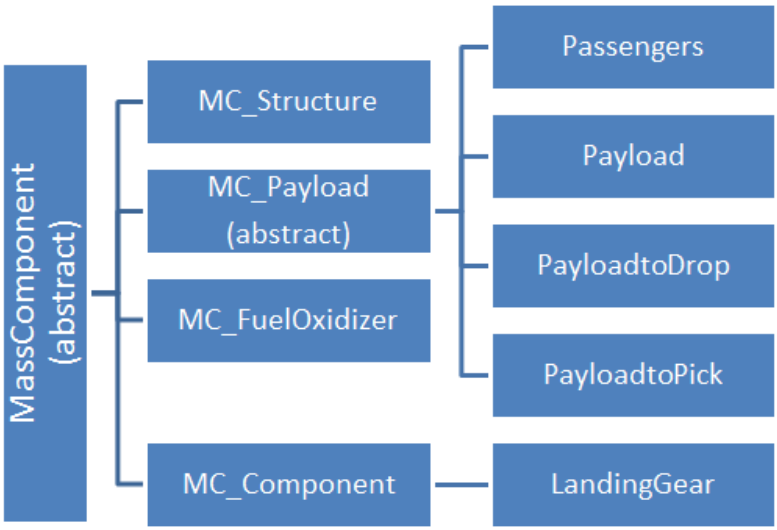


**Figure D.20:** Hierarchy of Mass Components and Sub-Classes in the GMDSO Tool.

- myShape: myShape is used to describe the shape of each mass components using basic shapes such as :
  - Box.
  - Cylinder.
  - Sphere.
  - Conformal.
  - Distributed.
- myVolume: MyVolume is used to define the volume of the component. It is taken as -1 if the volume was not known when the shape was generated.
- myCGPos: myCGPos is an array of the CG positions for all mass components.
- myMaster: MyMaster is used to specify the reference part of the mass component when the component is linked to a GeometrycPart like in structural masses.
- myContainer: myContainer specifies the reference component when a mass component is linked to another. For instance, fuel to the fuel tank.
- myName: myName is the unique designation of the mass component.
- myMass: myMass is the estimated mass of the component. MyMass should always be defined. If the mass of the component is unknown, myMass should be set to zero.

It is essential to specify as many of the properties of a mass component as possible. This is because such comprehensive description enables the GMDSO Tool to accurately package the components and determine the aircraft CG. Other inputs of the mass components depending on the selected shape and whether the volume is known or unknown are given in Table D.1. In addition to the mass of the various components, the mass - breakdown module also calculate the MTOM, ZFM, OEM and MLM.

**Table D.1:** Shape and Volume Dependent Inputs to the Mass Component

| Shape | Characteristic | Inputs with Unknown Volume | Input with Known Volume |
|---|---|---|---|
| Box | X,Y,Z | X,Y,Z | Y/X, Z/X |
| Cylinder | L,R | L,R | L/R |
| Sphere | R | R | None |
| Conformal | None | None | None |
| Distributed | None | None | None |

## D.4 4 - Aerodynamics Analysis Module

The aerodynamic module predicts the aerodynamic coefficients from the mission flight conditions and the geometry specified in the geometry module using any of the implemented analysis methods. The analysis methods implemented in the GMDSO Tool are the AVL methods, SHABP, Digital Datcom and the empirical methods. Besides the empirical method, all the other analysis methods are pre-coded in the FORTRAN programming language. The aerodynamic analysis module integrates the FORTRAN written codes into the JAVA development environment through the C++ using the JAVA Native Interface. The aerodynamic analysis module as implemented in the GMDSO Tool is shown in Figure D.21.

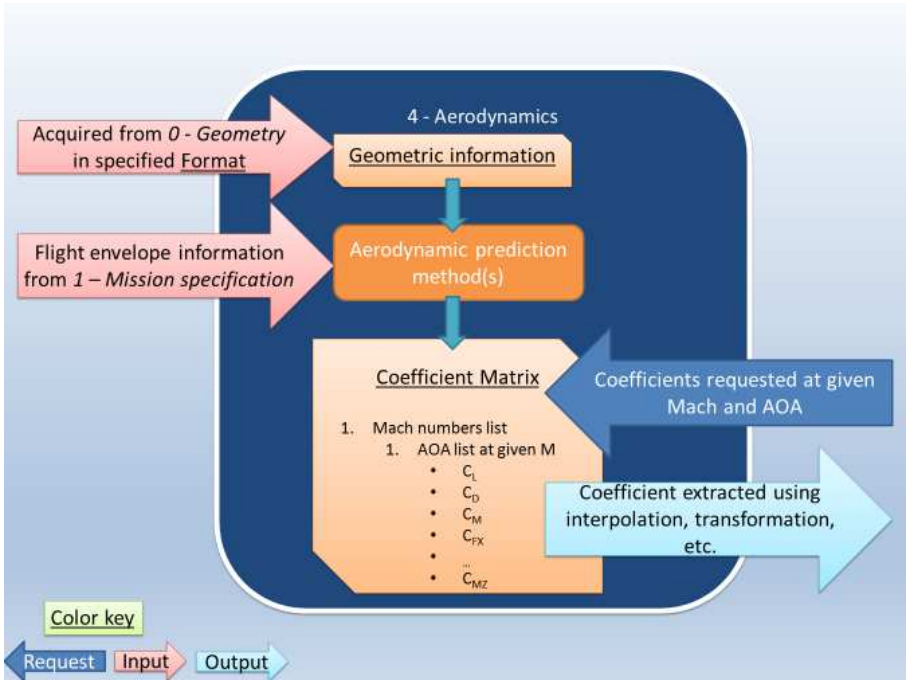


**Figure D.21:** Layout of the Aerodynamic Analysis Module.

The aerodynamics coefficients derived from the analysis method is stored in a common format called the Coefficient Matrix. The Coefficient Matrix enables a uniform and structured storage of the aerodynamic coefficients. In addition, it contains reference values used to non-dimensionalise the forces and moments. The reference values ensure consistency in the derived coefficient irrespective of the analysis method applied. The reference values

used in the aerodynamics module of the GMDSO Tool are the reference area, usually the gross wing area or plan - form area; the reference longitudinal dimension or the Mean Aerodynamic Chord (MAC); and the reference dimension normal to flow, usually the wing span. The structure of the coefficient matrix in the GMDSO Tool is shown in Figure D.22.

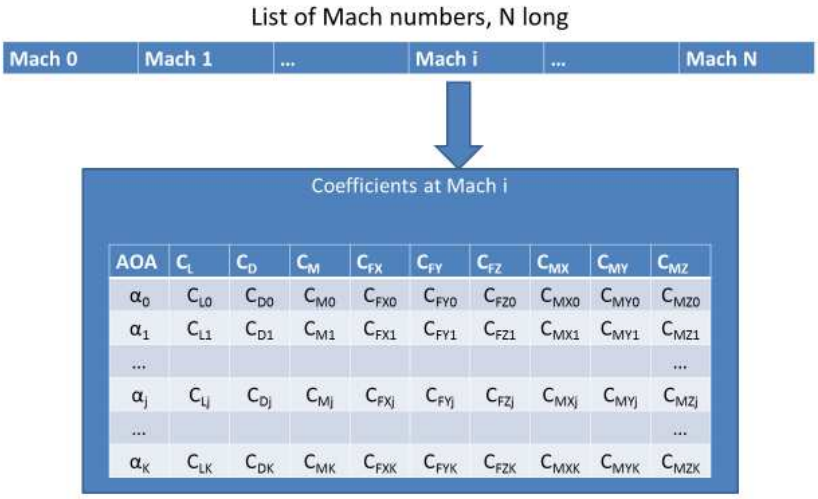


**Figure D.22:** Structure of the Coefficient Matrix in the GMDSO Tool.

The main coefficients extracted from the aerodynamic analysis methods are:

- The lift coefficient ($C_L$).
- The drag coefficient ($C_D$).
- The pitching moment coefficient ($C_M$).
- The rolling moment coefficient ($C_{MY}$).
- The axial force ($C_{FX}$).
- The side force ($C_{FY}$).
- The normal force ($C_{FZ}$) coefficients in the body axis coordinate system.

Only $C_L$, $C_D$ and $C_M$ must always be extracted from any analysis method. Other forces and coefficients are optional. It is therefore essential for the knowledgeable user to understand the coefficients evaluated while requesting for coefficients in any analysis module before making request for coefficient in subsequent modules of the GMDSO Tool.

In order to protect the modularity property of the GMDSO Tool, aerodynamic and stability derivatives are not extracted within the aerodynamics analysis modules. The derivatives could nonetheless be derived from the coefficient matrix by manipulating the coefficients accordingly. For instance, to determine the lift curve slope with respect to

angle of attack can be determined by Equation D.4.

$$C_{L\alpha}@\alpha_j = \frac{C_{Li} - C_{Li-1}}{\alpha_i - \alpha_{i-1}} \tag{D.4}$$

Where:
$\alpha_i$ and $\alpha_{i-1}$ are the bounding angles of attack values to the angle of attack of interest $\alpha_j$ available in the coefficient matrix closest.

The determination of derivatives in this manner permits the treatment of non-linear aerodynamic coefficients. This is because it permits the calculation of local derivatives at every point or angle of interest. However, in order to fully characterise the aircraft longitudinal aerodynamic performance, only the $C_L$ values at $\alpha_{min}$ and $\alpha_{max}$ and the $C_D$ values at corresponding $C_L$ are required.

The coefficient matrix implemented in the GMDSO Tool does not differentiate between Mach or Reynolds number derived coefficients. However, an array of coefficient matrices for coefficients at same Mach Number but different Reynolds Number could be created. This is how the effect of side - slip, roll, pitch etc are included in the coefficient derivative matrix.

An important feature of the aerodynamic analysis module is the flexibility to override the Coefficient Matrix or set it up to perform evaluations on demand rather than mapping the whole flight envelope. The list of methods used in the extraction of required information in the Coefficient Matrix class are as follows:

- addResultatMach: The addResultatMach adds results at a given mach number. Additionally, it stores the calculated coefficients and corresponding angles of attack and its corresponding mach number in ascending order in a matrix.
- getCoeffatMandAlpha: This method extracts the selected type of coefficient at the given mach number and angle of attack. If no evaluations were performed at the exact mach number and angle of attack, the values are linearly interpolated between the 2 closest bounding values. If the requested value exceeds the range of evaluated angles of attack, the extreme values are returned.
- getMaxCoeff: The method 'getMaxCoeff' returns the maximum value of the requested coefficient type from the range of angles of attack evaluated.
- getMinCoeff: The getMinCoeff method returns the minimum value of the requested coefficient type from a range of angles of attack evaluated.
- getAOAatMachatCL: This method returns the angle of attack corresponding to a given lift coefficient at the given mach number. If the requested values exceed the minimum or maximum values, the extreme value would be returned.

## D.5 6 - Propulsion Module

The propulsion module estimates the thrust available and the specific fuel consumption at any given flight condition and thrust setting. This is necessary in order to determine the fuel efficiency and assess if a given configuration is capable of providing the thrust required at a specified flight condition. The main requirement of the propulsion module is that it must be capable of handling arbitrary number of propulsion systems in any flight condition. The design of the propulsion module showing constituent parts is given in Figure D.23.

Further to determining the thrust available and specific fuel consumption, the propulsion module includes logic for distributing the thrust amongst the different types of power -

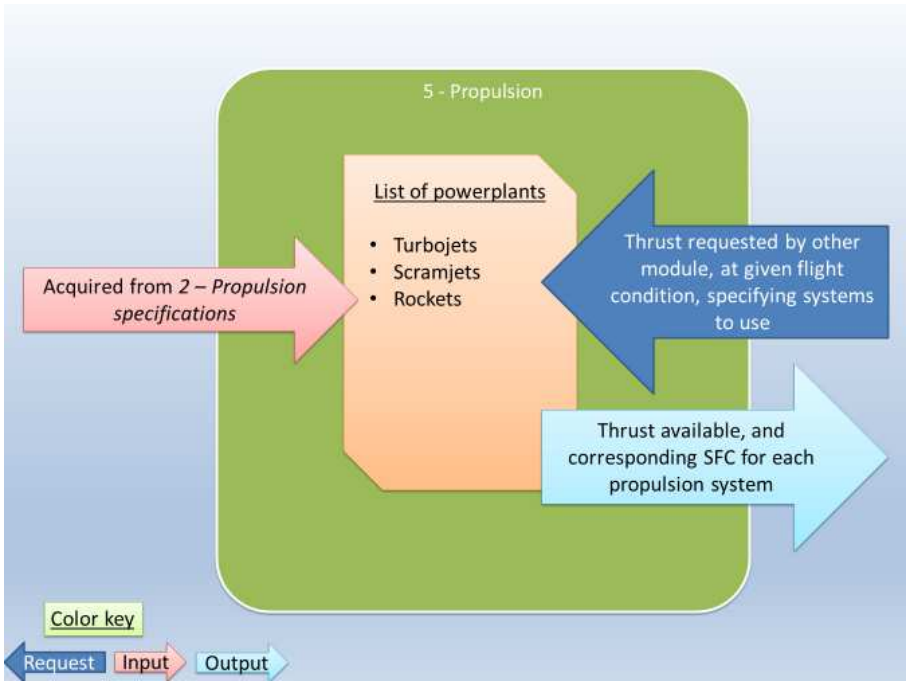


**Figure D.23:** Design of the Propulsion Module.

plants on-board the vehicle. The logic could be to provide the required thrust with the least amount of fuel consumption or maximize fuel consumption in order to complete mission in the least possible. This is useful in emergency situation where speed is the essence. For instance in emergency landing.

The methods used to extract the thrust from the propulsion module are the 'getPropulsion' Method and the 'ThrustOutput' class. The 'getPropulsion' is an abstract method used to determine available thrust from the Mach Number, altitude, required thrust and the list of power - plant where applicable. The power - plant list allows other modules to keep track of such power - plant conditions as running out of fuel, warm-up or cool down, and disabling air - breather engines above a certain altitude if the power - plant list is not suitably designed to deal with it.

The ThrustOutput class calls other methods with all the power - plant enabled. The ThrustOutput takes an array of distributed thrust values and SFC as well as the thrust and total fuel flow. The propulsion module decouples the performance of the power - plants and the logic controlling the selection of different systems from the performance calculations.

## D.6 Packaging and Centre of Gravity

The packaging module positions aircraft components within the vehicle geometry in order to determine the centre of gravity as well as ensure that the components are suitably enclosed within the geometry. The CG is evaluated for conditions with and without fuel and payload using individual masses and CGs of the mass components generated from the mass breakdown module.

The design of the packaging and CG module showing the constituent parts is shown in Figure D.24.

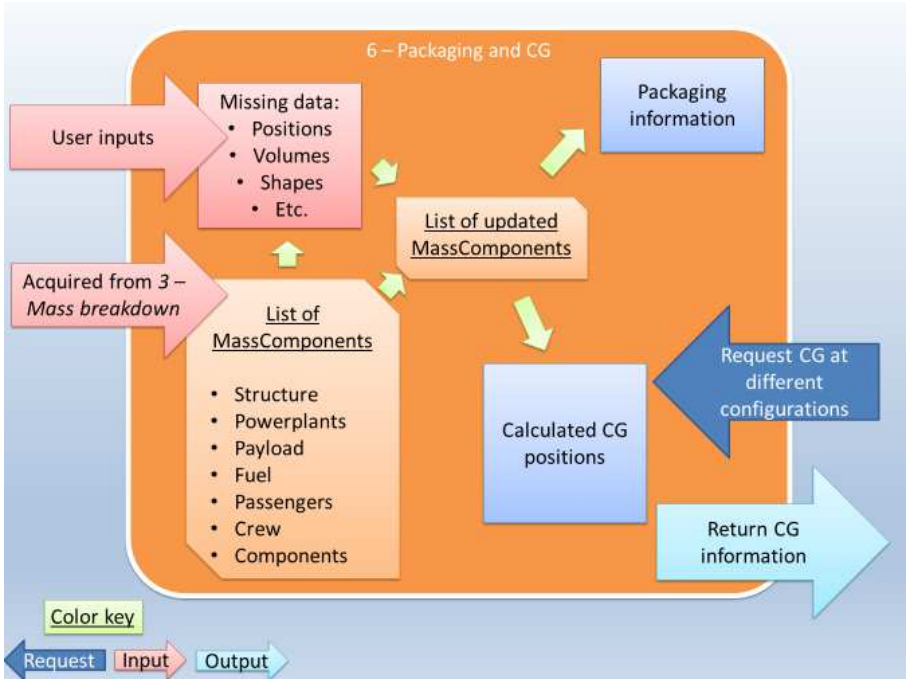


**Figure D.24:** Design of the Packaging and CG Module.

The CG positions are returned from the packaging module as XYZ coordinates in the body axis coordinate system. These coordinates are stored within the GMDSO Tool as an array of $N \times 3$ matrix.

Where:
$N$ is the number of CG positions generated.
$N$ has a minimum value of 4.

The first four elements of the $N \times 3$ matrix are the MTOM, ZFM, OEM and MLM in ascending index values from 0 - 3.

Additional CG positions could be evaluated as required and added as the fifth and subsequent elements of the matrix. However, it is expedient to maintain the order of the first 4 elements as specified. This is necessary in order to be able to calculate the CG during various flight phases. With the order of the $N \times 3$ retained, the CG in various phases of the flight can be determined by interpolating between the CG positions at the specified mass values.

In order to fit the components within the aircraft configuration, the packaging module compares the volume of internal components to the volume of the aircraft external geometry. The result of the comparison is an error information that determines if the internal volume fits into the structure of the vehicle under design or not. Further to the volume error, the packaging module also ensures no component interferes with the external geometry by carefully manipulating the volume and distance of each component.

Ordinarily, it would have been ideal for the internal components to fit in perfectly into the external geometry. However, this is quite a computational challenge in a computer based design synthesis due to round-off and truncation error. Hence, forcing the components to fit in perfectly could lead to slow or no convergence. Consequently, its always a good programming practice to allow a reasonable but negligible tolerance between the internal and external volume.

## D.7 8 - Performance Module

The performance module evaluates whether a single instance of the GMDSO Tool is capable of fulfilling the specified mission. The GMDSO Tool performance module assesses the field and point performance of the given design. Point performance is concerned with the aircraft's ability to perform certain manoeuvres at different points of the mission including climb gradient and instantaneous or sustained turn rates amongst others.

The inputs to a performance module are usually the performance targets or settings for the methods. The outputs are the the calculated performance characteristics and error indicators between the calculated and target values. The calculated values can be used as the target/objective/cost function by the optimiser while the error indicators are used as constraints in the optimisation process.

The layout of the performance module showing the constituent parts is given in Figure D.25.By virtue of its function, the performance module usually do not send inputs to any other module, except to the stability evaluation module. The performance module sends a list of the various flight conditions to the stability module as an array of the FlightCondition class. Each member of the FlightCondition class consist of the flight Mach Number, altitude, thrust distribution and mass configuration (fuel, payload,etc).

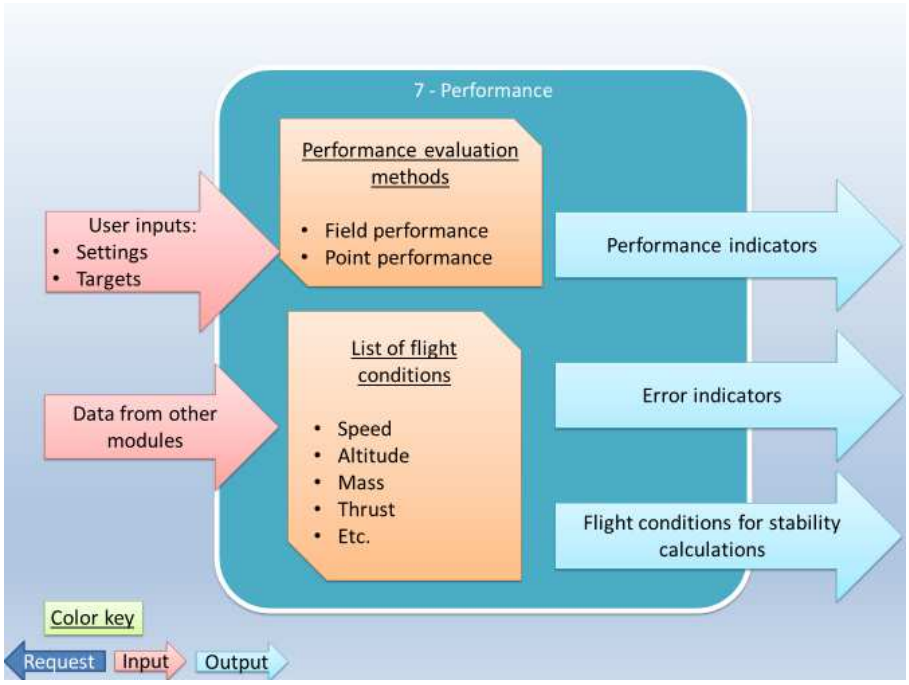


**Figure D.25:** Design of the Performance Module.

Methods implemented in the performance module could be as simple as the Bereguet range equation or as complex as a time domain simulation of the whole mission or mission segments.

## D.8 9 - Stability and Control

The stability and control module is used to evaluate the static margin, longitudinal stability and trim-ability of the aircraft at various flight conditions and configuration. The

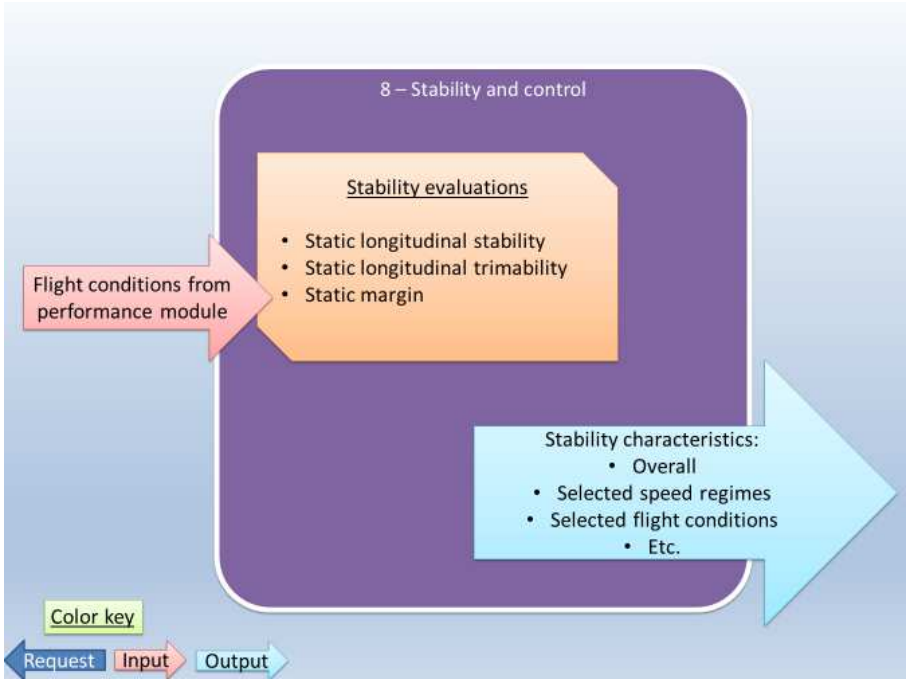


**Figure D.26:** Layout of the Stability and Control Module.

design of the stability and control module is described in Figure D.26.

The stability and control module does not provide inputs for any module but generates outputs that could be used to drive the optimisation process. These outputs are usually error indicators that state whether the aircraft is stable or not in a given flight condition, speed regime and/or the whole mission envelope.

The stability and control module uses a list of flight conditions obtained from the performance module to evaluate the stability and control characteristics. The list of fields in the flightCondition class are:

- The flight mach number[-].
- The Cruise altitude[m].
- CG position [m,m,m].
- current mass of the vehicle[kg].
- Power - plant thrust distribution[N].
- Angle of attack[rad].
- Flight path angle[rad].
- The name of the flight condition or phase of flight.